DEVELOPMENT OF AUTONOMOUS IN SITU TECHNIQUES TO EXAMINE THE IMPACTS OF DYNAMIC FORCINGS ON SEDIMENT BIOGEOCHEMISTRY IN HIGHLY PRODUCTIVE ESTUARINE ECOSYSTEMS

A Dissertation
Presented to
The Academic Faculty

by

Deidre J Meiggs

In Partial Fulfillment
of the Requirements for the Degree
Doctor of Philosophy in the
School of School of Earth and Atmospheric Sciences

Georgia Institute of Technology
December 2010

COPYRIGHT 2010 BY DEIDRE J MEIGGS

DEVELOPMENT OF AUTONOMOUS IN SITU TECHNIQUES TO EXAMINE THE IMPACTS OF DYNAMIC FORCINGS ON SEDIMENT BIOGEOCHEMISTRY IN HIGHLY PRODUCTIVE ESTUARINE ECOSYSTEMS

Approved by:

Dr. Martial Taillefert, Advisor
School of Earth and Atmospheric Sciences
Georgia Institute of Technology

Dr. E. Michael Perdue
School of Earth and Atmospheric Sciences
Georgia Institute of Technology

Dr. Ellery Ingall
School of Earth and Atmospheric Sciences
Georgia Institute of Technology

Dr. George W. Luther III
College of Earth, Ocean and Environment
University of Delaware

Dr. Philippe Van Cappellen
School of Earth and Atmospheric Sciences
Georgia Institute of Technology

Date Approved: Nov 8th, 2010

ACKNOWLEDGEMENTS

Many thanks are due to my adviser, Dr. Martial Taillefert, for six and a half years of support, guidance, and inspiration. Through all the ups and downs, sea sickness, rejections, and broken ankles, one could not ask for a more assiduous and skillful adviser. Thank you for giving me the opportunity to complete my thesis at such a prestigious institution, and for aiding me throughout this stage of my professional development. Through your example I have learned countless life lessons, and I am beholden to you for helping me realize my true vocation.

Additionally, I wish to thank the members of my committee, Dr. Ellery Ingall, Dr. George Luther III, Dr. Michael Perdue, and Dr. Philippe Van Cappellen for their well thought criticisms and valuable insights that have improved this dissertation.

I wish to thank various past and present members of the Taillefert lab who have positively impacted this research through their helpful comments in group meetings including Jordon, Patrick, Kate, Melanie, Emily, Anna, Keaton, and Colin. Special thanks are due to Gwen Bristow for being a wonderful officemate and friend and to Morris Jones for his innovative ideas and electronic expertise.

Finally, I wish to thank my parents and brother for their loving support, my friends for all their bolstering affirmations, and Jim for steadying me on the tight rope of life. I know in my heart that without your daily support, reassurance, and love, I never would have finished this dissertation.

TABLE OF CONTENTS

LIST OF TABLES

LIST OF FIGURES

.

LIST OF SYMBOLS AND ABBREVIATIONS

NOM	Natural Organic Matter
DOU	Dissolved Oxygen Uptake
TOU	Total Oxygen Uptake
SWI	Sediment Water Interface
CSB	Colorless Sulfur Bacteria
SOB	Sulfide Oxidizing Bacteria
GSB	Green Sulfur Bacteria
PSB	Purple Sulfur Bacteria
CYA	Cyanobacteria
SAT 1 – 5	Satilla River Sampling Locations
SERF	Salt Marsh Ecosystem Research Facility
CB	Creek Bank
MF	Mud Flat
ISEA	In situ Electrochemical Analyzer
LSV	Linear Sweep Voltammetry
CSW	Cathodic Square Wave Voltammetry
ASW	Anodic Square Wave Voltammetry
CV	Cyclic Voltammetry
DIC	Dissolved Inorganic Carbon

SUMMARY

Characterized by high levels of terrestrial organic carbon inputs, estuaries and coastal marshes are among the most productive ecosystems on earth and significantly impact the global carbon cycle. Unfortunately, rates of natural organic matter (NOM) degradation in these environments are difficult to quantify directly due to the complex interaction between microbial respiration processes and abiotic reactions in these sediments, yet estuaries and marshes are considered both net sources and sinks of carbon. Typically carbon remineralization rates are determined by measuring total (TOU) and diffusive (DOU) oxygen uptake fluxes assuming oxygen is the ultimate oxidant. This assumption, however, requires any reduced metabolites produced during microbial respiration to be reoxidized by oxygen. In this study, voltammetric sensors were used to measure terminal electron acceptors or their reduced by-products. By simultaneously considering oxygen as well as anaerobic respiration accepting processes, this study demonstrates that oxygen does not function as the ultimate oxidant in coastal marine sediments due to precipitation and burial of reduced species.

Furthermore, the biogeochemistry of coastal sediments is typically investigated ex situ after collection of sediment cores. However, coastal sediments are subject to complex subsurface hydrological forcing that cannot be accounted for with ex situ measurements. Consequently, in situ approaches are required to better understand the impact of physical processes on sediment biogeochemistry, and two novel in situ voltammetric systems were developed as part of this research. First, a new autonomous benthic lander equipped with a benthic chamber to measure TOU fluxes with a high

temporal resolution and a potentiostat and micromanipulator to simultaneously acquire voltammetric depth profiles of the main redox species in pore waters was deployed in a pristine river-fed estuary to characterize the seasonal variability of coastal sediment biogeochemistry and examine the impact of riverine discharge on carbon remineralization processes. Simultaneously, a new electrochemical analyzer equipped with a solar and wind power charging system to ensure continuous monitoring capability and a VHF radio to transmit data was operated remotely via the internet from the Georgia Tech campus to investigate the dynamic coupling between hydrological, chemical, and biological processes in intertidal marsh sediments. Finally, new microelectrodes were deployed in microbial mats to examine the chemical and biological oxidation of sulfide with submillimeter resolution. Typically, only biological processes are considered to oxidize sulfide in these environments. Depth profiles during diel studies were able to demonstrate the formation of thiosulfate as an intermediate oxidation product of sulfide oxidation, suggesting that the chemical oxidation of sulfide is much more prevalent than previously recognized when compared to biological oxidation.

Overall, using a novel in situ sampling technique with high temporal resolution, these studies confirm that biogeochemical processes in coastal sediments vary seasonally. More importantly, these studies also reveal that estuarine sediments are significantly influenced by riverine discharge, demonstrate that the biogeochemical response of these sediments to natural perturbations is rapid, and indicate that respiration processes in continental shelf sediments are controlled by a combination of temperature, supply of inorganic and organic substrates, and hydrological processes, which has important

implications regarding the effect of climate change on the biogeochemical cycling of carbon in these environments.

CHAPTER 1

INTRODUCTION

The Importance of Carbon Remineralization

Increased industrialization over the last century, the burning of fossil fuels for energy, and the clear-cutting of forests are rapidly changing the balance of present day carbon reservoirs. These actions have caused atmospheric carbon dioxide levels to rise, reaching amounts heretofore never experienced by the majority of current species on this planet (Berner and Lasaga, 1989). The increasing flux of carbon dioxide into the atmosphere over the last 50 years has raised environmental concerns regarding the impacts of anthropogenic forcings on natural environments, and carbon dioxide is now the most widely discussed greenhouse gas in the context of global climate change (Metz et al., 2007). The recently recognized importance of riverine and continental margin sediments to carbon cycling has heralded their incorporation into carbon budgetary analyses, possibly as an important atmospheric carbon sink that was previously neglected (Liu et al., 2000; Solomon et al., 2007). However, these systems experience extremely high levels of terrestrial carbon input (Hedges et al., 1997), and it has been suggested that the export of organic carbon from coastal marshes to continental margin sediments and subsequent remineralization may actually be a source of atmospheric carbon (McKenzie et al., 1998; Cai et al., 2000).

Quantifying the rate of carbon preservation in sediments is of crucial importance to determining the net flux of carbon to the oceans accurately (Hedges et al., 1997). Continental margins cover a modest 20% of ocean surface area, and therefore the

majority of diagenetic investigations have focused on the deep ocean. Yet, continental margins are responsible for ~15% of the ocean's net primary productivity (Wollast, 2003), and transport models predict less than 10% of the particulate organic carbon (POC) from this primary production is transported to ocean depths below 1500 m (Martin et al., 1987; Pace et al., 1987). More recent findings indicate that 40% of annual organic carbon burial occurs in continental margin sediments (Muller-Karger et al., 2005) where sedimentation rates are enhanced due to abrupt changes in salinity (Hakanson, 2006). When the fresh water from these estuaries mixes with marine water, the corresponding increase in ionic conductivity and pH promotes rapid removal of particles by adsorption and flocculation (Sholkovitz, 1976; Eisma, 1986). These areas receive an enhanced supply of nutrients and carbon from upwelling and riverine inputs (Wollast and Chou, 1998) and act as a filter and trap for both natural and anthropogenic materials transported from land to the open ocean (Mantoura et al., 1991). Consequently, to assess the changing role of the land-ocean transition in regulating fluxes of carbon dioxide to the atmosphere, a comprehensive understanding of organic carbon cycling in coastal ecosystems is crucial to assess the changing role of the land-ocean transition in regulating fluxes of carbon dioxide to the atmosphere.

Coastal habitats are complex blends of terrestrial, aquatic, and marine communities. Unfortunately, these ecosystems have been neglected from general circulation models, as their complexity is extremely difficult to model and requires analyses of time- consuming, regional-scale processes (Ver et al., 1999). The complex web of intertwined physical, chemical, and biological interactions enhances modeling difficulties and exacerbates the methodological problems associated with sampling and

measurements. For example, the complex, heterogeneous nature of natural organic matter (NOM) makes it impossible to ascertain its rate of decomposition directly (Burdige, 2006). Oxidation of NOM occurs through a complex web of processes including fermentation and oxidation of organic acids that are not clearly understood (Burdige, 2006). As a result, geochemists have used sediment incubations to quantify rates of carbon remineralization. Incubations are generally conducted using either whole cores or sections of sediment (e.g. Howarth and Giblin, 1983; Hines et al., 1989; Canfield et al., 1993 a), and flow-through reactors are also frequently used to study the biogeochemical complexity of sediments in more realistic conditions (e.g. Carey and Taillefert, 2005; Pallud, et al., 2007). Unfortunately, these measurements are time-consuming and may modify the activities of microbial assemblages (Hammond et al., 2004). Thus, the ability to perform in situ measurements, though more complicated logistically, is required to determine more accurate rates of carbon remineralization.

Chemical oceanographers have quantified rates of carbon remineralization in situ using incubations in benthic chambers and depth profiles using oxygen microelectrodes to measure oxygen consumption near the sediment water interface (e.g. Archer and Devol, 1992; Glud and Gundersen, 2002; Wenzhofer et al., 2002; Berg et al., 2003). Oxygen consumption rates are then related to carbon remineralization rates using appropriate C:N ratios of NOM in the sediment (Burdige, 2006) and electron equivalents provided by the oxidation of reduced metabolites by oxygen (Canfield et al., 1993a;Wenzhofer et al., 2002). Oxidation rates of NOM determined in this manner assume oxygen to be the ultimate oxidant and thus presume that nitrite, ammonium, manganese (II), iron (II), and sulfides produced during the anaerobic oxidation of NOM

are reoxidized when they diffuse to the oxic sediment layers. This assumption may be more appropriate for pelagic sediments, which lack the microbial diversity and the complex geochemistry of continental shelf sediments, in response to the low carbon fluxes to the sea floor (Burdige, 2006). Riverine and estuarine ecosystems however, have potentially the highest biotic diversity and productivity in the world (Bianchi, 2007) suggesting that a complex web of abiotic and biotic reactions may interfere with these processes. Therefore additional steps must be taken to more accurately estimate NOM degradation rates.

Another source of error generally associated with these calculations is the use of the Redfield ratio to determine the average oxidation state of carbon, as it assumes irrealistically all NOM to be in the form of carbohydrates (Table 1.1). It has been shown, using a combination of size exclusion chromatography, empirical calculations, and mass spectrometry, that the oxidation state of marine phytoplankton is not 0 as predicted by the Redfield ratio, but rather ranges between -0.45 (Anderson, 1995) and -0.49 (Hedges et al., 2002). More recently, the average oxidation state of carbon in NOM from coastal waters has been determined to be around +0.27 (Perdue, 2009).

Table 1:1: The order of thermodynamically favorable decomposition reactions assuming that (1) the oxidation state of carbon is zero and (2) the C:N:P ratio is 106:16:1 as per the Redfield ratio (Froelich et al., 1979; Berner and Berner, 1996).

Organic Matter Oxidation Reaction	ΔG_{rxn}^{o} (kJ/mole)
$(CH_2O)_{106}(NH_3)_{16}(H_3PO_4) + 138\ O_2 \rightarrow$ $106\ CO_2 + 16\ HNO_3 + H_3PO_4 + 122\ H_2O$	-3190
$(CH_2O)_{106}(NH_3)_{16}(H_3PO_4) + 236\ MnO_2 + 472\ H^+ \rightarrow$ $236\ Mn^{+2} + 106\ CO_2 + 8\ N_2 + H_3PO_4 + 366\ H_2O$	-3050
$(CH_2O)_{106}(NH_3)_{16}(H_3PO_4) + 94.4\ HNO_3 \rightarrow$ $106\ CO_2 + 55.2\ N_2 + H_3PO_4 + 177.2\ H_2O$	-3030
$(CH_2O)_{106}(NH_3)_{16}(H_3PO_4) + 424\ FeOOH + 848\ H^+ \rightarrow$ $424\ Fe^{+2} + 106\ CO_2 + 16\ NH_3 + H_3PO_4 + 742\ H_2O$	-1330
$(CH_2O)_{106}(NH_3)_{16}(H_3PO_4) + 53\ SO_4^{-2} \rightarrow$ $53\ S^{-2} + 106\ CO_2 + 16\ NH_3 + H_3PO_4 + 106\ H_2O$	-380
$(CH_2O)_{106}(NH_3)_{16}(H_3PO_4) \rightarrow$ $53\ CH_4 + 53\ CO_2 + 16\ NH_3 + H_3PO_4$	-350

To accurately calculate carbon remineralization rates, the corresponding changes in carbon equivalents during anaerobic respiration processes may be calculated from the changes in concentrations of terminal electron acceptors or their corresponding reduced species and the appropriate electron transfer equivalents for denitrification, dissimilatory reduction to ammonium, dissimilatory manganese, iron, and sulfate reduction (Equation 1; assuming an initial carbon oxidation state of zero).

$$\Delta[N_2] + \Delta[NO_3^-] + \Delta[Mn^{2+}] + \Delta[Fe^{2+}] + \Delta[H_2S] =$$

$$0.4*\Delta[CH_2O] + 0.5*\Delta[CH_2O] + 2*\Delta[CH_2O] + 4*\Delta[CH_2O] + 0.5*\Delta[CH_2O] =$$

$$7.40*\Delta[CH_2O] \quad (1)$$

If different carbon oxidation states of marine and coastal NOM are utilized for carbon remineralization calculations, the number of carbon equivalents remineralized by anaerobic respiration processes can be estimated more accurately (Table 1.2).

Table 1.2: The effect of changing the initial carbon oxidation state of NOM on the calculation of the carbon equivalents remineralized by anaerobic respiration processes.

Carbon Oxidation State	Carbon Equivalents Remineralized
0	$7.40*\Delta[CH_2O]$
+0.27	$6.90*\Delta[CH_2O]$
-0.45	$8.23*\Delta[CH_2O]$
-0.49	$8.31*\Delta[CH_2O]$

The two end member oxidation states only yield a 17% difference in the total amount of carbon equivalents remineralized. As the river system examined in this study receives fresh water inputs from the surrounding estuaries, it was assumed that an initial oxidation

state of organic carbon of +0.27 (Perdue, 2009) was accurate enough to estimate carbon remineralization rates.

While by-products of these anaerobic respiratory processes (e.g. sulfides, ammonium, manganese (II) and iron (II)) may be either chemically or biologically reoxidized by oxygen, burial can also occur by precipitation of iron sulfide minerals, including amorphous FeS, mackinawite, and pyrite or carbonate minerals (siderite and rhodocrosite) (Morse et al., 1992; Canfield et al., 1992; Luther et al., 1992). The removal of reduced species by carbonate precipitation (Eq. 2) (Postma, 1982; Ellwood et al., 1988), sulfide precipitation (Eq. 3) (Postma, 1982; Luther et al., 1992), or chemical reduction of iron and manganese oxides by sulfides (Eq. 4) (Thamdrup et al., 1993) may lead to an innate error in carbon remineralization rate calculations which can be estimated as follows:

$$\Delta[Fe^{2+}] + \Delta[Mn^{2+}] = (-3.73 + -1.86)* \Delta[CH_2O] = -5.59*\Delta[CH_2O] \quad (2)$$

$$\Delta[Fe^{2+}] + \Delta[H_2S] = (-3.73 + -0.47)* \Delta[CH_2O] = -4.2*\Delta[CH_2O] \quad (3)$$

$$2*\Delta[Fe^{2+}] + 2*\Delta[Mn^{2+}] - 1*\Delta[H_2S] =$$

$$(7.46 + 3.72 - 0.47)* \Delta[CH_2O] = 10.71*\Delta[CH_2O] \quad (4)$$

These processes may be falsely attributed to microbial degradation of NOM and thus lead to the underestimation of heterotrophic iron, manganese, and sulfate reduction and an overall miscalculation of NOM oxidation.

Nevertheless, due to the added simplicity of dissolved oxygen measurements, most carbon remineralization studies are performed ex situ using whole-core incubations or dissolved oxygen depth profiles to calculate diffusive oxygen uptake (DOU) fluxes or total oxygen update (TOU) fluxes. These fluxes can then be used to calculate carbon

remineralization rates assuming oxygen functions as the ultimate oxidant. In situ oxygen consumption is quantified based on the DOU flux across the sediment-water interface (SWI), and is generally calculated from depth microprofiles obtained with Clark-type microelectrodes or optodes (e.g. Glud and Gundersen, 2002; Reimers et al., 2004; Glud et al., 2005). Alternatively, calculation of TOU can also be accomplished by monitoring the decline of oxygen concentration in the overlying water using benthic chambers deployed across the SWI (e.g. Berelson and Hammond, 1986) or, more recently, using eddy correlation techniques (Berg et al., 2003). Differences between TOU and DOU fluxes have been attributed to fauna-mediated oxygen uptake (Glud and Gundersen, 2002; Wenzhofer et al., 2002).

Impacts of Hydrological Forcing

Future biogeochemical models need to be based around hydrologic data to enhance their predictive capabilities (Carter et al., 1979); however, tidal advection artificially enhances exchange processes between sediment pore waters and the water column, which substantially complicates carbon remineralization rate calculations, and tests the limits of diagenetic models. Coastal sediments are subjected to complex hydrological features that are influenced by tidal forcing, annual rainfall patterns, and sediment permeability. The propagation and distortion of tides in these environments are influenced by channel geometry, bottom friction, sediment deposition, and the presence of tidal flats all of which affect the tidal and geomorphological sediment properties (Friedrichs and Aubrey, 1994; Huettel et al., 1998; Van Leeuwen et al., 2000). Strong

tidal fluctuations in sediments with high permeability generally lead to higher oxygen uptake (Ziebis et al., 1996), deeper oxygen penetration (Forster et al., 1996), higher degradation rates of natural organic matter because of the constant supply of oxidants (Huettel and Rusch, 2000), and more efficient removal of dissolved reaction products (Huettel et al., 1998). Simultaneously, it has been demonstrated that permeable sediments previously subjected to advective transport processes either through wave action or tides re-equilibrate to a diffusive transport regime within hours of collection (Cook et al., 2007), and fluxes determined from external core incubations were reported to be up to 65% lower than the same fluxes measured with benthic chambers in situ (Hammond et al., 2004). Additionally, a recent study performed under controlled conditions demonstrated that ignoring advective fluxes in sediments leads to the underestimation of NOM remineralization rates (Cook et al., 2007). Finally, sediment topography may enhance advective transport of pore water and solute exchange, because the presence of mounds or ripples forces oxygenated overlying water into the sediment, which generates localized zones for the reoxidation of reduced species and affects the release of reduced metals into the water column (Huettel et al., 1998). These studies all demonstrate that the impact of advection on coastal sediments is not negligible. Advection significantly increases the delivery of oxygen as well as organic particles to deeper sediments, and results in enhanced oxygen consumption and carbon remineralization (Reimers et al. 2004; Franke et al., 2006). It was suggested that these effects were responsible for increasing the rate of removal of oxygen and tracers from benthic chambers in the Satilla River estuary (Jahnke et al., 2003) and for enhancing the rates of oxygen consumption and carbon dioxide production in nearby continental shelf

sediments (Rao et al., 2008). Yet, advective processes are assumed to be negligible in fine-grained sediments, compared to the contributions of bioturbation and irrigation from macrophytes and macrofauna in both intertidal marsh (Christiansen et al., 2000; Kostka et al., 2002; Koretsky et al., 2008) and estuarine (Burdige and Zheng, 1998; Pratiharyet al., 2009) sediments. Macrophytes decrease the horizontal flow velocity in sandy sediments, but not in fine-grained sediments, such as the majority of those examined in these studies (Christiansen et al., 2000; Mann and Wetzel, 2000). The most commonly found plant species in most Atlantic coastal marshes is *Spartina alterniflora* (Otero et al., 2000), and these plants have developed an evolutionary adaptation to maintain their high growth rates and avoid root anoxia during prolonged period of inundation (Lee, 2003). Air spaces referred to as aerenchyma in their root systems (Burdick and Mendelssohn, 1990) allow for transport of oxygen from the aerial portions of the plant into the roots. Red and brown deposits around the roots of *S. alterniflora*, have been documented and identified as ferric and manganese oxide deposits (Teal and Kanwisher, 1966; Mendelssohn and Postek, 1982), which form when oxygen from root aerenchyma comes in contact with reduced metal species found in the surrounding sediments (Sundby et al., 1998). Furthermore, in the intertidal zones of Georgia salt marshes, population densities of Fiddler crabs range from 80 – 200 individuals per square meter (Teal, 1958). These crabs are burrowing organisms, that transport large amounts of living and dead biomass from the lower sediment layers to the surface (Mitsch and Gosselink, 1993). Although crabs are the most common species in marsh ecosystems, polychaete worms *Nereis diversicolor* and *Schizocardium sp*., and the shrimp *Callianassa subterranea* are other examples of burrowing organisms found in estuarine environments, whose burrows affect

oxygen concentrations in sediments (Furukawa et al., 2001; Koretsky et al., 2002). Bioturbation increases sediment permeability and the surface area of sediments exposed to dissolved oxygen from the overlying waters (Taillefert et al., 2007). Sediments around the burrows receive oxygen injections when the surface sediments are exposed to the atmosphere at low tide, and possibly during rising and ebb tides (Hollins et al., 2009). Thus, oxygen transport through macrophyte roots combined with the burrowing activity of macroorganisms transforms anoxic marsh sediments into complex, highly heterogeneous environments characterized by sporadic patches of oxidized and reduced sediment.

In summary, hydrological forcing clearly impacts sediment biogeochemistry and carbon remineralization. However, advective transport, while accounted for in sandy sediments, is largely ignored in fine-grained sediments, where only bioturbation and bioirrigation are considered to affect the transport of dissolved constituents and particles. In addition, previous in situ and ex situ measurements have revealed that the chemical composition of pore waters is highly affected by advective transport induced during tidal cycles (Taillefert et al., 2007), suggesting that ex situ sediment cores should be carefully used to investigate the biogeochemistry of marsh sediments. Thus the complex transport mechanisms of estuarine and coastal marsh sediments require in situ geochemical sampling techniques to obtain an accurate representation of sediment geochemistry for improved calculation of carbon remineralization rates.

Recycling of Reduced Metabolites

Hydrological processes clearly impact the transport of constituents in pore waters and also affect the recycling of reduced metabolites. For example, to sustain the high rates of metal oxide reduction measured in coastal sediments, a rapid reoxidation cycling of Fe has been proposed (Canfield et al., 1993b, Taillefert et al., 2007). Each atom of iron was suggested to be recycled between oxidized and reduced phases 100 – 300 times within a given residence period (Canfield et al., 1993b) as Fe(II) is oxidized extremely rapidly to iron (III) oxides by dissolved oxygen at circumneutral pH (Davison and Seed, 1983; King et al., 1995), thus providing more substrate for iron-reducing bacteria. Consequently, oxygen injection into surface sediments through bioturbation or intertidal advection may promote the rapid recycling of reduced iron (Figure 1.1) and significantly influence carbon remineralization rates.

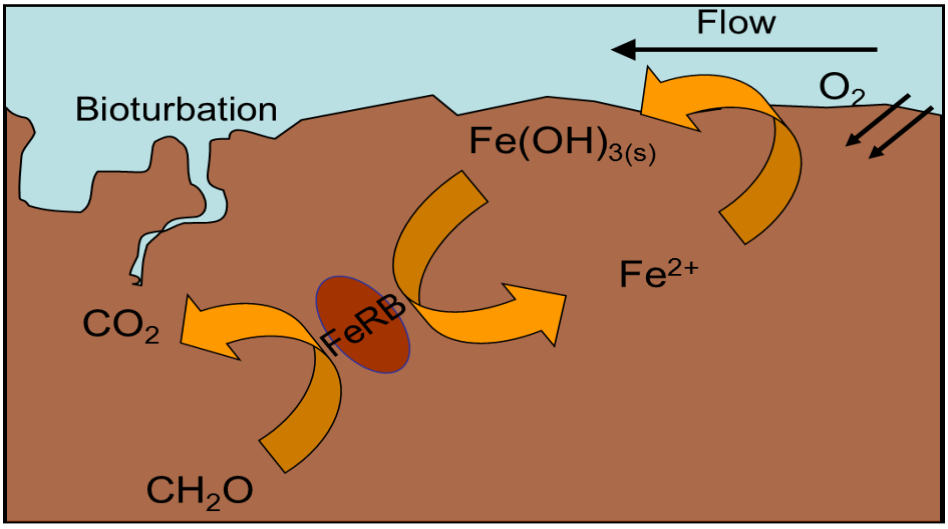

Figure 1.1: The metabolism of iron reducing bacteria involves the reduction of iron oxides to produce iron(II) and the oxidation of organic carbon to produce carbon dioxide. These bacteria are commonly found in coastal marine sediments where tidal advection and bioturbation increase oxygen delivery to surface sediments which rapidly reoxides iron(II) back to iron oxides.

At high concentrations of dissolved oxygen, the chemical oxidation of iron(II) in sediment porewaters is rapid and probably does not compete with microbial iron oxidation. However, depth profiling indicates that oxygen is generally reduced to less than micromolar concentrations within millimeters of the sediment water interface (e.g. Taillefert et al., 2002; Taillefert et al., 2007). Iron oxidizing bacteria inhabit these microaerobic zones to more successfully compete with abiotic iron oxidation (Druschel et al., 2008). Similarly manganese(II) can also be oxidized chemically or biologically; however, the rate of the chemical reaction at circumneutral pH (Morgan, 2005) is slow enough that manganese-oxidizing bacteria catalyze this reaction at a faster rate (Zhang et al., 2002) and are not challenged by the chemical oxidation mechanism. Similar to iron oxidizing bacteria, manganese oxidizers can function at microaerobic oxygen

concentrations below the limits of detection for most analytical techniques employed by chemical oceanographers (Clement et al., 2009). Thus, in general, when examining iron or manganese oxidation in surface sediments, the chemical and biological mechanisms are not in competition. The sulfide oxidation process falls in between these two extremes because sulfide oxidizing bacteria compete with the chemical oxidation mechanisms.

The rate law for the chemical oxidation of sulfides is first order with respect to both oxygen and sulfide, and the rate of oxidation increases with increasing pH to a maximum rate occurring around pH 8 (Chen and Morris, 1972). The reaction mechanism is complex and poorly understood due to the number of reactions that can occur at circumneutral pH in natural systems and the lack of techniques available to quantify intermediate products. This reaction requires a one electron transfer from the highest occupied molecular orbital (HOMO) of the sulfide (a p-orbital), to the lowest unoccupied molecular orbital (LUMO) of the oxygen (a π^* orbital) (Luther, 1990). The pH effect arises from the energy difference between these two orbitals (Luther, 1990), and the overall reaction product varies as a function of pH (Zhang and Millero, 1993). From thermondynamic calculations, the elementary steps likely involved in the oxidation process can be evaluated either through one or two electron transfer steps (Table 1.3).

Table 1.3: A list of sulfide oxidation reactions that are thermodynamically favorable at circumneutral pH in natural systems. (N.C. indicates that the ΔG was not calculated)

Reaction	ΔG = f(pH)	Reference	Equation #
$H_2S + OH^{\cdot} \rightarrow HS^{\cdot} + H_2O$	Constant	Luther, 2010	(5)
$H_2S + 2O_2^{-} + 2H^{+} \rightarrow S(0) + 2H_2O_2$	$\Delta G_{pH} \downarrow$ as pH↑	Luther, 2010	(6)
$H_2S + H_2O_2 \rightarrow S(0) + 2OH^{-} + 2H^{+}$	Constant	Luther, 2010	(7)
$H_2S + O_2 \rightarrow S(0) + H_2O_2$	Constant	Luther, 2010	(8)
$H_2S + H_2O_2 \rightarrow S(0) + 2H_2O$	Constant	Luther, 2010	(9)
$HS^{-} + O_2 \rightarrow HS^{\cdot} + O_2^{-\cdot}$	N.C.	Chen and Morris, 1972	(10)
$HS^{\cdot} + O_2 \rightarrow S(0) + HO_2$	N.C.	Chen and Morris, 1972	(11)
$HS^{\cdot} + O_2^{\cdot -} \rightarrow S(0) + HO_2^{-}$	N.C.	Chen and Morris, 1972	(12)
$HS^{-} + (x\text{-}1)S \rightarrow H^{+} + S_x^{-2}$	N.C.	Chen and Morris, 1972	(13)
$HS^{\cdot} + OH^{-} + H^{+} \rightarrow S(0) + H_2O$	$\Delta G_{pH} \downarrow$ as pH↑	Luther, 2010	(14)
$HS^{\cdot} + O_2^{-} + H^{+} \rightarrow S(0) + H_2O_2$	$\Delta G_{pH} \downarrow$ as pH↑	Luther, 2010	(15)
$HS^{\cdot} + H_2O_2 \rightarrow S(0) + OH^{\cdot} + OH^{-} + H^{+}$	$\Delta G_{pH} \downarrow$ as pH↑	Luther, 2010	(16)
$HS^{\cdot} + O_2 \rightarrow S(0) + O_2^{-} + H^{+}$	$\Delta G_{pH} \downarrow$ as pH↑	Luther, 2010	(17)
$S(0) + SO_3^{-2} \rightarrow S_2O_3^{-2}$	N.C.	Zhang and Millero, 1993	(18)
$nS(0) + HS^{-} \rightarrow HS_n^{-}$	N.C.	Zhang and Millero, 1993	(19)
$2SO_3^{-2} + O_2 \rightarrow 2SO_4^{-2}$	N.C.	Zhang and Millero, 1993	(20)

Reaction (6) is less favored than reactions (5, 7, 8, and 9) because multiple species would need to simultaneously react with sulfide to instigate a one electron transfer (Luther, 2010). Reactions (8 and 9) are favorable two electron transfer reactions; however, these reactions are predominantly biologically mediated (Luther, 2010). At circumneutral pH, HS^{-} is more prevalent than H_2S, and reactions (10 – 13) were proposed for the formation of polysulfides (Chen and Morris, 1972) which can subsequently react with sulfite to form thiosulfate and sulfate (equations 18 – 20) (Zhang and Millero, 1993). At pH 4,

sulfate was shown to be the major oxidation product, but at circumneutral and higher pH, reaction 20 does not proceed to completion and thiosulfate and sulfite are formed preferentially (Figure 1.2; Zhang and Millero, 1993; Druschel et al., 2003). Futhermore, polysulfides were not found in experiments performed above pH 7.2 (Chen and Morris, 1971) suggesting that reactions 13 and 19 do not progress at higher pH. However, provided that the sulfide radical is formed through equation 5, reactions 14 – 17 are all favorable for the formation of elemental sulfur at circumneutral pH which should react with available sulfite to form thiosulfate (equation 18).

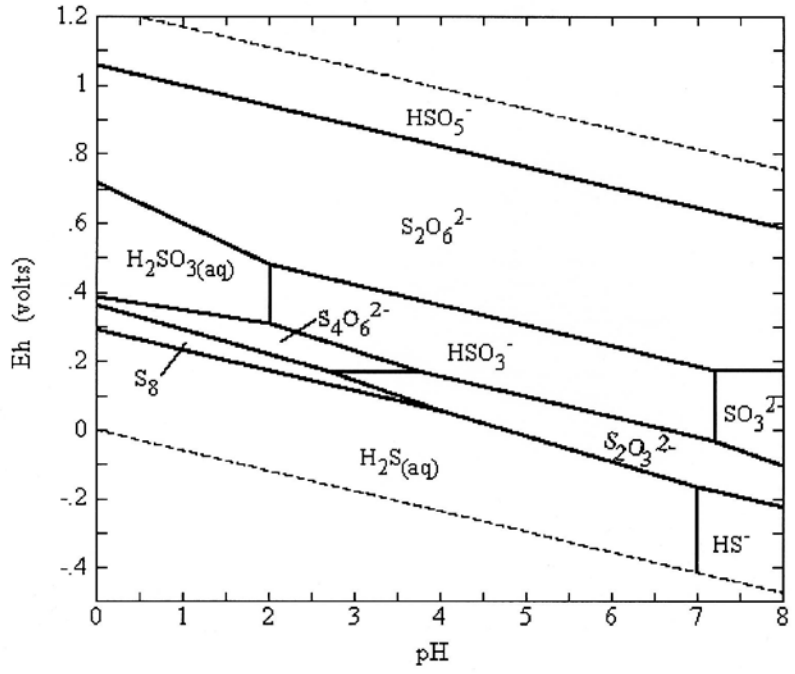

Figure 1.2: Eh-pH diagram produced by suppressing sulfate to show the occurrence of polythionate intermediates (Druschel et al., 2003).

In terms of bacterial sulfide oxidation, two types of oxidation processes have been identified, including an aerobic chemoautotrophic pathway by which bacteria derive the energy needed for growth from the oxidation of fully or partially reduced sulfur

compounds to sulfate (Frigaard and Dahl, 2009), and an anoxygenic phototrophic pathway by which bacteria oxidize hydrogen sulfide to sulfate while fixing carbon dioxide autotrophically (Friedrich et al., 2005; Frigaard and Dahl, 2009). The members of the family *Thiobacteriaceae* are probably the most important chemotrophic colorless sulfur bacteria (CSB) but *Thiobacillus* is the most studied genus of sulfide oxidizing bacteria (SOB) (Friedrich et al., 2005). *Thiobacteriaceae* utilizes the chemautotrophic pathway while C*hlorobiaceae*, an anoxygenic phototrophic green sulfur bacteria (GSB), and *Thiobacillus*, an anaerobic phototrophic purple bacteria (PSB), utilize the second pathway. The photosynthetic pathways require photon energy to actively transfer electrons from a reduced sulfur compound to carbon (Li et al., 2005); however they require different wavelengths for their respective photosystems.

Purple sulfur bacteria are predominantly anoxygenic phototrophs, but some species may function as aerobic chemolithotrophs (Frigaard and Dahl, 2009). Anaerobic purple bacteria remain at the maximum depth of light penetration and oxidize sulfide that is diffusing upward (Oren, 2005). Comparatively, CSB are aerobes that position themselves at the sulfide-oxygen boundary layer where sulfide rising from anoxic layers meets oxygen that is diffuses from the water column or is produced by cyanobacteria (CYA). All three of these species utilize some permutation of the Sox gene cluster (Figure 1.3).

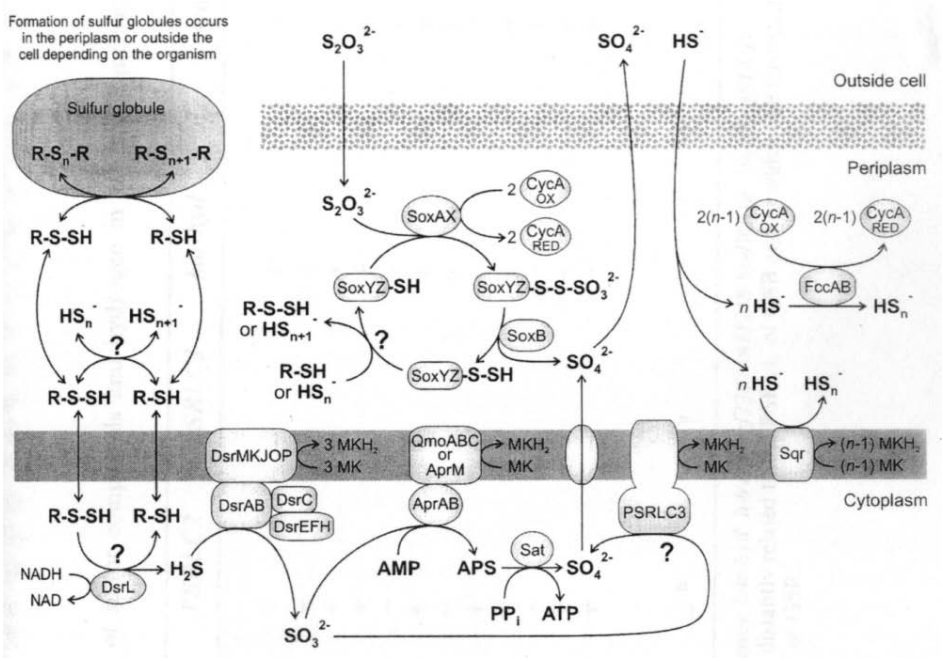

Figure 1.3: An overview of the proposed pathways of the biological sulfide oxidation mechanism. This figure illustrates the phototrophic system, but the *Sox* gene cluster illustrated here is common to other forms of sulfur oxidizing bacteria (Frigaard and Dahl, 2009).

Reduced or partially reduced sulfur compounds are oxidized by c type cytochromes, and the S*ox* gene cluster encodes for the ability to oxidize sulfur. This gene has been isolated from a couple different species (Bardischewsky and Friedrich, 2001; Frigaard and Dahl, 2009), and produces a remarkably versatile enzyme that reacts with hydrogen sulfide, sulfur, thiosulfate, and sulfite (Friedrich et al., 2005). The reactions depicted in Figure 1.3 indicate that the only product leaving the cell is sulfate; however thiosulfate, tetrathionate, and other polysulfides can potentially be used by the bacteria as an electron donor and can be released as intermediate oxidation species in bacterial strains that have an incomplete *Sox* system (Friedrich et al., 2005), which should be a rare occurrence. This information suggests that thiosulfate is a unique product of chemical reactions and

thus can be used as a measure for chemical oxidation, but production may be underestimated due to competition with SOB.

Microbial mats are miniature benthic ecosystems that are laminarly stratified according to chemical microgradients of oxygen and sulfide, consequently these systems are ideal for examining the interplay between biological and chemical sulfide oxidation. Within only a few millimeters, CYA, CSB, and PSB compete for light, carbon, and the sulfide produced by sulfate reducing bacteria (SRB). To utilize light as an energy source, CYA use a combination of Photosystem I and II which optimally absorb light of wavelengths 700 nm and 680 nm respectively (Konhauser, 2007). The PSB are known to be equipped with photosystem II, but they also possess an additional light harvesting system (LH II) complex with an absorption band 820 – 860 nm (Drews, 1996). Comparatively, CSB lack pigments, and therefore do not photosynthesize and instead utilize the Calvin Cycle for CO_2 fixation (Patriskaya et al., 2001). During the day, oxygen is produced to the point of supersaturation by cyanobacteria as a by-product of photosynthesis (Decker et al., 2005), and is consumed by CSB that position themselves at the oxygen sulfide interface. Photosynthesis for both CYA and PSB functions as an inorganic carbon sink.

Sulfate reducing bacteria are chemoorganoheterotrophs that transfer electrons from organic carbon exudates to sulfate and eventually produce sulfide. Their metabolism functions throughout the diel cycle because they are not dependent on light for an energy source (DesMarais, 1995). Maximum sulfate reduction rates have been detected in the photic zone presumably because the SRB utilize organic exudates from the cyanobacteria (Decker et al., 2005), therefore a substantial amount of sulfide is

produced in the surface mat layers and sustains both the PSB and CSB. In the presence of oxygen, CSB have a much higher affinity for sulfide and will potentially out-compete PSB (Visscher et al., 1992). Therefore it is currently accepted that all sulfide produced in the oxic zone is completely oxidized by CSB (Canfield and DesMarais, 1994), while chemical oxidation is typically not taken into consideration.

Overall Research Objectives

In summary, most carbon remineralization studies are performed ex situ using incubations and/or depth profiles. Additionally these studies generally assume oxygen functions as the ultimate oxidant which may not be a valid assumption for highly productive estuarine and coastal marsh sediments that are characterized by high burial rates of reduced species. This work addresses these issues through the development and deployment of new in situ instrumentation based on voltammetric microsensors to study biogeochemical processes in coastal sediments. These microsensors were also reduced in size to investigate some of the biogeochemical processes involved in microbial mats. This dissertation synthesizes the results and evaluates the success of these techniques. The first section presents the different field sites where these instruments were employed, the sampling strategies that were used, and summarizes the methods that were developed (Chapter 2). A novel, completely autonomous benthic lander equipped with a micromanipulator for pore water profiles and a benthic chamber to characterize fluxes of chemical constituents across the SWI was developed. This lander was used to estimate carbon remineralization rates for this estuary (Chapter 3) and to examine the seasonal

variability of the diagenetic processes that regulate carbon transformation in the sediments of the Satilla River estuary, Georgia (U.S.A.) (Chapter 4). Additionally, water level monitoring wells and an in situ voltammetric monitoring system with continuous sampling capability were installed in a coastal marsh to better elucidate the effects of tidal hydrology on marsh sediment biogeochemistry (Chapter 5). Finally, a collaboration with scientists at the NASA Ames Research Facility was initiated to study the interplay between the chemical and biological sulfide oxidation in microbial mats from the Guerrero Negro Basin in Baja California (Mexico). This work details the use of a single microelectrode to better characterize the competition between chemical and biological sulfide oxidation pathways in a model ecosystem (Chapter 6).

CHAPTER 2

STUDY AREAS, SAMPLING TECHNIQUES, AND ANALYTICAL METHODS

Study Areas

To address the missing near-shore component of the carbon budget, all coastal marine ecosystems must be examined, including the continental shelf, rivers, creeks, estuaries, and salt marshes. This work focuses on three representative sampling sites. The Satilla River estuary along the Atlantic coast of southern Georgia (U.S.A.) serves as an example for a relatively pristine tidal estuary, and sampling was performed on the nearby continental shelf as well. The Skidaway Ecosystem Research Facility (SERF) on Skidaway Island near Savannah Georgia (U.S.A.) was chosen to represent an ideal coastal marsh ecosystem. Finally, microbial mats from the Guerrero Negro Basin, Baja California (Mexico) were selected to examine the interplay between biological and chemical sulfide oxidation.

The Satilla River

The Satilla River is classified as a black water river that originates on a sandy coastal plain. The waters are characterized by a high dissolved organic carbon content, relatively low pH, low nutrient content, and low sediment loads (Schilling and Lockaby, 2006). The overlying waters contain an average of 16.6 mg/L of suspended solids and

exhibit a pH gradient from 5.71 upriver to 7.64 at the mouth (Alber et al., 2003). The surrounding area has recently experienced a 20% population decrease, and during the last 100 years the land use has been converted from agriculture to forests of cultivated pine (Alber et al., 2003). Consequently, industrial, residential, and agricultural pollution sources are minimal (Jahnke et al., 2003), and this system represents an ideal example of a pristine coastal estuary.

Overall, the river spans 420 km through a primarily rural watershed. This area experiences strong semidiurnal tidal fluctuations ranging from 2 – 3 m at spring and neap tides, and the river flow velocity averages about 1 m s^{-1} (Alber et al., 2003). Freshwater discharge averages around 70 m^3 s^{-1} and fluctuates between 300 and 0 m^3 s^{-1} depending on the local precipitation conditions (Alber et al., 2003). Under normal conditions, the salinity averages around 29 at the river mouth and declines to 0 by 50 km upstream (Alber et al., 2003); however, the salinity gradient is highly variable depending on the river discharge. A slight temperature gradient of less than 4^{o}C is apparent along the river but only during the winter months.

Beginning in 2005, five sampling sites were established along the river, and a sixth site was added on the continental shelf in late 2007 (Figure 2.1). The lander was deployed from the Research Vessel Savannah, operated by the Skidaway Institute of Oceanography. The station farthest upriver (SAT 1) was located at 30^{o}58'N and 81^{o}40'W. The upper sediment layers at this location were mainly flocculent silts and muds with progressively more dense clay layers at depth. Contrastingly, the sediments from sampling station SAT 5, located at 31^{o}00'N and 81^{o}26'W, were predominantly sandy in nature deposited on top of mud filled with shells and detritus.

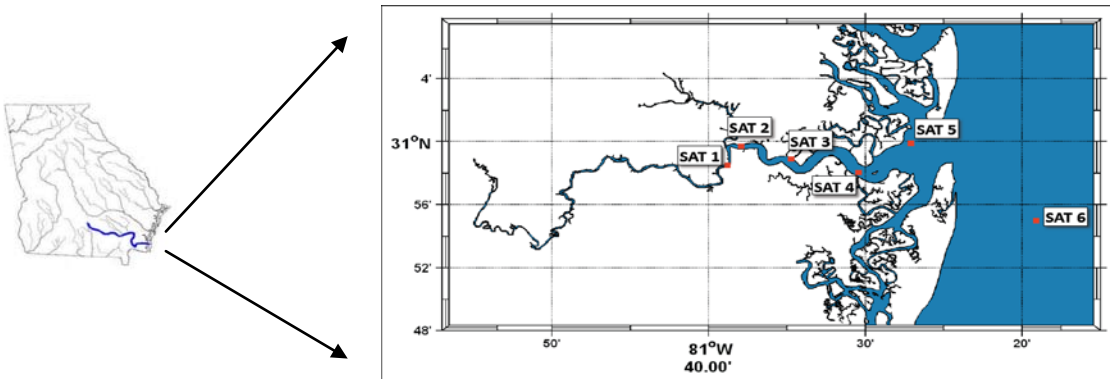

Figure 2.1: The Satilla River is located 15 miles north of the Georgia state border with Florida. Seasonal sampling was conducted here for 3 years. The station furthest from the river mouth was approximately 20 km upstream (SAT 1).

A benthic lander was designed to perform in situ voltammetric pore water depth profiles and benthic chamber incubations to study the effect of river discharge on benthic biogeochemistry. Mercury/gold amalgam voltammetric microelectrodes (Brendel and Luther, 1995) were used to simultaneously measure dissolved oxygen, Fe(II), Mn(II), ΣH_2S, and other iron complexes. The details of the lander construction, deployment schedule, and electrode preparation are presented in Chapter 3. Polycarbonate 7.5 cm diameter core liners were used with a single coring device (Marinelli et al., 1998) to collect the cores within 30 m of the lander deployment site to corroborate in situ data.

Sampling trips were organized about every three months because high temporal resolution is required to best examine the effects of seasonal variability on the diagenetic processes that regulate carbon transformation in coastal sediments. Consequently, the study area was visited at least four times per year over a three year time span between 2005 and 2008. River discharge declined precipitously beginning in May 2006 and remained low throughout 2007 before returning to average volumes in January 2008.

This phenomenon was a consequence of an extended drought, which impacted the entire southeast United States. The results of this study are reported in Chapter 4.

SERF Facility

The Saltmarsh Ecosystem Research Facility (SERF) is located on the leeward side of Skidaway Island (Figure 2.2), near the Skidaway Institute of Oceanography.

Figure 2.2: SERF located on Skidaway Island between the Skidaway River and the Wilmington River south east of Savannah (GA).

This marsh experiences diurnal tides but is not exposed to direct wave action from the Atlantic Ocean or the nearby rivers. The study area is accessed through a 213 m long boardwalk that extends from an inland salt marsh meadow out into the marsh. The boardwalk follows the transition of the marsh through a mud flat (122 m) and into a tidal creek (Figure 2.3).

Figure 2.3: Bird's eye view of the salt marsh area (modified from Google Maps). The boardwalk originates inland, runs west though the mud flat (MF), and terminates near the creek bank (CB) sampling location. Two sets of four monitoring wells were installed along the boardwalk, four in the mud flat and four in the creek bank (left). The instrument was mounted along the side of the boardwalk (right) while the solar panel and batteries were positioned at the end of the boardwalk (not shown).

The mud flat is predominantly unvegetated with sporadic stalks of short S*partina patens*. This portion of the marsh is slightly elevated compared to the creek bank at the end of the boardwalk and is exposed to the atmosphere for about 12 hours daily, in 6 hour increments between tides. In contrast, the center of the tidal creek retains a small amount of water the majority of the time. The sides of the creek bank are characterized by thick stands of *Spartina alterniflora* and are exposed to the atmosphere for about 3 hours during each tidal cycle. The mud flat and sides of the creek bank are intensely bioturbated by fiddler crabs, most commonly *Uca pugnax* (Teal, 1958; Kostka et al., 2002).

Although it is not exposed to direct wave action, this area is characterized by unique flood dynamics. Two sets of four monitoring wells with 5 cm long screens made of 0.15 mm slit width positioned at 0, 15, 30, and 60 cm below the SWI (Figure 2.4) were installed in 2003 in the mud flat and the creek bank (Figure 2.3). These wells were capped to prevent contamination during rain events, but the caps were pierced to avoid overpressurization. Solinst level loggers were positioned at the bottom of the wells at a depth of 120 cm below the screens to monitor changes in water pressure as a function of time. A barologger (Solinst) was placed in the vicinity to monitor changes in atmospheric pressure over time. To normalize for atmospheric pressure fluctuations, the barologger readings were subtracted from the water level readings. These wells were pumped periodically to ensure that particles did not clog the screens or fill the wells over time. Barologger measurements indicate that air temperatures at this site range from 2^{o}C in the winter to as high as 40^{o}C in the summer, while overlying water temperatures vary between 12 and 25 ^{o}C.

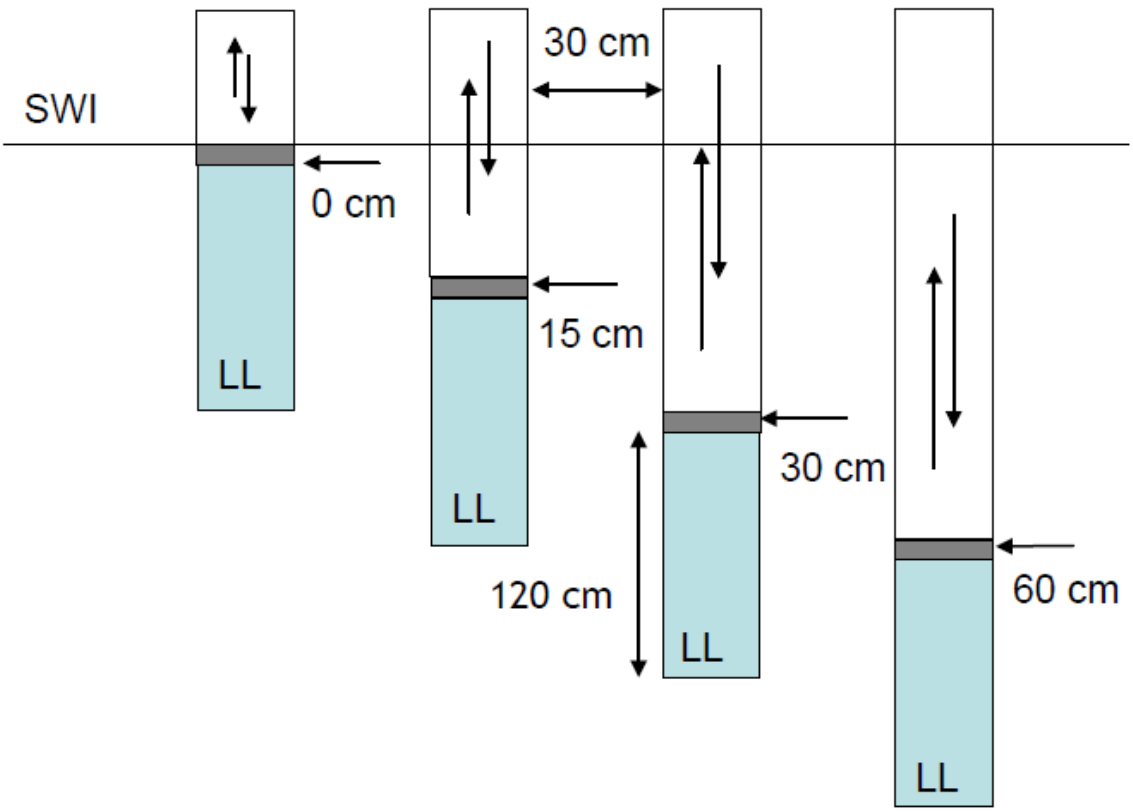

Figure 2.4: Diagram of the nest of four monitoring wells placed at the creek band and mud flat sites. The wells were positioned 30 cm apart laterally and were designed such that water flows into and out of the screens (dark rectangles) at rising and ebb tides. Level loggers (LL) were positioned at the bottom of each well 120 cm below the screens.

In addition to monitoring tidal fluctuations, temperature, and pressure in the wells, a remote sensing In Situ Electrochemical Analyzer (ISEA – III, Analytical Instrument Systems, Inc.) coupled with a Microcat (Seabird) was installed to observe changes in sediment pore water chemistry over time as well as flow rate, temperature, salinity, and the height of the overlying water. The instrument was powered with two 12 V batteries in series, recharged by a solar panel and wind turbine to enable continuous monitoring capability. The system was also equipped with a VHF radio and antenna to permit long range communication and data downloading. Complete instrument specifications and

system construction are outlined in Chapter 5. Instrument testing began in the summer of 2006, and the system has been collecting data almost full time since May 2007.

Guerrero Negro Basin

The microbial mats used for this analysis were obtained from the evaporite basins (Figure 2.5) of Exportadora de Sal salt works located in the Guerrero Negro basin, Baja California Sur, Mexico.

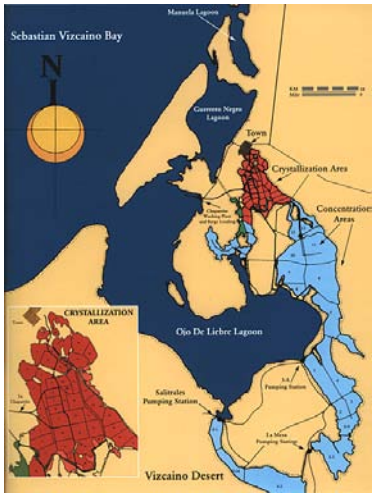

Figure 2.5: A pictorial representation of the evaporation basins at Exportadora de Sal (Baja California, Mexico) (http://www.essa.com.mx/) where sea water from the Ojo de Liebre lagoon flows into the ponds and progressively evaporates depositing different minerals including calcite, gypsum, and halite.

The mats were collected by members of the Ecogenomics Focus Group, a part of the National Aeronautics and Space Administration (NASA) Astrobiology program, and they were maintained in roof top greenhouses at the NASA Ames Research Facility, Moffett Field, California (U.S.A.). Each mat was encased in a rectangular plastic container to

maintain shape, and the containers are aligned in trenches of constantly flowing artificial marine water to maintain surface oxygenation. The overlying water of each trench was identical except the sulfate concentration was varied (0.2mM, 1mM, and 80mM) to mimic possible ranges of seawater composition during the early earth.

While in the greenhouse, voltammetric depth profiles were taken to examine the effects of diel cycling on oxygen, sulfide, and thiosulfate concentrations in these mats. Values were compared to a Clark type microelectrode (for oxygen) and an ion selective electrode (for sulfide). Additionally, each mat was individually relocated into a dark box with a gentle pump to maintain oxic conditions at the mat surface and allowed to reequilibrate for 3 hours. Light was focused through two different filters onto a small portion of the mat. Light intensity was adjusted to mimic the noontime greenhouse conditions (1600uE s^{-1} m^{-2}). The first filter removed all wavelengths greater than 700 nm and the second removed all wavelengths less than 700 nm. Voltammetric profiles were taken under both conditions and for each of the mat treatments.

Electrochemistry Techniques and Principles

Voltammetry with mercury-gold (Hg/Au) microelectrodes was employed at all three of these sampling sites because these electrodes can detect multiple redox species simultaneously, they are capable of low detection limits, and can even provide the speciation of iron and sulfide species (Luther et al., 2008). Consequently this technique is uniquely suited for the examination of complex heterogeneous environments. In amperometry, the concentration of an analyte is derived from the current response

generated by a redox reaction that occurs when a potential is applied at the electrode surface (Skoog et al., 1998). In voltammetry, a potentiostat is used to apply a different potential between a working electrode (Au/Hg microelectrode) and a Ag/AgCl reference electrode, and the potential is varied over time (between -0.1 and -1.8 V for this study). The resultant current is generated when redox species are oxidized or reduced at the working electrode surface, and the potential at which this current is generated is species specific. Consequently, voltammetry is most commonly used to study dissolved oxygen and redox species such as iron(II), dissolved iron monosulfide ($FeS_{(aq)}$), organically complexed iron(III), manganese(II), total dissolved sulfide ($\Sigma H_2S = H_2S + HS^- + S^0 + S_x^{-2}$), thiosulfate, and iodide (Luther et al., 2008). The reaction mechanisms as well as the reduction potentials for the redox transitions accounted for in this manuscript are listed in Table 2.1.

Table 2.1: Electrode reactions for various electrochemically active species including reduction potentials and sensitivity ratios for the Pilot Ion Method using manganese(II) as the pilot ion. Values are based on a scan rate of 200 mV sec^{-1}, and a conditioning step at -0.1 V for 10 s was always applied. For measurements involved sulfides and org-Fe(III), an additional conditioning step at -0.9 V for 10 s was added prior to the -0.1 V step to clean the electrode. *ND signifies not determined because calibrations have not been carried out with these species. **Sensitivity ratios determined within this manuscript.

Reaction	Species	Reduction Potential	Sensitivity Ratio
$Mn^{+2} + Hg + 2e^- \rightarrow Mn(Hg)$	Mn(II)	-1.5 V	1
$Fe^{+2} + Hg + 2e^- \rightarrow Fe(Hg)$	Fe(II)	-1.42 V	0.36
$Fe^{+3} + e^- \rightarrow Fe^{+2}$	org-iron(III)	(-0.2) – (-0.7) V	ND*
$FeS_{(aq)} + 2e^- + H^+ \rightarrow Fe(Hg) + HS^-$	$FeS_{(aq)}$	-1.1 V	ND*
$Hg + S_x^{-2} \rightarrow HgS_x + 2e^-$	polysulfide	-0.8 V	ND*
$S^0 + Hg \rightarrow HgS$	elemental sulfur	-0.8 V	ND*
$HS^- + Hg \rightarrow HgS + H^+ + 2e^-$	sulfide	-0.6 V	Cathodic 12.6 Anodic (-3.5)
$2I^- + Hg \rightarrow HgI_2 + 2e^-$	iodide	-0.25 V	7.08**
$2S_2O_3^{-2} + Hg \rightarrow Hg(S_2O_3)_2^{-2}$	thiosulfate	-0.15 V	2.38**

Dissolved oxygen and peroxides were measured by linear sweep voltammetry (LSV), and all other species are measured using square wave voltammetry (SQW) - a more sensitive potential wave form (Figure 2.6).

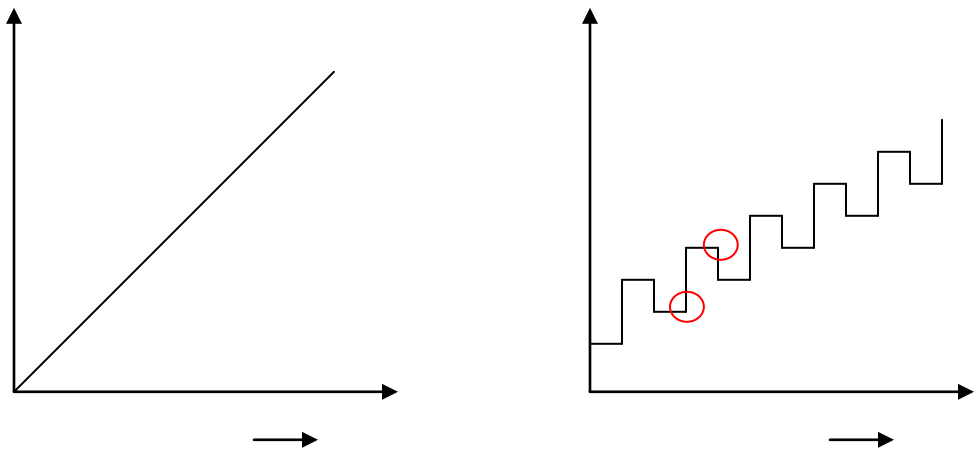

Figure 2.6: Potential wave forms used in voltammetry for the analysis of dissolved oxygen, peroxide, ΣH_2S (= $H_2S + HS^- + S^0 + S_x^{-2}$),Mn(II), Fe(II), $FeS_{(aq)}$ and org-Fe(III) complexes. A linearly increasing potential is applied in linear sweep voltammetry (left). Square wave voltammetry is more sensitive and characterized by a pulsed potential (right) and the resultant current is the difference between the current measured at the minimum and maximum points of each pulse.

The square wave pulse can be applied from a positive to negative potential in the case of cathodic square wave voltammetry (CSW), or from a negative to positive potential for anodic square wave voltammetry (ASW). This technique is more sensitive than LSV for reversible reactions because the current is measured twice during each pulse, at the minimum and the maximum and the resultant current is the difference of these values ($I_f - I_b = I_{res}$). Anodic square wave voltammetry was only used to measure extremely high concentrations of dissolved sulfide because it avoids artifacts that may arise during cathodic scans. At high sulfide concentrations, formation of a cinnabar (HgS) film in the mercury layer at potentials greater than -0.6 V during CSW can prevent diffusion of sulfide species to the mercury film at the electrode surface and consequently lead to peak distortion that does not occur when ASW is used (Davison et al., 1988). The current

response was measured between the Hg/Au microelectrode and a platinum wire counter electrode using a picoammeter incorporated into the potentiostat.

Three different types of electrodes were used throughout these studies. PEEK™ (polyethyletherketone) electrodes were inserted into the benthic chamber and used for the long term marsh deployments, and tapered glass electrodes were used for pore water profiles to minimize sediment perturbation. The compact laminar structure of the microbial mats required new working electrodes to attain submillimeter resolution. The new electrodes were fashioned from PEEK™ tubing lined with glass capillary tubes (Figure 2.7). A comprehensive description of electrode construction and preparation is detailed in Chapter 3.

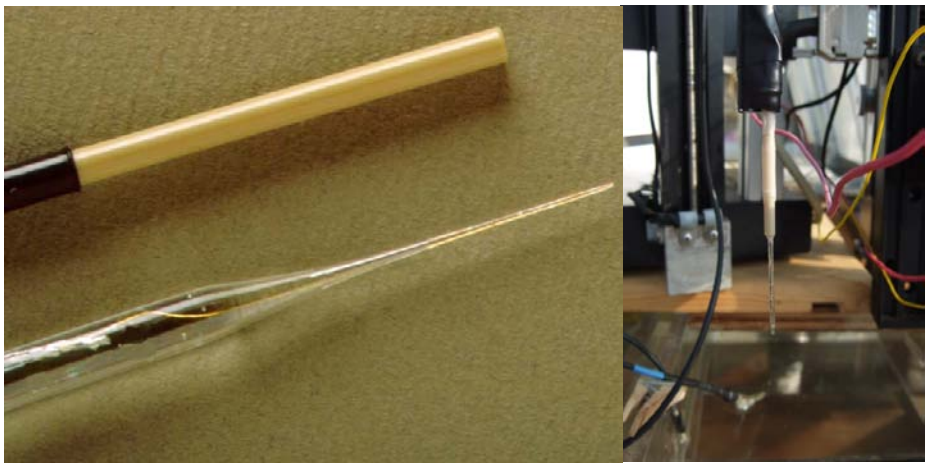

Figure 2.7: Three types of Hg/Au electrodes were utilized in these studies. For the lander and the Satilla River, PEEK™ electrodes (top left) were inserted into the benthic chamber, and glass electrodes (bottom left) were used for pore water profiling. In the SERF marsh, four PEEK™ electrodes were inserted at fixed depths into the sediment near the creek bank. The electrodes for the microbial mats (right) were made of glass capillary tubes reinforced with PEEK™ tubing.

The current response depends on the number of electrons that are transferred. For example, dissolved oxygen is reduced to peroxide and then to water in two consecutive steps. Each step is a two electron transfer and the resultant current contains two peaks of equal intensity (Figure 2.8 (top)). Iron(II) and Mn(II) as well as Fe(II) from $FeS_{(aq)}$ are all reduced to their elemental form with a single transfer of two electrons, while org-Fe(III) undergoes a single electron transfer and is reduced to Fe(II). Sulfidic species, thiosulfate, and iodide oxidize Hg(0) to Hg(II) with two one electron transfers (Table 2.1). Each of these reactions occurs at a species specific redox potential and can be easily identified on a voltammogram (Figure 2.8).

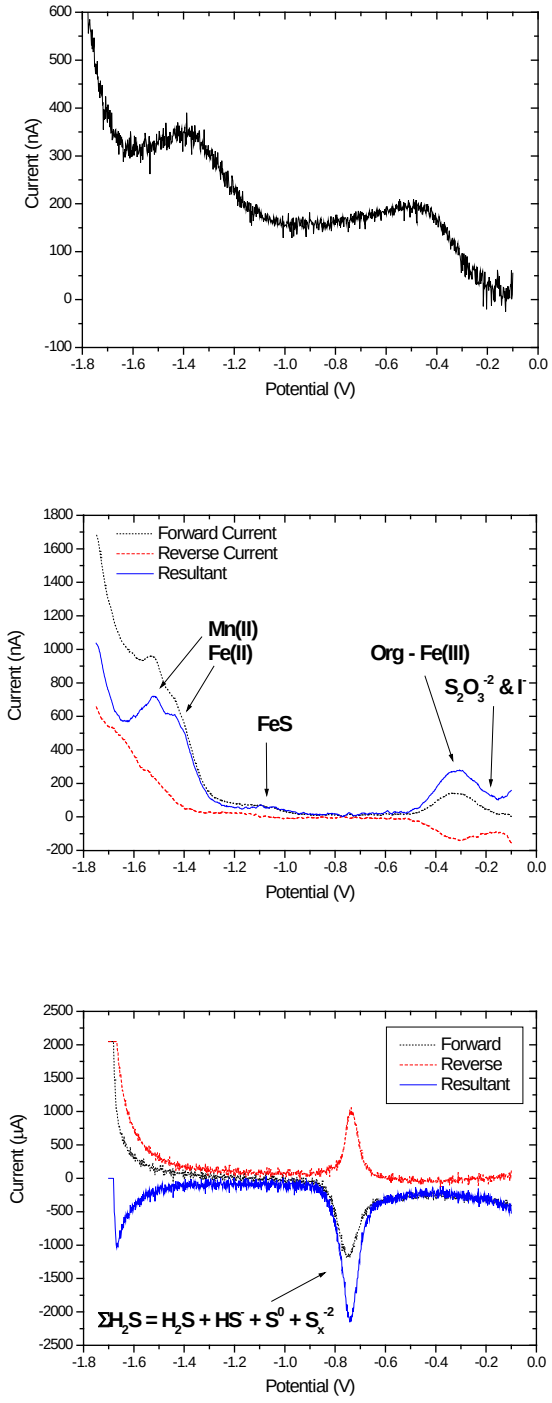

Figure 2.8: Example voltammograms including LSV (top) for oxygen and peroxide; CSW (middle) with forward, reverse, and resultant currents for iron(II), dissolved iron monosulfide ($FeS_{(aq)}$), organically complexed iron(III), manganese(II), total dissolved sulfide ($\Sigma H_2S = H_2S + HS^- + S^0 + S_x^{-2}$), thiosulfate, and iodide ; and ASW (bottom) with forward, reverse, and resultant currents used exclusively for total dissolved sulfide.

The electrochemical analyzers used in this study were all constructed by Analytical Instrument Systems, Inc. (AIS, Inc.). The lander and solar panel systems were equipped with preprogrammable, underwater ISEA II™ and ISEA III™ systems respectively. Both systems are equipped with multiplexers to accommodate 4 working electrodes. For lander deployments, one working electrode was inserted into a benthic chamber, two were used for profiling and the fourth was positioned in the water column just above the sediment water interface. The 4 working electrodes used in the salt marsh were inserted into the sediment at fixed depths of 0, 7, 15 and 24 cm. Reference and counter electrodes were affixed to the body of the lander in the river and to a home-made PVC holder in the marsh. The preprogrammed potentiostats collected binary data onto internal memory cards. The data was downloaded and converted into text files which were then integrated using VOLTINT, a semi-automated program implemented in Matlab™ that was created for these applications (Bristow and Taillefert, 2008). The program loads individual voltammograms, allows the user to select the peak baseline, and calculates the peak potential and peak current intensity for LSV, CSW, ASW, and CV, and calculates the peak area for CSW and ASW. Because the reduction potentials are close together (Table 2.1), peak overlap sometimes occurs (Figure 2.8). VOLTINT is equipped with a deconvolution function which uses the second derivative of the voltammogram to locate the individual modes and subsequently generates Gaussian curves to fit each mode. With these tools, even complex voltammograms can be integrated accurately.

The conversion process between the peak heights of the voltammagrams and species concentration is different for dissolved oxygen than for the other redox species.

Dissolved oxygen was calibrated in situ based on water column temperature and salinity measurements, which were used to determine the dissolved concentration, assuming saturation was reached. For square wave measurements, current response was converted into species concentration using the Pilot Ion Method (Brendel and Luther, 1995), with Mn(II) serving as the pilot ion. The sensitivity of the electrodes depends largely on the size of the mercury film (Brendel and Luther, 1995). In turn, the relative sensitivity of each species should remain constant for a particular electrode. The Pilot Ion Method uses a pilot ion to predict the sensitivities of other ions using the predetermined sensitivity ratios listed in Table 2.1. Manganese(II) was chosen as the "Pilot Ion" because it was stable at seawater pH and the ratio of the slopes for the calibration curves between Mn(II) and the other species remain constant. The sensitivity ratios for the Pilot ion method are displayed in Table 2.1; however, those for thiosulfate and iodide, were determined as a part of the current work.

Pilot Ion Sensitivity Ratios for Thiosulfate and Iodide

Thiosulfate does not change its redox state at the Hg electrode, instead it facilitates the oxidation of Hg(0) at a potential around -0.15 V (Figure 2.9).

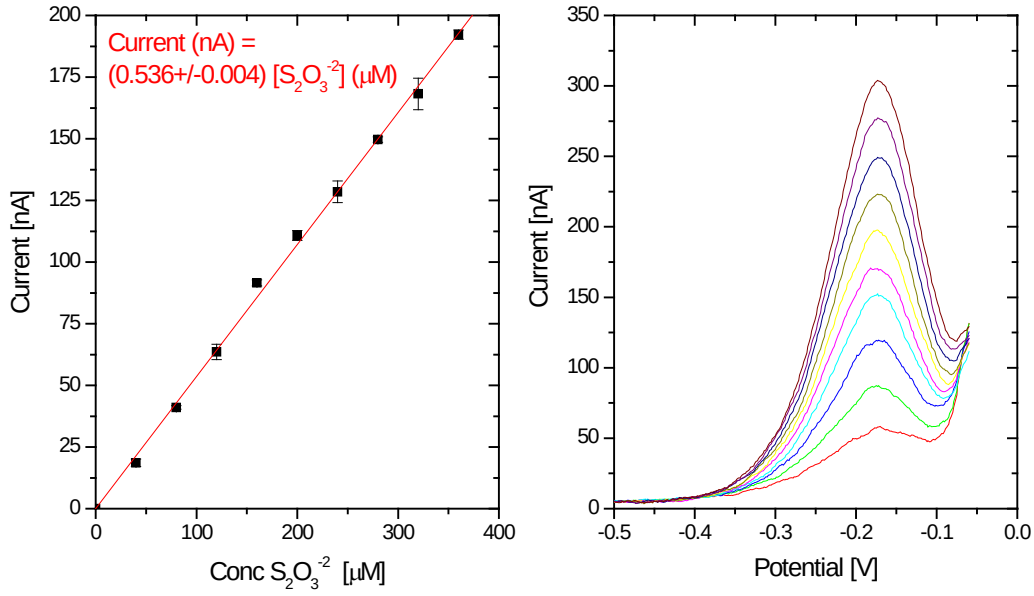

Figure 2.9: A 10 point thiosulfate calibration from 0 – 360 µM in 0.54 M NaCl (left). The voltammetric scans for the left calibration plot, measured on the microamp scale (right).

Three electrodes were utilized and calibrated 25 times in total for thiosulfate and 16 times for Mn(II) to calculate a ratio between the two species for use with the Pilot Ion method. The average of five voltammetric scans were used for each standard and about five standards were used to obtain each calibration. Overall, an average manganese calibration slope of 0.244 (+/- 0.057) nA/µM, and an average thiosulfate calibration slope of 0.570 (+/- 0.140) nA/µM were obtained. The detection limit for thiosulfate is 20 µM without incorporating a preconcentration step, aside from the normal conditioning step at

-0.1 V for 10 s, and the calibration curve is linear up to 400 µM. The average ratio based on a scan rate of 200 mV s^{-1} using square wave voltammetry and a 0.54 M NaCl medium was determined to be 2.38 (+/-0.58).

A similar procedure was performed to determine the Pilot Ion Sensitivity Ratio of iodide to manganese (Figure 2.10).

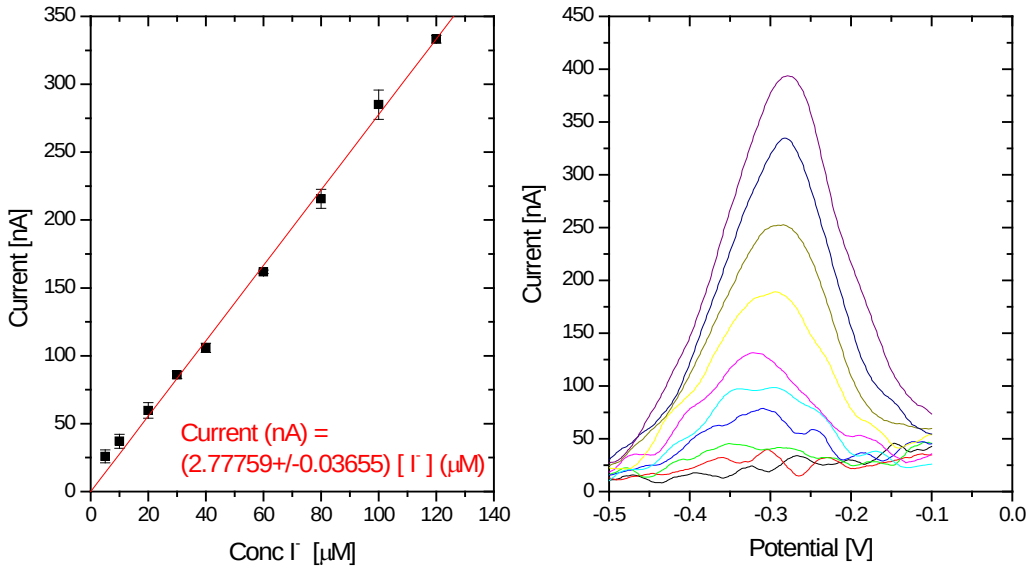

Figure 2.10: A 10 point iodide calibration from 0 – 120 µM in 0.54 M NaCl (left). The voltammetric scans corresponding to the left calibration plot (right).

Six electrodes were utilized and calibrated 46 times in total for manganese and 75 times for iodide. Again, five scans were collected and averaged for each standard and about five standards were used for each calibration. An average manganese calibration slope of 0.340 (+/- 0.110) nA/µM and an average iodide calibration slope of 2.59 (+/- 2.23) nA/µM were obtained. The minimum detection limit for iodide was 5 µM. The average Pilot Ion Ratio based on a scan rate of 200 mV sec^{-1} with square wave voltammetry and a 0.54 M NaCl medium was determined to be 7.08 (+/- 2.24).

The substantial variation in the iodide calibration curves is problematic and requires further investigation. A memory effect was observed on a number of occasions akin to a similar issue when measuring large quantities of sulfide. Just as sulfide electrochemically oxidizes the mercury to form cinnabar, iodide also electrochemically oxidizes the mercury to form an insoluble precipitate (HgI_2) and therefore a film may form on the electrode surface during the conditioning step and the scan. The substantial variability in the iodide slope can be attributed to memory effects caused by the formation of this film. To confirm this hypothesis, cyclic voltammetry (CV) was used to determine the reversibility of the reaction at the electrode surface. This type of voltammetry is similar to LSV except the potential is modulated between -0.1 V and -1.8 V, and then returned to the original potential. If a reaction is reversible, a reverse wave should be evident at a potential shifted from the forward wave by 56 mV per electron exchanged (Bard and Faulkner, 2000). The absence of a reverse wave when CV was performed with iodide (Figure 2.11), indicates that the reaction at the electrode surface is irreversible and suggests the formation of a precipitated film.

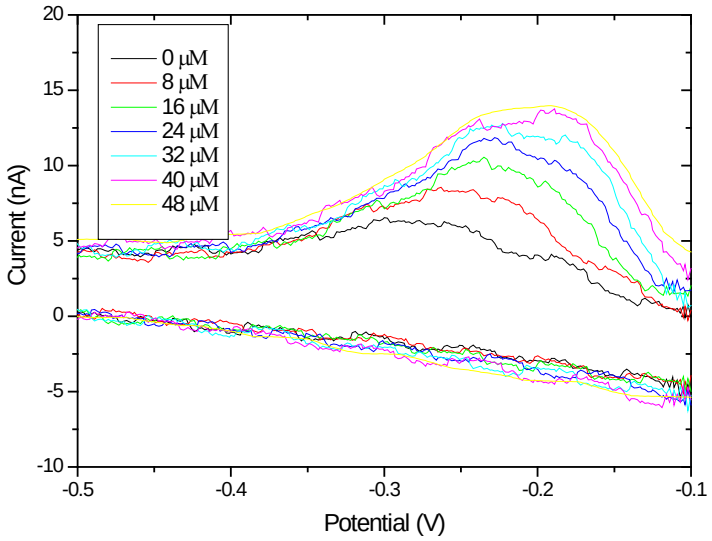

Figure 2.11: A 7 point iodide calibration from 0 – 48 µM performed with CV and filtered with a smoothing average of 11 pts. Clearly there is no measureable response in the reverse wave which indicates that this reaction nonreversible.

Customarily a conditioning step is added for 10 s at a potential of -0.9 V to clean the sulfidic double film from the electrode surface. The same technique was used with iodide to investigate whether this memory effect could be eliminated. In these experiments, the concentration of iodide was held constant at 25 µM, the duration of the conditioning steps at both -0.9 V and -0.1 V were individually varied. Increasing the length of the conditioning time at -0.1 V resulted in electrode saturation, but the added step at -0.9 V generated highly reproducible results, which suggests that this added cleaning step successfully removed any artifacts that were formed during the previous scan (Figure 2.12).

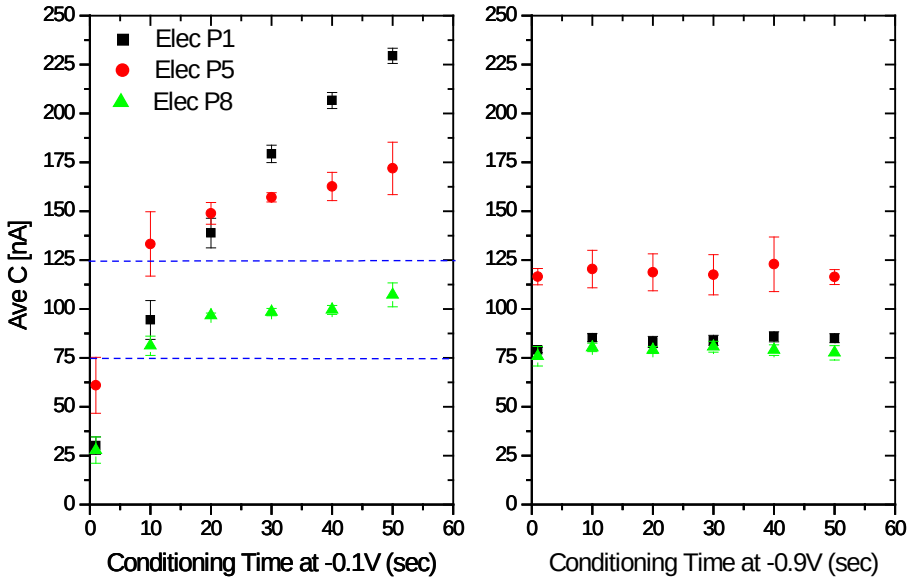

Figure 2.12: The iodide concentration was held constant while the length of the conditioning step and potential was varied for three different electrodes. Increasing the length of the conditioning step at -0.1 V resulted in electrode saturation (left), suggesting that the irreversible precipitation of HgI_2 may generate memory effects. To remove this artifact, a variable conditioning potential at -0.9 V was added in addition to the standard 10 s at -0.1 V. The added conditioning step at -0.9 V generated highly reproducible results (right), and the dashed lines on the left represent the current variability of the scans on the right for comparison.

These results suggest that the irreversible precipitation of HgI_2 at the electrode surface may generate memory effects that can be avoided by applying a cleaning step before each scan at -0.9 V for 10 s.

These experiments were performed because iodide was used as a conservative tracer in the benthic chamber incubations described in Chapter 3. Injection of a conservative tracer into benthic chamber incubations has previously been performed with bromide as a tracer (Rao and Jahnke, 2004). In this study, iodide was employed as a tracer because it is electrochemically active at Hg electrodes. The tracer was injected into the benthic chamber at the start of each deployment to quantify the impact of

advective transport on sediment pore waters in the Satilla River (Chapter 3). The artifact issues were still being resolved when the field deployments examined in Chapters 3 and 4 were performed, therefore only freshly polished and plated electrodes were used for those benthic chamber studies. However, the lander will be used for future studies at other locations and this cleaning step will be added to all new measurements.

Other Analytical Techniques

A variety of analyses including voltammetric profiling and pore water analysis for dissolved phosphate, iron, and dissolved inorganic carbon (DIC), were also performed ex situ on sediment cores collected simultaneously with each lander deployment. Voltammetric depth profiles of redox species were obtained within an hour of sampling and using a DLK MAN-1 micromanipulator and the same type of glass electrodes employed on the lander. After profiling, cores were sectioned into approximately 8 mm slices in a glove bag under a nitrogen atmosphere to prevent oxygen contamination. Sediment slices were immediately centrifuged to extract pore waters, sealed, and frozen to halt diagenetic processes until the samples could be returned to the lab for solid phase analyses. Under a nitrogen atmosphere, the pore waters were subsequently filtered using 0.2 micron Puradisc polyetherfulfone filters (Whatman). Aliquots were stabilized in ferrozine reagent for spectrophotometric analysis of iron(II) and total dissolved iron concentrations (Stookey, 1970). Separate aliquots were used within an hour for the analysis of total dissolved phosphate and DIC. Any remaining pore waters were immediately sealed and frozen for future use. Total dissolved phosphate was measured

by spectrophotometry at 800 nm (Murphy and Riley, 1962) with a SPV 100 spectrophotometer coupled to an autosampler (AIS, Inc.). Dissolved inorganic carbon was quantified by flow injection analysis (Hall and Aller, 1992) with a multichannel Rainin Dynamax Model RP-1 peristaltic pump, VWR Scientific EC Meter Model 1054, and a LCC-100 Integrator (AIS, Inc.). Data files were integrated with a modified version of VOLTINT (Bristow and Taillefert, 2008).

CHAPTER 3

DEVELOPMENT OF A NEW AUTONOMOUS BENTHIC LANDER EQUIPPED WITH AN IN SITU ELECTROCHEMICAL ANALYZER (ISEA) FOR THE SIMULTANEOUS MEASUREMENT OF BENTHIC FLUXES AND DEPTH PROFILING IN CONTINENTAL SHELF SEDIMENTS

Abstract

Rates of natural organic matter (NOM) degradation are difficult to quantify directly in marine sediments and are typically determined by measuring total (TOU) and diffusive (DOU) oxygen uptake fluxes, assuming oxygen as the ultimate oxidant. In areas of high NOM input, oxygen is usually depleted within a few millimeters of the sediment-water interface, and nitrate, manganese and iron oxides, sulfate, and carbonates are used as terminal electron acceptors at depth. To accurately quantify NOM mineralization rates using DOU or TOU fluxes, reduced metabolites produced during these processes have to be completely reoxidized by oxygen. In coastal sediments, however, DOU and TOU fluxes may underestimate NOM oxidation rates, as the chemical reduction of manganese and iron oxides by sulfides and the burial of sulfur and carbonate minerals may prevent aerobic reoxidation of these metabolites. To accurately assess carbon oxidation rates in coastal sediments, it is therefore necessary to consider individual terminal electron accepting processes simultaneously. In this study, a new autonomous benthic lander has been constructed

to study these processes in situ. The lander is equipped with a benthic chamber to measure TOU fluxes with a high temporal resolution and a potentiostat and micromanipulator to simultaneously acquire voltammetric depth profiles of the main redox species in pore waters. This chapter reports the details of the lander design, construction, and deployment procedures as well as the voltammetric sequence developed for unattended measurements. Preliminary data is used in conjunction with a mathematical model to estimate carbon remineralization rates in coastal shelf sediments.

Introduction

Quantifying carbon preservation in sediments is of crucial importance to determining the net flux of carbon to the oceans accurately (Hedges et al., 1997). Interestingly, the majority of diagenetic investigations have focused on the deep ocean, though transport models predict less than 10% of the particulate organic carbon (POC) from primary production is transported to depths below 1500 m (Martin et al., 1987; Pace et al., 1987). More recent findings indicate that 40% of annual organic carbon burial occurs in continental margin sediments (Muller-Karger et al., 2005) where sedimentation rates are enhanced due to abrupt changes in salinity (Hakanson, 2006). Simultaneously, rates of carbon remineralization are increased in these areas, and these ecosystems may oscillate between autotrophy and heterotrophy seasonally (e.g. Ram et al., 2003). Overall, these findings indicate that the focus of carbon flux studies should expand to include continental margin sediments (Cai et al., 2006).

Because of the complex, heterogeneous nature of natural organic matter (NOM), it is not possible to ascertain its rate of decomposition directly (Burdige, 2006). In addition, dissolved inorganic carbon (DIC) measurements cannot directly provide estimates of NOM remineralization because DIC is also produced by calcium carbonate dissolution (Jahnke et al., 1997). To increase the complexity of the problem, oxidation of NOM occurs through a complex web of processes including fermentation and oxidation of organic acids that are not clearly understood (Burdige, 2006). As a result, chemical oceanographers have quantified rates of carbon remineralization using techniques that measure oxygen consumption near the sediment water interface (e.g. Archer and Devol, 1992; Glud and Gundersen, 2002; Wenzhofer et al., 2002; Berg et al., 2003). Oxygen consumption rates are then related to carbon remineralization rates using appropriate C:N ratios of NOM in the sediment (Burdige, 2006) and electron equivalents provided by the oxidation of reduced metabolites by oxygen (Canfield et al., 1993a; Wenzhofer et al., 2002). In situ oxygen consumption is quantified based on the diffusive oxygen flux (DOU) across the sediment-water interface (SWI) from depth microprofiles obtained with Clark-type microelectrodes or optodes (e.g. Glud and Gundersen, 2002; Reimers et al., 2004; Glud et al., 2005). Alternatively, calculation of total oxygen uptake (TOU) can also be accomplished by monitoring the decline of oxygen concentration in the overlying water using benthic chambers deployed across the sediment water interface (SWI) (e.g. Berelson and Hammond, 1986) or, more recently, using eddy correlation techniques (Berg et al., 2003). Differences between TOU and DOU fluxes have been attributed to fauna-mediated oxygen uptake (Glud and Gundersen, 2002; Wenzhofer et al., 2002). Typically, NOM oxidation rates, determined from TOU or DOU fluxes, assume oxygen

to be the ultimate oxidant and thus presume that nitrite, ammonium, manganese (II), iron (II), and sulfides produced during the anaerobic oxidation of NOM are reoxidized when they diffuse to the oxic upper sediment layers. This assumption may be more appropriate for pelagic sediments which lack the microbial diversity and the more complex geochemistry of continental shelf sediments due to low carbon fluxes to the sea floor (Burdige, 2006). Continental shelf sediments are characterized by a web of complex chemical and biological reactions which suggest that assuming oxygen as the ultimate oxidant may lead to a gross miscalculation of remineralization rates.

In continental margin sediments, oxygen is often depleted within a few millimeters of the SWI, and anaerobic respiratory processes, such as denitrification (Jahnke et al., 2003), manganese and iron reduction (e.g. Canfield et al., 1993b; Taillefert et al., 2002b), and sulfate reduction (e.g. Howarth and Giblin, 1983; Hines et al., 1989) dominate. The average oxidation state of carbon in natural organic matter found in coastal waters is around +0.27 (Perdue, 2009). The corresponding changes in carbon equivalents during anaerobic respiration processes can therefore be calculated from the changes in concentrations of terminal electron acceptors or their corresponding reduced species using the average oxidation state of carbon and the appropriate electron transfer ratios during denitrification, dissimilatory reduction to ammonium (DNRA), dissimilatory manganese, iron, and sulfate reduction according to Eq 1.

$$\Delta[N_2] + \Delta[NO_3^-] + \Delta[Mn^{+2}] + \Delta[Fe^{+2}] + \Delta[H_2S] = 0.37*\Delta[CH_2O] + 0.47*\Delta[CH_2O] + 1.86*\Delta[CH_2O] + 3.73*\Delta[CH_2O] + 0.47*\Delta[CH_2O] = 6.90*\Delta[CH_2O] \quad (1)$$

Although by-products of these anaerobic respiratory processes (e.g. sulfides, ammonium, manganese (II) and iron (II)) may be either chemically or biologically reoxidized by

oxygen rapidly, burial can also occur by precipitation of iron sulfide minerals, including amorphous FeS, mackinawite, and pyrite or carbonate minerals (siderite and rhodocrosite). In addition, the chemical reduction of iron and manganese oxides by sulfides (Afonso and Stumm, 1992) may simultaneously produce (Mn(II) or Fe(II)) and consume (sulfides) reduced species. Using the above average carbon oxidation state of coastal waters, the removal of reduced species by carbonate precipitation (Eq. 2), sulfide precipitation (Eq. 3), or chemical reduction of iron and manganese oxides by sulfides (Eq. 4) may lead to an innate error in carbon remineralization rate calculations which can be estimated as follows:

$$\Delta[Fe^{+2}] + \Delta[Mn^{+2}] = (-3.73 + -1.86)*\Delta[CH_2O] = -5.59*\Delta[CH_2O] \quad (2)$$

$$\Delta[Fe^{+2}]+ \Delta[H_2S] = (-3.73 + -0.47)*\Delta[CH_2O] = -4.2*\Delta[CH_2O] \quad (3)$$

$$2*\Delta[Fe^{+2}] + 2*\Delta[Mn^{+2}] - 1*\Delta[H_2S] =$$

$$(7.46 + 3.72 - 0.47)*\Delta[CH_2O] = 0.71*\Delta[CH_2O] \quad (4)$$

These processes may be falsely attributed to microbial degradation of NOM and thus lead to the underestimation of heterotrophic iron, manganese, and sulfate reduction and an overall miscalculation of NOM oxidation depending on the type of ongoing processes. Thus, the use of TOU and DOU fluxes in sediments where reduced metabolites are not always reoxidized aerobically may lead to inaccurate estimations of NOM oxidation rates (Glud and Gundersen, 2002).

To overcome these issues and estimate NOM degradation rates more accurately, sediment incubations have been used to quantify rates of multiple individual terminal electron accepting processes simultaneously. Incubations are generally conducted using either whole cores or sections of sediment (e.g. Howarth and Giblin, 1983; Hines et al.,

1989; Canfield et al., 1993b). Flow-through reactors are also frequently used to study the biogeochemical complexity of sediments in more realistic conditions (e.g. Carey and Taillefert, 2005; Pallud, et al., 2007). Unfortunately, these measurements are time consuming and may modify the activities of microbial community assemblages. Introduction of artifacts or sample alteration due to pressure fluctuations during sampling can also potentially complicate ex situ incubations (Hammond et al., 2004). Thus, the ability to perform in situ measurements, though more complicated logistically, is warranted to determine more accurate rates of carbon remineralization.

Construction of benthic landers to measure depth profiles and benthic fluxes of dissolved oxygen in situ is not a novel idea. Landers have been built in many shapes and sizes depending on the type of environment investigated and measurements performed (e.g. Berelson et al., 1987; Jahnke and Christiansan, 1989). Most of these landers are equipped with benthic chambers and syringes triggered by timers to extract water samples that are analyzed later (Archer and Devol, 1992; Berelson and Hammond, 1986; Cook et al., 2007; Hammond et al., 2004). Alternatively, some landers have been equipped with Clark type microelectrodes (Archer and Devol, 1992; Berg et al., 2003; Glud et al., 2005) and, more recently, planar optodes, to quantify oxygen gradients with depth (Glud et al., 2005). Some of these landers have also been equipped with video cameras to visually locate the SWI. Concurrently, an eddy correlation technique combining vertical velocity measurements with a Doppler velocimeter and oxygen concentrations using microelectrodes has been developed to measure oxygen benthic fluxes from the overlying water (Berg et al., 2003). This novel technique samples over a larger area than traditional benthic chambers and ensures that neither the sediment nor the

boundary layer flow is disturbed (Berg and Huettel, 2008). These measurements, however, can only provide limited information on carbon remineralization processes in continental shelf sediments because they cannot account for the transformation of all the various reduced metabolites at depth.

In this study, an autonomous benthic lander carrying a micromanipulator for pore water profiles and a benthic chamber, positioned less than 30 cm apart, was designed to simultaneously measure TOU and DOU fluxes and characterize the main diagenetic processes in surficial estuarine sediments in situ. Mercury/gold amalgam voltammetric microelectrodes (Brendel and Luther, 1995) were used to concurrently measure oxygen and other redox species. These electrodes can be utilized in a variety of media including sediments, fresh and marine waters, brines, microbial mats, and hydrothermal vents (Luther et al., 2008). Fine tips minimize sediment perturbations and allow for fine scale resolution over several centimeters (Taillefert et al., 2000; Luther et al., 2008). This paper reports the details of the lander design, construction, and deployment procedures as well as the voltammetric sequence developed for unattended autonomous measurements. Some preliminary data is presented to illustrate that the technique is well suited for investigations of early diagenetic processes in coastal sediments.

Procedures & Materials

The lander is a four legged frame constructed with 5 cm diameter schedule 60 aluminum tubes arranged in a pyramidal fashion (Figure 3.1). The sides are 1.30 meters

long and the base is equipped with tear-shaped feet that are pierced with holes to facilitate retrieval from muddy sediments.

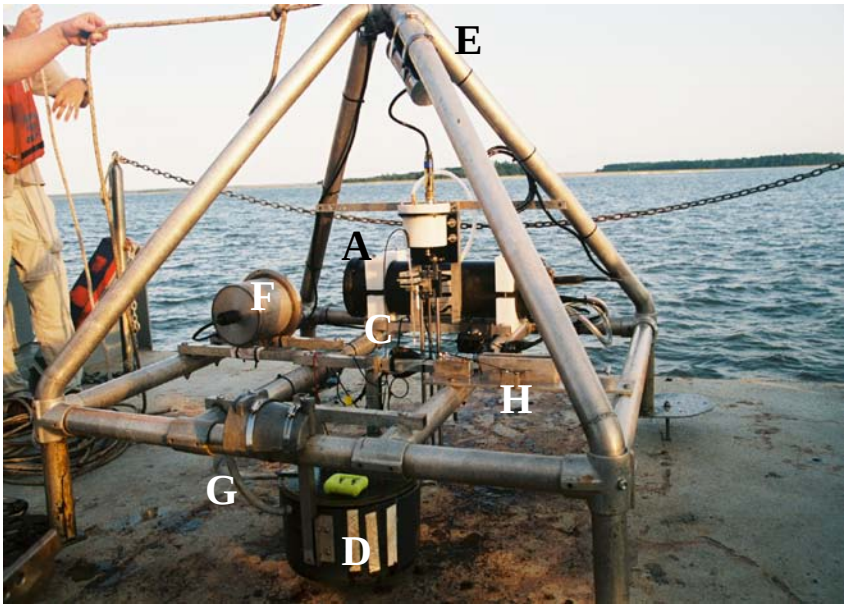

Figure 3.1: Free benthic lander equipped with: A) an ISEA II^{TM} submersible potentiostat; B) multiplexer electrode cable for reference, counter, and up to 4 working electrodes; C) computer-operated micromanipulator; D) a benthic chamber; E) solenoid to close the benthic chamber lid and activate the tracer injector; F) a battery housing for the solenoid; G) a Seabird pump to gently mix the waters in the chamber; and H) a spring-loaded KI tracer injector. Hidden from view is a probe for measuring temperature in the overlying water.

The lander is equipped with a portable in situ electrochemical analyzer (ISEA II^{TM}) from Analytical Instrument Systems, Inc. (AIS) (Figure 3.1A) for the simultaneous voltammetric measurements of iron (II), organically complexed iron (III), manganese (II), total dissolved sulfide ($\Sigma H_2S = H_2S + HS^- + S^0 + S_x^{-2}$) , thiosulfate, iron monosulfide, iodide, oxygen, and other electroactive species (Luther et al., 2008). The submersible potentiostat (characteristics provided in Table 3.1) is encased in an aluminum housing of 1 meter long and 20 cm in diameter, pressure-proofed to 300 m and powered by an internal 12 V DC lead acid battery with a lifetime limitation of 13 hours.

Table 3.1. Characteristics of the ISEA II™ system

Instrumentation:	AIS ISEA II
Compliance:	+/-12 V @ 30 mA
Current Range:	100 nA to 10 mA
Diameter/Length:	20 cm / 1m
Weight:	13.6 kg
Power and Consumption:	External and Internal (12 V), (500 – 800 mA)
Voltammetric Techniques:	DC, Sampled DC, Normal Pulse, Differential Pulse, Square Wave, Linear Sweep, & Cyclic and all stripping analysis techniques
Max Number of Working Electrodes:	4
Other capabilities:	Temperature & pH or Seabird MicroCat 37SI

If needed, a standard Deep-Sea power and Light battery can be externally attached for longer deployments. The system is also equipped with two independent temperature and pH sensors (not shown in Figure 3.1) and inputs for a Seabird MicroCat, although one was not included for these deployments. The potentiostat is equipped with a multiplexer (Figure 3.1B) that enables measurements from four independent working electrodes. Generally, one of the working microelectrodes is inserted in the benthic chamber lid to monitor in situ fluxes across the SWI, while two working electrodes are deployed on a water-proof AIS MAN-2 micromanipulator for depth profiles (Figure 3.1C). The micromanipulator is rated to full ocean depth pressure and consists of a precision-ground lead screw driven by a precision-stepper motor and drive circuit to move electrodes with submillimeter accuracy. It carries an electrode holder that extends 14 cm away from the lead screw. The electrodes are solidly held in the holder with nylon screws to ensure they

remain stationary. A computer inside the ISEA II™ controls the micromanipulator and the resolution step can be preset to fixed increments between 0.05 and 50 mm.

Two different benthic chambers were designed to be interchangeable on the lander. Each benthic chamber is fashioned from a truncated piece of PVC pipe (Figure 3.1D). The taller chamber is deployed in soft, fine-grained sediments where fluxes are generally highest. It measures 33 cm in diameter and 30 cm in height. The shorter chamber was designed for deployment in sandy shelf sediments where fluxes of dissolved species across the SWI are expected to be lower. The decreased volume of the smaller design, 33 cm in diameter and 18 cm in height, helps ensure that the concentrations of reduced species diffusing out of the sediment remain above the limit of detection of the microelectrodes. Each chamber is closed by a hinged clear acrylic lid to allow light to reach the enclosed sediment. The chamber lid is held open during the descent to the sea floor by a string connected to a magnetic solenoid mounted to the top of the lander (Figure 3.1E) and powered by a 12 V lead acid battery enclosed in a housing rated for full ocean depth (Figure 3.1F). Just prior to deployment, a timer connected to the solenoid is set to hold the lid in the open position for twenty minutes. Two five pound diving weights are fastened to the lid to ensure it remains closed after the pin is released from the solenoid. This twenty minute delay was incorporated to allow the settling of any particulate matter that may have been resuspended when the lander reached the seafloor. To ensure adequate mixing of the contained water, the benthic chamber is equipped with a Sea-Bird 5M-1 Mini Submersible Continuous Duty Pump (Figure 3.1G) powered by the same battery as the solenoid. The pump intake and output ports are located 120^{o} apart from one another on the side of the benthic chamber, 3 cm from the top. In addition to

releasing the chamber lid, the solenoid also triggers a spring-loaded piston (Figure 3.1H) to inject a 0.25 M KI tracer solution from a 20 mL syringe into the benthic chamber 3 cm from the chamber top. This tracer is conservative and can therefore be used to monitor diffusive exchanges across the sediment water interface (Reimers et al., 2004). Electrochemical measurements are synchronized with the release of the tracer to accurately quantify the initial concentration of iodide injected into the chamber.

Voltammetric analyses are conducted with a system of three electrodes including reference, counter, and working electrodes. Working electrodes were fashioned as previously described by Brendel and Luther (1995) and Taillefert et al. (2007). They consist of a 100 μm diameter gold wire encased in an electrode housing with a blend of West System 105 epoxy resin and 206 hardener. The electrodes used in the underwater benthic chamber are about 6.5 cm long and made of PEEK^{TM} tubing (Luther et al., 2008). The working electrodes for depth profiling are made of Pyrex glass pulled to a tip of 0.4 mm diameter. All electrodes are built with wet pluggable connectors (Impulse, Inc). After construction the working electrodes are sanded to ensure no epoxy is obstructing the exposed wire. They are then polished with diamond grit pastes (Buhler Inc.) of progressively decreasing abrasiveness (15, 6, 1, and 0.25 μm) to clean the tip surface. The gold wire electrodes are then plated with a thin film of mercury by reducing a degassed 0.1 mol L^{-1} $Hg(NO_3)_2H_2O$ in 2% HNO_3 solution for 240 s at a potential of -0.1 V. Following plating, the electrodes are conditioned at -9.0 V in 1 mol L^{-1} NaOH for 90 s. This step is designed to ensure the mercury forms an amalgam with the gold wire and increases the stability and durability of the electrode (Brendel and Luther, 1995). The counter electrode consists of a 0.5 mm diameter platinum wire soldered to a RG 174

braided copper conductor wire and fixed into a 7 cm long housing of a 3 mm diameter PEEK^{TM} (polyethyletherketone) tubing. The reference electrodes are constructed in a similar fashion, save the use of a 1 mm silver wire soldered directly to RG 174 braided copper wire. Before use, the silver wire is conditioned for 90 s at +0.9 V in 3 mol L^{-1} KCl to deposit a thin layer of AgCl on the surface. The working benthic chamber and profiling electrodes use the same set of reference and counter electrodes. Both reference and counter electrodes are mounted to the frame of the lander such that they are never inserted into the sediment. Working electrodes are calibrated for oxygen using the in situ temperature and salinity to calculate oxygen saturation (Luther et al., 2008). In this analysis, it is assumed that the average current response of the initial voltammograms corresponds to the dissolved oxygen concentration at saturation (Luther et al., 2008). The average current of replicate measurements in the overlying waters is then used to calculate the electrode sensitivity. The salinity of the overlying water captured by the sediment corer is measured with a RHS-10ATC portable refractometer. For all species other than oxygen, each electrode is calibrated ex situ according to the Pilot Ion Method with standard additions of 0.1 mol L^{-1} $MnCl_2$ (Brendel and Luther, 1995). A comprehensive list of detectable redox species as well as their detection limits can be found elsewhere (Luther et al., 2008). A typical voltammogram collected in situ is shown in Figure 3.2.

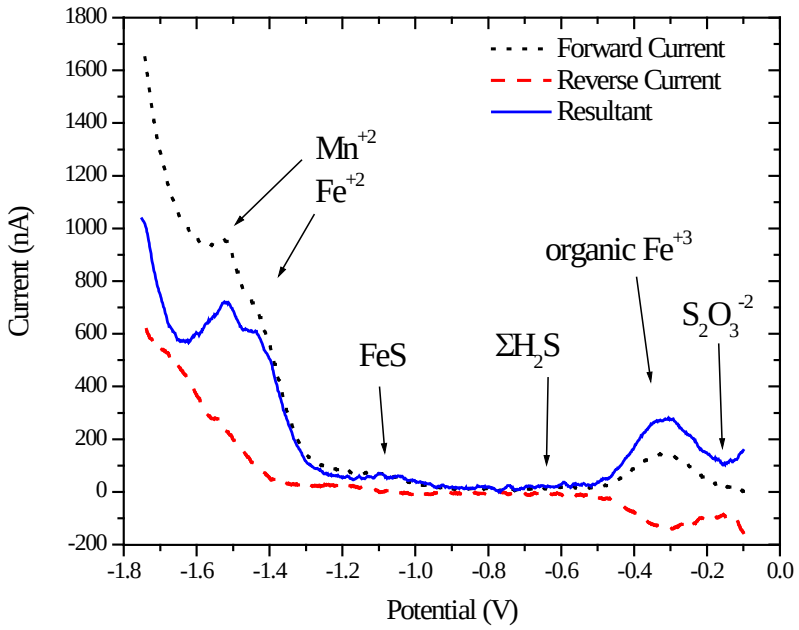

Figure 3.2: A typical cathodic square wave voltammogram obtained in situ during a depth profile dominated by organic Fe(III), Fe^{+2}, and Mn^{+2}. All currents have been smoothed with an 11 point adjacent average filter. The resultant current (solid line) is the sum of the forward and reverse currents. The resultant current is used for all calculations because it allows for better sensitivity than forward or reverse currents.

Prior to the deployment, the electrode sequence is uploaded into the ISEA II™ computer with a preset start time. After the lander is moved into position on the back of the ship, the electrodes are affixed to the lander and the solenoid timer armed. The lander is then lowered slowly into the water with the ship's A-frame until it gently rests on the seafloor and freed by a quick release. A long anchor line is attached to the top of the lander frame with two reflective surface buoys and two underwater buoys. The surface buoys are used to locate and retrieve the lander. The underwater buoys ensure that, during low tides, excess slack in the line does not catch on the lander or interfere with measurements or recovery.

Moments before lander deployment, a sediment core is collected for ex situ voltammetric analysis and other ancillary analyses of pore waters using a single core collector (Marinelli et al., 1998). Cores are taken within a maximum of 30 meters from the site where the lander is deployed. In addition to providing pore water dissolved inorganic carbon (DIC), NO_3^-, NO_2^-, ΣPO_4^{-3}, and total dissolved Fe concentrations that cannot be measured by voltammetry, these sediment cores can also be used for solid phase analyses, and their profiles compared to in situ measurements.

Iodide, dissolved oxygen, iron (II), manganese (II), and total dissolved sulfide are measured voltammetrically as a function of time in the benthic chamber to determine their fluxes across the SWI. As the measured flux of species across the SWI depends on the volume of water contained within the chamber, three features were added to determine the penetration depth of the benthic chamber into the sediment. The first involves a layer of double-sided mounting tape on the sides of the benthic chamber to trap sediment particles. Strips run from lid to base every 90^o around the outside of the chamber and are replaced prior to each deployment (Figure 3.1D). When the lander is retrieved, the distance between the bottom of the chamber and the top of the sediment mark on the tape is measured to calculate the volume of water present in the chamber. As a secondary measure, a mini corer is also attached to the side of the chamber (not shown in Figure 3.1). The top of the core barrel carries a flapper valve to retain the sediment in the core liner when the lander is retrieved. The amount of sediment contained within the core is used as a proxy for determining the volume of the benthic chamber that remains out of the sediment. Finally, the solenoid that releases the benthic chamber lid also injects a conservative tracer into the chamber. Immediately following injection, the

tracer concentration is measured voltammetrically and quantified using the Pilot Ion Method (Brendel and Luther, 1995). The initial concentration can be used to estimate the volume of the chamber since the concentration and volume of tracer injected are known. At the conclusion of each deployment, data is downloaded from the ISEA onto a laptop computer. Voltammetric scans are integrated with a modified version of VOLTINT, a semi-automated integration software developed for these applications (Bristow and Taillefert, 2008).

The diffuse flux of each chemical species detected during the ex situ core profile can be estimated based on Fick's First Law for porous media assuming the transport is controlled by molecular diffusion, sediment porosity, and tortuosity (Boudreau, 1997).

$$F_{Ex} = -\frac{\Phi D^0}{\Theta^2}\left(\frac{\partial C}{\partial x}\right) \tag{5}$$

where F_{Ex} is the flux (mmol m^{-2} day^{-1}), Φ is sediment porosity, D^0 is the molecular diffusion coefficient of solutes in water (cm^2 s^{-1}), Θ is tortuosity, C is the concentration (mol L^{-1}) and x is the depth (cm). Tortuosity is calculated with Archie's Law ($\Theta^2 = \Phi^{1-m}$) assuming m = 3 in fine-grained sediments (Ullman and Aller, 1982). The molecular diffusion coefficient of dissolved oxygen is determined using (Boudreau, 1997):

$$D^0 = (4.72 * 10^{-9})\left(\frac{T}{\mu V_b^{0.6}}\right) \tag{6}$$

where T represents the absolute temperature (K) and V_b is the molar volume of dissolved oxygen at its normal boiling temperature (27.9 cm^3 mol^{-1}) (Boudreau, 1997). The dynamic viscosity of water (μ) is corrected for temperature and salinity (Pilson, 1998).

For dissolved species, including sulfides, iron(II), and manganese(II), the molecular diffusion coefficient is calculated according to:

$$D^0 = (m_0 + m_1 * T) * 10^{-6} \quad (7)$$

where T is temperature (^oC) and m_0 and m_1 are species-dependent constants (Boudreau, 1997).

The governing equation to calculate in situ fluxes of reduced species is more complicated because advection and bioturbation below the SWI have to be taken into consideration (Eq. 8). Bioturbation irrigates sediment pore water in three dimensions but can be simplified to a one dimensional non-local exchange flux that depends on advection, burrow depth, and the concentration of solutes surrounding the burrow walls (Boudreau, 1997).

$$F_x = -\Phi D^T \left(\frac{\partial C}{\partial x}\right)\Big|_x + v\Phi C_x + \alpha L(C_0 - \Phi C_L) \quad (8)$$

where F_x (mmol m^{-2} day^{-1}) is the in situ flux, v (cm min^{-1}) is the advection (cm day^{-1}) , α represents the non-local exchange which affects concentrations at sediment depths less than L (cm), C_0 is the concentration of reduced species at the SWI, C_x is the concentration in the median point of the gradient, C_L is the concentration at depth L, and D^T represents the dispersion coefficient and Φ represents the change in porosity as a function of depth according to the exponential function (Rabouille and Gaillard, 1990):

$$\Phi = \Phi_{INF} + (\Phi_0 - \Phi_{INF}) \exp(-\gamma * x) \quad (9)$$

where γ is a constant and Φ_0 and Φ_{INF} were determined to be 0.88 and 0.7 for these sediments**.** Advective-dispersive oxygen uptake fluxes (ADOU) are also determined

using Eq. 8 except that the effect of non-local exchange processes was not considered at the SWI.

To quantify non-local exchange, advection, and dispersion, the temporal evolution of the iodide tracer at the SWI was modeled using the one dimensional governing equation (Boudreau, 1997):

$$\Phi \frac{dC}{dt} = D^T \frac{d}{dx}\left(\frac{\Phi}{\Theta^2}\frac{\partial C}{\partial x}\right) - v\frac{d(\Phi C)}{dx} + \alpha(C_0 - \Phi C) \qquad (10)$$

where D^T is the dispersion coefficient ($cm^2\ s^{-1}$), v represents advection ($cm\ s^{-1}$), α (s^{-1}) is a rate constant for non-local exchange between the sediment and the overlying waters (i.e., either bioturbation or bioirrigation). A central finite difference method in space and a Crank-Nicholson scheme in time were implemented in Matlab® to integrate this partial differential equation. A non-linear least square optimization procedure, also implemented in Matlab®, was used to find the dispersion coefficient (D^T), advection (v), and the non-local exchange rate constant (α) that best fit the benthic chamber data.

Assessment

Voltammetric techniques for in situ depth profiling have been previously validated using tethered systems (Luther et al., 1999; Reimers et al., 2004; Taillefert et al., 2007; Luther et al., 2008), as has the use of in situ temperature and salinity to calibrate dissolved O_2 (Luther et al., 1999; Luther et al., 2008). In turn, the use of a benthic chamber to monitor the flux of multiple chemical species across the SWI using

Hg/Au voltammetric electrodes and the application of voltammetric techniques for autonomous depth profiling are novel concepts. Because the lander is completely autonomous, the sequence of voltammograms acquired during each deployment has to be programmed and uploaded into the potentiostat prior to deployment. Thus, this sequence has to be designed to account for all the potential species detectable in natural sediments and simultaneously avoid potential artifacts that may be encountered during measurements. The tip of the working electrodes used for profiling is small enough (~0.4 mm) to minimize particle entrainment in the sediment. However, chemicals may advect to the electrode surface while the electrodes are lowered in the sediment and artificially enhance voltammetric currents. In addition, the potentiostat can only apply a potential to a single working electrode at a time and the inactive electrodes are exposed to an open circuit potential. During this idle period, diffusion of chemical species at the electrode surface could lead to an unwanted build-up of soluble organic Fe(III) complexes, iodide, and ΣH_2S as these species either adsorb (i.e. soluble organic Fe(III) complexes at potentials exceeding -0.4 V), or oxidize (i.e. iodide at potentials higher than -0.2 V, Hg^0 in the presence of ΣH_2S at potentials higher than -0.6 V) (Taillefert et al., 2000). Finally, voltammograms are typically acquired cathodically (i.e. from -0.1 V to -1.8 V) without preconcentration as concentrations of Fe(II), $FeS_{(aq)}$, and Mn(II) are usually high enough in sediments. In the cathodic mode, however, these electrodes are highly sensitive to sulfide species including HS^-, S^0, and S_x^{-2} (Brendel and Luther, 1995), and formation of a cinnabar (HgS) double layer in the mercury film at potentials greater than -0.6 V may prevent diffusion of sulfide species to the mercury film and lead to peak distortion (Davison et al., 1988).

To ensure the integrity of the measurements, the reactive surface of the working electrode is cleaned before each scan by conditioning at a potential where the redox species measured are not active (Brendel and Luther, 1995). A conditioning potential of -0.1 V for 10 s reoxidizes Fe(0) and Mn(0) concentrated on the mercury by reduction of Fe(II) and Mn(II) during the previous scan. When sulfide or organic Fe(III) species are anticipated, an additional conditioning step is added at a potential of -0.9 V for 10 s prior to the normal conditioning step at -0.1 V. This step does not influence Mn(II) and Fe(II) measurements, as these species are not electrochemically active at that potential, but instead ensures that sulfide or organic Fe(III) that may have accumulated on the electrode surface during the previous scan or the idle period is removed by reduction of HgS and organic Fe(III) just before the next measurement. While these conditioning steps help prevent sulfide poisoning of the electrode surface, anodic square wave voltammetry (ASWV) is the preferred technique to quantify high concentrations of sulfides (Davison et al., 1988) that may be found in marine pore waters (typically up to 2 mM). Scanning anodically prevents the mercuric sulfide film from forming initially until a potential of -0.6 V is reached and thus avoids formation of a cinnabar double layer. To measure I^-, ΣH_2S, Fe^{+2}, Mn^{+2}, soluble organic Fe(III), and $FeS_{(aq)}$, cathodic scans (-0.1 V to -1.8 V) with a maximum sensitivity of +/- 200 nA are collected first, followed by measurements with a sensitivity of +/- 2 μA. The initial use of the more highly sensitive technique helps in identifying eventual memory effects that may be encountered with sulfides and organic Fe(III) at potentials greater than -0.6 V. The sequence is concluded with linear sweep voltammetry (LSV) to measure oxygen concentration and determine whether the electrode has crossed the sediment water interface. A scan rate of 200 mV s^-

[1] is normally used in sediments, but in the water column, the scan rate is increased to 2000 mV s^{-1} to minimize background noise when the overlying water flows over the sediment (Luther et al., 2008). The best combination of voltammograms to measure all species of interest (i.e. O_2, H_2O_2, Mn(II), Fe(II), FeS, ΣH_2S, I^-, and organic Fe(III)) autonomously at each electrode in marine sediments is summarized in Table 3.2.

Table 3.2: Optimal sequence of voltammograms applied for sediment profiling (top) and benthic chamber time series (below) with Hg/Au voltammetric microelectrodes. The lower three experiments were assigned to the benthic chamber, and the upper four experiments were run at each time point for the other working electrodes. Thus for a 3 electrode deployment (one benthic chamber and two profiling electrodes), 44 scans would be conducted at each time point.

Number of Scans	**Voltammetric Wave Form**	**Scan Rate** (mV/s)	**Sensitivity** (+/- range)	**Conditioning applied**
4	Anodic Square Wave	200	100 nA (+/- 200 nA)	-0.9 V, 10 s (depending on location)
4	Cathodic Square Wave	200	100 nA (+/- 200 nA)	-0.9 V, 10 s -0.1 V, 10 s
4	Cathodic Square Wave	200	1 μA (+/- 2 μA)	-0.9 V, 10 s -0.1 V, 10 s
4	Linear Sweep	2000	1 μA (+/- 2 μA)	-0.1 V, 10 s
4	Cathodic Square Wave	500	1 μA (+/- 2 μA)	-0.9 V, 10 s -0.1 V, 10 s
4	Cathodic Square Wave	200	100 nA (+/- 200 nA)	-0.9 V, 10 s -0.1 V, 10 s
4	Linear Sweep	2000	1 μA (+/- 2 μA)	-0.1 V, 10 s

The sequence of voltammograms used for the benthic chamber is similar but consists of only three sets of voltammetric scans (Table 3.2) as ASWV scans are not necessary in the presence of low sulfide concentrations and CSWV can be used to

monitor the concentration of the iodide tracer as well as quantify reduced species eventually diffusing out of the sediment. Uncontrolled diffusion of species to the electrode remains an issue during periods of open circuit potential and is enhanced due to the constant circulation provided by the pump. Thus, the same cleaning steps are applied to this electrode to increase accuracy and precision of the measurements. Usually each scan is completed in less than 30 s, and each voltammetric technique is applied in quadruplicates to ensure good reproducibility. Thus, typical deployments for 6 to 13 hours with a working electrode in the benthic chamber and two on the micromanipulator provide two depth profiles of 20 to 40 data points with a spatial resolution of 5 mm.

As the lander does not carry a video system and measurements are not conducted live, the SWI is identified during the data integration in three different ways. First, a sharp decline in oxygen concentration is indicative of the electrode crossing the SWI (Figure 3.3).

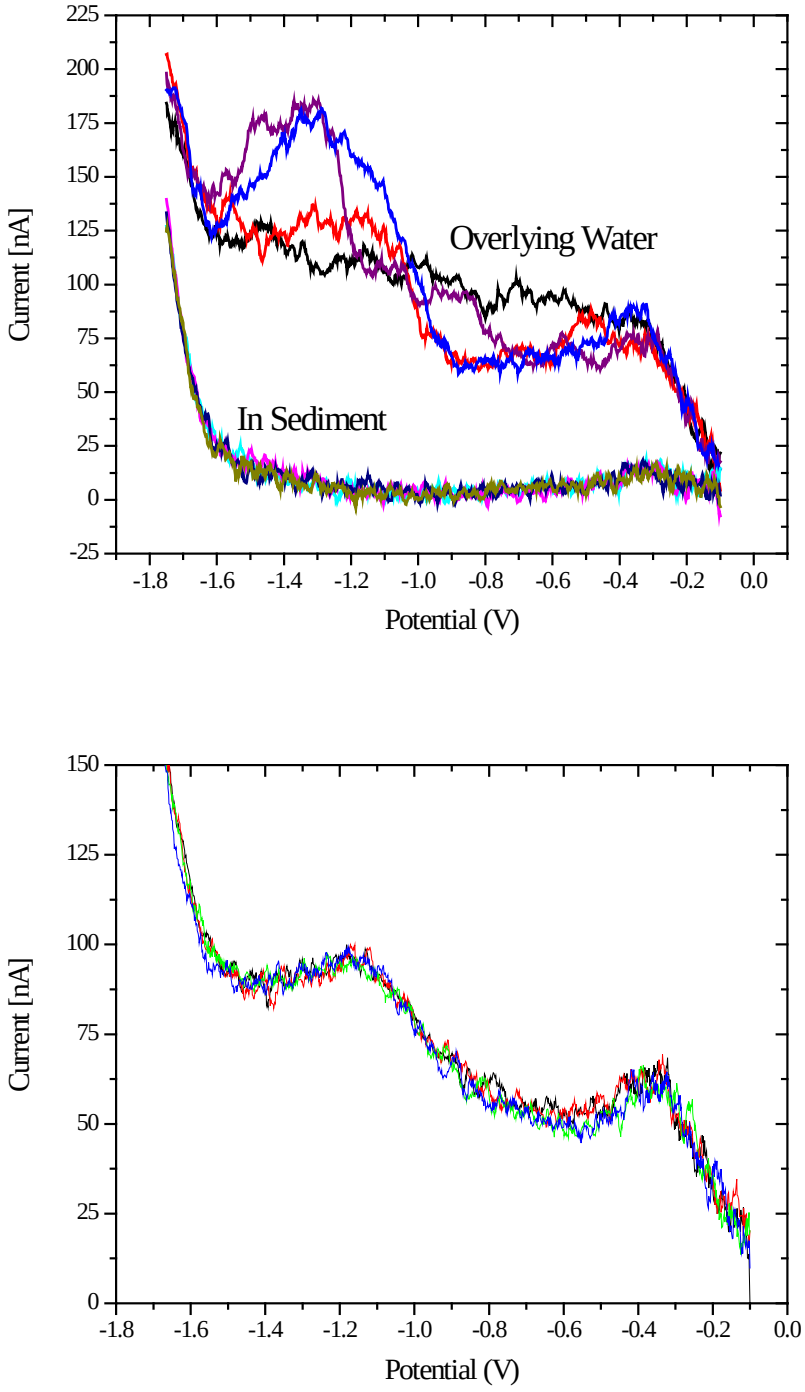

Figure 3.3: Dissolved oxygen individual measurements obtained by LSV during an in situ depth profile collected at 80 mm above the SWI and < 5 mm below the SWI (top); and in the benthic chamber (bottom). All scans were filtered with an 11 point adjacent average filter.

Second, the background noise of the voltammetric signal generated by the water flow, decreases significantly when the electrode crosses the SWI (Figure 3.3). Comparatively, voltammetric scans obtained from the benthic chamber during the same deployment display little deviation between replicates (Figure 3.3) which demonstrates that the pump only gently mixes the chamber water and confirms that the chamber is sealed from outside turbulences. Third, two profiling electrodes, positioned 2.5 cm from each other laterally and 5 cm apart vertically, provide two measurements to more accurately locate the SWI. Inspection of the shallower electrode profile confirms the location of the SWI by the marked decrease in oxygen at that depth (Figure 3.4).

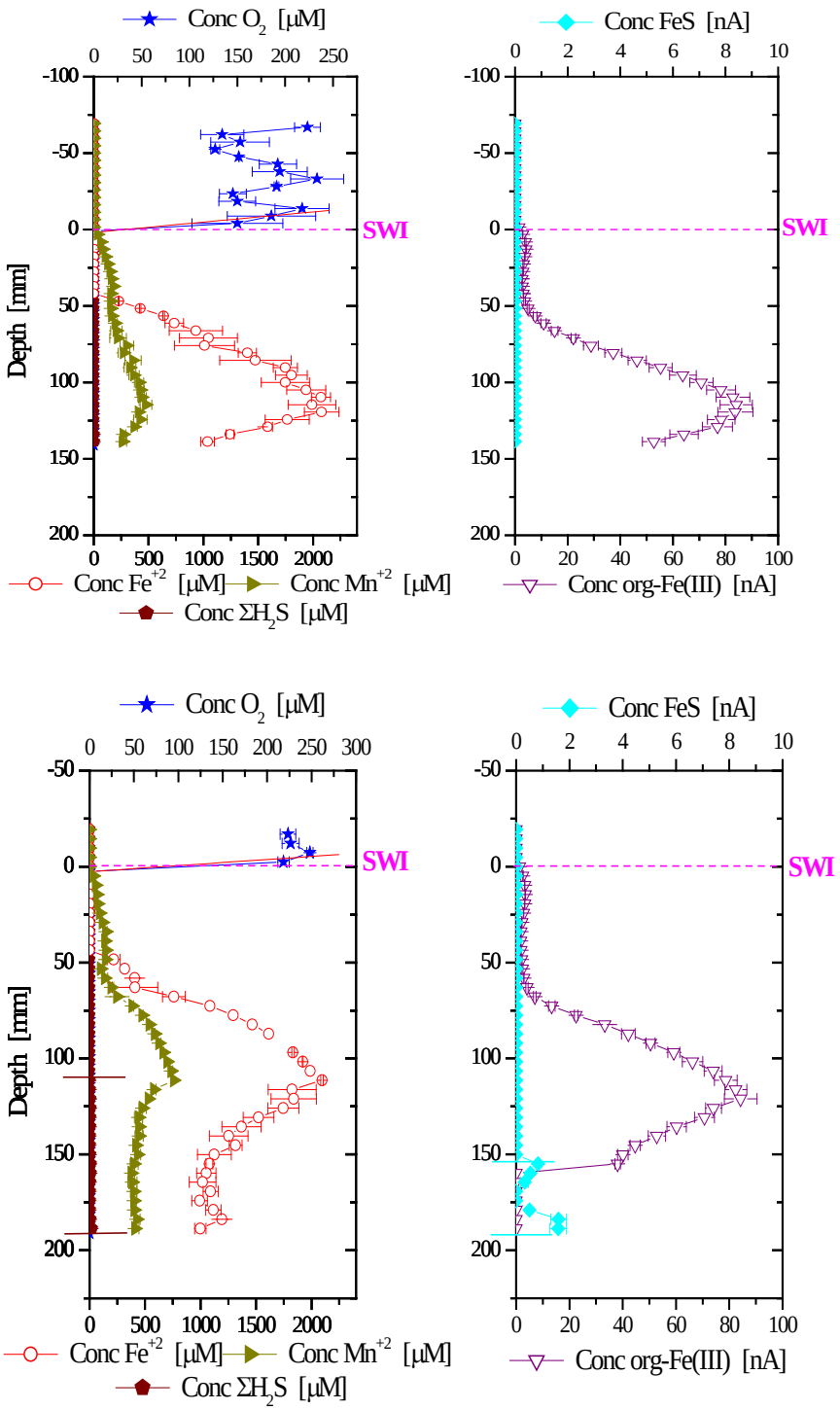

Figure 3.4: Typical in situ depth profiles illustrating a two electrode deployment from a moderately saline river site in May 2007. Depth profiles of O_2, Fe^{+2}, Mn^{+2}, ΣH_2S, organic Fe(III), and $FeS_{(aq)}$ at A) electrode 1 and B) electrode 2. Both electrodes were positioned 2.5 cm apart from each other laterally. The tip of electrode 1 was positioned 5 cm higher than that of electrode 2 to ensure that the sediment water interface was crossed by at least one electrode.

Using these techniques, the SWI can be located without direct observation with a +/- 2.5 mm accuracy, half the depth increment used during these deployments**.**

The new benthic lander and voltammetric sequence developed in the current study was tested more than 100 times in the estuarine sediments of the Satilla River and the continental shelf sediments of southeastern Georgia (USA). The quality of profiles generated by these autonomous measurements is displayed in the remarkable reproducibility obtained by the two electrodes (Figure 3.4). Concentrations of Mn(II), Fe(II), and organically bound Fe(III) increased with depth in the sediment and reached their maximum concentrations at relatively the same depth. While not evident on this profile, due to their low concentrations, sulfide species were detected at depth by each electrode. Accompanying this sulfide signal, were small current intensities from aqueous iron sulfide complexes as well as a marked decline in all other aqueous species. These concurrent events indicate the transition into an area dominated by sulfate reduction. This stratification illustrates the progressive respiration of the most to the least efficient electron acceptor.

To validate the accuracy of the in situ measurements, ex situ voltammetric analysis is conducted in sediment cores collected just before lander deployment (Figure 3.5).

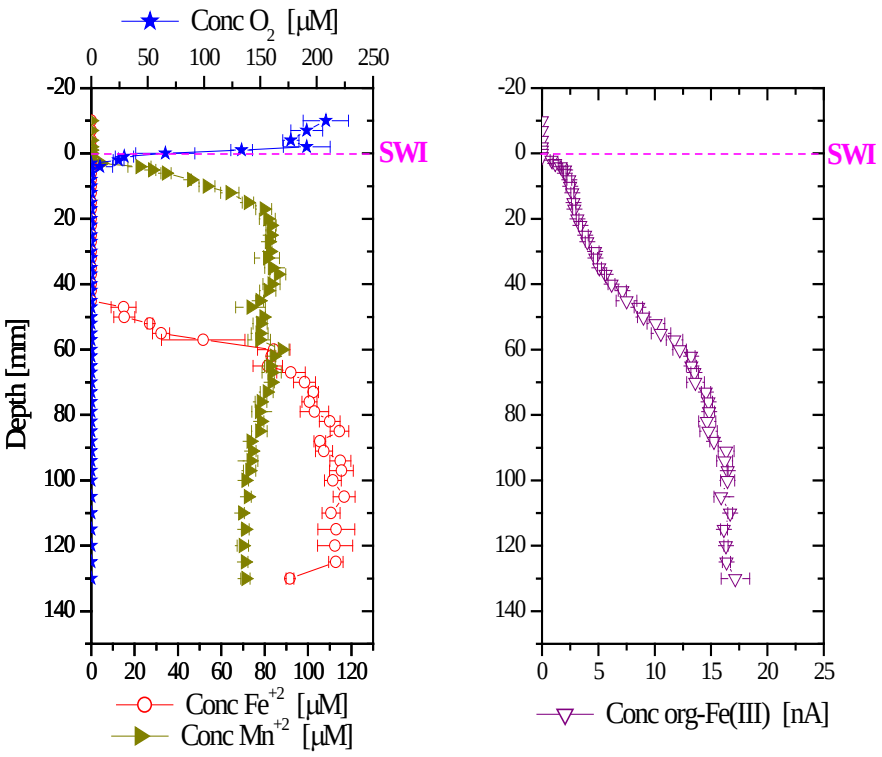

Figure 3.5: Typical ex situ core depth profile including O_2, Fe^{+2}, Mn^{+2}, and organic Fe(III), measured by voltammetric Au/Hg microelectrodes, with enhanced resolution compared to in situ profiles.

These ancillary cores, however, can only be obtained within a maximum distance of 30 m from the in situ measurements, as the currents and winds prevent the ship from maintaining position precisely where the lander is deployed. As in the in situ profiles, a sharp decline in oxygen concentration was apparent when the electrode approached the SWI, manganese and iron reduction dominated the upper and lower sediment layers, respectively, while dissolved sulfide was either low (Figure 3.4) or not observed (Figure 3.5) in the pore waters. A lack of evidence supporting sulfate reduction and the presence of aqueous Fe(II) and organic Fe(III) complexes at 50 mm suggests that iron-reducing organisms may be present at depth (Taillefert et al., 2007). In turn, the concentrations of Mn(II) and Fe(II) were significantly lower in the ex situ profiles and spread both in the

upward and downward directions from the sediment surface (Figure 3.5). The alteration of profile shape most likely results from reequilibration to a diffusion dominated system, while the differences in concentration suggest either that oxidation or precipitation of Mn(II) or Fe(II) occurred during the analysis of the sediment cores or that the sediment collected was not from the exact same location as the in situ deployments. In either case, they compare relatively well to in situ measurements and thus validate the sequence designed for the autonomous in situ deployments.

Time series obtained with the benthic chamber illustrate how benthic fluxes can be measured with a high temporal resolution (Figure 3.6).

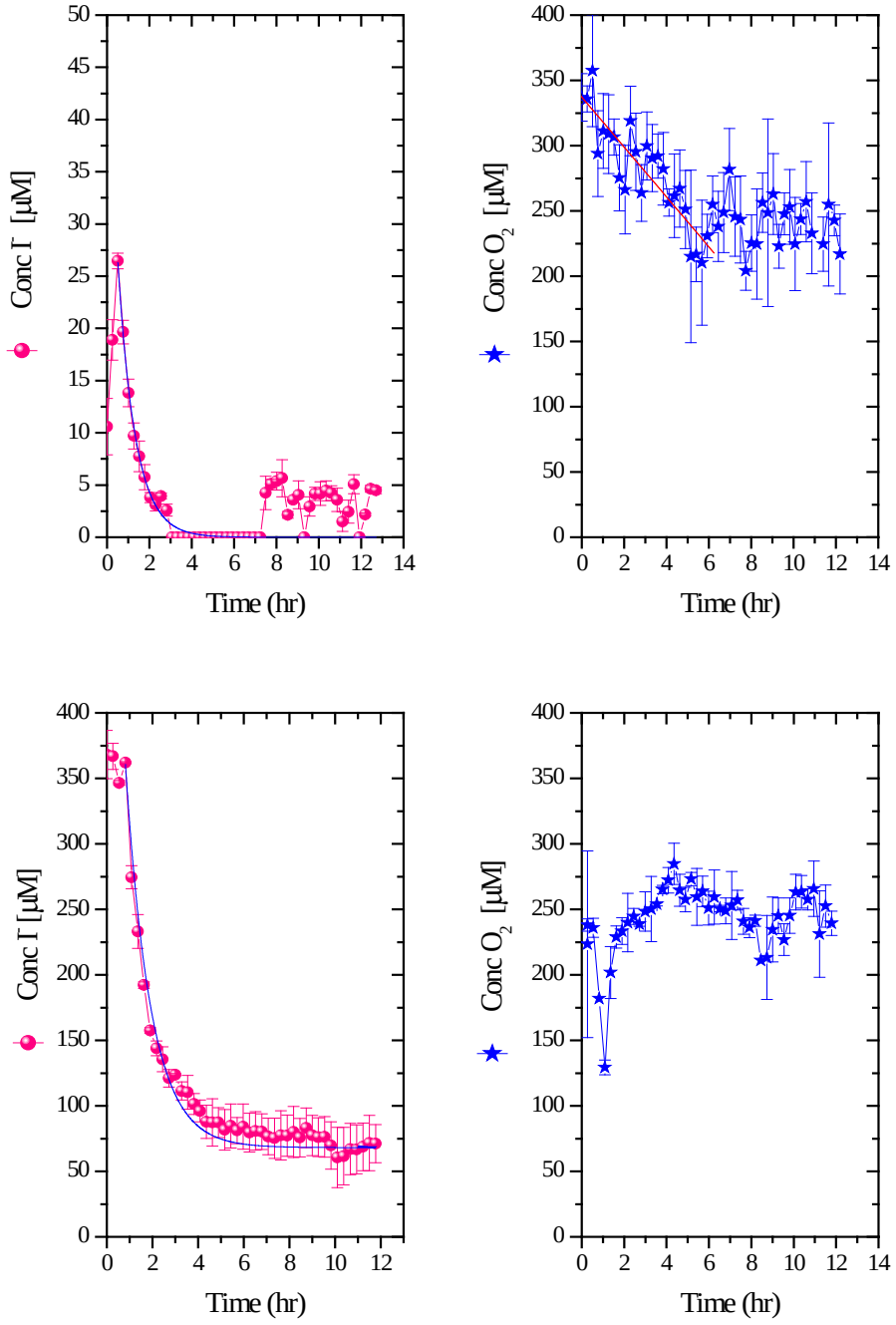

Figure 3.6: Two benthic chamber time series displaying dissolved oxygen and KI tracer concentrations. Deployments were performed at A) a fresh water sampling station in November 2006 and B) a moderately saline station in May 2007. The decline of the iodide tracer was modeled and the results represented by the solid lines on the left graphs.

Both deployments displayed sharp decreases in the tracer concentration initially and achievement of a quasi steady state concentration by the end of the deployment (Figure 3.6A and B). The November 2006 deployment also manifested a subtle yet constant decrease in the oxygen content of the chamber over the course of the deployment (Figure 3.6A). Oxygen concentrations remained relatively constant throughout the deployment at a more saline station in May 2007 (Figure 3.6B), although small variations of +/- 15 μM were visible. Depending on measurement conditions, a mere 1 nA variability in the background noise can easily correspond to roughly a 7 μM variance in concentration. This variability most likely reflects the complex eddy currents that persist along the sediment surface as a result of riverine discharge and tidal fluctuations (Berg et al., 2003; Berg et al., 2007).

Discussion

In this study, a new autonomous benthic lander has been developed to measure benthic fluxes and depth profiles of the main redox species consumed or produced during the remineralization of natural organic matter. These measurements are used to calculate rates of carbon remineralization from benthic oxygen fluxes and depth profiles of reduced metabolites. To our knowledge, this benthic lander is the first free autonomous lander that combines benthic chamber measurements and depth profiling of multiple redox species including Mn^{+2}, Fe^{+2}, ΣH_2S, and other intermediate complexes. It has been tested and refined through multiple deployments over a three year time span. Instead of adopting the tall, slim design, ideal for deep sea sediments (Berelson and Hammond,

1986; Black et al., 2001), this lander was constructed with a more squat design to limit sinking in fine-grained sediments and minimize the drag associated with the strong currents that occur in riverine and continental shelf environments.

Most in situ profiles have typically been garnered from tethered systems, which can be particularly advantageous when electrochemical techniques are employed (Berg et al., 2003; Glud and Gundersen, 2002; Luther et al., 1999; Reimers et al., 2004). Data collection can be monitored live, and measurements can be altered, depending on the chemical composition of the sediment, to prevent artifacts and memory effects (Luther et al., 1999). Unfortunately, tethered systems are poorly suited for deep sea measurements, and research vessels carrying tethered systems are required to remain stationary for the duration of the deployment, which can be an issue especially in rough weather. With autonomous systems, the ship is not required to anchor, and the science party has more time to conduct ancillary research. Thus, autonomous systems are more efficient in terms of ship time and cost than tethered systems. In turn, autonomous measurements with voltammetric techniques require the optimization of a sequence of voltammograms and their conditioning steps to minimize unwanted interferences. The pre-programmed voltammetric sequence developed during this study has been tested and refined to produce more than 150 data sets of high quality (e.g. Figure 3.4, 5, and 6). The majority of the deployments lasted between six and twelve hours and, within that time frame, the electrodes traveled between 13 and 21 cm into the sediment. Overall, most sediment profiles are comprehensive, with consistent concentrations between depths, and display relatively low standard deviations (i.e. 6 – 10% for Mn(II), Fe(II), and organic Fe(III), 29% for sulfides, and 18% for $FeS_{(aq)}$ due to their low concentrations in these sediments)

while maintaining short deployment durations. The in situ micromanipulator can presently only be programmed for one depth increment per deployment only, and a depth increment of 5 mm was determined to be ideal to obtain deep, comprehensive sediment profiles while maintaining a reasonable resolution for oxygen profiles. Thus, the spatial resolution achieved without cameras or other devices to locate the SWI pales in comparison to other amperometric and potentiometric techniques that have the ability to achieve up to 50 μm resolution (e.g. Archer and Devol, 1992; Glud and Gundersen, 2002; Wenzhofer et al., 2002). Voltammetric measurements, however, are capable of providing direct information about anaerobic respiration processes as deep as 20 cm into the sediment.

Differences between in situ and ex situ depth profiles (e.g. Figures 3.4 and 3.5) may be due to sediment heterogeneities as previously observed for nutrient profiles (Hammond et al., 2004). Recently, however, it was demonstrated that permeable sediments previously subjected to advective influences and relocated to strictly diffusion-dominated conditions, re-equilibrate to a diffusive transport regime within hours (Cook et al., 2007). Thus, the broadening of the depth profiles of each reduced metabolite (Figure 3.5) may indicate reequilibration processes due to the suppression of advective forcing upon sampling, and the decrease in Fe(II) concentrations in the ex situ profile suggests that Fe(II) may have been precipitated either by sulfides produced during sulfate reduction or carbonates produced during respiration. The ex situ fluxes of reduced species, ranging between 26.6 and 932 μmol m^{-2} day^{-1} for Mn(II) and 0.4 and 3.8 mmol m^{-2} day^{-1} for Fe(II), compare well to other studies (Berelson et al., 2003; Point et al., 2007; Warnkin et al., 2001). Benthic chamber flux measurements of manganese ranging

between -11 to 246 μmol m^{-2} day^{-1} have been reported (Point et al., 2007). Additionally, fluxes ranging between 3 and 17.7 μmol m^{-2} day^{-1} for manganese and 1.26 to 10.79 μmol m^{-2} day^{-1} for iron depending on the season, were obtained in the shelf of Monterey Bay (Berelson et al., 2003). Finally, fluxes ranging between 20 and 365 μmol m^{-2} day^{-1} for manganese and 7 and 94 μmol m^{-2} day^{-1} for iron were also obtained using benthic chambers in Galveston Bay (Warnkin et al., 2001). While the ex situ manganese fluxes measured in the Satilla River are comparable to the fluxes measured at these sites, iron reduction appears to contribute more significantly to carbon remineralization in the Satilla River estuary. Simultaneously, carbon fluxes based on the ex situ depth profiles of reduced species are markedly less than corresponding carbon fluxes calculated from the dissolved oxygen profile (Table 3.3) which suggests either that aerobic respiration, reoxidation of reduced metabolites, or burial of reduced metabolites is significant in these sediments. Indeed, saturation states of the pore waters calculated using the measured pH, Fe(II), Mn(II), and dissolved organic carbon concentrations at the same station indicate that they are supersaturated with respect to both rhodocrosite and siderite (data not shown).

Table 3.3: Ex situ vs. in situ seasonal DOU and carbon flux calculations from a periodically saline sampling location in the Satilla River (GA). Diffusive fluxes were calculated from ex situ measurements using Fick's first law. Advective- diffusive fluxes were calculated from in situ measurement using transport parameters determined by simulation of the temporal evolution of the tracer in the benthic chamber. Carbon fluxes were calculated from DOU and ADOU assuming oxygen as the ultimate oxidant of NOM. Carbon fluxes were calculated from the fluxes of reduced species assuming that each reduced metabolite was produced by anaerobic respiration of NOM. An average carbon oxidation state of +0.27 in NOM was used for these calculations.
* Denotes deployments in which benthic chamber was completely submerged and oxygen was not measurable

	Ex Situ Measurements			In Situ Measurements			
Date	Diffusive Oxygen Uptake (DOU) ($mmol\ m^{-2}\ day^{-1}$)	Carbon Flux From DOU ($mmol\ m^{-2}\ day^{-1}$)	Carbon Flux From Reduced Species ($mmol\ m^{-2}\ day^{-1}$)	Total Oxygen Uptake (TOU) ($mmol\ m^{-2}\ day^{-1}$)	Advective Diffusive Oxygen Uptake (ADOU) ($mol\ m^{-2}\ day^{-1}$)	Carbon Flux From ADOU ($mol\ m^{-2}\ day^{-1}$)	Carbon Flux From Reduced Species ($mol\ m^{-2}\ day^{-1}$)
5-Sep '05	N/A	N/A	N/A	N/A	2.4 (+/- 0.4)	1.3 (+/- 0.2)	0.00 (+/- 0.00)
5-Dec '05	N/A	N/A	N/A	N/A	1.2 (+/- 0.5)	0.6 (+/- 0.3)	0.1 (+/- 0.0)
6-Jan '06	N/A	N/A	N/A	245.1 (+/- 39.4)	2.9 (+/- 0)	1.6 (+/- 0.0)	1.7 (+/- 0.1)
6-Jun '06	N/A	N/A	N/A	N/A*	N/A	N/A	3.3 (+/- 0.8)
6-Aug '06	3.2 (+/- 0.9)	1.7 (+/- 0.5)	1.0 (+/- 0.3)	N/A*	N/A	N/A	N/A
6-Oct '06	61.8 (+/- 15.5)	33.2 (+/- 8.3)	3.1 (+/- 0.1)	N/A*	1.3 (+/- 0.6)	0.7 (+/- 0.3)	1.6 (+/- 0.2)
6-Nov '06	13.8 (+/- 0.7)	7.4 (+/- 0.4)	0.2 (+/- 0.1)	56.9 (+/- 7.9)	2.1 (+/- 0.4)	1.2 (+/- 0.2)	1.3 (+/- 0.6)
7-Jan '07	3.1 (+/- 0.5)	1.7 (+/- 0.3)	0.2 (+/- 0.0)	70.2 (+/- 20.9)	2.4 (+/- 0.5)	1.3 (+/- 0.2)	0.6 (+/- 0.2)
7-May '07	4.3 (+/- 0.9)	2.3 (+/-0.5)	0.1 (+/- 0.0)	11.2 (+/- 3.4)	0.8 (+/- 0.1)	0.4 (+/- 0.1)	0.1 (+/- 0.0)
7-Jul '07	8.7 (+/- 1.7)	4.7 (+/- 0.9)	1.5 (+/- 0.8)	15.8 (+/- 11.7)	1.6 (+/- 0)	0.9 (+/- 0.0)	1.6 (+/- 0.1)
7-Sep '07	10.2 (+/- 2.9)	5.5 (+/- 1.6)	0.7 (+/- 0.0)	N/A*	N/A	N/A	N/A
7-Nov '07	3.1 (+/-0.3)	1.7 (+/- 0.2)	0.5 (+/- 0.1)	96.9 (+/- 26.9)	1.9 (+/- 0.2)	1.0 (+/- 0.1)	0.2 (+/- 0.0)
8-Jan '08	2.3 (+/-0.1)	1.2 (+/- 0.0)	0.3 (+/- 0.1)	124.7 (+/- 10.8)	2.8 (+/- 0.4)	1.5 (+/- 0.2)	0.01 (+/- 0.00)

To determine the fluxes of reduced species measured from the in situ depth profiles, the advection, dispersion, and non-local exchange coefficients were fitted to the iodide tracer data measured in the benthic chamber. While the model fits the data appropriately (Figure 3.6), the non-derivative component of equation 11, the non-local exchange, exhibits the highest influence on the evolution of the tracer with time at the SWI for a number of deployments, such that the advection and dispersion coefficients do not change significantly. The optimized α values (Table 3.4) are generally one order of magnitude higher than the range (19.5 – 116 yr^{-1}) reported previously for coastal sediments (Boudreau, 1997).

Table 3.4: Results of the 1-D diffusion corrected equation model for optimization of advection, dispersion, and non-local exchange at different stations along the Satilla River estuary using equations 9 and 10 (Φ=0.88;Φ_{INF} = 0.70).

Station	Date	v ($cm\ s^{-1}$)	D^T ($cm^2\ s^{-1}$)	Alpha (hr^{-1})
SAT 1	Nov '06	0.01	$3x10^{-4}$	21.72
	Nov '07	0.01	$3x10^{-4}$	20.20
SAT 3	May '07	0.01	$3x10^{-4}$	9.39
SAT 4	May '07	0.01	$3x10^{-4}$	8.62
	Jan '08	0.01	$3x10^{-4}$	4.46
SAT 5	Nov '07a	0.01	$3x10^{-4}$	52.50
	Nov '07b	0.01	$3x10^{-4}$	15.45

However, they are much closer to the average value of 55 hr^{-1} obtained in a study focusing on a Belgian estuary (Laverman et al., 2007). A high α indicates enhanced non-local exchange due to increased bioirrigation, and it has indeed been shown that in near shore sediments the impact of non-local exchange is greater in summer compared to

winter (Martin and Sayles, 1987). An advection of 0.01 cm s^{-1} was necessary to reproduce the decline in iodide concentration from the benthic chamber data (Table 3.4), about twice as much as previous estimates for the Satilla River (Jahnke et al., 2003). The advection determined in this study, however, is in the range of other estimates obtained in continental shelf sediments (Reimers et al., 2004) and a coastal marsh (Miller et al., 2007). Similarly, dispersion coefficients estimated from the model fall within the previously published range of $8.62x10^{-5} – 1.42x10^{-3}$ cm^2 s^{-1} for estuarine sediments (Roychoudhury, 2001). These calculations confirm that the flow of water above the sediment enhances the exchange of chemicals across the SWI as previously observed (Jahnke et al., 2003).

Carbon fluxes at the same moderately saline station were calculated with Eq. 1 and the fluxes of reduced species obtained from the in situ profiles and equation 8 to account for advection and non-local exchange. Nitrate and nitrite concentrations were not considered in this analysis as their concentrations in the overlying water are relatively low along the river (Jahnke et al., 2003). Carbon fluxes are nearly three orders of magnitude higher than the corresponding carbon fluxes from the ex situ measurements (Table 3.3). Similarly, ADOU fluxes calculated a the same station during the same time period are nearly three orders of magnitude higher than DOU fluxes calculated from ex situ profiles (Table 3.3). These uncharacteristic findings illustrate the substantial impact of advection on the flux of dissolved oxygen and reduced metabolites in the sediments of this estuary. These incongruities also concur with a recent investigation performed under controlled conditions which demonstrated that ignoring advective fluxes in sediments leads to the underestimation of NOM remineralization (Cook et al., 2007). In the Satilla

River estuary, the combined effect of river flow and tidal forcing most likely increases oxygen penetration into the surface layers of these fine-grained sediments. Given the fact that dissolved oxygen penetration depths measured in situ do not exceed a few millimeters (Figure 3.4), the present study suggests that carbon remineralization and redox recycling of reduced metabolites (e.g. Mn(II), Fe(II), and ΣH_2S) are significantly enhanced in these sediments. Irrespective of its magnitude, the in situ carbon flux determined from the flux of reduced species increases during the summer months and decreases in winter (Table 3.3), indicating that anaerobic respiratory processes are significantly more intense during the summer. Additionally, the carbon flux based on the reduced species tends to exceed the carbon flux calculated from the ADOU flux during the summer months, which indicates that reduced species are not completely reoxidized by dissolved oxygen. During the winter months, however, carbon oxidation by dissolved oxygen is either equivalent to, or exceeds the reduced species contribution. These findings suggest that assuming oxygen as the ultimate oxidant is a good approximation in the winter but not in the summer. Finally, the contribution of the reduced species flux to carbon remineralization may be underestimated during the summer especially, as burial processes may remove a significant fraction of manganese and iron in the form of $FeS_{(s)}$, pyrite, or carbonate minerals. Sediment extractions of acid volatile sulfur (AVS) and carbonate minerals could quantify the amounts of reduced metabolites that were lost to burial (Rickard and Morse, 2005).

The overall purpose of the benthic chamber was to calculate TOU fluxes and determine whether other dissolved species were transported across the SWI. The three independent methods used to calculate the volume of the overlying water in the benthic

chamber generally display similar results (Table 3.5), demonstrating that it can be accurately determined.

Table 3.5. Benthic chamber volume determined using the mini corer, mounting tape and iodide tracer methods for four deployments at varying stations in the Satilla River estuary.

Date	Corer Depth (cm)	Tape Depth (cm)	Ave Mud Depth (cm)	Chamber Volume (L)	Conc KI (μM)	Chamber Volume (L)
May '07	17	17.0 (+/- 0)	17.0 (+/- 0)	11.1 (+/- 0)	368.1 (+/- 18.5)	13.6 (+/- 0.7)
Nov '07	16	17.0 (+/- 1.7)	16.8 (+/- 1.5)	11.3 (+/- 1.0)	384.4 (+/- 230.6)	13.0 (+/- 7.8)
Nov '07b	12	12.0 (+/- 1.7)	12.0 (+/- 1.4)	15.4 (+/- 1.8)	326.7 (+/- 0.3)	15.3 (+/- 0.0)
Jan '08	10.5	9.7 (+/- 0.6)	9.9 (+/-0.6)	17.2 (+/- 1.3)	343.2 (+/- 29.6)	14.6 (+/- 1.3)

The slight overestimation of the overlying water volume determined electrochemically may be the result of a small amount of iodide remaining in the injection tube or a small leak at the injection port. Similarly, a small loss of sediment during retrieval may explain the slightly high water volume estimated with the mini corer. In contrast, the tape potentially underestimates the chamber volume due to adhesion of particles in suspension. The height of the overlying water (H) was used together with the rate of oxygen change in the benthic chamber to calculate the flux of dissolved oxygen across the sediment-water interface, or total oxygen uptake (TOU), according to (Rao and Jahnke, 2004):

$$TOU = \frac{\partial [O_2]}{\partial t} H \qquad (11)$$

Overall, TOU fluxes measured seasonally over more than a year at the same station (Figure 3.6 and Table 3.3) are much higher than average estimates reported for the Atlantic Ocean (10 mmol O_2 $m^{-2}day^{-1}$; Wenzhofer et al., 2000) but are in the same range of other recently reported flux measurements. Fluxes ranging between 98 (+/- 21) mmol O_2 $m^{-2}day^{-1}$ at night and 1138 mmol O_2 $m^{-2}day^{-1}$ during daylight hours were measured using Eddy correlation techniques in shelf sediments (Berg and Huettel, 2008). Similarly, a flux of 92 mmol O_2 m^{-2} day^{-1} was determined in sediments exposed to advective transport (Plant et al., 2009). Finally, fluxes determined with parallel benthic chambers designed to simulate the effect of advection on the flux across the SWI ranged between 25 and 100 mmol O_2 $m^{-2}day^{-1}$ depending on the applied flushing rate (Cook et al., 2007). These findings suggest that advective processes were responsible for increasing the removal of oxygen and iodide near the SWI as already observed previously in the same estuary (Jahnke et al., 2003). In addition, TOU fluxes correlate to ADOU fluxes and are generally higher in the late fall and winter months than during the summer seasons (Table 3.3), suggesting either that reoxidation of reduced metabolites by oxygen predominates during the winter or that burial rates are increased during the summer months due to the increased production of reduced metabolites by anaerobic heterotrophic processes. As the independent carbon fluxes calculated from the fluxes of reduced metabolites indicate that anaerobic respiration is enhanced during the summer months, the latter explanation is favored. Inconsistencies between TOU and ADOU fluxes are remarkable and suggest that advective processes due to the exposure of the benthic chamber to the river flow may have modified SWI exchange processes in the chamber. Previous studies have demonstrated that the presence of mounds on the

sediment surface exposed to flowing water generates inward and outward advective fluxes before and after the mound that result in complex temporal and spatial variations in dissolved oxygen and other reduced metabolites immediately above and below the sediment surface (Huettel et al., 1998). Similarly, inflow of anaerobic or partially aerated pore waters in the chamber as a result of its presence above the sediment may have artificially enhanced the loss of tracer from the chamber and therefore increased exchanges at the SWI, while supplying dissolved oxygen to the benthic chamber. This explanation is supported by the episodic influx of iodide or dissolved oxygen in the chamber observed during deployments that correlates with tidally-related changes in flow direction (e.g. Figure 3.6). These findings indicate that benthic chambers may have to be avoided in dynamic coastal systems, especially when tracers are used to parameterize the transport in sediments. In environments where the flow of water does not interfere with benthic exchange processes, however, the present method offers several ways to calculate carbon fluxes in sediments that could be used to check for consistency.

Comments and Recommendations

A new autonomous benthic lander carrying an electrochemical analyzer has been developed to simultaneously measure benthic fluxes of redox chemical species across the sediment-water interface and their depth profiles in pore waters. The benthic lander carries a tracer-delivering system that releases iodide during deployments. The temporal evolution of the tracer concentration in the benthic chamber is used to quantify transport and non-local exchange processes across the sediment-water interface. These parameters

together with in situ depth profiles can be used to calculate fluxes of reduced metabolites involved in carbon remineralization and further infer carbon remineralization rates in continental shelf sediments assuming an average carbon oxidation state. Despite their large differences in magnitude, which can be attributed to the artificial enhancement of exchange processes at the SWI as a result of the strong water flow above the sediment, ADOU and TOU fluxes correlate well seasonally. To our knowledge, carbon remineralization fluxes derived from these in situ depth profiles are the largest ever reported, mainly because they are strongly affected by transport processes across the SWI. Future studies will focus on determining net rates of transformation of individual terminal electron acceptors using a reactive transport model (Carey and Taillefert, 2005) to obtain integrated rates of carbon remineralization. Despite these issues, the present study demonstrates that assuming dissolved oxygen as the ultimate oxidant is not appropriate in coastal environments as burial of solid phases and accumulation of reduced species likely underestimates carbon remineralization rates. Additional lander modifications under consideration include addition of a water sampling device for the benthic chamber to monitor the flux of nutrients (i.e. nitrate, nitrite, ammonium, phosphate) that cannot be detected electrochemically, addition of a resistivity sensor to improve the resolution of the micromanipulator near the SWI, and ability to maintain a holding potential on working electrodes that are not in use to increase electrode life in sulfidic conditions.

Acknowledgements

This study was funded by the CAREER Program of the National Science Foundation (OCE-239376). We are very appreciative of the help granted by the captain and crew of the R/V Savannah. Additionally, we would like to thank Morris Jones, Jordon Beckler, and Hong Wu, who have helped in the data collection for this project.

CHAPTER 4

IMPACT OF RIVERINE DISCHARGE ON BIOGEOCHEMICAL PROCESSES IN ESTUARINE SEDIMENTS

Abstract

Over the last decade, the spatial and temporal resolution of geochemical measurements in aquatic sediments has improved significantly thanks to the development of in situ analytical techniques. As most sediment measurements are time consuming, however, seasonal variations in biogeochemical processes are typically not resolved at the ecosystem scale. The objectives of this project were to characterize the seasonal variability of sediment biogeochemistry and to examine the impact of riverine discharge on carbon remineralization processes in an estuary fed by an organic-rich river. A recently developed autonomous benthic lander was deployed seasonally for three years at multiple stations along the Satilla River estuary (Georgia, U.S.A.). The lander was equipped with an underwater potentiostat and a micromanipulator for in situ voltammetric depth profiling of the main redox species in sediment pore waters. These measurements confirmed that biogeochemical processes vary seasonally and revealed that these processes are influenced by riverine discharge in the estuary. During the study, the southeastern United States experienced a prolonged drought which decreased river discharge into the Satilla River estuary. This change in hydrologic conditions altered the salinity gradient in the estuary and profoundly affected anaerobic respiratory processes in the underlying sediments. Under normal hydrologic conditions, iron reduction was the dominant anaerobic respiratory process across the estuary, likely due to the significant

supply of iron from the surrounding coastal plain and low salinity of the estuary. Under drought conditions, however, the salinity of the estuary increased to full seawater strength and carbon remineralization was significantly enhanced. Yet, sulfate reduction was only observed near the mouth of the estuary, while a substantial increase in iron reduction was evidenced upriver. Evidence indicates that the increase in iron-reducing activity during the drought resulted mainly from the deposition of mineral particles in the upper estuary when the local salinity gradient increased at low discharge. Altogether, this study demonstrates that the biogeochemical response of these sediments to natural perturbations is rapid and indicates that respiration processes in continental shelf sediments are controlled by a combination of temperature, supply of inorganic and organic substrates, and hydrological processes. These findings have important implications on the effect of climate change on the biogeochemical cycling of carbon in these environments.

Introduction

Despite covering a modest 20% of ocean surface area, continental margins are responsible for ~15% of the ocean's net primary productivity (Wollast, 2003) and contain approximately 40% of the carbon buried annually in the oceans (Mueller-Karger et al., 2005). These areas receive an enhanced supply of nutrients and carbon from upwelling and riverine inputs (Wollast and Chou, 1998) and act as a filter and trap for both natural and anthropogenic materials transported from land to the open ocean (Mantoura et al., 1991). Overall, coastal ecosystems have been neglected from general circulation models, as the complexity of these environments is extremely difficult to model and requires time

consuming regional scale process analyses (Ver et al., 1999). Recently however, coastal environments have received more attention as mounting evidence indicates the majority of terrestrial organic matter is degraded on continental shelves (Middelburg and Herman, 2007).

In general, near shore ecosystems are considered heterotrophic and net sources of carbon to the atmosphere, while marginal seas are classified as autotrophic and atmospheric carbon sinks (Chen and Borges, 2009). The metabolic state of coastal environments depends on their size and average salinity (Caffrey, 2004), but seasonal variations in light intensity and temperature (Caffrey, 2004), rainfall (Ram et al., 2003), as well as carbon and nutrient inputs from neighboring marshes (Pomeroy et al., 2000) and rivers (Chanton and Lewis, 2002), ultimately influence primary production (Chanton and Lewis, 2002; Rozan et al., 2002), community respiration (Cai et al., 1999; Pomeroy et al., 2000; Caffrey, 2004; Green et al., 2004), trophic status (Ram et al., 2003; Caffrey, 2004 Dell'Anno et al., 2008), the metabolic balance of the community (Cai et al., 2000; Pomeroy et al., 2000), and the geochemical composition of sediments (Rozan et al., 2002, Taillefert et al., 2002b).

As less than 5% of riverine sediments delivered to continental margins reaches the deep sea, river-ocean margins must be active zones of particle transformation and sediment deposition (Ver et al., 1999; McKee et al., 2004). Sedimentation rates in estuaries depend on turbulence, particle size, current velocity, and the intensity of the salinity gradient (Sholkovitz, 1976; Eisma, 1986). In estuaries fed by rivers, water discharge controls the concentration of particles in suspension such that large sedimentation rates are generally associated with low discharge (McKee et al., 2004).

Consequently, a decline in river discharge and flow velocity generally results in greater seawater inputs and an increase in pH, which, together promote the rapid removal of particles by adsorption and flocculation (Sholkovitz, 1976; Eisma, 1986). In addition to particle deposition, biogeochemical processes in margin sediments are also controlled by the composition and flux of the delivered lithogenic and biogenic materials (McKee et al., 2004) as well as sediment remobilization events (Aller et al., 1986). Higher discharge increases lithogenic inputs, including iron and manganese oxides that are concentrated in the particulate phase during weathering (Canfield, 1997). Simultaneously, the fraction of labile organic matter originating from autochthonous production decreases at high discharge (Cowie and Hedges, 1992; McKee et al., 2004). Conversely, low discharge promotes microbial growth in upstream estuaries (Mortazavi et al., 2000; Chanton and Lewis, 2002) and the fraction of autochthonous organic material in the sediment increases (Dai and Sun 2007). The increase in organic matter inputs stimulates benthic microbial metabolism (Aller et al., 1996; Dai and Sun, 2007) and oxygen consumption which can potentially contribute to bottom water anoxia (Hagy et al., 2004; Wei et al., 2007). Sediment remobilization events that typically occur during high discharge also influence sediment diagenesis by reoxidizing iron and manganese to sustain metal reducing conditions for months despite the high sulfate concentrations available in pore waters (Aller et al., 1986; Aller et al., 2004a and b). Most of these studies, however, relied on a few select samples collected in specific discharge conditions. Determining the role of riverine discharge on carbon remineralization in estuaries requires the characterization of seasonal variations in sediment biogeochemistry with a high spatial and temporal resolution. Unfortunately, such studies remain scarce, as analytical tools

that can evaluate sediment biogeochemical processes in situ have only been recently developed (Tercier-Waeber and Taillefert, 2008; Chapter 3).

The overall objective of this study was to examine the seasonal variability of the diagenetic processes regulating carbon transformation in the sediments of the Satilla River estuary in south Georgia (U.S.A.). To obtain high temporal and spatial resolution, a newly developed autonomous benthic lander (Chapter 3) was deployed seasonally at multiple stations along the river. The autonomous lander was designed with a micromanipulator for comprehensive in situ depth profiling of sediment pore waters. Mercury/gold amalgam voltammetric microelectrodes (Brendel and Luther, 1995) were used to simultaneously measure dissolved oxygen, Fe(II), Mn(II), ΣH_2S, and other iron complexes. A variety of analyses, including voltammetric profiling and pore water analysis for dissolved phosphate, iron, and dissolved inorganic carbon (DIC), were also performed ex situ on sediment cores collected simultaneously. The combination of in situ and ex situ measurements revealed that hydrological processes have a clear impact on the sediment biogeochemistry of estuaries dominated by riverine inputs.

Methods

The Satilla River located along the coast of southeastern Georgia (U.S.A) is a black water river that originates on the coastal plain. The overlying waters contain an average of 16.6 mg/L of suspended solids and exhibit a pH gradient from 5.71 upriver to 7.64 at the mouth (Alber et al., 2003). Overall, the river spans 420 km through a primarily rural watershed and experiences strong semidiurnal tidal fluctuations ranging from 2 – 3 m at spring and neap tides (Alber et al., 2003). The flow velocity averages

about 1 m s^{-1} and salinity averages 29 at the river mouth but declines to 0 by 50 km upstream (Alber et al., 2003). Five sampling locations were established along the river (Figure 4.1).

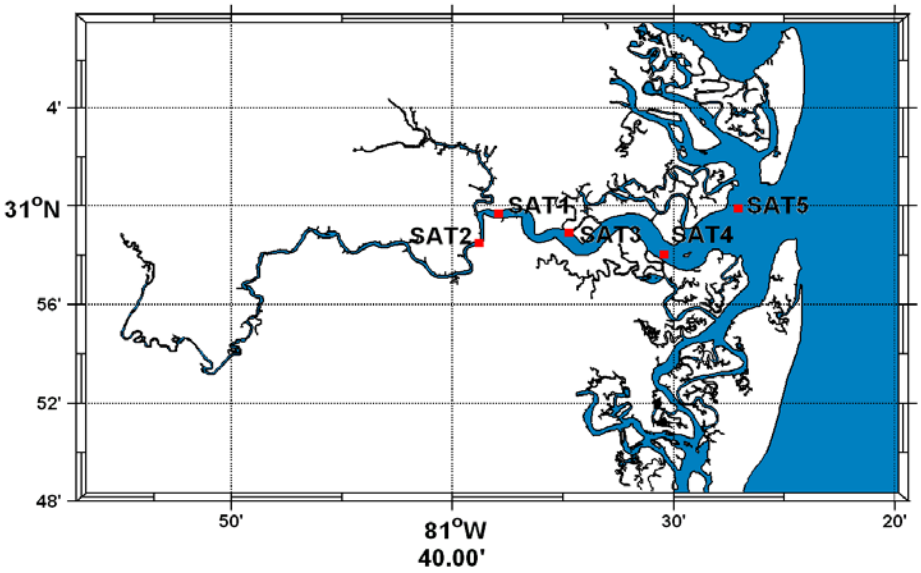

Figure 4.1: The Satilla River study site located 15 miles north of the state border between Georgia and Florida. The sampling station farthest upriver (SAT 1) is located 20 km upstream from the river mouth.

Sediment characteristics vary from predominantly coarse and sandy at SAT 5 to fine grained clays and mud at SAT 1. The consequences of an extended drought, which impacted the entire southeast United States, were first noted in the Satilla River in late summer 2006. River discharge declined precipitously throughout 2006 and 2007 before returning to average volumes near the conclusion of this study in January 2008 (Figure 4.2).

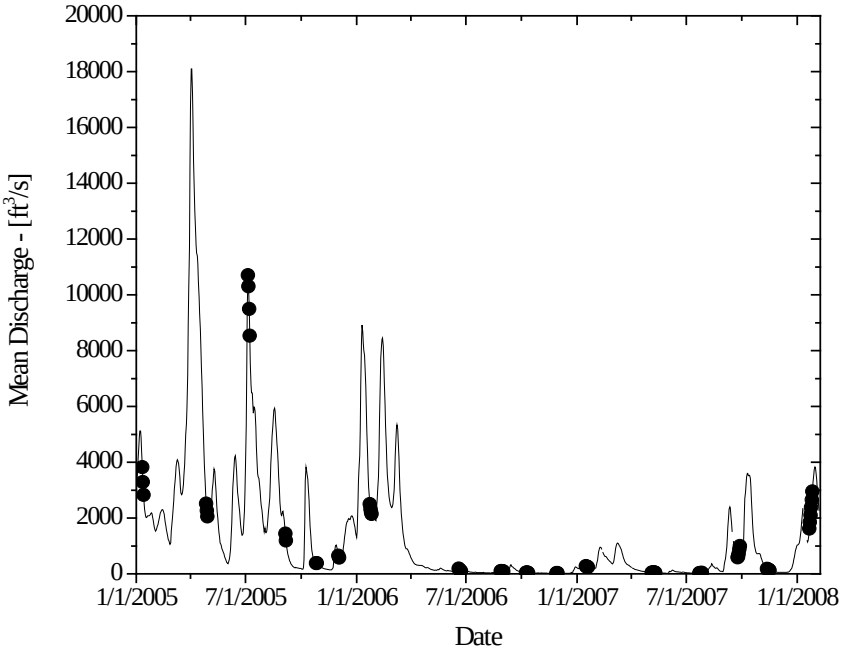

Figure 4.2: Satilla River discharge for 2005 – 2008 measured at the USGS gage #02228000 at Atkinson, approximately 133 km upstream (http://LPDAAC.usgs.gov). Markers denote dates of deployments and sampling during this study.

The benthic lander used for this research was equipped with a portable, programmable, battery-powered, in situ electrochemical analyzer (ISEA II^{TM}) from Analytical Instrument Systems, Inc. (AIS, Inc.). All voltammetric analyses were conducted with a system of three electrodes: a silver wire conditioned in 3 mol L^{-1} KCl (Ag/AgCl) as reference electrode, a platinum counter electrode, and a mercury/gold amalgam (Au/Hg) working microelectrode. The electrochemical analyzer also contained a multiplexer to allow sequential measurements at up to four working electrodes. Using a combination of linear sweep and anodic and cathodic square wave voltammetry, the potentiostat is able to simultaneously quantify dissolved oxygen, dissolved iron(II), dissolved manganese(II), thiosulfate, total dissolved sulfide ($\Sigma H_2S = H_2S + HS^- + S^0 + S_x^-$

^{2}), as well as organic complexes of iron(III) (org-Fe(III)) and iron sulfide clusters ($FeS_{(aq)}$) that are not quantifiable and usually reported in current intensities (Tercier-Weber and Taillefert, 2008). A comprehensive list of detectable redox species as well as their detection limits can be found elsewhere (Luther et al., 2008).

For each deployment, two working electrodes were mounted on a water-proof MAN-2 micromanipulator (AIS, Inc.) to acquire depth profiles of redox chemical species in the pore water, a third was inserted into a benthic chamber to monitor solute transport across the sediment water interface (SWI), and a fourth was positioned in the water column. The profiling working electrodes were made of Pyrex glass and pulled to a tip of 0.4 mm diameter to minimize particle entrainment during the profiles. Additional details regarding microelectrode construction and lander design have been described previously (Brendel and Luther, 1995, Chapter 3). As the system was designed to be completely autonomous, the sequence of voltammetric scans collected in situ had to be preprogrammed before each deployment. The sequence is capable of accurately measuring all detectable redox species that may be present in natural sediments while avoiding artifacts or memory effects (Chapter 3). The sediment water interface was located based on the decrease of ambient noise levels caused by turbulence in the overlying waters when approaching the SWI, the use of two profiling electrodes positioned at known vertical distances relative to each other, and a characteristic decline in oxygen concentration near the SWI (Chapter 3). Working electrodes were calibrated for dissolved oxygen in situ using the temperature and salinity of the overlying water to calculate oxygen saturation (Luther et al, 2008). For all other species, electrodes were

calibrated ex situ according to the Pilot Ion Method with standard additions of reagent grade 0.1 mol L^{-1} $MnCl_2$ (Brendel and Luther, 1995).

In addition to lander deployments, sediment cores were collected using a single core collector (Marinelli et al., 1998) within 30 meters from the site where the lander was deployed. The salinity of the overlying water captured by the sediment corer was measured with a RHS-10ATC portable refractometer. Ex situ voltammetric pore water depth profiles were obtained using glass Au/Hg amalgam microelectrodes constructed, prepared, and calibrated in an identical manner to those used for the lander deployments (Luther et al., 2008; Chapter 3). For ex situ analysis, a DLK–100 potentiostat (AIS, Inc.) was utilized along with a DLK MAN–60 micromanipulator (AIS, Inc.). Voltammetric data for both in situ and ex situ profiles was integrated using VOLTINT a semi-automated Matlab^{TM} script with peak recognition software (Bristow and Taillefert, 2008). The sediment cores were sectioned, and the sediment centrifuged and filtered under N_2 atmosphere using 0.2 μm Puradisc polyethersulfone syringe filters (Whatman) to extract pore waters. The pore waters were analyzed onboard ship for dissolved inorganic carbon (DIC) concentrations with flow injection analysis (FIA) (Hall and Aller, 1992). Dissolved phosphate concentrations were also determined spectrophotometrically onboard using the paramolybdate method (Murphy and Riley, 1962). Finally, dissolved iron(II) and total dissolved iron were also measured onboard ship spectrophotometrically with the Ferrozine method (Stookey, 1970).

Advective-diffusive oxygen uptake (ADOU) fluxes were calculated from the in situ depth profiles using a modified version of Fick's First Law for porous media that accounted for the influence of advection (Boudreau, 1997):

$$F_{ADOU} = -\Phi D^T (\frac{\partial C}{\partial x}) + \nu \Phi C_0 \quad (1)$$

where F_{ADOU} is the flux (mmol m^{-2} day^{-1}), Φ is sediment porosity, D^T is the dispersion coefficient of solutes in water (cm^2 s^{-1}), C_0 is the concentration of oxygen in the overlying water (mol L^{-1}), and ν is the advection calculated from the removal of a tracer from the benthic chamber (Chapter 3). The dispersion coefficient of dissolved oxygen was determined from hydrodynamic dispersion and axial diffusion (Hu and Brusseau, 1994; Roychoudhury, 2001):

$$D^T = \frac{D^0}{\Theta^2} + \alpha_L \nu^n \quad (2)$$

where Θ^2 represents tortuosity, n is a constant that was assigned a value of 1.0 based on regression analysis for well packed, homogenous sediments (Hu and Brusseau, 1994), and α_L is the longitudinal dispersivity. Tortuosity was calculated with Archie's Law ($\Theta^2 = \Phi^{1-m}$) assuming m = 3 in fine-grained sediments (Ullman and Aller, 1982). Molecular diffusion (D^0) of dissolved oxygen was determined from (Boudreau, 1997):

$$D^0 = (4.72 * 10^{-9})(\frac{T}{\mu V_b^{0.6}}) \quad (3)$$

where T represents the absolute temperature (K) and V_b is the molar volume of dissolved oxygen at its normal boiling temperature (27.9 cm^3 mol^{-1}) (Boudreau, 1997). The dynamic viscosity of water (μ) is corrected for temperature and salinity (Pilson, 1998).

The net fluxes of dissolved sulfides, iron(II), and manganese(II), were also determined from their in situ depth profiles and (Eq. 1 and 2). For these species however, the molecular diffusion coefficient was calculated according to:

$$D^0 = (m_0 + m_1 * T) * 10^{-6} \quad (4)$$

where T is temperature (^oC) and m_0 and m_1 are species-dependent constants (Boudreau, 1997). This method assumes that the sediments are isothermal from the SWI to the maximum depth of the profile (usually around 15 cm).

Ex situ cores were assumed to become diffusion-dominated just after sampling, such that the advective component could be ignored. Ex situ diffusive oxygen fluxes were therefore calculated based on Fick's First Law (Boudreau, 1997):

$$F_{Ex} = -\Phi D^0 (\frac{\partial C}{\partial x}) \quad (5)$$

where F_{Ex} is the flux (mmol m^{-2} day^{-1}), Φ is sediment porosity, D^0 is the molecular diffusion coefficient of solutes in water (cm^2 s^{-1}), C is the species concentration (mol L^{-1}) and x is the depth (cm). The molecular diffusion coefficient for the ex situ dissolved oxygen was also calculated based on equation 3.

Results

Typical voltammetric profiles from the fall season at stations SAT 1 and SAT 4 are displayed in Figure 4.3 to illustrate the differences in microbial respiratory dynamics between an upriver, freshwater station and a saline station close to the mouth of the estuary.

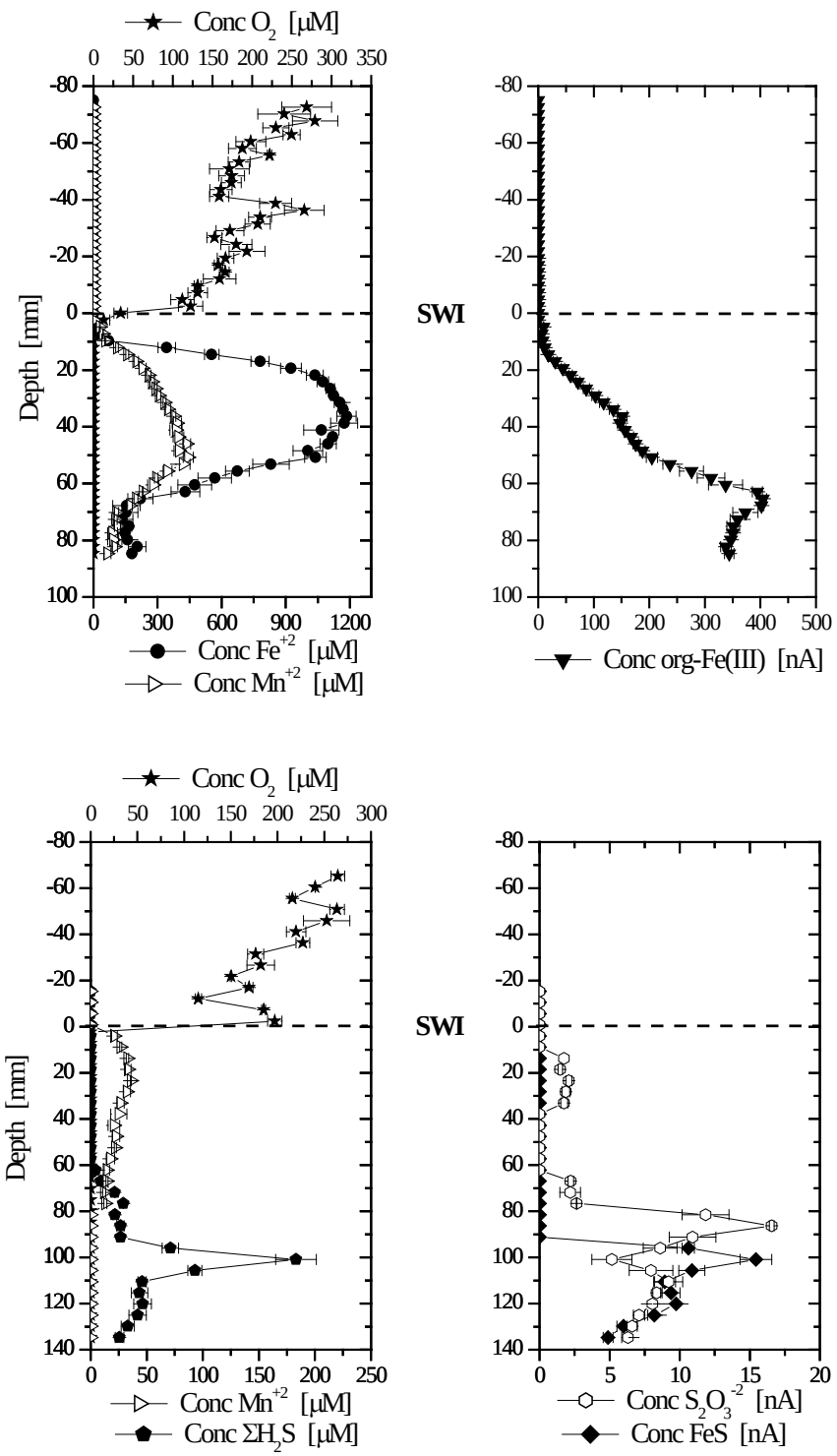

Figure 4.3: Two typical in situ depth profiles, including O_2, Fe^{+2}, Mn^{+2}, ΣH_2S (= H_2S + HS^- + S^0 + S_x^{-2}), thiosulfate, $FeS_{(aq)}$ and org-Fe(III), measured by voltammetric Au/Hg microelectrodes. These profiles are displayed to illustrate the differences in microbial respiration associated with SAT 1 (top), a freshwater station, in October 2005 and SAT 4 (bottom), a estuarine station, in Nov 2007.

In both cases, dissolved oxygen was consumed just below the sediment water interface, and manganese(II) was the first reduced metabolite detected. Iron(II) and manganese(II) were sometimes found concurrently with high current intensities of org-Fe(III) at SAT 1, while dissolved sulfide remained below the detection limit. Conversely, SAT 4 was characterized by a distinct lack of iron(II) in conjunction with detectable levels of thiosulfate, $FeS_{(aq)}$, and concentrations of total dissolved sulfide as high as 180 μM at depths greater than 60 mm (Figure 4.3).

To better characterize the seasonal variations in sediment biogeochemistry, the benthic lander was deployed 83 times over three complete seasonal cycles at the different stations along the Satilla River estuary. At each station, the in situ concentration of all reduced species was integrated as a function of depth assuming that diffusion at the electrode surface was laterally limited to a 0.05 mm radius and the concentration was constant across the distance represented by the depth of resolution. The total number of moles of each slice were then summed and normalized to total volume delimited by the total depth and surface area sampled by each electrode. When organized by station, this data clearly illustrates that the concentrations of the dominant reduced metabolites in these sediments varied significantly on a seasonal basis (Figure 4.4).

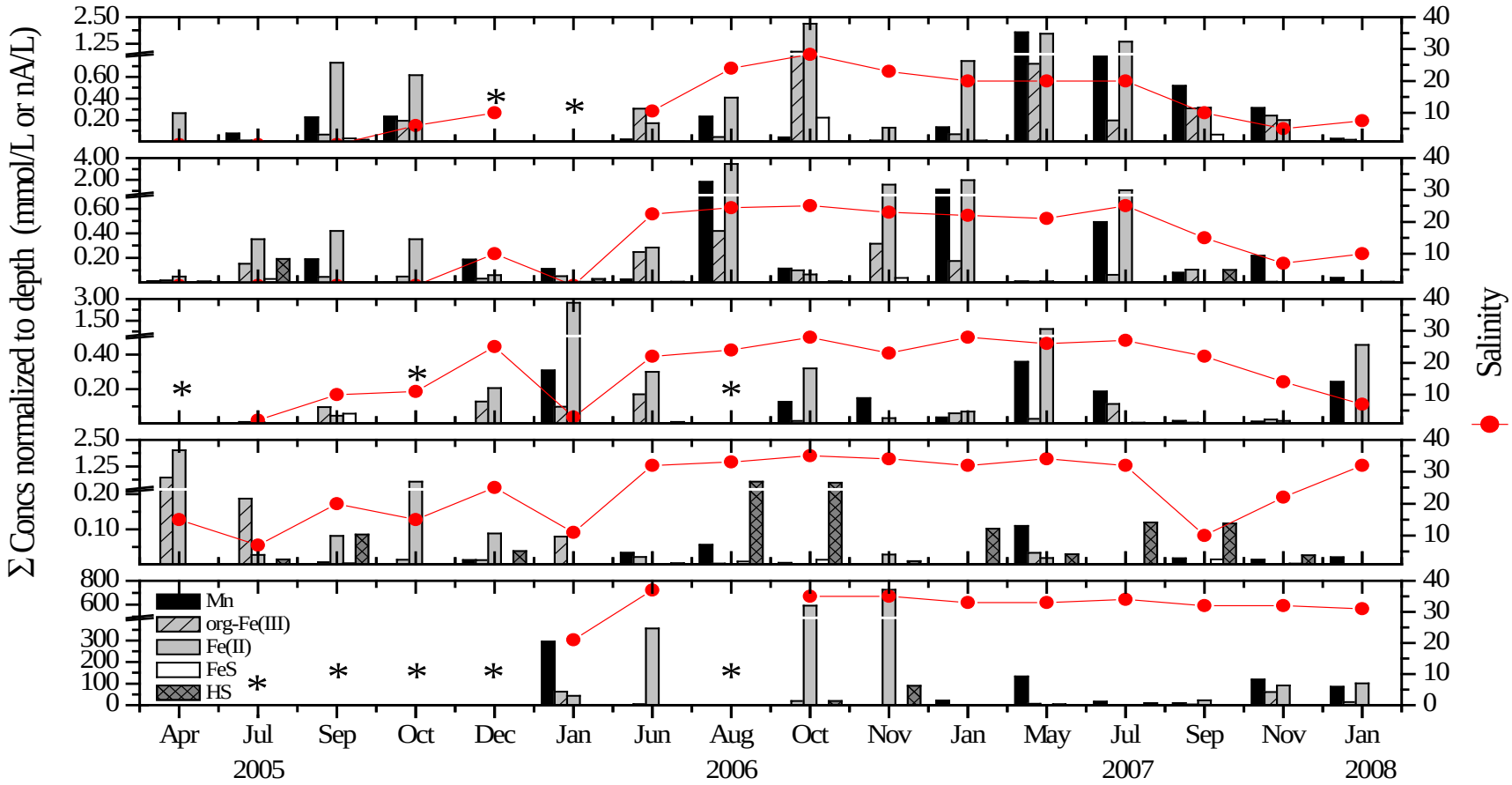

Figure 4.4: Three years of in situ depth profiles of O_2, Fe^{+2}, Mn^{+2}, ΣH_2S, $FeS_{(aq)}$ and org-Fe(III), integrated and normalized to total depth at SAT 1, SAT 2, SAT 3, SAT 4, and SAT 5. The corresponding salinity measurements taken from the overlying water of the ex situ core samples are superimposed to display the increase in salinity observed at each station during 2006 and 2007. The stars denote sampling locations where in situ data were not obtained.

Regardless of sampling location, production of reduced metabolites generally increased during the summer months and declined during the winter season. In 2005 it was apparent that metal reduction was the dominant respiratory pathway throughout the estuary. Both iron(II) and manganese(II) were observed throughout the year, though a slight increase was noticeable in September and October at SAT 1 and SAT 2, the freshest part of the estuary (Figure 4.4 a and b). While these reduced metabolites were not detected at SAT 3 until the winter months (Figure 4.4c), the concentrations of dissolved iron(II) exceeded those of dissolved sulfide, and current intensities of org-Fe(III) were the highest at SAT 4 despite the relatively high salinities at this location in 2005 (Figure 4d). In fact, during this seasonal cycle, sulfidic species and $FeS_{(aq)}$ were only detected in low concentrations or current intensities in July and September at SAT 2, SAT 3, and SAT 4 (Figure 4.4 b, c and d). River discharge decreased precipitously in the spring of 2006 and remained low for the remainder of 2006 and all of 2007 (Figure 4.2). This decrease in discharge was accompanied by a drastic shift in the salinity gradient from SAT 3 in 2005 to as far upriver as SAT 1 in 2006 (Figure 4.4 a and c), and the salinity remained elevated during the rest of 2006 and most of 2007. After the decline in river discharge and corresponding salinity increase across the estuary, concentrations of iron(II) and current intensities of org-Fe(III) in the pore waters rose significantly at SAT 1 and SAT 2 (Figure 4.4 a and b). During the summer 2006 and 2007 seasons, concentrations of both iron(II) and manganese(II) consistently reached millimolar levels at SAT 2 and even exceeded those at SAT 1. In general however, concentrations of reduced metals and current intensities of org-Fe(III) were not nearly as large at SAT 3 (Figure 4.4c), and sulfidic species, though detected almost year round at these three

stations, were consistently insignificant. The biogeochemical processes at SAT 4 displayed the most pronounced change throughout the course of this study. In contrast to 2005, the summer season of 2006 was characterized by little manganese reduction and a complete lack of iron reduction (Figure 4.4d). Instead, concentrations of ΣH_2S rose significantly to the highest levels measured at any station and remained elevated throughout the period of decreased river discharge. While sampling was not initiated at SAT 5 until January 2006, sediments at this station were also characterized by significant metal reduction during most of the low discharge period, as this station receives inputs from other river systems in addition to the Satilla.

The depth-integrated concentrations of each species at each station were averaged on a yearly basis to study the effect of the drought on biogeochemical processes in the estuary (Table 4.1).

Table 4.1: Depth-integrated concentration of reduced species measured at each station averaged on an annual basis. The standard deviations represent the temporal variation during the seasonal cycles. On average, metal concentrations measured upriver tend to increase over the course of the study while, except for manganese(II) at SAT 4, metal concentrations at stations near the river mouth noticeably declined.

		Mn(II) (μmol/L)	Org-Fe(III) (nA/L)	Fe(II) (μmol/L)	$FeS_{(aq)}$ (nA/L)	ΣH_2S (μmol/L)
SAT 1	2005	133.0 +/- 113.9	67.5 +/- 89.0	404.4 +/- 335.1	7.5 +/- 15.1	4.8 +/- 7.5
	2006	72.5 +/- 107.7	309.0 +/- 400.6	725.7 +/- 988.3	56.9 +/- 110.6	0.5 +/- 1.0
	2007	708.5 +/- 651.7	307.9 +/- 248.1	863.3 +/- 652.4	16.4 +/- 27.6	1.0 +/- 1.6
SAT 2	2005	77.9 +/- 100.8	59.0 +/- 53.4	246.5 +/- 178.0	6.7 +/- 12.8	40.5 +/- 84.6
	2006	416.0 +/- 791.0	226.6 +/- 152.7	1075.4 +/- 1482.2	9.2 +/- 15.4	9.7 +/- 10.9
	2007	381.4 +/- 446.3	70.5 +/- 71.4	606.1 +/- 887.5	0.8 +/- 1.5	21.2 +/- 45.9
SAT 3	2005	0.8 +/- 1.3	76.7 +/- 61.0	85.6 +/- 105.3	19.7 +/- 33.2	0.6 +/- 1.0
	2006	145.4 +/- 126.5	70.7 +/- 77.5	848.8 +/- 1271.4	0.2 +/- 0.3	2.6 +/- 4.4
	2007	121.0 +/- 151.0	45.4 +/- 42.9	198.3 +/- 398.1	1.6 +/- 2.4	1.3 +/- 1.5
SAT 4	2005	2.5 +/- 5.6	189.1 +/- 308.9	545.5 +/- 840.7	1.3 +/- 1.6	28.1 +/- 35.3
	2006	18.9 +/- 24.6	21.1 +/- 34.0	5.9 +/- 12.6	4.9 +/- 6.1	205.2 +/- 275.0
	2007	28.1 +/- 46.3	6.7 +/- 14.8	3.7 +/- 8.4	4.2 +/- 5.8	78.8 +/- 46.9
SAT 5	2005	N/A	N/A	N/A	N/A	N/A
	2006	73.7 +/- 147.4	22.2 +/- 28.6	429.4 +/- 299.3	0.0 +/- 0.0	27.6 +/- 41.8
	2007	59.8 +/- 60.7	14.1 +/- 26.5	22.5 +/- 39.4	1.0 +/- 2.0	2.3 +/- 4.1

Average reduced metal concentrations were highest at SAT 1 and SAT 2, followed by SAT 3, SAT 5, and finally SAT 4. They generally increased during the two years of drought in the upriver portion of the estuary (SAT 1, SAT 2, and SAT 3), while average current intensities of org-Fe(III) rose substantially from 2005 to 2006, but decreased more significantly during the second year of the drought. In contrast, a progressive decline in the average concentrations of manganese(II) and iron(II), as well as the average current intensities of org-iron(III) was evidenced during the last year of the drought at SAT 4 and SAT 5. Total dissolved sulfide concentrations and $FeS_{(aq)}$ current

intensities were generally low at SAT 1, SAT 2, and SAT 3, and did not vary significantly during the years of low discharge. Conversely, concentrations of these species increased between 2005 and 2006 at SAT 4, then declined between 2006 and 2007. No data were obtained in 2005 at SAT 5, but the decrease in total dissolved sulfide concentrations and $FeS_{(aq)}$ current intensities observed between 2006 and 2007 suggest that these stations behaved similarly.

Voltammetric measurements performed in the sediment cores collected for conventional pore water analyses revealed similar depth profiles as the in situ measurements, except that the distribution of most chemical species was indicative of diffusion dominated systems (e.g. Figure 4.5).

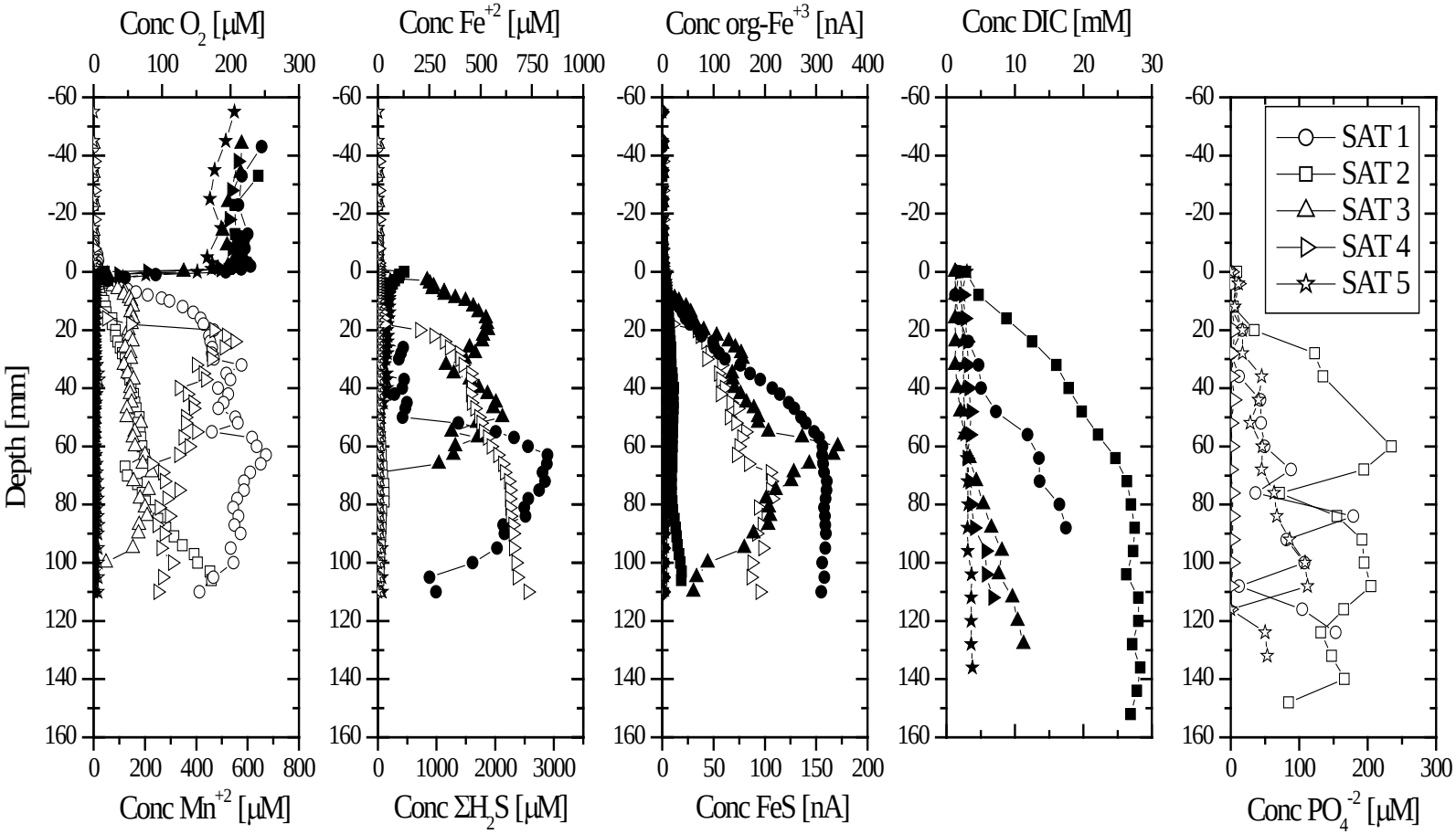

Figure 4.5: Depth profiles of dissolved O_2, Fe^{+2}, Mn^{+2}, ΣH_2S, $FeS_{(aq)}$ and org-Fe(III) measured electrochemically as well as ΣPO_4^{-3} and DIC measured in pore waters extracted from the same sediment cores collected at each site along the Satilla River in September 2007. Closed symbols correspond to the top scales, while open symbols correspond to the bottom scales. No DIC data are available at SAT 3.

In general, large concentrations of manganese(II) and iron(II) were measured near the SWI at the upriver stations, indicating that these reduced species were fluxing out of the sediments. Depth profiles of org-Fe(III) usually mirrored iron(II) profiles although org-Fe(III) was at times measured in the absence of iron(II). Following the onset of the drought, total dissolved sulfide and $FeS_{(aq)}$ were frequently detected in low quantities below the metal reduction layers in the upriver sediments (e.g. Figure 4.5). Comparatively, the voltammetric depth profiles collected at SAT 3 resembled those of the upriver stations, except that the concentrations of reduced metals were generally lower and sulfidic species were detected more frequently. In turn, the highest concentrations of total dissolved sulfide (up to millimolar levels) were observed in sediments at SAT 4. Thiosulfate (not shown) and $FeS_{(aq)}$ (e.g. Figure 4.5) were also commonly observed along with manganese(II), but iron (II) and org-Fe(III) were only detected at SAT 4 prior to the drought. SAT 5 was expected to mirror SAT 4 akin to the relationship of SAT 1 and SAT 2; however, concentrations of sulfidic species, manganese(II), iron(II), and the current intensities of org-Fe(III), were consistently lower at SAT 5 than at SAT 4. The concentrations of DIC in the pore waters at each station and each season tended to increase with depth reflecting the process of organic matter degradation (e.g. Figure 4.5). Simultaneously, DIC concentrations correlated with distance from the mouth of the estuary, indicating that remineralization of natural organic matter was much more intense upriver than near the mouth of the estuary. Finally, dissolved phosphate concentrations also increased with depth, though not as regularly as the DIC concentrations (e.g. Figure 4.5). The highest concentrations were customarily measured at SAT 1 and SAT 2, though SAT 2 concentrations were generally higher than

SAT 1. Lower concentrations of orthophosphates were measured in SAT 4 and SAT 5 pore waters, though these species diffused all the way up to the SWI. In contrast, orthophosphates in the upriver stations were removed from the pore waters in the first couple of centimeters below the SWI. Dissolved phosphates were generally variable at SAT 3 following the trends observed for iron(II) and sulfide species, suggesting that orthophosphates were removed by iron oxides near the SWI when iron reduction dominated in these sediments and were free to diffuse to the overlying waters under sulfidic conditions as observed in previous studies (Rozan et al., 2002). Ex situ DOU and DIC fluxes calculated from the measured depth profiles of dissolved oxygen and DIC in the sediment cores over three years of sampling were highly variable depending on the season. Despite these temporal variations, average DIC fluxes were highest at SAT 1 and SAT 2, while average DOU fluxes remained constant across the estuary (Table 4.2).

Table 4.2: Average DOU and DIC fluxes measured over the three years of this project at each station, listed in order of increasing salinity along the Satilla River. The surface area is the calculated river area between adjacent stations. Diffusive fluxes were calculated from ex situ measurements using Fick's First Law (Eq. 2 and 4). The high standard deviations are caused by large temporal variability.

Sampling Location	Surface Area (km^2)	Average DIC Flux (mmol C m^{-2} day^{-1})	Average DOU Flux (mmol C m^{-2} day^{-1})
SAT 1		18.4 (+/- 13.4)	7.8 (+/- 6.5)
SAT 2	2	34.3 (+/- 43.7)	8.7 (+/- 4.0)
SAT 3	6.3	8.0 (+/- 4.8)	9.3 (+/- 10.7)
SAT 4	13.8	10.0 (+/- 9.6)	7.9 (+/- 3.7)
SAT 5	38.7	13.0 (+/- 16.1)	8.1 (+/- 2.6)

Discussion

The main objective of this study was to characterize the seasonal variability of sediment biogeochemistry with high spatial and temporal resolution along an estuary using a novel autonomous benthic lander. The lander was deployed seasonally along the salinity gradient of the Satilla River estuary, and the dynamics of early diagenetic processes in this area were investigated using a combination of in situ depth profiles and ex situ measurements after collection of sediment cores to examine the impacts of seasonal variations on carbon remineralization. The sequence of electron accepting processes measured as a function of depth in these sediments follows the order of Gibbs Free Energy yield of these reactions. Dissolved oxygen is completely consumed within a few millimeters of the SWI, as previously reported in other studies (e.g. Taillefert et al., 2002a; Wenzhofer et al., 2002; Chapter 3). Manganese reduction occurs in the upper sediment layers, followed by iron reduction, and sulfate reduction in the deeper sediment layers (e.g. Figure 4.3). Org-Fe(III) complexes observed concurrently with Fe(II) in the Satilla River sediments have been detected in a variety of anoxic marine pore waters (e.g. Taillefert et al., 2000; Bull and Taillefert, 2001; Tercier-Waeber and Taillefert, 2008) and were shown to form as intermediates during iron(II) oxidation in the presence of organic ligands (Taillefert et al., 2000) and, more recently, during microbial iron reduction (Taillefert et al., 2007; Fennessey et al., 2010; Jones et al., 2010). $FeS_{(aq)}$ is detected in the transition zone between iron and sulfate reduction in over 60% of the profiles that contain dissolved sulfides, which indicates that iron is being chemically precipitated by sulfide in these sediments (Taillefert et al., 2002a; Carey and Taillefert, 2005). Of all the locations sampled, sulfate reduction was the most active at SAT 4, though iron(II) was

also detected seasonally at this location in 2005 (Figure 4.4d). Chemical reduction of iron oxides by sulfide could potentially account for some of the reduced iron observed, but not all as iron(II) was measured in substantial excess compared to dissolved sulfides (Chappelle et al., 2009). More likely, the dominant respiratory process at SAT 4 shifted from iron reduction to sulfate reduction over the study period, and this shift was concurrent with an increase in salinity and decrease in river discharge.

Beginning in the summer of 2006, the southeastern area of the United States entered into a prolonged period of drought. Lack of rainfall in the surrounding area caused a decrease in mean river discharge (Figure 4.2) and resulted in a marked increase in salinity at least 20 km upstream (SAT 1) due to marine water intrusion into the estuary that was much more significant than usually observed in this system (Alber et al., 2003; Blanton et al., 2003; Seim et al., 2009). The additional input of sulfate into the freshwater portion of the estuary should have enhanced sulfate reduction and thus sulfide oxidation by dissolved oxygen near the SWI; however, no increase in sulfate reduction products (Figure 4.4) or advective-diffusive oxygen uptake (ADOU) fluxes (Figure 4.6 left) were observed when the salinity increased. Instead, a modest inverse correlation was found between ADOU and temperature (Figure 4.6 right).

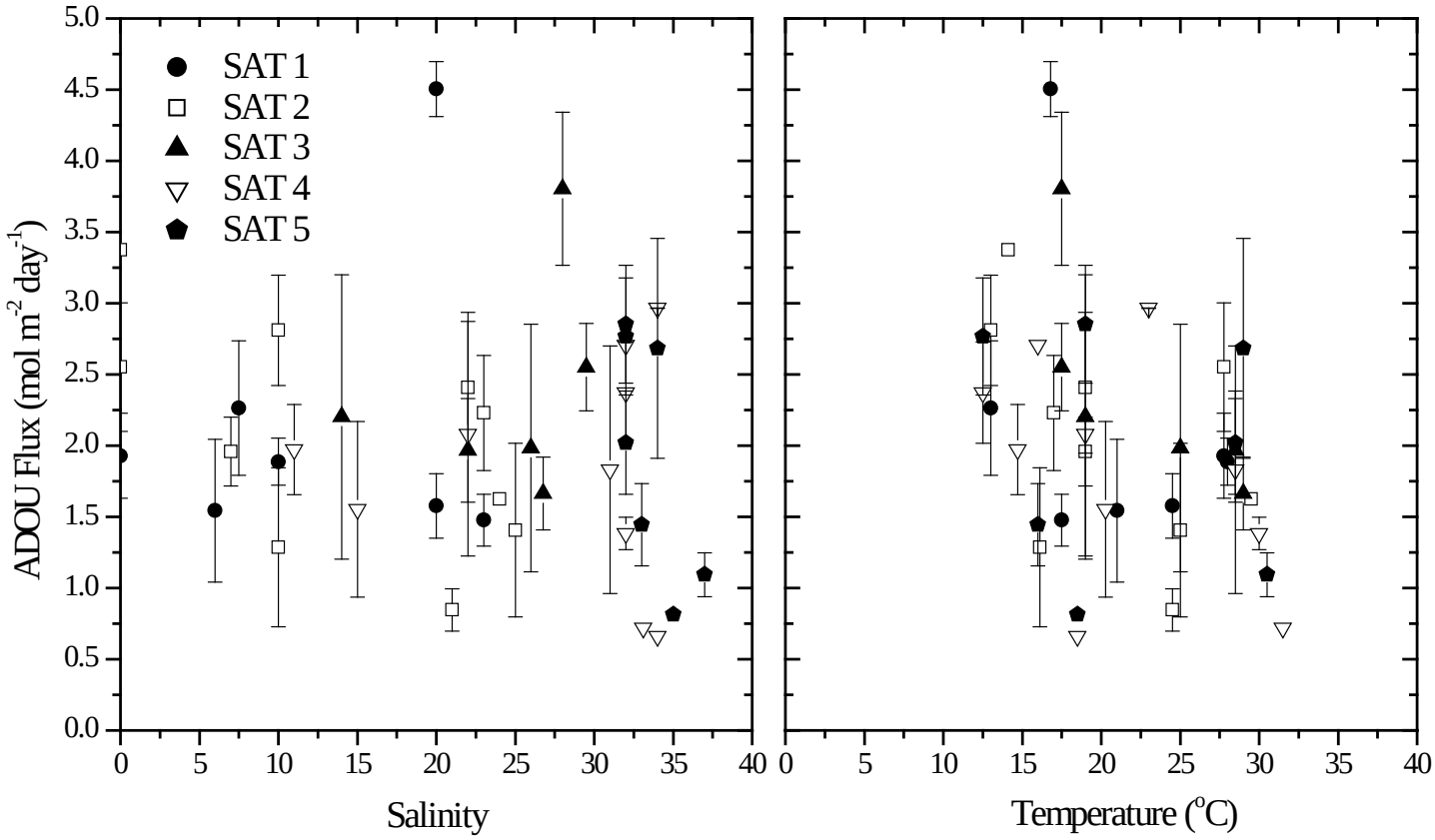

Figure 4.6: Advective-diffusive oxygen uptake flux (ADOU) as a function of salinity and temperature. Salinity was measured in the overlying water of the ex situ cores collected along the Satilla River estuary in tandem with lander deployments. Temperature was measured in situ with a temperature probe affixed to the lander.

As respiration processes are usually enhanced during the summer months, when the bottom water temperatures can reach 30^{o}C in the Satilla River, the increase in oxygen uptake fluxes at low temperature can only be explained if oxygen consumption was significantly affected by the oxidation of reduced metabolites in the winter. Indeed, concentrations of dissolved iron(II) in sediment pore waters were generally larger upriver (Figure 4.4), suggesting that Fe(II) and Mn(II) may have been recycled efficiently as previously proposed (Canfield et al., 1993b; Taillefert et al., 2007; Homoky et al., 2009).

The changes in diagenetic processes induced by the decreased river discharge must have subsequently impacted rates of carbon remineralization in this estuary. Rates of carbon remineralization are generally quantified by measuring oxygen consumption near the sediment water interface (e.g. Archer and Devol, 1992; Berg et al, 2003; Glud and Gundersen, 2002; Wenzhofer et al, 2002). This method assumes oxygen to be the ultimate oxidant and thus presumes that nitrite, ammonium, manganese (II), iron (II), and sulfides produced during the anaerobic oxidation of NOM are reoxidized when they diffuse to the oxic upper sediment layers. Simultaneously, dissolved inorganic carbon and orthophosphates can be used as a proxy for carbon mineralization as long as carbonate mineral dissolution does not interfere with carbon produced by metabolic processes (e.g. Green et al., 2004) and iron oxides do not scavenge orthophosphates (McManus et al., 1997; Rozan et al., 2002). The lack of phosphate near the SWI across the entire estuary (e.g. Figure 4.5) suggests that high rates of iron reduction combined with enhanced oxygen penetration due to advection (Jahnke et al., 2003; Chapter 3) resulted in the precipitation of iron oxides and scavenging of orthophosphates in the upper sediment layers. As it would be difficult to use these data to quantify remineralization rates, the

rest of the discussion focuses on the combination of DOU fluxes and DIC data to study remineralization processes.

Interestingly, DOU fluxes obtained from sediment cores do not vary seasonally, while DIC fluxes are lowest in the spring, highest in the summer or early fall, and intermediate in the winter months (not shown). The DOU fluxes reported here do not differ significantly from previously published values (6 - 9 mmol O_2 m^{-2} day^{-1}) for North Atlantic sediments (Wenzhofer et al, 2002), but are lower than previously published estimates (18.2 – 22.9 mmol O_2 m^{-2} day^{-1}) for continental margin environments (e.g. Middelboe et al., 2003). Low DIC fluxes were expected because the carbon source material for the Satilla River is derived mainly from the coastal plain and thus is predominantly humic in nature (Cai and Wang, 1998). However the DIC fluxes measured during the drought at the upriver stations (Figure 4.7) are in the range of other values obtained for coastal environments (Dollar et al., 1991; Giblin et al., 1997; Berelson et al., 2003) as would be expected if carbon remineralization in these sediments was fueled by primary production in the estuary or adjacent marshes (Peterson and Howarth, 1987; Chanton and Lewis, 2002).

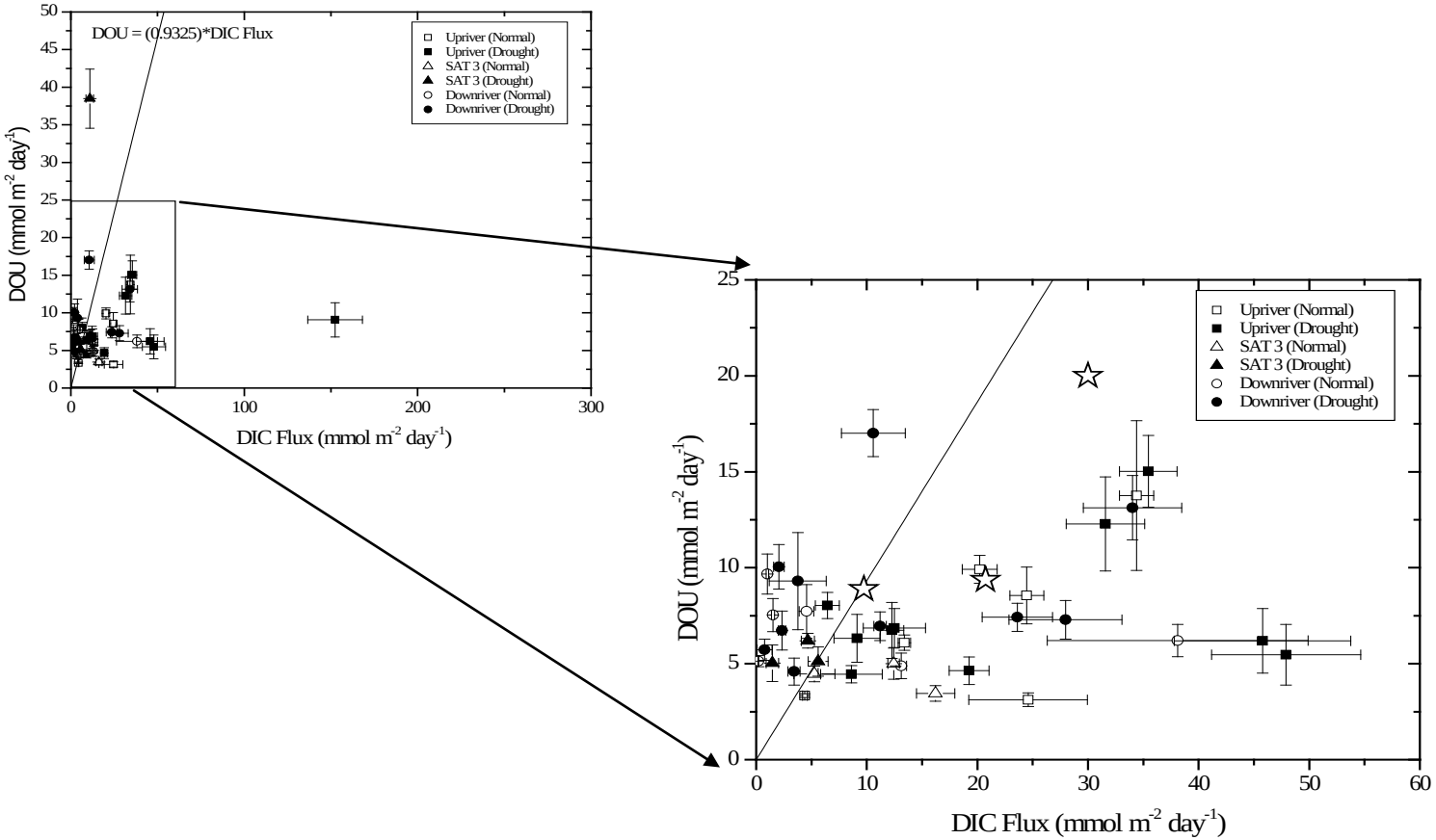

Figure 4.7: Correlation between DOU and DIC fluxes measured seasonally at each station along the Satilla River estuary. The solid line represents the expected correlation between DOU and DIC fluxes if NOM remineralization was dominated by aerobic respiration. The star symbols correspond to previously published literature values (Berelson et al., 2003, Giblin et al., 1997 and Dollar et al., 1991).

The fluxes of DOU and DIC can be compared directly to examine the effects of the drought on NOM remineralization rates (Figure 4.7). If oxygen is assumed to be consumed solely during aerobic respiration, the relationship between DOU and DIC can be estimated by the following relationship based on the composition of NOM (Perdue, 2009):

$$C_c H_h O_o N_n + (\frac{4 - Z_C}{4}) cO_2 \text{ --> } cCO_2 + (n)NH_3 + 0.5((h) - 3(n))H_2O \qquad (6)$$

For this relationship Z_C represents the average oxidation state of carbon and c, h, o, and n are stoichiometric coefficients. The oxidation state of carbon in natural organic matter of freshwater origin that eventually enters coastal environments is slightly more oxidized than predicted by the Redfield ratio with an average of +0.27 (Perdue, 2009). Thus a linear relationship linking DOU and DIC fluxes can be derived from the stoichiometric coefficients in equation 6:

$$F_{DOU} = (\frac{4 - (+0.27)}{4})(c)(\frac{1}{c})F_{DIC} = 0.93 * F_{DIC} \qquad (7)$$

In cases where reoxidation of reduced metabolites by oxygen is significant, the DOU flux should exceed the DIC flux and therefore fall above the relationship predicted by equation 7 (solid line shown in Figure 4.7). If anaerobic processes dominate in these sediments however, the DIC flux should exceed the DOU flux and thus fall below the relationship predicted by equation 7. All but two DOU-DIC pairs measured at SAT 3 and three at each of the down river stations (SAT 4, and SAT 5) lay above this relationship,

suggesting that dissolved oxygen oxidizes most of the respiration byproducts as they diffuse to the SWI in the low estuary. The two exceptions at SAT 3 were measured in the fall of 2007, immediately following strong rain events, suggesting that anaerobic respiration processes may have been enhanced due to an increased supply of organic or inorganic material as a result of increased river discharge (Figure 4.2). The three exceptions at the two down river stations, measured during the drought years, displayed a higher DIC than during other seasons, suggesting that anaerobic respiration processes dominated in these sediments. By requiring only one mole of sulfate to oxidize two moles of carbon, sulfate reduction more efficiently oxidizes NOM than iron reduction, which required 4 moles of iron(III) to fully oxidize one mole of carbon. Consequently, it was unexpected to note that the data points with low DIC fluxes and high DOU fluxes occurred at the stations where significant concentrations of reduced sulfur were observed (SAT 4 and 5 in late summer 2006 and spring/summer 2007). These low DIC fluxes suggest that sulfate reduction contributes less to carbon remineralization than iron reduction in the sediments of the Satilla River. Conversely, DIC fluxes were highest in the freshwater end of the estuary (SAT 1 and SAT 2), which is dominated by iron reduction, regardless of the intensity of river discharge (Table 4.2, Figure 4.4). High DIC fluxes in combination with high fluxes of reduced iron indicate either that the supply of oxygen to these sediments allows for the efficient recycling of iron(II), or these sediments are subjected to an increased supply of iron oxides and/or organic material from freshwater sources. In over 50% of the profiles however, the sum of the flux of reduced species far exceeds that of the ADOU flux. These data provide evidence against a strong manganese(II) and iron(II) recycling mechanism, and instead display conditions ideal for

the precipitation and burial of rhodocrosite and siderite. Indeed, equilibrium calculation using the measured pH, iron(II), manganese(II), and DIC concentrations at SAT 2 indicate that the pore waters are supersaturated with respect to both rhodocrosite and siderite supporting the hypothesis that burial of manganese(II) and iron(II) is significant and carbon remineralization may be underestimated.

Additionally, the highest DIC fluxes were observed concurrently with relatively low DOU fluxes during the low discharge conditions at the upriver stations (Figure 4.7). If the iron recycling mechanism was the most likely explanation for the increased DIC flux, the DOU flux should be significantly higher at the iron-dominated stations. Instead, average DOU fluxes along the river are very similar (Table 4.2) and generally vary between 3 and 10 mmol m^{-2} day^{-1} (Figure 4.7). A linear regression through all the data from Figure 4.7 (0.03+/-0.02 mmol m^{-2} day^{-1} DOU per mmol m^{-2} day^{-1} DIC) translates into a 30(+/-20):1 $C:O_2$ ratio, which is much higher than expected if all the reduced metabolites were reoxidized by dissolved oxygen. If the upriver stations (SAT 1 and SAT 2) are removed from the calculation, though, the slope increases to 0.29(+/-0.04) mmol m^{-2} day^{-1} DOU per mmol m^{-2} day^{-1} DIC, which corresponds to a 3.4(+/-0.5):1 ratio of $C:O_2$, much closer to the expected ratio if all the reduced metabolites were reoxidized by dissolved oxygen. These results suggest that reduced metabolites produced during anaerobic respiration are more efficiently reoxidized by dissolved oxygen in the low end of the estuary, in contrast to what was hypothesized previously (Cai et al., 1999). These findings also suggest that iron(II) recycling was not the most significant source of iron oxides to stimulate iron reduction at SAT 1 and SAT 2. Instead, these data suggest the decrease in river flow combined with the increased salinity may have enhanced the

flocculation and sedimentation rates of iron oxide particles (Sholkovitz, 1976; Hakanson, 2006; Taljaard et al., 2009) and sediment trapping upriver (e.g. Blake et al., 2001). If this hypothesis is correct, the enhanced supply of iron oxides to the sediment may have promoted iron reduction at SAT 1 and 2. Thus, even when bottom water salinity exceeded levels common for sulfate reducing activity (Canfield, 2001), iron reduction remained the dominant respiratory process in the sediments upriver. In turn, the added deposition upriver must have inhibited transport of particulate material, including iron oxides to the mouth of the estuary. The diminished supply of iron oxides to SAT 4 combined with enhanced chemical reduction of iron oxides by dissolved sulfide, shifted the dominant anaerobic respiratory pathway of these sediments away from iron reduction toward sulfate reduction. Iron reduction was still active at SAT 5 throughout 2006 (Figure 4.4e), probably because SAT 5 also receives particulate inorganic material from other nearby rivers (Figure 4.1).

To determine how the intensity of respiratory processes varied seasonally, the in situ fluxes of dissolved oxygen (ADOU) and the three predominant reduced species present in these sediments were reported as the sediment oxidizing capacity (SOC) according to:

$$SOC = \frac{F_{ADOU} - \sum_i (\frac{1}{n_i}) F_{\mathrm{Re}d_i}}{F_{ADOU}} \quad (8)$$

where F is the flux, Red_i represents the i reduced byproduct of anaerobic respiration, and n_i is the stoichiometric coefficient for the reoxidation of Red_i by dissolved oxygen. A positive SOC represents sediment with significant oxidizing power, while a negative

SOC represents primarily reduced sediment. In general, the fluxes of reduced species exceed the fluxes of dissolved oxygen in the summer and fall seasons, compared to the winter months during which the sediments generally display excess oxidizing power (Figure 4.8).

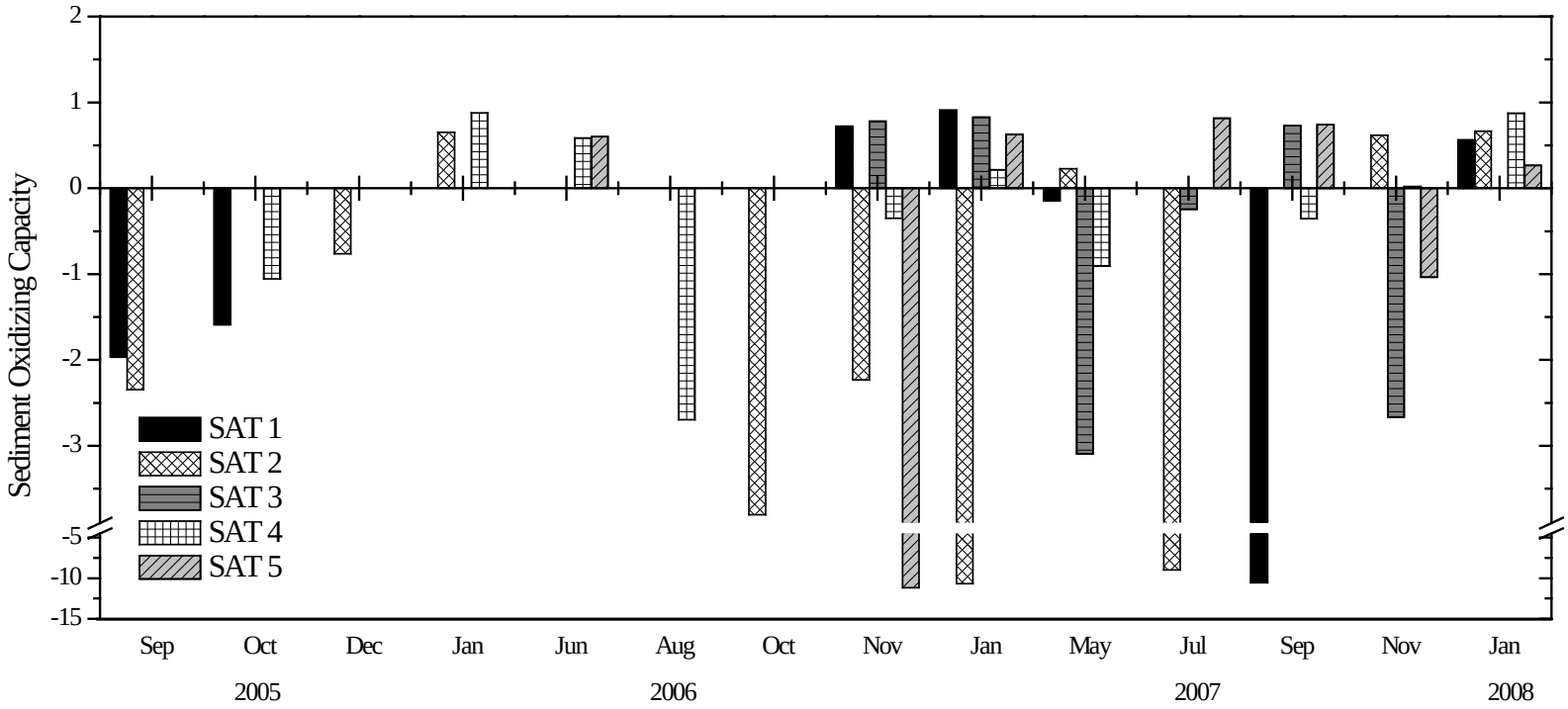

Figure 4.8: The sediment oxidizing capacity of these Satilla River sediments calculated from the in situ fluxes of dissolved oxygen and reduced species determined voltammetrically over three seasonal cycles. Positive values denote sediments with oxidizing capacity while negative values indicate reducing conditions.

The reducing capacity of the sediment is further enhanced during the drought years compared to 2005, suggesting that seasonal signatures are overlaid by the effect of the drought.

Using +0.27 as the average oxidation state of carbon in natural organic matter (Perdue, 2009), the corresponding changes in carbon equivalents during anaerobic respiration processes can be calculated based on the change in concentration of terminal electron acceptors or their corresponding reduced byproducts with depth, assuming that chemical reactions do not affect fluxes significantly. The sulfide flux measured in situ over the lifetime of the drought ranged between 5.6 (+/- 1.5) and a maximum of 922.6 (+/- 91.1) mmol m^{-2} day^{-1} at SAT 4. For this estuary, the carbon remineralization flux calculated from the sulfide flux at SAT 4 frequently exceeded that determined from the ADOU. In August 2006, for example, the calculated sulfide flux (Eqs. 1 and 3) corresponded to a carbon remineralization flux of 744.4 mmol m^{-2} day^{-1} or 2.78 times the carbon remineralization flux of 268.3 mmol m^{-2} day^{-1} determined from the ADOU flux. Similarly, the reduced iron flux at SAT 2 ranged between 247.5 (+/- 11.5) prior to the drought and a maximum of 15904.3 (+/- 662.6) mmol m^{-2} day^{-1} during the drought, and accounted for up to 6.24 times the ADOU contribution to carbon remineralization. These findings indicate that oxygen uptake fluxes are not appropriate proxies for carbon remineralization, likely due to the amount of burial occurring in these sediments.

The Satilla River estuary was found to be heterotrophic in nature, with overlying waters characterized by abnormally high partial pressures of dissolved carbon dioxide, and estimated losses of CO_2 to the atmosphere ranging between 15 mol m^{-2} yr^{-1} at the mouth of the estuary and 200 mol m^{-2} yr^{-1} in the freshwater end member (Cai and Wang,

1998; Cai et al., 1999). The high CO_2 flux in the low salinity region of the estuary was attributed to the accumulation of small concentrations of CO_2 transported tidally from the large marshes neighboring the estuary into the smaller surface area of the Satilla River (Cai et al., 1999). Despite the large flux of DIC produced during respiration processes, the dynamic cycling between the atmosphere and the estuary resulted in the fast exchange of CO_2 between these reservoirs, such that the actual export of DIC to the continental shelf was proposed to represent merely 10% of the total flux of DIC in the estuary (Cai et al., 1999; Cai et al., 2000). The carbon remineralization fluxes for each individual station can be combined to display the overall effect of the drought on sediment respiratory processes in the Satilla River estuary (Figure 4.9).

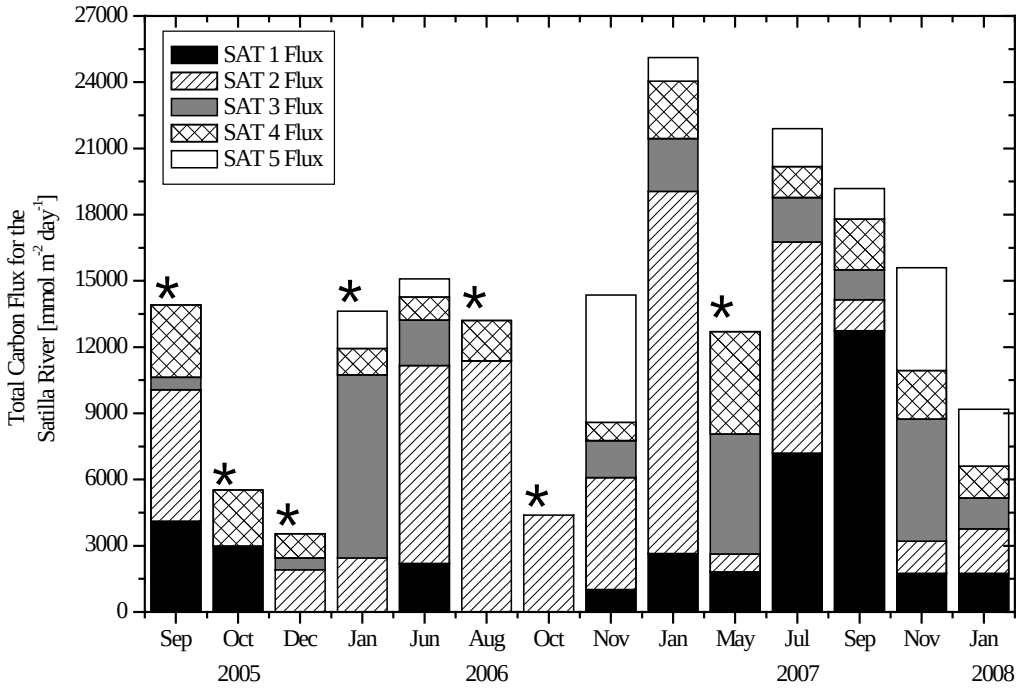

Figure 4.9: Total carbon remineralization estimated seasonally for the Satilla River using in situ depth profiles of the main terminal electron acceptors or their reduced byproducts. An average carbon oxidation state of +0.27 was assumed for all these calculations. Asterisks denote sampling trips where data was not collected at all the stations.

With the exception of November 2006, the total carbon flux from the sediments substantially increased as the drought progressed and declined when river discharge increased at the end of 2007. These results suggest that low river discharge in estuaries fed by rivers most likely decreases the amount of DIC delivered to the continental shelf and increases the amount of carbon dioxide released to the atmosphere. When these DIC fluxes from the sediments are combined with the atomospheric CO_2 fluxes quantified previously (Cai and Wang 1998; Cai et al., 1999), the net flux of DIC that is exported to the continental shelf can be determined for the Satilla River system (Table 4.3).

Table 4.3: The total carbon fluxes from Figure 4.9 were averaged between adjacent stations and then multiplied by the river surface area (Table 4.2) to determine the annual sediment carbon flux for the Satilla River. These values were then compared to previously determined fluxes of atmospheric CO_2 (Cai et al., 1999) to calculate the annual DIC flux to the contintental shelf.

Date	Sediment Flux (mol C yr^{-1})	Shelf Flux (mol C yr^{-1})
Sep 2005	4.40E+10	4.22E+10
Oct 2005	2.55E+10	2.37E+10
Dec 2005	1.53E+10	1.35E+10
Jan 2006	5.75E+10	5.57E+10
Jun 2006	3.78E+10	3.60E+10
Aug 2006	3.46E+10	3.28E+10
Nov 2006	6.29E+10	6.11E+10
Jan 2007	6.70E+10	6.52E+10
May 2007	6.62E+10	6.44E+10
Jul 2007	5.01E+10	4.83E+10
Sep 2007	4.35E+10	4.18E+10
Nov 2007	7.72E+10	7.54E+10
Jan 2008	4.08E+10	3.90E+10

Thus the annual export of DIC to the continental shelf from the Satilla River estuary varies from 1.35 – 7.54e10 mol C yr^{-1}. The annual worldwide carbon flux from rivers to the surface ocean was previously estimated to be 0.8 Pg C (Sarmiento and Gruber, 2002). Thus the Satilla River would be responsible for up to 0.01% of the worldwide riverine carbon flux to the surface ocean. Comparatively, the annual flux of DIC to the South China Sea from the Pearl River estuary system is 5e11 mol C yr^{-1} (Guo et al., 2009), but the average discharge of the Pearl River is 343 km^3 yr^{-1} compared to 2.21 km^3 yr^{-1} for the Satilla River (Alber et al., 2003). Normalizing to their average discharge, the carbon flux of the Satilla River to the continental shelf measured in situ is about 10 times more intense than that of the Pearl River

Overall, the results of this study indicate that dissolved oxygen alone does not provide an adequate proxy for carbon remineralization in coastal sediments and suggest that the total flux of carbon from continental margin sediments is substantially larger than previously estimated, even without accounting for burial processes. More importantly, the results of this study clearly indicate that drought conditions substantially enhanced carbon remineralization processes and impacted the biogeochemistry of this estuary by steepening and relocating the salinity gradient, decreasing river flow, and altering the delivery of mineral constituents used for respiration. Iron reduction was shown to outcompete sulfate reduction as the dominant respiratory process active in these sediments even when the salinity of the overlying waters approached 30. These findings imply that an increase in the frequency of drought conditions as a result of global climate change in northern temperate regions may enhance the resilience of iron-reducing bacteria in river-fed estuarine sediments for extended periods of time.

Acknowledgements

This study was funded by the CAREER Program of the National Science Foundation (OCE-239376).

This work would not have been possible without the skills and patience of the captain and crew of the R/V Savannah. Additionally, we would like to thank Morris Jones, Jordon Beckler, Gwendolyn Bristow, Jason Peart, Wellington Merritt, Patrick Wilson, and Lin Hui who participated in the data collection for this project.

CHAPTER 5

A NEW REMOTE SENSING ELECTROCHEMICAL ANALYZER TO CHARACTERIZE BIOGEOCHEMICAL PROCESSES IN INTERTIDAL COASTAL MARSH SEDIMENTS WITH A HIGH TEMPORAL RESOLUTION

Abstract

Characterized by high levels of terrestrial organic carbon input, coastal marsh ecosystems are among the most productive ecosystems on earth and significantly impact the global carbon cycle. Coastal marshes also help prevent flooding, curtail shoreline erosion, are repositories for pollutants, and provide habitats for commercially important fish, shellfish, and shrimp. The biogeochemistry of coastal sediments is typically investigated after collection of sediment cores, but these areas are subject to complex subsurface hydrological forcing that cannot be accounted for with ex situ measurements. Consequently, in situ approaches are required to better understand the physical and biogeochemical processes that regulate the functioning of intertidal sediments. In this study, an in situ electrochemical analyzer (ISEA III^{TM}) coupled to a Microcat to monitor water temperature, depth, salinity, and flow velocity, was installed in an intertidal creek along the boardwalk of the Salt Marsh Ecosystem Research Facility (SERF) at the Skidaway Institute of Oceanography (SkIO) (Georgia, U.S.A.). The system was equipped with a solar and wind power charging system to ensure continuous monitoring capability for temporal sampling with high resolution. Additionally, a VHF radio

transmits data over the internet so the system can be operated remotely from the Georgia Tech campus. This system is deployed in conjunction with a nest of four monitoring wells with screens positioned at different depths in the sediment to survey pore water transport in the first 60 cm of the sediment. These tools provide an excellent mechanism to study the effect of tidal forcing on sediment biogeochemistry and for monitoring long term ecosystem health. This paper explains the details of system construction, the voltammetric sequence that was developed and implemented, and provides preliminary data to validate the use of this technique for investigations into the hydrological, chemical, and biological dynamics of salt marsh ecosystems.

Introduction

The increasing flux of carbon dioxide into the atmosphere has enhanced environmental concerns regarding the impacts of anthropogenic forcings on natural environments. Long term monitoring of individual ecosystems and a balanced carbon budget are required to best evaluate future responses to environmental changes instigated by natural or anthropogenic forcings. Global carbon budgets estimate that a large portion of terrestrial organic carbon is remineralized in coastal settings (Hedges et al., 1997). Recent research also indicates that 40% of annual carbon burial occurs in continental margin sediments (Muller-Karger et al., 2005). Salt marsh ecosystems in particular are among the most productive ecosystems on Earth, representing net primary productivity exceeding 1,000g C m^{-2} yr^{-1} (Alongi, 1998). Globally, coastal marshes have been proposed to function as net sinks of carbon dioxide from the atmosphere (Solomon et al., 2007), because these systems experience extremely high levels of terrestrial carbon inputs

(Hedges et al., 1997). However, the export of organic carbon from coastal marshes to continental margin sediments and subsequent remineralization may actually be a source of atmospheric carbon (Cai et al., 2000, Chapter 4). Consequently, a comprehensive understanding of organic carbon cycling in intertidal salt marsh ecosystems is crucial to accurately assessing the role of the land-ocean transition boundary in regulating fluxes of carbon dioxide to the atmosphere. This understanding hinges on the ability to elucidate and quantify the key factors that influence microbial respiration (Hyun et al, 2007).

In addition to playing a central role in the carbon cycle, coastal marshes and estuaries are vital to marine ecosystems because they control nutrient exchange at the land-sea boundary, help protect coastal municipalities from storm induced flooding, curtail erosion, and serve as a repository for pollutants (Pomeroy and Wiegert, 1981; Mitsch et al., 1993). Coastal marshes function as unique habitats for a variety of plant and animal species including *Spartina alterniflora* and Fiddler crabs (*Uca pugnax*). *Spartina alterniflora* constitutes the main plant species in most Atlantic coastal marshes and produces the majority of organic matter in these environments (Otero et al., 2000). These species develop air spaces referred to as aerenchyma in their root systems (Burdick and Mendelssohn, 1990), and these pockets allow for transport of oxygen from the aerial portions of the plant into the roots. Additionally, Fiddler crabs create burrows which provide a conduit for oxygenated water to travel deep into the sediment. Consequently, both these species have a significant impact on the physical and chemical characteristics of the surrounding sediment by enhancing advection and increasing permeability, sediment-water surface area, and pore water flushing (Boudreau. 1997; Christiansen et al., 2000; Furukawa et al., 2001). .

The high concentration of organic carbon in coastal marsh sediments fuels aerobic and anaerobic respiration processes which lead to the complete removal of dissolved oxygen millimeters below the sediment water interface (e.g. Bull and Taillefert, 2001; Taillefert et al., 2007). Sulfate, iron oxide, and manganese oxide minerals are then the most abundant electron acceptors available to microbial communities for carbon remineralization (Kostka et al, 2002). Originally, it was widely accepted that sulfate reduction dominated organic matter oxidation in salt marsh sediments, due to the abundance of sulfate in sea water and because one mole of sulfate can be used to oxidize eight moles of organic carbon (Howarth, 1984). In productive aquatic ecosystems, sulfate reduction accounts for about 50% of organic remineralization in sediments under 0 – 20 m of water (Jorgensen, 1982). Additionally, sulfate reduction has been shown to annually degrade >90% of the organic carbon generated from net primary productivity (Howarth and Giblin, 1983). However, more recent evidence suggests that dissimilatory iron(III) reduction constitutes another efficient and significant pathway for organic carbon remineralization even in sulfate-rich sediments (Canfield et al 1993b; Lowe et al, 2000; Kostka et al., 2002). Because four moles of iron(III) are required to oxidize one mole of organic carbon, microbial iron reduction can compete with sulfate reduction only if the iron(II) byproduct is rapidly recycled to iron(III) oxides. Plants, crabs, and tidal fluctuations all enhance the delivery of oxygen into the sediment, and facilitate the oxidation and recycling of reduced species to replenish microbial substrates (Furukawa et al., 2001; Koretsky et al., 2002). Indeed, iron(III) reduction was the dominant respiratory process coupled to carbon oxidation in vegetated, bioturbated salt marsh sediments (Kostka et al, 2002). Sulfate reduction also occured in these sediments, but further below

the sediment water interface compared to sediments that lacked vegetation (Kostka et al., 2002). Thus, sulfate reduction appears to dominate in unvegetated areas and iron reduction dominates in sediments occupied by macrofauna and macrophytes, clearly illustrating that higher order biological activity influences the redox processes occurring in these sediments.

In addition to biological influences, abiotic reactions further complicate the study of carbon remineralization in coastal marsh sediments. When the sediments are saturated with water, they transition to more reducing character. Under these conditions, maximum rates of sulfate reduction are noted in the first few centimeters of the sediment and reduction of iron oxides by sulfide occurs (Hines et al, 1989). Conversely, desiccation shifts the sulfate reduction zone deeper into the sediment, and leads to the oxidation of reduced sulfur compounds, the removal of dissolved iron(II), and the oxidation of reduced iron sulfur minerals (Hines et al, 1989). Isotopic studies have shown that only 8 – 16% of reduced sulfate remains in the form of soluble sulfide or acid volatile sulfide (FeS). The remainder undergoes abiotic reactions and precipitates predominantly as pyrite with a small percentage forming elemental sulfur (Howarth and Giblin, 1983). Failure to account for formation of precipitates and burial in these sediments leads to an underestimation of sulfate reduction rates by 70 – 95% (Howarth and Giblin, 1983). These interactions also impact iron reduction calculations and thus failure to account for abiotic reactions and precipitation of reduced byproducts leads to a substantial underestimation of total carbon remineralization rates.

Finally, coastal marsh sediments are subjected to complex hydrological features including tidal advection which artificially enhances exchange processes between

sediment pore waters and the water column, substantially complicates carbon remineralization rate calculations, and tests the limits of diagenetic sediment modeling capabilities. Seawater inundation affects sediment redox conditions, salinity distribution, and nutrient availability. Inundation frequency and tidal range partially controls plant zonation (Osgood, 2000). Vegetation has been shown to decrease horizontal flow velocity in sandy sediments, but not in fine grained sediments (Mann and Wetzel, 2000) which clearly illustrates that macrophytes and hydrodynamics are intricately linked. The propagation and distortion of tides in these environments has also been well studied (e.g. Friedrichs and Aubrey, 1994; Van Leeuwen et al., 2000) along with channel geometry, bottom friction, sediment deposition, and the presence of tidal flats all of which affect the tidal and geomorphological sediment properties (Van Leeuwen et al., 2000). Sediment topography may also enable advective pore water transport such that the solute exchange due to advection near the sediment water interface may exceed molecular diffusion by several orders of magnitude (Huettel et al., 1998; Reimers et al. 2004; Franke et al., 2006). Strong tidal fluctuations in sediments with high permeability generally lead to higher oxygen uptake (Ziebis et al., 1996), deeper oxygen penetration (Forster et al., 1996), higher degradation rates of natural organic matter because of the constant supply of oxidants (Huettel and Rusch, 2000), and more efficient removal of dissolved reaction products (Huettel et al., 1998).

The effect of advective transport on sedimentary biogeochemistry is largely ignored in fine grained sediments, and bioturbation and bioirrigation are considered for the physical transport of material and water in such environments. Recently, comparisons of in situ and ex situ measurements have revealed that pore water chemical

composition is highly affected by advective transport induced during tidal cycles (Taillefert et al., 2007), and that using ex situ measurements to investigate sediment biogeochemistry in marsh sediments may not yield accurate estimates of these processes. Thus, in situ sampling techniques are required to study the effect of hydrological forcing on the biogeochemistry of estuarine and marsh sediments.

In summary, the complexity of interactions between physical, chemical and biological processes limits the ability to quantify the biogeochemical cycling of many elements in these systems (Cai and Wang, 1998; Caffrey, 2004). This complexity could be better addressed using in situ sampling techniques with high spatial and temporal resolution. This paper details the construction and installation of a state of the art, solar and wind powered, in situ voltammetric monitoring system in an intertidal coastal marsh for remote monitoring of the geochemical composition of the sediment pore water as a function of time. This new system is able to simultaneously acquire temporal measurements of the main terminal electron acceptors including dissolved oxygen, dissolved iron(II), dissolved manganese(II), thiosulfate, total dissolved sulfide ($\Sigma H_2S = H_2S + HS^- + S_0 + S_x^{2-}$), and other species to trace biogeochemical processes (Tercier-Weber and Taillefert, 2008). The combination of the recharging system and the remote communication feature allows the instrument to constantly generate data with high temporal resolution for use in future transport models.

Procedures and Methods

The Saltmarsh Ecosystem Research Facility (SERF) at the Skidaway Institute of Oceanography (SkIO) is geographically isolated on the leeward side of Skidaway Island (Figure 5.1).

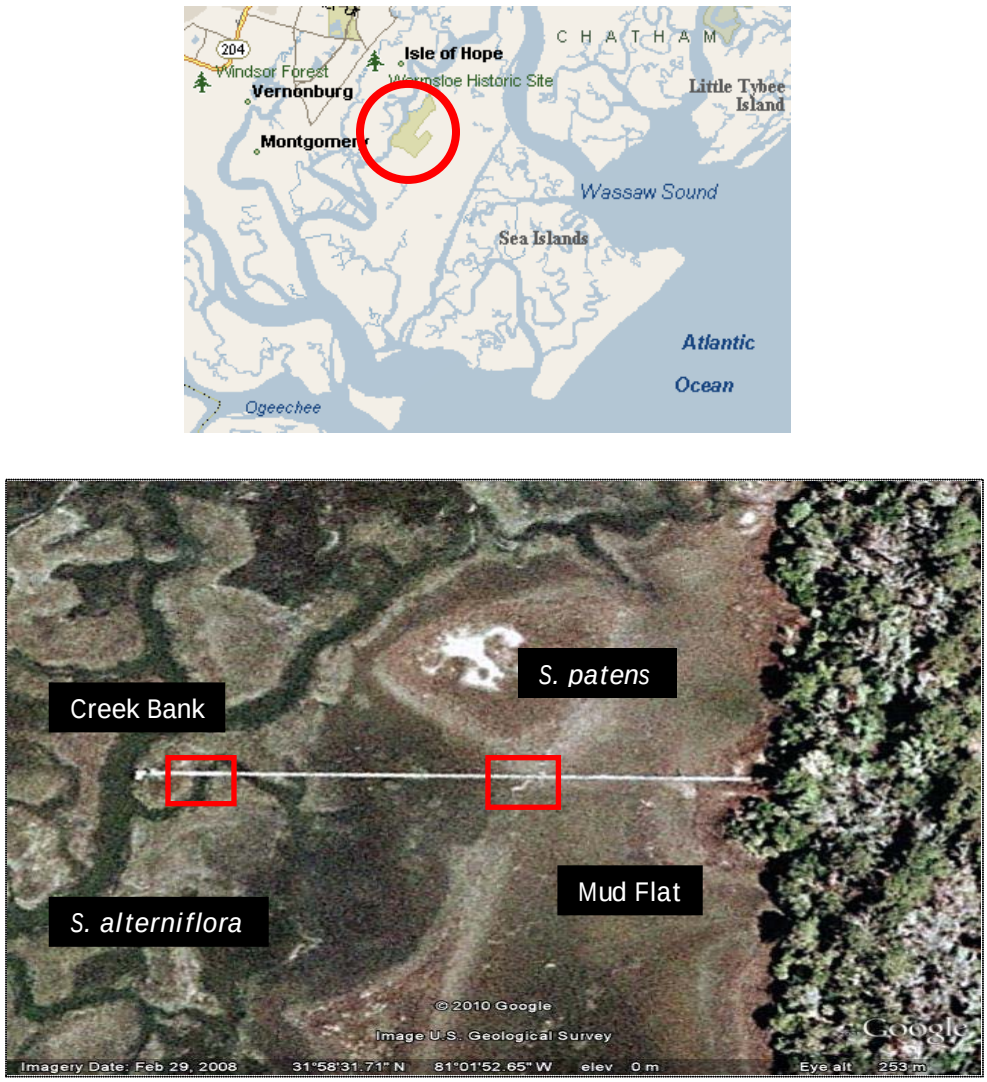

Figure 5.1: The Skidaway Ecosystem Research Facility is located on the sheltered side of one of the Sea Islands off the Georgia (U.S.A.) coastline, south east of the city of Savannah (top). Larger map (modified from Google Maps) illustrates the boardwalk originating inland and running west thought the mud flat and terminating near the creek bank. The locations of marsh fauna in relationship to the boardwalk are labeled, and the red boxes denote the placement of the water level wells (bottom).

The marsh experiences diurnal tides, but is not exposed to direct wave action from the Atlantic Ocean or the nearby river system. The study area was accessed through a 250 m long boardwalk that extends into the salt marsh. The boardwalk originates amongst an inland marsh meadow and follows the transition of the marsh through a mud flat (122 m) and into a tidal creek. The mud flat is predominantly unvegetated with sporadic stalks of short *Spartina patens*. This area is slightly elevated compared to the creek bank and is exposed to the atmosphere for about 12 hours daily in 6 hour increments between tides. The tidal creek sampling area is located at the end of the boardwalk. Whereas the mud flat is fully exposed to the atmosphere for portions of the diel cycle, the center of the creek customarily retains a small amount of water at all times. The banks of the creek are populated by thick stands of *Spartina alterniflora* and are exposed to the atmosphere for about 3 hours of each tidal cycle.

A portable electrochemical analyzer, ISEA III^{TM} (Table 5.1), from Analytical Instrument Systems (AIS, Inc) was mounted to the side of the boardwalk, along with a MicroCAT probe (Seabird Electronics Inc.) for concurrent measurements of the ambient conditions including surface flow, water depth, temperature, and salinity taken at 10 min intervals.

Table 5.1: Characteristics of the ISEA III™ System that was deployed in the SERF marsh for long term voltammetric measurements of sediment pore water chemistry.

Instrumentation:	AIS ISEA III
Compliance:	+/-12 V @ 30 mA
Current Range:	100 nA to 10 mA
Diameter/Length:	15 cm/35 cm
Weight:	10 kg
Power and Consumption:	External and Internal (12 V), 500 – 800 mA)
Voltammetric Techniques:	DC, Sampled DC, Normal Pulse, Differential Pulse, Square Wave, Linear Sweep, & Cyclic and all stripping analysis techniques
Max Number of Working Electrodes	4
Other capabilities:	Temperature & pH or Seabird Microcat 37SI

This instrument requires a system of three electrodes including a working, counter, and reference electrode. The counter electrode was constructed from platinum wire, while the reference electrode was made of silver wire conditioned in 3 M KCl solution at a positive potential to deposit a thin layer of AgCl on the surface. The working electrodes consisted of mercury/gold (Hg/Au) amalgam microelectrodes were positioned at fixed but different sediment depths in the center of the tidal creek (Figure 5.2).

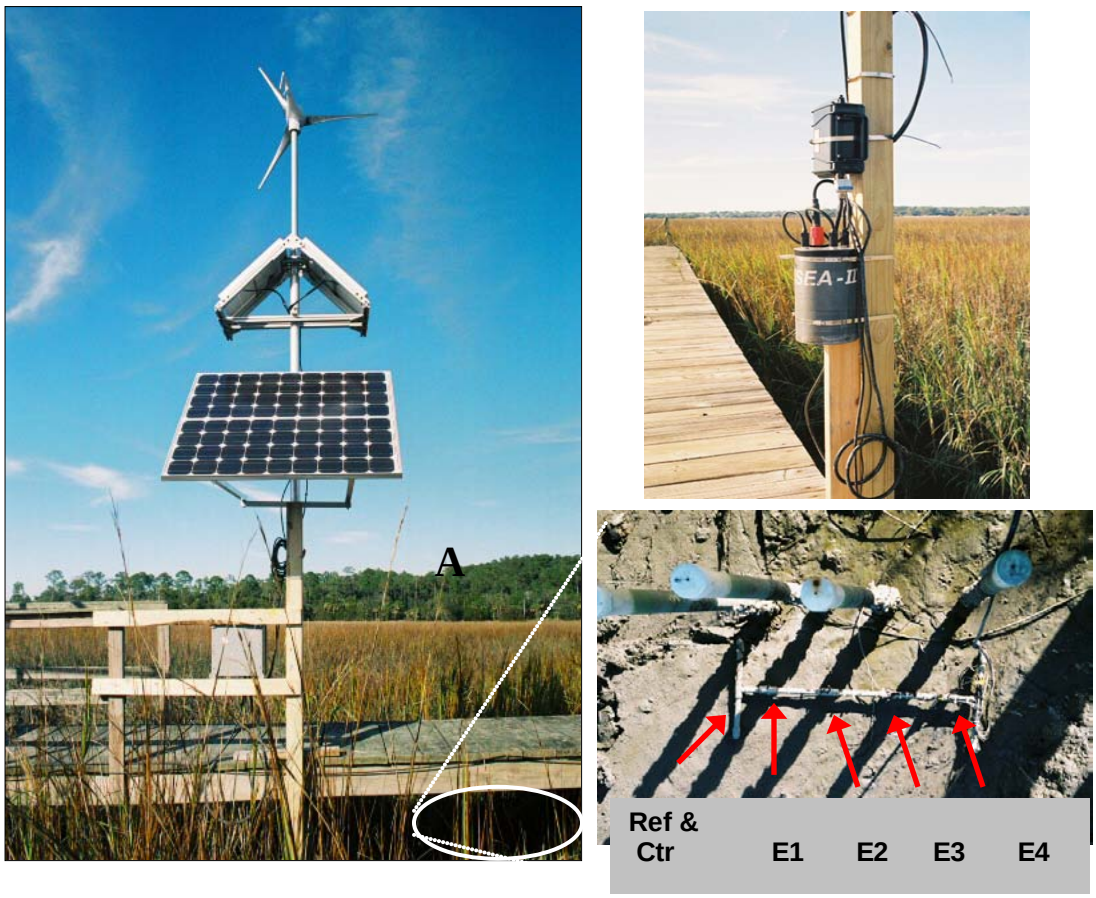

Figure 5.2: Remote sensing set up to monitor the geochemical composition of pore waters as a function of time and depth in the sediment. The potentiostat is anchored to the northern side of the boardwalk (top right). The solar panels and wind turbine recharge the system batteries to ensure continuous measurement (left). The 6 required electrodes (4 working Au/Hg microelectrodes, 1 Ag/AgCl reference and 1 Pt counter electrode) are fastened to a PVC holder. The working electrodes are positioned in the sediment such that E1 is near the surface, and increasing with depth from E2 to E4 (bottom right).

These electrodes are designed for the simultaneous voltammetric measurement of dissolved oxygen, iron(II), manganese(II), total dissolved sulfide (ΣH_2S), and thiosulfate, as well as other electrochemically active species such as organically complexed iron(III) and iron monosulfide ($FeS_{(aq)}$) (Luther et al, 2008). Before deployment, the working electrodes were calibrated for these redox species (except dissolved oxygen) using the Pilot Ion Method with manganese(II) as the pilot ion (Brendel and Luther, 1995).

Electrodes were calibrated for oxygen independently as a function of temperature and salinity (Luther et al., 1999). An in-depth discussion of electrode construction and preparation for the Hg/Au amalgam electrodes can be found elsewhere (Brendel and Luther, 1995; Luther et al, 2008; Chapter 3).

The two batteries were recharged continuously using six solar panels mounted at a 45^{o} angle and oriented in a north-south direction to maintain optimal sun exposure onto a large surface area (Figure 5.2). The six solar panels included two Sunmodule SW75 (75 W, 17.4 V) monocrystalline panels (Solarworld AG) and four BSP 1012 (10 W, 17.3V) multi-crystalline panels (PowerUp). The total energy generating capacity of the system was 190 W at 24 V or 7.9 Amp. In addition to solar components, a 400 W, 24 V Air X Marine wind turbine (Southwest Windpower) was also installed as a back-up power generation system to maintain battery charge even under cloudy conditions. The wind and solar charging systems are independent of one another and can be used in conjunction or individually. A 25 Amp, 24 V taper charge controller (model NC25A-24, SES Flexcharge USA) is connected to the two 12 V deep cycle batteries (Werker SLI24MDC) connected in series to provide 24 V output. The potentiostat draws approximately 0.5 Amp continuously, such that batteries provide approximately 6 days of uninterrupted instrument power in the absence of charge.

The AIS, Inc ISEA III^{TM} includes software capable of running both real time and preprogrammed sequences of measurements. Different types of voltammetric scans can be obtained including linear sweep, cyclic, normal pulse, differential pulse, and square wave voltammetry with stripping techniques between +2 and -2 V at scan rates ranging between 1 and 10,000 mV s^{-1} with or without stripping techniques. The system also

includes an internal trigger function to switch between the 4 working electrodes manually or electronically. With the remote communication capabilities, the sequence can be altered at any time; however, over the course of this study an ideal sequence was developed and applied periodically every 3 hrs (Table 5.2).

Table 5.2: This electrode sequence was tested in the SERF marsh and proven optimal to maintain electrode integrity over long term deployments.

Number of Scans	Voltammetric Wave Form	Scan Rate (mV/sec)	Sensitivity (+/- range)	Conditioning applied
4 (summer only)	Anodic Square Wave	200	1 μA (+/- 2)	-0.9 V, 10 sec
4	Anodic Square Wave	200	100 nA (+/- 200)	-0.9 V, 10 sec
4	Cathodic Square Wave	200	100 nA (+/- 200)	-0.9 V, 10 sec -0.1 V, 10 sec
4	Cathodic Square Wave	200	1 μA (+/- 2)	-0.9 V, 10 sec -0.1 V, 10 sec
4 (winter only)	Linear Sweep	2000	1nA (+/- 200)	-0.1 V, 10 sec
3	Linear Sweep	2000	1 μA (+/- 2)	-0.1 V, 10 sec

This sequence had to be designed to account for all the potential species detectable in natural sediments and simultaneously avoid potential artifacts that may be encountered during measurements. In addition, the potentiostat can only apply a potential to a single working electrode at a time and the inactive electrodes are exposed to an open circuit potential. During this idle period, diffusion of chemical species at the electrode surface could lead to an unwanted build-up of soluble organic Fe(III) complexes and ΣH_2S as these species either adsorb (i.e. soluble organic Fe(III) complexes at potentials exceeding -0.4 V), or oxidize Hg(0) in the presence of ΣH_2S (i.e. at potentials higher than -0.6 V)

(Taillefert et al., 2000). To maintain the reproducibility and integrity of the electrodes, a conditioning potential was applied at -0.9 V for 5 min after the lag between sequence repetitions to remove any previously deposited electroactive species from the electrode surface. Voltammograms are typically acquired cathodically (i.e. from -0.1 V to -1.8 V) without preconcentration as concentrations of Fe(II), $FeS_{(aq)}$, and Mn(II) are usually high enough in sediments. In the cathodic mode, however, these electrodes are highly sensitive to sulfide species including HS^-, S_0, and S_x^{2-} (Brendel and Luther, 1995), and formation of a cinnabar (HgS) double layer in the mercury film at potentials greater than -0.6 V may prevent diffusion of sulfide species to the mercury film and lead to peak distortion (Davison et al., 1988). Thus a series of voltammograms were run anodically first to eventually clean the electrodes of any sulfide species. Overall, the total running time of this sequence was 48 minutes followed by a 2 hour and 12 minute lag between measurement time points such that measurements are obtained every three hours at each depth in the sediment.

Data is stored on an internal memory card and can be downloaded remotely through cellular modem technology. A 900 MHz VHF broadband radio transmitter communicates with a local computer at the SkIO facility, this docking computer is accessed from Georgia Institute of Technology through the remote desktop application of Windows XP. Thus data is downloaded remotely for processing, and electrodes are periodically monitored for quality. The scans generated using this approach are processed with VOLTINT, an in-house Matlab based software with a deconvolution program for overlapping peaks (Bristow and Taillefert, 2008).

The hydrology of the pore waters was monitored using two separate nests of four monitoring wells, each positioned less than 30 cm apart laterally. The eight wells were constructed from PVC pipes with screens 5 cm in length and 0.15 mm slit width (Diedrich Drill, Inc.) and installed along the boardwalk, four in the creek and four in the mud flat at 0, 15, 30, and 60 cm (Figure 5.3).

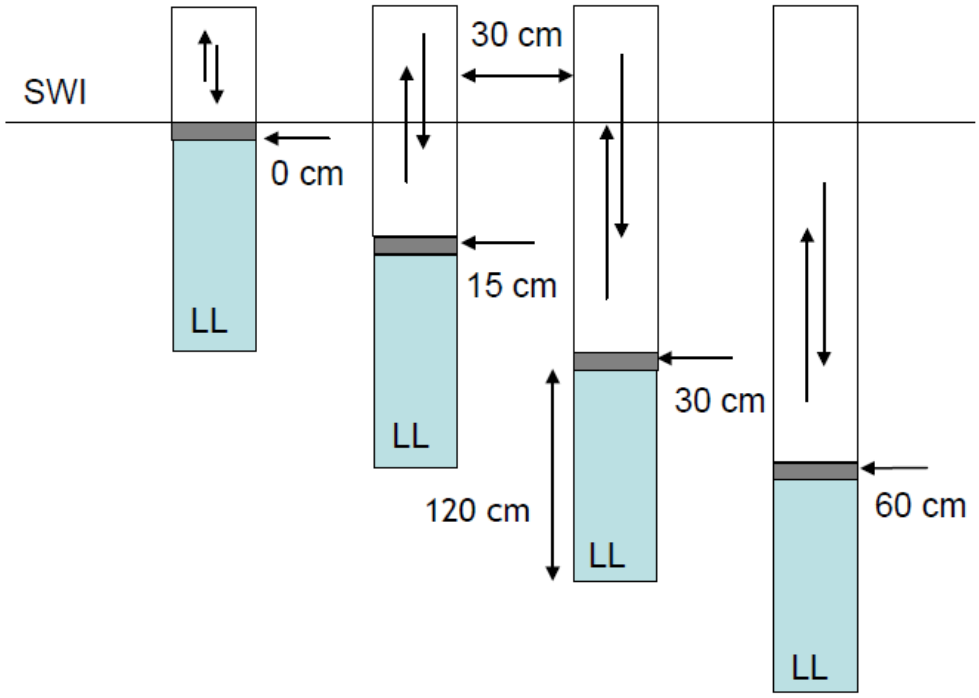

Figure 5.3: Level loggers (LL) were positioned at the bottom of four monitoring wells to monitor the effect of tidal fluctuations on the transport of pore water over time. Suites of 4 wells with screens at depths of 0, 15, 30, and 60 cm were installed in both the mud flat and creek bank sediments.

These wells are plugged at the bottom and capped at the top to prevent contamination from rainfall events. Small holes were added to the caps to maintain atmospheric pressure in the wells. Combined pressure transducers and temperature sensors (Solinst, Inc.) were placed at the bottom of each well to monitor water level and temperature

fluctuations over multiple tidal cycles. Fourier transform analysis in Matlab was performed on both the temperature and water level data to examine tidal strength and periodicity.

Results

The wells for the level loggers were installed to examine the effects of tidally induced advection on sediment biogeochemistry. Examining the data from the creek bank wells, it was apparent that water begins filling the deepest wells initially followed by the surface wells (Figure 5.4 top). The converse was true for the mud flat wells in which the wells filled in order from shallowest to deepest (Figure 5.4 bottom).

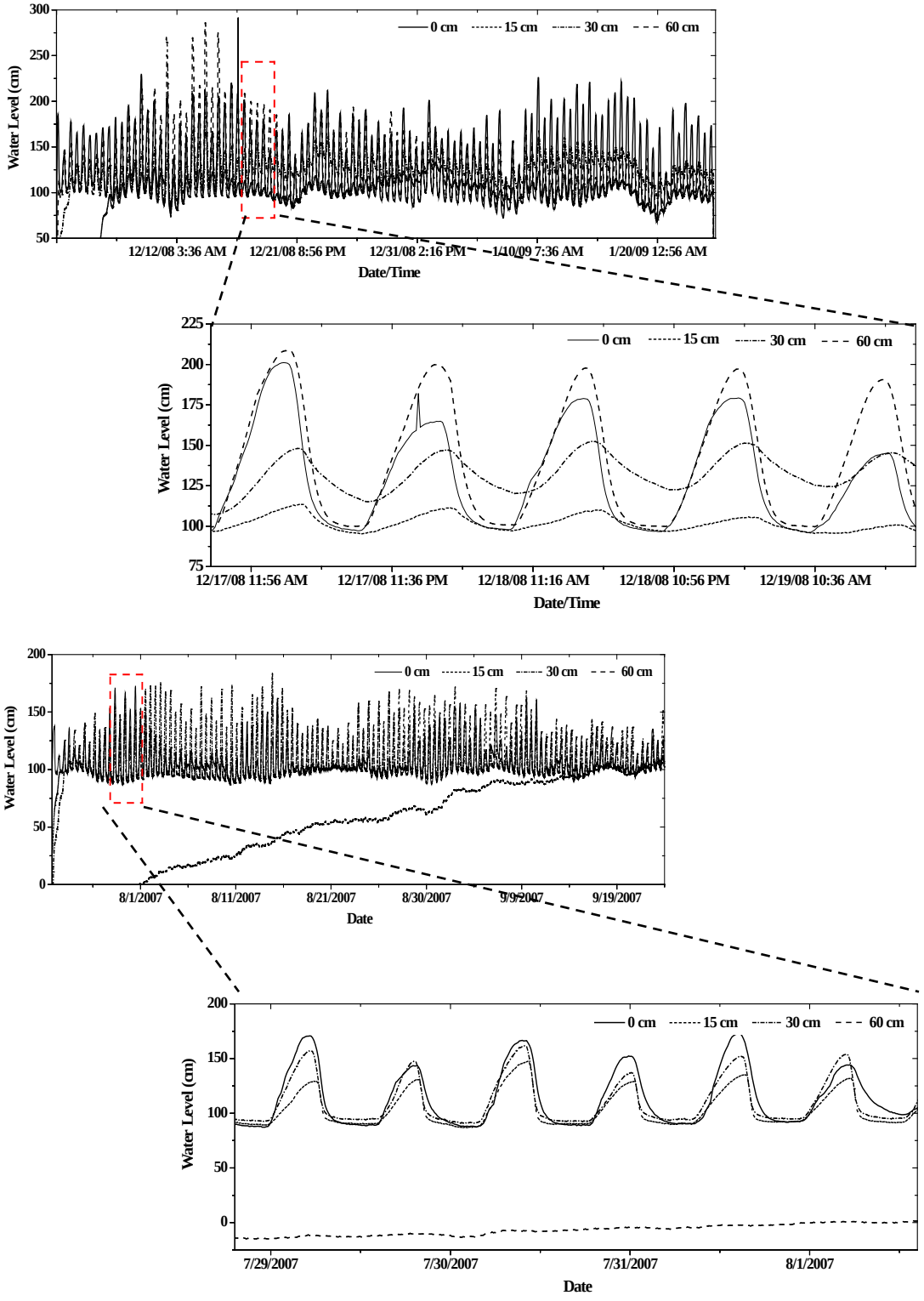

Figure 5.4: Sections of level logger data from the creek bank (top) and the mud flat (bottom). The insets from the creek bank data clearly illustrate that the deeper wells fill up first indicating a upward transport flow. Conversely, in the mud flat, the shallowest wells fill first which more characterizes a downward transport regime.

To ensure sediment did not build up in the well bottoms, each was pumped periodically. After this process, the water levels in the mud flat wells took longer to reequilibrate than the creek bank wells (Figure 5.4).

The Fourier transform analysis performed on the level logger data from the creek bank generated strong peaks at 114, 27, 15, 10, 5 days and 23.95, 12.41, 8.27, and 6.21 hours (Figure 5.5).

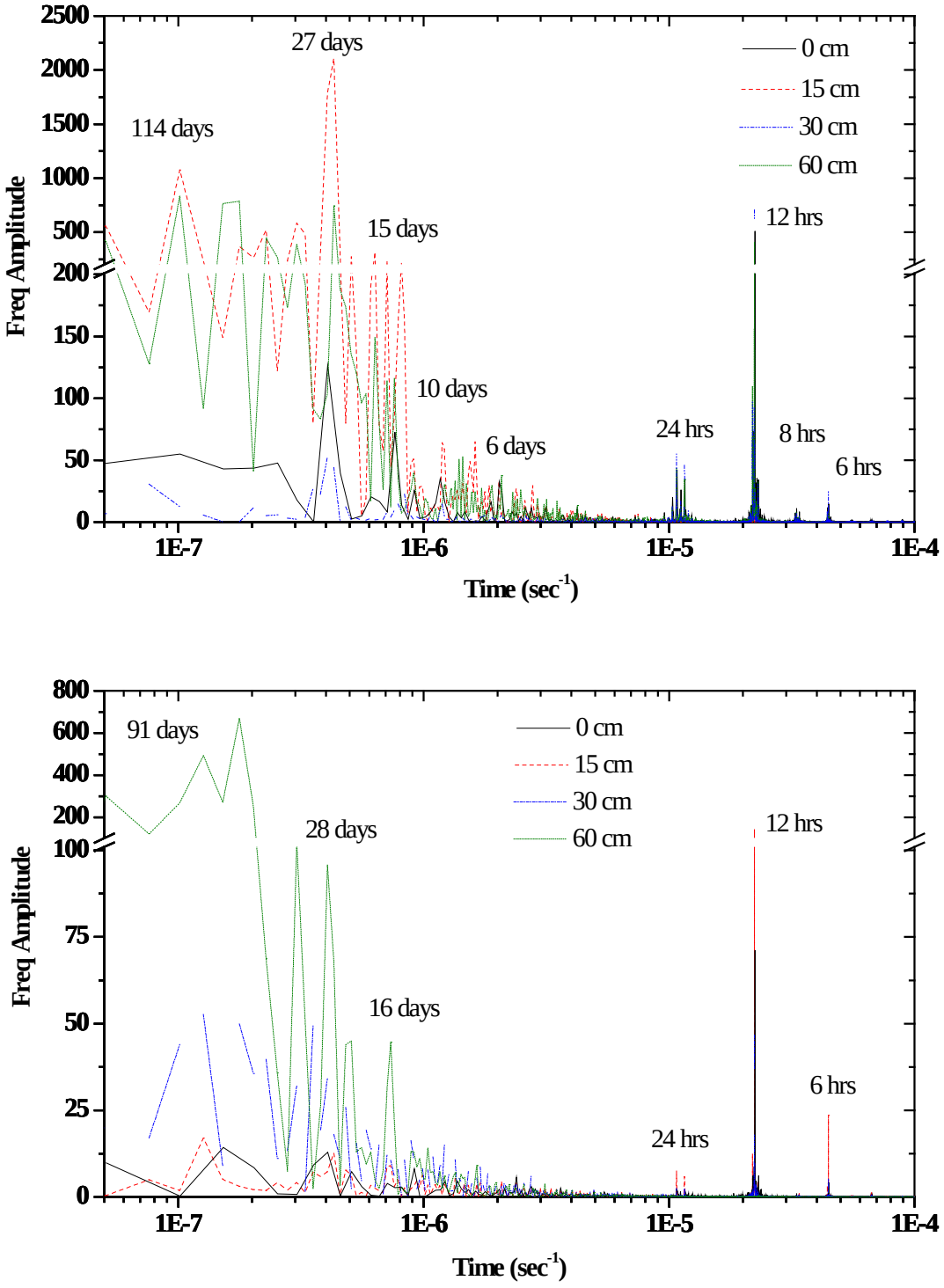

Figure 5.5: Fourier transform analysis was performed on an entire year of continuous level logger data to resolve daily and monthly events. The periodicity of the monthly lunar cycle can be distinguished in the transforms of both the mud flat and creek bank.

The same analysis performed on the level logger data from the mud flat did not generate peaks as intense as that of the creek bank, but peaks were still clearly visible at 28 and 16 days and 24, 12, and 6 hours (Figure 5.5). A full lunar cycle occurs approximately every 29 days, and two spring tide events occur every 14 or 15 days at the full and new moons. Neap tides occur during the first and third quarters, also approximately 15 days apart from one another. Perigee and apogee phases occur every 221 days or 7.5 lunar cycles, but it appears that a longer data set is required to detect any tidal periodicity caused by these phases. The set of peaks that occur on the hourly time scale represent components of the diurnal tide in the study area.

A 53 day data set with three working electrodes at fixed sediment depths is displayed in Figure 5.6, along with level logger data from the four wells in the creek bank for comparison.

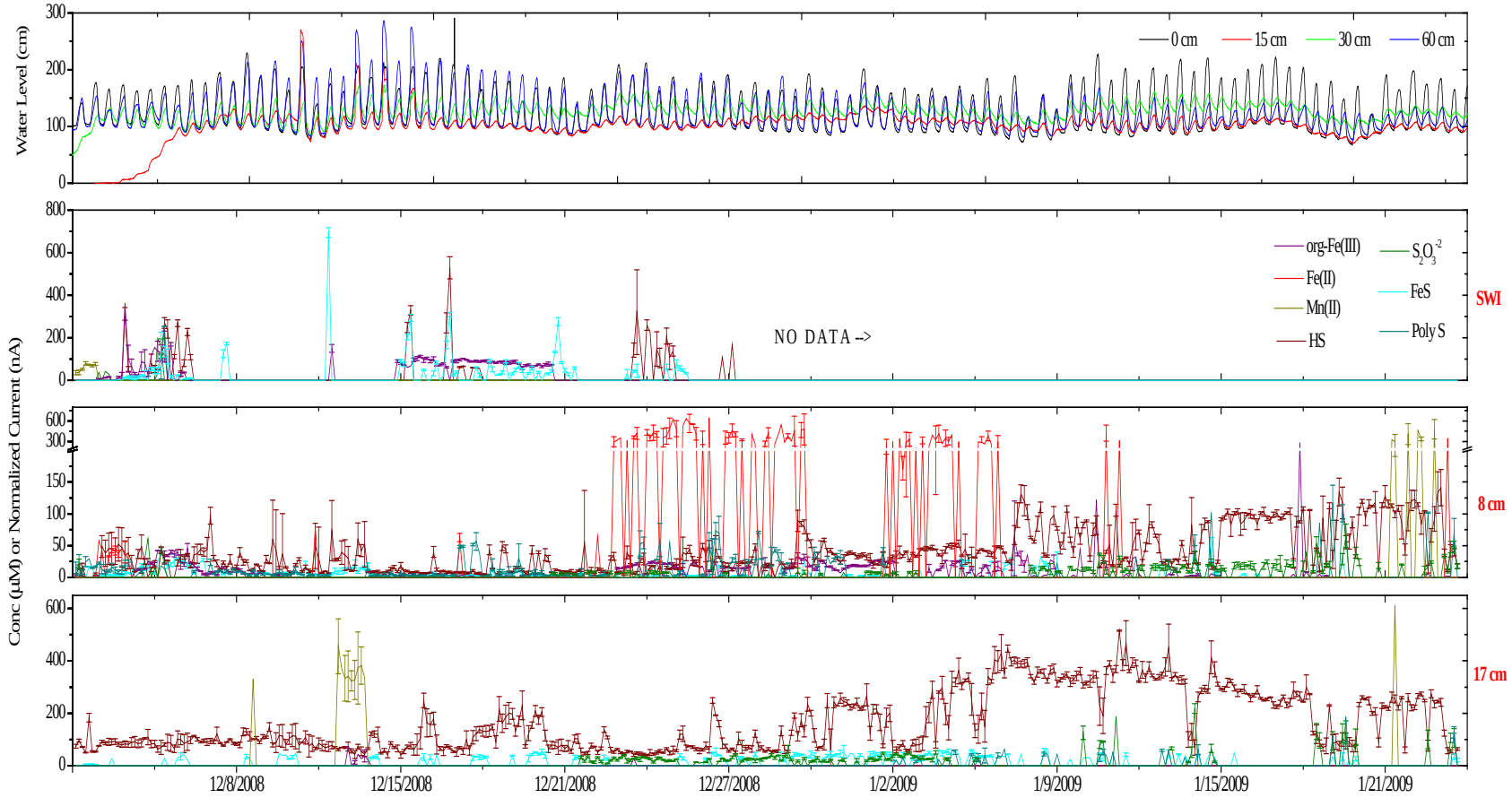

Figure 5.6: Sample time series from December 2008 thru January 2009. Top bar displays pore water depth based on the corresponding level logger data. The bottom four time series reflect the fluctuations of the reduced species found in sediment pore waters at the creek bank measured with the new voltammetric system described in this study. The system is capable of long term monitoring, but the chemical speciation does not appear to correlate with the tidal data.

The electrode positioned at the SWI detected spikes in concentration of sulfide (up to 500 μM), $FeS_{(aq)}$ (up to 600 nA), and org-Fe(III) (up to 300 nA), but this electrode ceased functioning after approximately one month. Electrode 2 was positioned 8 cm into the sediment and continued to produce high quality measurements for the full time period. This electrode shows clear cycles where sulfidic (i.e. ($\Sigma H_2S = H_2S + HS^- + S^0 + S_x^{-2}$) and metal species alternate. Initially sulfide was the dominant species measured along with thiosulfate, $FeS_{(aq)}$, polysulfides and a small amount of iron(II). However, in late December (21 days after sequence initiation) concentrations of dissolved iron(II) increased up to nearly 800 μM while sulfide and polysulfides decreased slightly. Fifteen days later the iron(II) was replaced by increased concentrations of sulfide and thiosulfate for about 14 days. For the last 3 days of this time series, sulfide remained elevated while Mn(II) concentrations increased up to 600 μM. The third electrode was positioned at 17 cm into the sediment and did not display as much complexity as electrode 2. At the beginning of the deployment sulfide was the predominant species detected along with small amounts of $FeS_{(aq)}$ and thiosulfate. This electrode mirrors the sulfide increase detected by electrode 2 that occurred 36 days into the deployment. Conversely, this electrode did not fluctuate between reduced metal and dissolved sulfide. In fact, except for a small spike in Mn(II) concentrations, this electrode is completely void of dissolved metals during this time series.

The same Fourier Transform analysis that was performed on the level logger time series was also used to analyze the pore water geochemical time series. Unfortunately, no regular patterns with depth or time were evident (Figure 5.7).

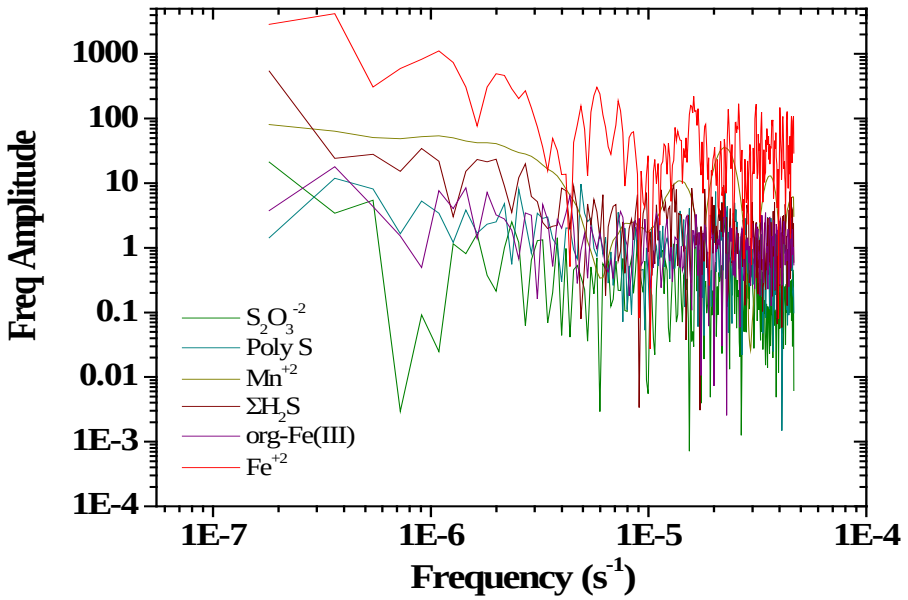

Figure 5.7: The results of Fourier transform analysis performed on the time series of the 8 cm electrode in Figure 5.6. No periodicity is recognized, and the same analysis performed on the 17 cm electrode yields similar results.

Discussion

The purpose of this study was to construct an autonomous in situ voltammetric system with remote communication capabilities for the long term monitoring of the hydrological, chemical, and biological dynamics of salt marsh ecosystems. This system was designed to collect high temporal resolution data for future incorporation into a three dimensional reactive transport model.

A common strategy for the geochemical investigation of coastal marsh sediments involves water sampling using pumps, followed by filtration, and finally acidification to preserve the sample speciation until it can be analyzed in a laboratory. Sediment cores can also be taken, sectioned, and centrifuged to recover pore waters, but all these steps must be performed under an

inert atmosphere to prevent contamination and alteration by oxygen. It has been recently demonstrated however, that permeable sediments previously subjected to advective transport processes such as tidal influences re-equilibrate to a diffusive transport regime within hours of removal (Cook et al., 2007), and fluxes determined from external core incubations were reported to be up to 65% lower than the same fluxes measured with in situ sampling techniques (Hammond et al., 2004). Additionally, based on previous in situ and ex situ comparisons at SERF, the pore water chemical composition is highly affected by advective transport induced during tidal cycles (Taillefert et al., 2007). Incubations are generally conducted using either whole cores or sections of sediment (e.g. Howarth and Giblin, 1983; Hines et al., 1989; Canfield et al., 1993a). Flow-through reactors are also frequently used to study the biogeochemical complexity of sediments in more realistic conditions (e.g. Carey and Taillefert, 2005; Pallud, et al., 2007). Unfortunately, these measurements are time consuming and may modify the activities of microbial community assemblages or introduce artifacts due to sediment smearing. Thus, the ability to perform in situ measurements, though more complicated logistically, is warranted to determine more representative pore water composition.

In situ voltammetry simultaneously quantifies a large number of environmentally significant redox species. The detection limits are relatively low, and measurements can be accomplished with minimal perturbation to the sample area. The necessary equipment is commonly available, has low energy requirements, and can be deployed in the field using renewable, environmentally friendly, energy resources. In situ measurements also prove more advantageous because they eliminate the time delay between sampling and analysis. Previous studies have experimented with in situ voltammetric techniques in coastal marsh sediments, but they experienced issues with long term monitoring, such as insufficient sensitivity and fouling of

the sensor surface due to organic matter adsorption (Tercier et al, 1990; Herdan et al, 1998). To combat these issues, the electrode potential in this method was scanned to -1.8 V which is sufficient to reduce the prevalent sodium ions. At such a negative potential, sodium metal reacts with water and releases hydrogen gas, which subsequently reduces any organic matter that may have adsorbed to the electrode surface (Tercier et al., 1990). Traditional voltammetric reference electrodes are capped with glass frits, which present potential fouling issues during long term deployments. Furthermore, glass electrodes are more likely to break when exposed to tidal fluctuations and detritus that flow in the marsh. To eliminate these issues, a Ag/AgCl reference electrode fashioned from a 2 mm thick silver wire conditioned in 3 M KCl was tested and was revealed to be significantly more durable and quite capable of withstanding the harsh conditions for long periods of time (Moore et al., 2009). The new instrumentation presented here enables the measurement of multiple redox species with high spatial and temporal resolution that is robust enough to withstand long term deployments.

Previous studies conducted in the same marsh identified broad differences in the character of the two sampling sites. The creek bank sediments were found to contain more iron oxides and dissolved ferrous iron compared to the strictly sulfate reducing character of the mud flat sediments (Taillefert et al., 2007). These findings were confirmed by three-dimensional measurements (Bull & Taillefert, 2001) and sediment incubations (Carey and Taillefert, 2005). The measurements obtained in these studies, however, were only limited to a few days seasonally, such that the exact reason for these differences could not readily be established. Continuous voltammetric measurements over long time periods coupled with water level measurements in the nested monitoring wells should provide a clearer view of the effect of marsh hydrology and geomorphology on the overall redox state of these sediments.

At low tide, the sediment surface of the mud flat is exposed to the atmosphere about twice as long as that of the creek bank. During this period, pore waters are static and sediment biogeochemical reactions likely result in the local accumulation of reduced species which could promote sulfate reduction. In contrast, the pore waters of the creek bank tend to accumulate iron(II) as opposed to dissolved sulfide in the upper sediment layers (Figure 5.6). If iron reduction is mainly driven by the anaerobic respiration of iron oxides, then it is also controlled by the recycling of iron oxides near the sediment-water interface either through infiltration of oxygenated water during tides or through advection of the deep reduced porewaters to the oxygenated overlying waters. Incorporation of dissolved oxygen into the upper sediment layers is enhanced by macrophyte roots (Sundby et al., 1998) and macrofaunal bioturbation (Wenzhofer and Glud, 2002). The long term sustainability of the salt marsh depends on the ability of *S. alterniflora* to maintain the marsh elevation and serve as a tidal break controlling the daily length of flood frequency and soil salinity (Morris et al, 2002, Morris, 2006). This species of flora has adapted to the sulfidic, water logged soils by developing an oxygen transport system that carries oxygen to the root zones. These roots subsequently serve as a conduit for oxygen exchange with the sediment (Kostka et al., 2002) and lead to the formation of small patches of oxidized sediments near the root systems (Sundby et al., 1998; Koretsky et al., 2008). Iron reducing organisms thrive in these small niches fueled by substrates provided by the plants. Additionally, macrofauna affects the transport of particulate matter by actively mixing the sediment (Christiansen et al., 2000) and that of pore water constituents by the passive or active flushing of burrows (Furukawa et al., 2001; Burdige, 2006). While the sides of the creek bank are lined with *S. alterniflora*, the electrodes are situated in the center of the channel which lacks vegetation, akin to the mud flat, indicating that plant roots do not aerate the soil immediately around the

electrodes. Simultaneously, the abundance of fiddler crabs does not differ significantly between the two locations and cannot explain these differences (Taillefert et al., 2007). Alternately, pore water advection at the creek bank could transport reduced species to the sediment water interface for oxidation at rising tides. Indeed, well water levels show that the deepest wells in the creek bank fill first compared to the shallow wells during incoming tides (Figure 5.4), suggesting that upward advection occurs during rising tide. Yet, water level data indicate the top 30 cm of sediment experiences the majority of tidally-induced pore water flow, while pore waters deeper than 30 cm below the SWI are virtually unaffected by the tides. These tools confirm the existence of strong, tidally driven advective transport in the sediments at the SERF facility and suggest that the different biogeochemical regimes at these two sites are primarily controlled by differences in hydrostatic pressure gradients as opposed to bioturbative influences. High advection in creek bank sediments should promote reoxidation of manganese(II) and iron(II) produced in the deep sediment layers near the sediment-water interface during rising tide, while oxygen penetration may be enhanced at ebb tide, when the hydrostatic pressure above the sediment is the highest. Interestingly, Fourier transform analysis on the geochemical data from the in situ electrodes indicated high temporal and spatial variability that could not be accounted for solely by tidal variability (Figure 7), suggesting that a complex biogeochemical network of reactions is superimposed to the hydrological component.

As water levels in the mud flat wells take longer to reequilibrate after the wells are flushed than in the creek bank sediments, lower hydrostatic pressure gradients must exist in these sediments. The surface area of the unvegetated mud flat is significantly greater than that of the creek bank (Figure 5.1) and must dissipate the water flow energy, thereby decreasing the hydrostatic pressure both above the sediment and in the subsurface compared to the creek bank.

These morphological differences could explain why advection at the mud flat appears to flow from the SWI down into the sediment once the hydrostatic pressure is high enough above the sediment (Figure 5.4 bottom). Coupled with the longer exposure to static conditions at low tide, the low hydrostatic pressure at rising tide and ebb tide must affect biogeochemical processes by decreasing the downward flux of dissolved oxygen to the sediment.

Iron(II) and org-Fe(III) were not detected continuously in the creek bank (Figure 5.6). At the SWI, $FeS_{(aq)}$ was measured along with org-Fe(III) and sulfides, but not in large quantities. However, at 8 cm depth iron(II) concentrations approached 600 μM and far exceeded sulfide concentrations. These events are not constant and may be influenced by tidal advections. Yet, these events may have never been captured without continuous long term monitoring.

Conclusions

Many coastal ecosystems are experiencing turmoil due to periodic hypoxia induced by cultural eutrophication. Additionally, effective coastal marsh management strategies require a detailed understanding of the coupling between tidal forcing, shallow subsurface hydrology, and sediment biogeochemistry. These systems significantly impact the global carbon cycle, thus long term monitoring of sediment hydrology and biochemistry is beneficial for maintaining overall ecosystem health.

The voltammetric measurements were collected in previous studies (Taillefert et al., 2007) in the mud flat and in the creek bank for this study to test the new instrumentation. These data sets clearly juxtapose the chemical differences between the two sampling sites. Sulfate reduction as the dominant respiratory process active in the mud flat, and the creek bank is characterize by a complex mixture of iron reducing and sulfate reducing components.

Examining the voltammetric data in conjunction with the level logger data indicates that tidal advection is most likely the dominant influence on sediment biogeochemistry, but the complex web of physical, chemical, and biological interactions cannot be completely deconvoluted.

Overall, this study illustrates that biogeochemical processes in coastal marsh sediments are controlled by a combination of physical forcing, including hydrodynamic pressure gradients and tidal fluctuations, and a complex web of microbial and chemical processes likely influenced by local sediment heterogeneities. The novel in situ monitoring system designed for this study was successfully tested and proven robust enough to acquire long term data sets. Additionally, this study demonstrates that remote sensing tools not only provide new opportunities to characterize the dynamics of environmental processes, but also provide scientists with the capability to generate data sets with high temporal resolution that can be used to improve current mathematical models.

While the level loggers clearly illustrate the different hydrodynamics of the two salt marsh regimes, the current arrangement can resolve the vertical component of fluid advection in only 2 dimensions. The spatial coverage of the wells needs to be broadened in order to resolve the entire three dimensional flow field.

CHAPTER 6

DECOUPLING CHEMICAL AND BIOLOGICAL SULFIDE OXIDATION THROUGH THE EXAMINATION OF MICROBIAL MAT COMMUNITIES

Introduction

Extremophiles broaden our understanding of the range of conditions in which life can persist on Earth and other planets. It has even been suggested that the present day extremophiles may be models of primordial organisms (Di Giulio, 2000), and their existence may provide insight into extraterrestrial habitats where life could develop (Dundas, 1998; Cavicchioli, 2002). The work contained within this chapter was a collaborative effort with the NASA Astrobiology and Life Sciences Laboratory, and focuses on halophilic microbial mat communities.

Sulfate reduction is one of the most ubiquitous anaerobic respiration processes in marine environments, and is thought to be one of the first microbial processes to evolve on earth (Canfield et al., 2000). Based on evolutionary biology studies, thermophilic sulfate reducing bacteria (SRB) evolved about 3.47 Gya (Shen et al.,2001). These bacteria possess the ability to respire on hydrogen and other small organic molecules (Stal, 1991) that should have been readily available during that time period; however, SRB utilize sulfate as a terminal electron acceptor, reducing it to sulfide in a multi-step process involving a sequence of redox reactions requiring ATP (adenosine triphosphate), formation of the APS (adenosine 5'-phosphosulfate) intermediate, and the sulfite reductase that reduces sulfite all the way to H_2S (Eq. 1).

$$SO_4^{-2} + ATP \rightarrow APS + 2e^- \rightarrow SO_3^{-2} + 6e^- \rightarrow H_2S \quad (1)$$

Sulfate was not abundant in the early oceans until well after the evolution of oxygenic photosynthetic bacteria, around 2.7 Gya (Shen et al., 2001), and did not start to accumulate in the oceans until the early Proterozoic Era (Canfield et al., 2000). Anoxygenic photosynthesis, however, may have evolved prior to oxygenic photosynthesis (Canfield, 2001) and the aerobic oxidation of sulfide may have been the first process to produce sulfate on the early earth (Friedrich et al., 2005). After photosynthesis became prevalent, oxygen concentrations began to rise and chemical oxidation of sulfide could have produced sulfate. However, chemical oxidation may not have been the only mechanism that produced sulfate for use by these organisms. Bacteria and Archaea capable of sulfide oxidation have been discovered in a variety of extreme environments (Kelly and Wood, 2000) and it has been suggested that these organisms were responsible for the initial production of sulfate in the early oceans (Friedrich et al., 2005).

Because they are representative of early earth communities, microbial mats present excellent media for studying the interactions between photosynthetic cyanobacteria (CYA), sulfide oxidizing bacteria (SOB) and sulfate reducing bacteria (SRB). The dense microbial communities found in the benthic microbial mats of hypersaline environments often exhibit high activities of photosynthesis, dissimilatory sulfate reduction, and other microbial processes, thereby exerting a profound influence on the biogeochemical cycles of carbon, nitrogen, sulfur, and other elements (Javor, 1989). Microbial mats are miniature benthic ecosystems that are laminarly stratified according to chemical microgradients of oxygen and sulfide. Within only a few millimeters, CYA, purple (PSB) and green sulfur bacteria (GSB), SRB, and colorless sulfur oxidizing bacteria (CSB) compete for light, carbon, and sulfide (Figure 6.1).

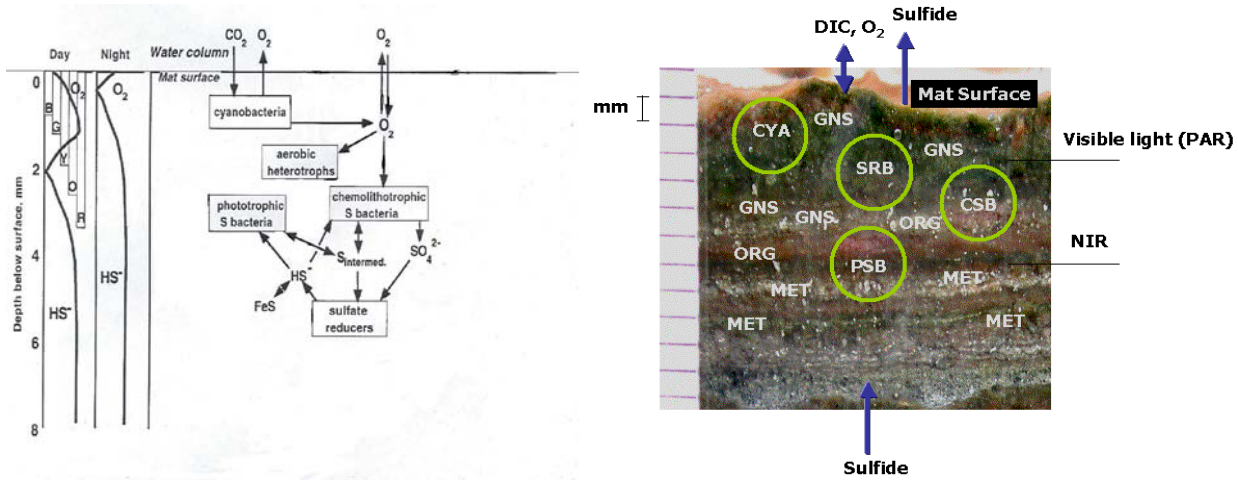

Figure 6.1: A. Simplified box model representation of the self-sustaining microbial interactions that occur in microbial mats. These mats only require inputs of oxygen and carbon dioxide from the overlying water (modified from DesMarais, 2003). The general shape of the diel profiles of oxygen and sulfide concentrations and the depth of visible light penetration separated by color are displayed on the left. B. The relative depth of vertical stratification and the general positions of common microorganisms that are present in these microbial mats.

The filamentous structure of CYA stabilizes the mats, ensuring they remain cohesive during tidal fluctuations. The CYA also excrete low molecular weight organic compounds such as lactate, acetate, and ethanol during photosynthesis, hydrogen during dark fermentation, and other organic moieties upon cell lysis (Stal et al., 1985). These compounds are excellent carbon sources and function as growth substrates for heterotrophic bacteria such as anaerobic SRB (Stal, 1991). Green nonsulfur bacteria (GNS) have diverse metabolic capabilities. They are preferentially photoheterotrophs, although they grow photoautotropically under anoxic conditions (Pierson et al., 1987). Purple sulfur bacteria are photosynthetic proteobacteria which are generally located just beneath the CYA layer (Oren, 2005). Sulfate reducers utilize sulfate as a terminal electron acceptor and in turn produce sulfide, which can be used by PSB with CO_2, as an electron donor

for anoxygenic photosynthesis (Table 6.1). Consequently, these communities function as complete ecosystems and can be self-sustaining for years (Van Gemerden, 1993) (Figure 6.1).

Table 6.1: Reactions catalyzed by the various microbiological populations in hypersaline microbial mats. These species form a self-sustained environment that only requires light and CO_2

Abbr	Species	Energy Source	Respiration Reaction
GNS	Green Non-Sulfur Bacteria	Photoheterotrophs	$CO_2 + 2H_2 \rightarrow CH_2O + H_2O$
CYA	Cyanobacteria	Photosynthetic	$CO_2 + H_2O \rightarrow CH_2O + O_2$
SRB	Sulfate Reducing Bacteria	Chemoorgano-heterotrophs	$CH_3COOH + SO_4^{-2} \rightarrow 2HCO_3^- + H_2S$
CSB	Colorless Sulfur Bacteria	Aerobic Chemoautotrophs	$HS^- + 2O_2 \rightarrow SO_4^{-2} + H^+$
PSB	Purple Sulfur Bacteria	Anaerobic Chemoautotrophs	$2HS^- + 4H_2O + 4CO_2 \rightarrow 2SO_4^{2-} + 4CH_2O$
MET	Methanogens	Chemoautotrophs	$CO_2 + 4H_2 \rightarrow CH_4 + 2H_2O$

Two types of bacterial oxidation processes have been identified, including a chemoautotrophic pathway by which bacteria derive the energy needed for growth from the oxidation of fully or partially reduced sulfur compounds to sulfate (Frigaard and Dahl, 2009), and an anoxygenic phototrophic pathway by which bacteria oxidize hydrogen sulfide to sulfate while fixing carbon dioxide autotrophically (Friedrich et al., 2005; Frigaard and Dahl, 2009). The members of the family *Thiobacteriaceae* are probably the most important chemotrophic

colorless sulfur bacteria (CSB) but *Thiobacillus* is the most studied genus of sulfide oxidizing bacteria (SOB) (Friedrich et al., 2005). *Thiobacteriaceae* utilizes the chemautotrophic pathway while C*hlorobiaceae*, an anoxygenic phototrophic green sulfur bacteria (GSB), and *Thiobacillus*, an anaerobic phototrophic purple bacteria (PSB), utilize the second pathway. The photosynthetic pathways require photon energy to actively transfer electrons from a reduced sulfur compound to carbon (Li et al., 2005); however they require different wavelengths for their respective photosystems. Purple sulfur bacteria are predominantly anoxygenic phototrophs, but some species may function as aerobic chemolithotrophs (Frigaard and Dahl, 2009). Anaerobic purple bacteria, remain at the maximum depth of light penetration and oxidize sulfide that diffuses upward (Oren, 2005). Comparatively CSB are aerobes which position themselves at the sulfide-oxygen boundary layer where sulfide rising from anoxic layers meets oxygen that diffuses down from the water column or is produced by cyanobacteria (CYA). All three of these species utilize some permutation of the Sox gene cluster (Frigaard and Dahl, 2009). Reduced or partially reduced sulfur compounds are oxidized by c type cytochromes, and the S*ox* gene cluster encodes for the ability to oxidize sulfur. This gene has been isolated from a couple different species (Bardischewsky and Friedrich, 2001; Frigaard and Dahl, 2009), and produces a remarkably versatile enzyme that reacts with hydrogen sulfide, sulfur, thiosulfate, and sulfite (Friedrich et al., 2005). From what is known from the biological oxidation of dissolved sulfides, sulfate is the only product leaving the cell; however thiosulfate, tetrathionate, and other polysulfides can potentially be used by the bacteria as electron donors and can be released as intermediate oxidation species in the rare case when bacterial strains have an incomplete *Sox* system (Friedrich et al., 2005).

The rate law for the chemical oxidation of sulfides is first order with respect to both oxygen and sulfide, and the rate of oxidation increases with increasing pH to a maximum rate occurring around pH 8 (Chen and Morris, 1972). The reaction mechanism is complex and poorly understood due to the number of reactions that can occur at circumneutral pH in natural systems and the lack of techniques available to quantify intermediate products. This reaction requires a one electron transfer from the highest occupied molecular orbital (HOMO) of the sulfide (a p-orbital), to the lowest unoccupied molecular orbital (LUMO) of the oxygen (a π^* orbital) (Luther, 1990). The pH effect arises from the energy difference between these two orbitals (Luther, 1990), and the overall reaction product varies as a function of pH (Zhang and Millero, 1993). At pH 4, sulfate was shown to be the major oxidation product, but at circumneutral and higher pH, thiosulfate and sulfite are formed preferentially (Zhang and Millero, 1993; Druschel et al., 2003). Futhermore, polysulfides were not found in experiments performed above pH 7.2 (Chen and Morris, 1971) suggesting that any occurrence of polysulfides in these microbial mats will be biologically mediated. However, any elemental sulfur at circumneutral pH should react with available sulfite to form thiosulfate. Overall, this information suggests that thiosulfate is a unique product of chemical reactions and thus can be used as a measure for chemical oxidation, even though its production may be underestimated due to competition with SOB.

Profiles for oxygen and sulfide had been previously measured using a Clark type microelectrode for oxygen and a sulfide ion selective electrode (Fike et al., 2009). These electrodes are designed to obtain high resolution profiles but are not able to measure any other intermediate sulfur species or metals. Simultaneously, the use of two electrodes may also not resolve the lateral heterogeneities that may be present in these mats. In this study, mercury/gold

(Hg/Au) amalgam voltammetric microelectrodes (Brendel and Luther, 1995) were designed and used to measure oxygen, sulfide, and thiosulfate depth profiles with a single electrode and examine the contribution of the chemical mechanism to sulfide oxidation. The intent of this study was to examine the regions of overlap between these three species, the effects of the diel cycle on the evolution of sulfide and oxygen, and the effects of the spectrum of light on the activity of sulfide oxidizing microorganisms.

Methods

The microbial mats used for this analysis were obtained from the evaporite basins of Exportadora de Sal salt works located in the Guerrero Negro basin, Baja California Sur, Mexico (Figure 6.2). These basins are home to large microbial mat communities that have been sampled extensively, and their bulk microbiological composition as been well characterized (e.g. Spear et al., 2003; Ley et al., 2006). Sodium chloride has historically been obtained through the boiling of brine from springs at inland locals or solar evaporation along sea coasts or in hypersaline inland lakes (Litchfield et al., 1999). Solar salterns are man-made hypersaline environments found in dry subtropical climates in which sea water is evaporated to produce salt. These systems take in sea water which flows in the direction of gravity through a series of progressively more saline ponds (http://www.essa.com.mx/) (Figure 6.2).

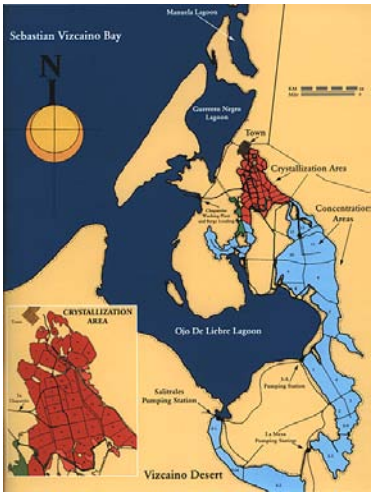

Figure 6.2: A pictorial representation of the evaporation basins at Exportadora de Sal (Baja California, Mexico) (http://www.essa.com.mx/) where sea water from the Ojo de Liebre lagoon flows into the ponds and progressively evaporates depositing different minerals including calcite, gypsum, and halite.

This process permits the sequential precipitation and harvesting of different minerals. These commercial systems are significantly easier to access and study than deep-sea anoxic hypersaline basins, but they still provide excellent comparisons to early earth environments. It was Darwin who first noted that green algae was a living part of natural salt-producing systems. Previously it had been assumed that the solar salterns were sterile (Litchfield et al., 1999), however, around the 1920s, scientists cultured bacteria from brines and solar salterns (Browne, 1922; Clayton and Gibbs, 1927). Since then interest in these halophilic bacteria, their metabolism, community structure, and survival mechanisms has continued.

The mats were sampled from a pool of salinity 85 and sulfate concentration of 50 mM by members of the Ecogenomics Focus Group, a part of the National Aeronautics and Space Administration (NASA) Astrobiology program, and were maintained in roof top greenhouses at the NASA Ames Research Facility, Moffett Field, California (U.S.A.) (Figure 6.3).

Figure 6.3: The greenhouses at the NASA Ames Research Facility. These greenhouses were designed to ensure that the mats are exposed to a full diel cycle and not shaded from the sun. The divided trenches for different mat treatments are highlighted on the right.

Each mat was encased in a rectangular plastic container to maintain shape, and the containers are aligned in trenches and irrigated by constantly flowing artificial marine water to maintain surface oxygenation. An artificial brine solution, containing different concentrations of sulfate 0.2 mM, 1 mM, 5 mM and 80 mM was used as overlying water in each trench. Interestingly, altering the sulfate concentration or the salinity does not have an effect on the percent abundance or functioning of the CYA (Green et al., 2008).

The voltammetric analyses were conducted with a three electrode system including a reference, counter, and working electrode. Due to the compact laminar structure of these mats, new working electrodes were fashioned from PEEK^{TM} (polyethyletherketone) tubing lined with 1 mm glass capillary tubes (Figure 6.4). A 100 μm diameter gold wire was inserted into the capillary and cemented in place with a blend of West System 105 epoxy resin and 206 hardener. This combination allowed for decreased tip size, while improving robustness.

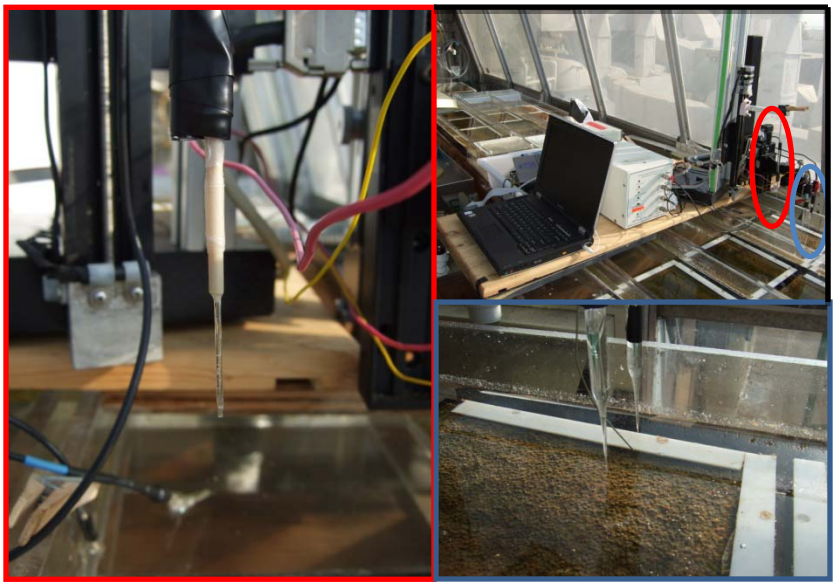

Figure 6.4: The two micromanipulators were arranged side by side over the mats (top right). Outlined in red is an example of the new working electrodes developed for this study and outlined in blue are the traditional oxygen and sulfide electrodes used for profiling.

After construction, the working electrodes were sanded and polished with diamond pastes of decreasing sizes (Chapter 3). The gold wires were plated at -0.1 V for 180 sec in a degassed 0.1 mol L^{-1} $Hg(NO_3)_2H_2O$ in 2% HNO_3 solution and conditioned in 1 mol L^{-1} NaOH for 90 sec to ensure the formation of a strong mercury amalgam with the gold wire. This process increases the stability and durability of the electrodes (Brendel and Luther, 1995). Reference and counter electrodes were constructed as described previously (Chapter 3). The working electrodes were calibrated for oxygen in situ in the overlying water using the temperature and salinity of the overlying water to calculate oxygen saturation (Luther et al., 2008). Electrodes were calibrated for sulfide and thiosulfate using the Pilot Ion Method and manganese as the pilot ion (Brendel and Luther, 1995) (Chapter 2).

To examine the diel biogeochemical cycle of these mats, depth profiles were collected in 6 hour intervals at 12 a.m., 6 a.m., 12 p.m., and 6 p.m on the 0.2 mM, 1 mM, and 80 mM mats. The majority of the profiles were performed live with a 200 μm vertical resolution; however, a preprogrammed sequence was used to collect the the 6 a.m. profiles (Table 6.2).

Table 6.2: The sequence of voltammograms preprogrammed for the 6am profiles.

Part 1:	**Number of Scans**	**Voltammetric Wave Form**	**Conditioning Steps**	
	3	Linear Sweep	-0.1 V, 10 s	
	2	Cathodic Square Wave	-0.1 V, 10 s	Repeated x10
Part 2:				
	2	Anodic Square Wave	-0.9 V, 10 s	
	3	Cathodic Square Wave	-0.9 V, 10 s -0.1 V, 10 s	Repeated x20

The electrodes were visually positioned just above the mat interface so that 10 depth increments were sufficient enough to exceed the depth of oxygen penetration below the surface. All scans were performed on the 1 μA (+/- 2 μA) sensitivity with a scan rate of 200mV/s, and a depth increment of 200 μm.

In addition to monitoring the diel variability, the 0.2 mM, 1 mM, and 80 mM mats were removed from the greenhouse (one per day) and relocated to the laboratory to examine the effects of infrared light on PSB. The mats were placed in a dark chamber with a focused lamp

that created a 2 inch diameter patch of light and allowed to reequilibrate for 3 hours before a depth profile was measured voltammetrically (Figure 6.5).

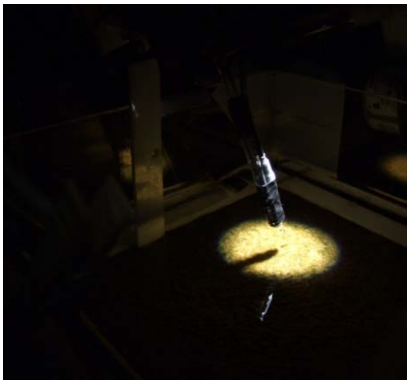

Figure 6.5: Set up of the modified light incubation experiment. The mats were relocated to a dark chamber equipped with a micromanipulator and a pump (not shown) to circulate the overlying water. A small hole in the top of the chamber was covered with special lenses to enhance and remove infrared light from the source beam.

Light was focused through two different filters onto a small portion of the mat, and the intensity was adjusted to mimic the noontime greenhouse conditions (1600 $\mu E\ s^{-1}\ m^{-2}$). The first filter removed all wavelengths greater than 700 nm (infrared light) and the second removed all wavelengths less than 700 nm (near UV portion). One profile was taken for each filter and the mats were allowed to requilibrate for 3 hours after the filters were changed. The chamber was equipped with a pump that gently circulated the overlying water to ensure it remained oxygenated during these experiments.

A transient one-dimensional reactive transport model (Equation 2) was used to determine net reaction rates as a function of depth in the mats (Berg et al., 1998; Beazley et al., 2010):

$$\phi \frac{dC}{dt} = D \frac{\partial}{\partial x}(\phi C) - v \frac{\partial(\phi C)}{\partial x} + \phi R \qquad (2)$$

where C is the concentration of an analyte, D the diffusion coefficient, v the advection, f the porosity, and R the net rate of reaction for that particular species. For these microbial mats, advection was assumed to be negligible and diffusion to be molecular. Diffusion coefficient for each species was calculated according to salinity and temperature (Boudreau, 1997). The porosity was assumed to decline exponentially with depth (Boudreau, 1997). Net production or consumption rates were calculated as zero-order with respect to the species of interest and determined for depth intervals which displayed changes in concentrations. The boundary conditions included a Dirichlet condition (fixed concentration) at the top of each depth interval and a Neumann condition (flux) at the bottom:

$$C(x,t_0) = C_0 \qquad C(x_0,t) = C_0 \qquad \frac{\partial}{\partial x} C(L,t) = 0 \tag{3}$$

where $t_0 \geq 0$ is the initial time selected to determine rates during a particular time period, C_0 is the initial concentration, and L the maximum depth of the sediment layer of interest. This equation was solved using a Crank-Nicholson scheme, and the steady-state solution used to optimize net reaction rates for each sediment layer. The optimization procedure, written in Matlab™, minimizes the difference between the data and the numerical solution of the differential equation using a least-square procedure.

Results

Cyanobacteria produce oxygen only during daylight hours. During this time period, the mat surface was predominantly brown (Figure 6.7) because the motile CYA migrate below the mat surface to avoid damage induced by UV light (Stal, 1995). Most types of GNS are known to be resistant to damage from ultra violet light and therefore these species do not migrate (Donkor

and Hader, 1991). At dusk, the mats turn bright green as the CYA return to the surface to utilize the last rays of light and await the sunrise. The zone of maximum oxygen production varied throughout the diel cycle, but was located at the greatest depth during the middle of the day which provides chemical evidence of the CYA migration (Figure 6.6a).

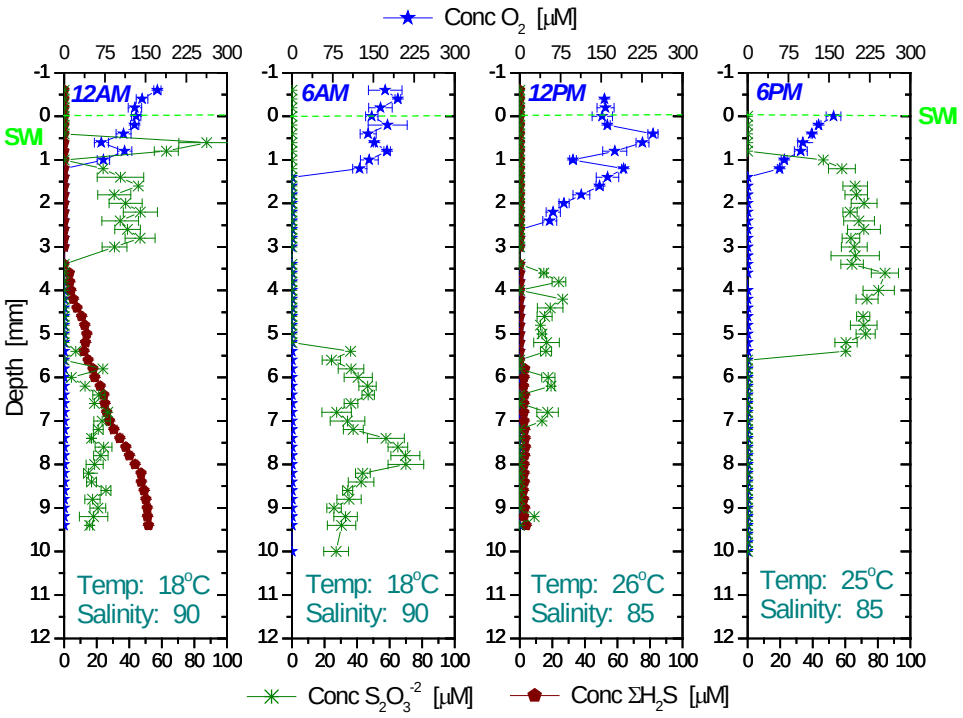

Figure 6.6a: The full diel cycle measured with the Hg/Au voltammetric microelectrodes for the 0.2 mM SO_4^{-2} treatment. The 6 a.m. profile was not performed live and instead generated using the sequence in Table 6.3.

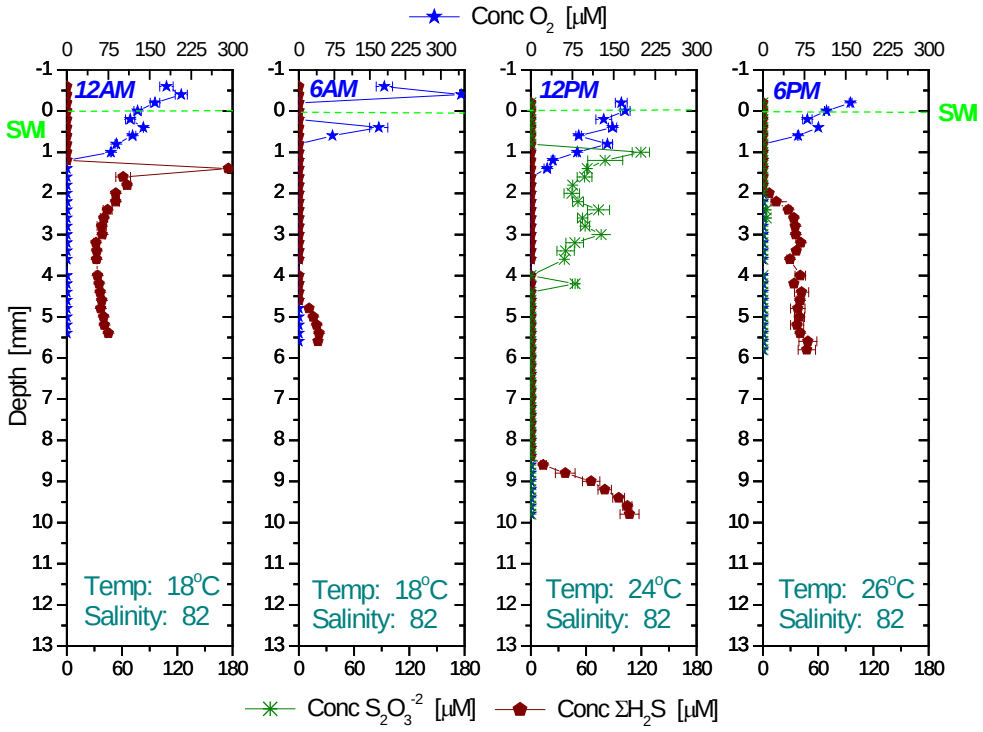

Figure 6.6b: The full diel cycle measured with the Hg/Au voltammetric microelectrodes for the 1 mM SO_4^{-2} treatment. The 6 a.m. profile was not performed live and instead generated using the sequence in Table 6.3. The maximum depth for these profiles was 6 mm; however, measurements for the 12 PM profiles were continuted until sulfide was detected.

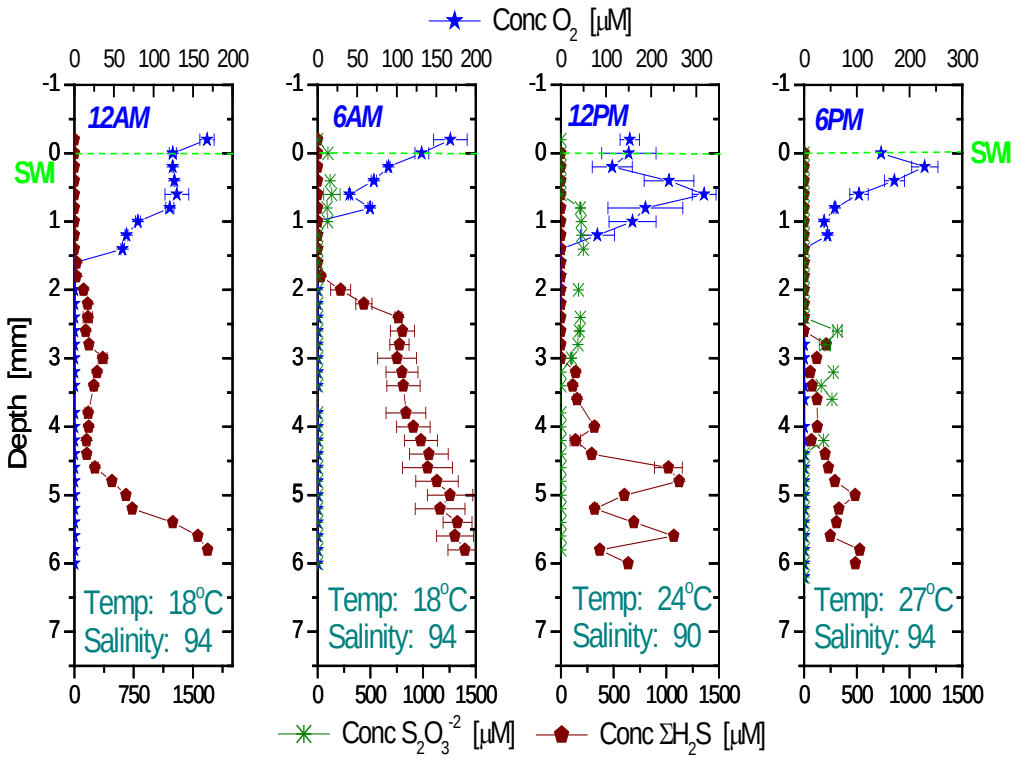

Figure 6.6c: The full diel cycle measured with the Hg/Au voltammetric microelectrodes for the 80 mM SO_4^{-2} treatment. The 6 a.m. profile was not performed live and instead generated using the sequence in Table 6.3.

The onset of dissolved sulfide production varied during the diel cycle and between treatments, but dissolved sulfides were generally never detected above 2 mm below the mat-water interface and did not overlap with dissolved oxygen in any of the treatments (Figure 6.6). For all treatments, the highest concentrations of sulfides were detected during the two dark profiles, and the highest concentrations approached 50 µM in both the 0.2 mM and the 1 mM SO_4^{-2} mats and 2 mM in the 80 mM SO_4^{-2} mats. In both the 1 mM and the 80 mM SO_4^{-2} treatments, thiosulfate concentrations generally increased to a maximum concentration of 120 µM in the 1 mM treatment and 250 µM in the 80 mM treatment.between 6 AM and 12 PM profiles, coinciding with the time period in which sulfide concentrations declined. In turn, thiosulfate production

was observed during each time period in the the 0.2 mM SO_4^{-2} mats but was highest at 6 PM (80 μM) and lowest at 12 PM (< 20 μM). Finally, the zone of thiosulfate production appeared to migrate toward the mat surface as the day progressed in the 0.2 mM and 1 mM SO_4^{-2} treatment, but progressively migrated deeper into the mat as the sulfide concentrations declined throughout the day in the 80 mM SO_4^{-2} treatment.

The light for the UV-removed and infrared-removed studies was focused over a very small area of the mat (Figure 6.5). The same color change that was detected in the greenhouse during sunset and sunrise was observed when the mats were relocated to the dark box in the laboratory. The small area on which the light was focused returned to a light brown color while the rest of the mat that was not in the direct light beam turned deep green (Figure 6.5). Oxygen penetration depths increased in all three treatments (Figure 6.7) compared to the diel cycle study (Figure 6.6 a – c) when exposed to the focused beam of light.

.

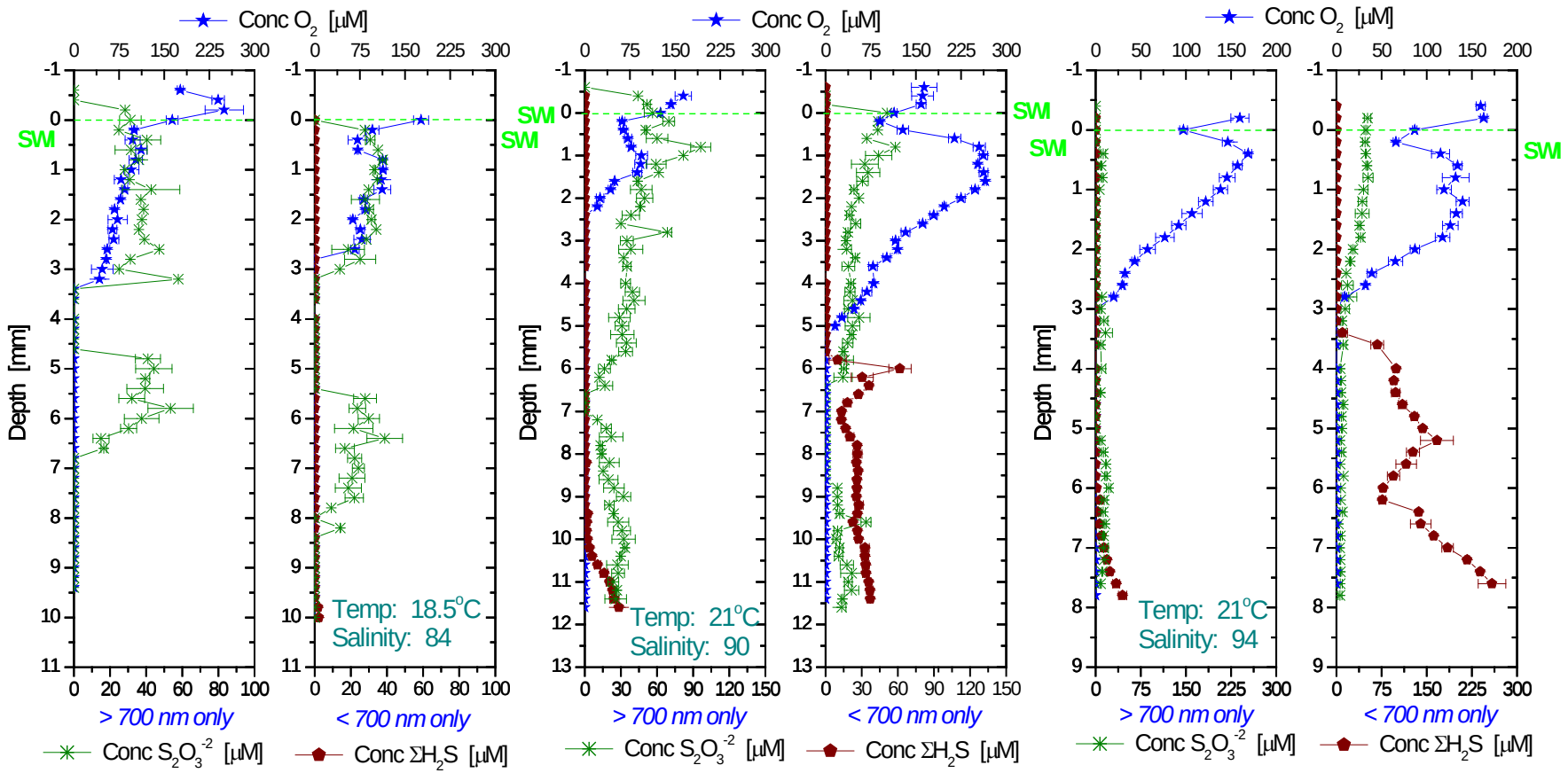

Figure 6.7: Profiles obtained after equilibration and alteration of the incident infrared light measured with the Hg/Au voltammetric microelectrodes for the 0.2 mM SO_4^{-2} (left), the 1 mM SO_4^{-2} (middle), and 80 mM SO_4^{-2} (right) treatments. The first filter that was used for each experiment removed the infrared wavelengths. Secondly the UV portion of the spectrum was removed, and the mats were allowed to requilibrate for 3 hours before the second profile was performed.

Thiosulfate production was not affected by the change in available wavelengths of light in the 0.2 mM SO_4^{-2} treatment; however, small concentrations of sulfide were detected at depth when the infrared wavelengths were filtered out. Akin to the 0.2 mM SO_4^{-2} treatment, thiosulfate production did not appear to be affected by the change in available wavelengths of light in the 1 mM SO_4^{-2} treatment; however, substantially greater amounts of sulfides were detected at a more shallow depth when the infrared wavelengths were filtered out. The 80 mM SO_4^{-2} exhibited the same changes in sulfide concentrations as the other two treatments; however, the thiosulfate concentrations behaved quite differently. Thiosulfate was detected at depth with both the removed near UV or infrared portion of the light spectrum, but the concentrations near the mat interface increased substantially when the infrared wavelengths were removed.

Discussion

In this study, the speciation of sulfur species in microbial mats was examined during a diel cycle and when the mats were exposed to light of different wavelengths to determine whether sulfide oxidation in these mats is chemical or biological. For this purpose, new voltammetric microelectrodes were constructed from glass capillaries and deployed with a micromanipulator to obtain depth profiles with a high spatial resolution. These measurements verified the spatial distribution of dissolved oxygen and sulfides previously detected using amperometric and potentiometric microsensors and revealed for the first time that thiosulfate is produced in microbial mats in a concentration range that appears to be proportional to the sulfate concentrations.

Cyanobacteria migrate away from the mat surface during peak daylight hours to avoid photo inhibition and damage from ultraviolet light (Stal, 1995), this behavior leads to a peak in oxygen production below the mat surface that is deepest at the noon hour, that was observed in all three treatments. During the UV-removed and infrared-removed experiments, the intensity of the light was adjusted to mimic the noontime conditions in the greenhouse, however the depth of CYA migration was considerably larger than observed in the greenhouse, suggesting that the light may have been more intense than previously thought. Cyanobacteria utilize photosystem I and II and therefore prefer light in the 680 – 700 nm range. These wavelengths were not altered during this experiment and no change in oxygen concentration was observed when the lenses were changed (Figure 6.7).

Sulfate reducing bacteria are not dependent on light and should therefore respire continuously during the diel cycle. In addition, these bacteria have the capability to reduce partially oxidized sulfur compounds and potentially produce thiosulfate (Table 6.3) if a powerful reductant such as H_2 is limiting (Cypionka, 1994).

Table 6.3: Sulfate reducing bacteria utilize organic carbon exudates from CYA to completely reduce sulfate and other partially oxidized sulfur compounds to sulfide (Cypionka, 1994).

Reduction of Sulfur Compounds:
$2SO_4^{-2} + 8H_2 + 3H^+ \rightarrow H_2S + HS^- + 8H_2O$
$S_2O_3^{-2} + 4H_2 + H^+ \rightarrow H_2S + HS^- + 3H_2O$
$2S + 2H_2 \rightarrow H_2S + HS^- + H^+$
Incomplete Sulfate Reduction:
$2SO_4^{-2} + 4H_2 + 2H^+ \rightarrow S_2O_3^{-2} + 5H_2O$

Thiosulfate and trithionate production during the in vitro reduction of sulfite by the sulfite reductase has suggested that these products are intermediates in the reduction of sulfate to sulfides, possibly mediated by thiosulfate and trithionate reductases (Kobayashi et al., 1974). More recent in vitro work with the sulfite reductase of a desulfovibrio strain, however, has shown that the production of trithionate and thiosulfate is relatively small (Steuber et al., 1994) and to date enzymes responsible for the production of thiosulfate and trithionate have yet to be isolated. Thus, whether the sulfite reduction pathway is a direct six-electron reduction of bisulfite or whether it involves trithionate and thiosulfate as

intermediates remains uncertain (Hansen, 1994). As sulfite reacts readily with elemental sulfur to produce thiosulfate (Zhang and Millero, 1993), it is possible that a chemical reaction was responsible for the production of thiosulfate and trithionate in these in vitro

experiments. Additionally, thiosulfate and elemental sulfur reduction were not expected to occur except maybe in the low sulfate treatment as sulfate was available in relative excess in the other mats, therefore any thiosulfate produced chemically should not be consumed. Although SRB do not require light, a clear diel cycle was evident from the suite of profiles taken in the greenhouse with the highest sulfide concentrations being observed during the night profiles (Figure 6.6). Sulfide concentrations also increased when the infrared spectrum was removed in the laboratory experiments (Figure 6.7). Thiosulfate was detected concurrently with sulfide suggesting that thiosulfate production was mainly due to abiotic oxidation of dissolved sulfides. Simultaneously, the sulfide produced by SRB is subsequently oxidized by either CSB near the oxygen gradient or PSB if light penetration is sufficient (Table 6.1).

A transient one-dimensional reactive transport model (Equation 2) was used to determine net reaction rates as a function of depth in the mats (Berg et al., 1998; Beazley et al., 2010) to examine how sulfate reduction, sulfide oxidation, and thiosulfate production interact in these microbial mats. Net rates were calculated in separate depth increments (Figure 6.8) and summed as a function of depth to provide an overall net rate of production (positive rates) or consumption (negative rates) for all of the diel profiles (Table 6.4).

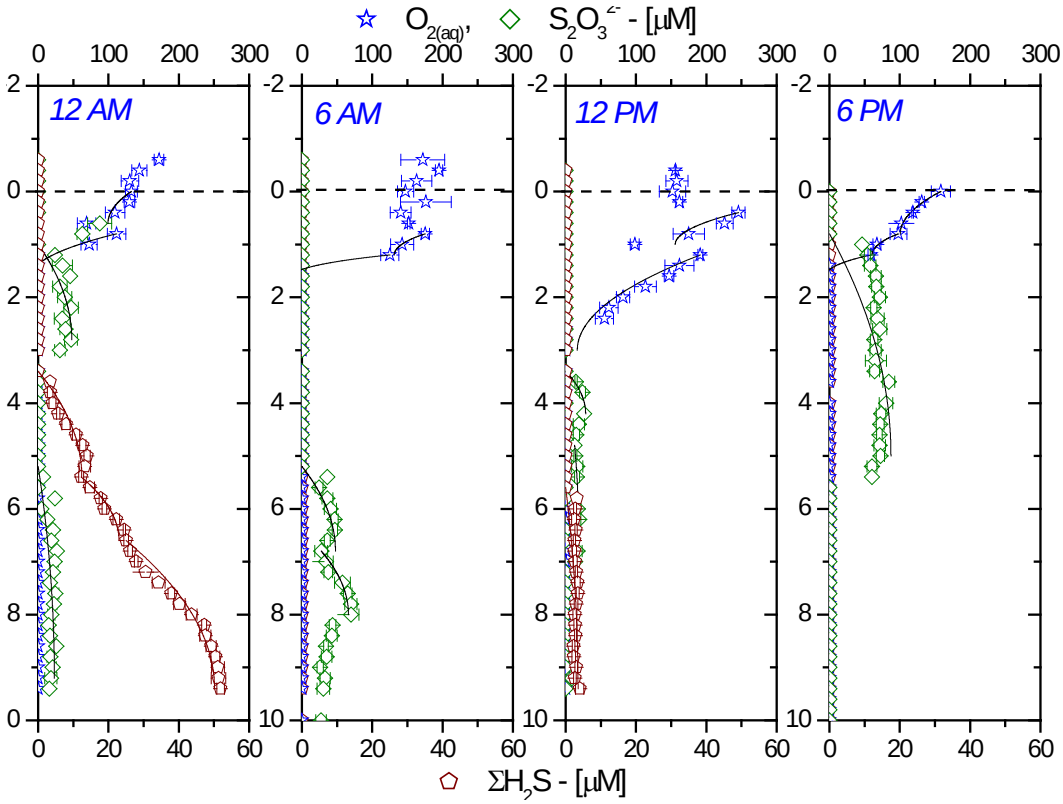

Figure 6.8a: The transient one-dimensional reactive transport model (Equation 2) was applied to the 0.2 mM SO_4^{-2} suite of profiles to determine net reaction rates as a function of depth in the mats.

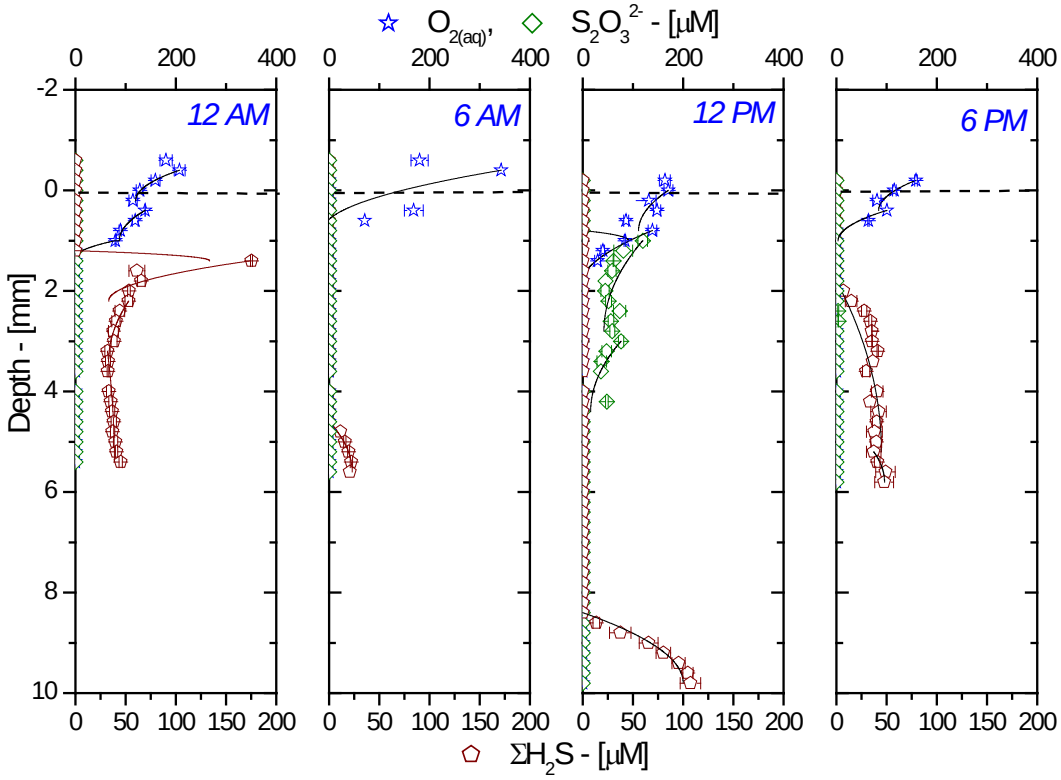

Figure 6.8b: The transient one-dimensional reactive transport model (Equation 2) was applied to the 1 mM SO_4^{-2} suite of profiles to determine net reaction rates as a function of depth in the mats.

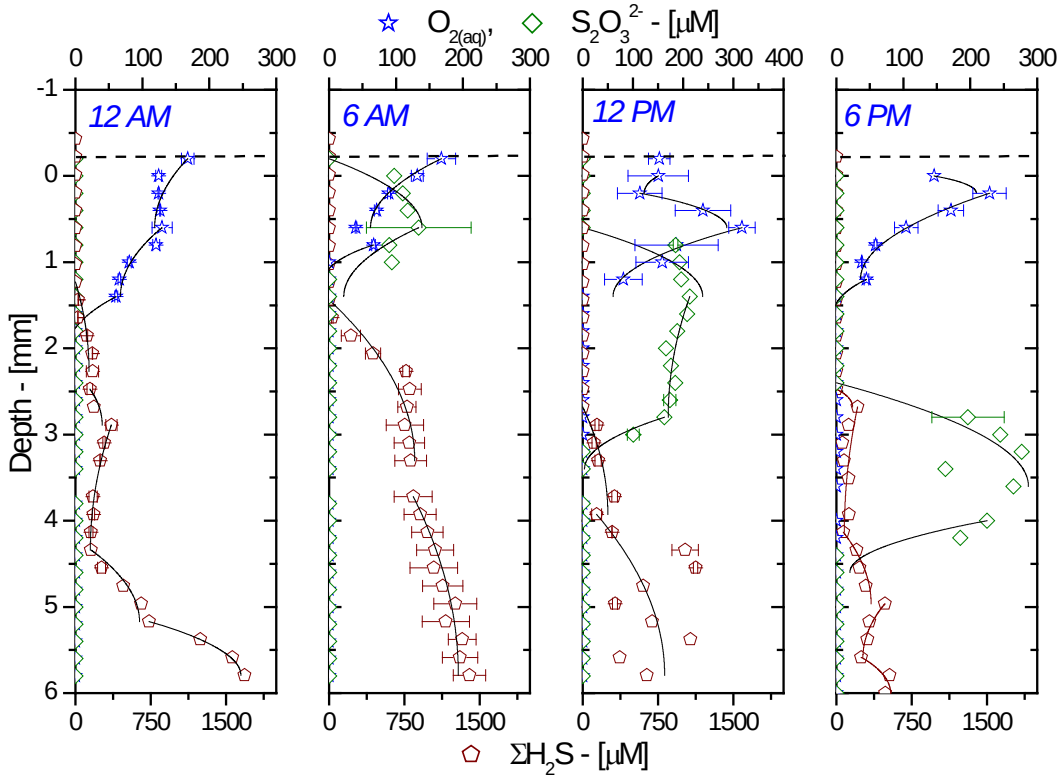

Figure 6.8c: The transient one-dimensional reactive transport model (Equation 2) was applied to the 80 mM SO_4^{-2} suite of profiles to determine net reaction rates as a function of depth in the mats.

Table 6.4: A transient one-dimensional reactive transport model was used to determine net reaction rates as a function of depth in each of the mat treatments over the diel cycle. These rates were then summed to provide an integrated net rate of production (positive sign) or consumption (negative sign).

Treatment	Time in Diel Cycle	Oxygen (mmol hr^{-1})	Thiosulfate (mmol hr^{-1})	Sulfide (mmol hr^{-1})
80 mM	12:00 AM	-4.07	0	45.27
	6:00 AM	-6.79	0.29	4.15
	12:00 PM	0.10	-0.63	4.23
	6:00 PM	11.15	-2.57	60.71
1 mM	12:00 AM	-10.19	0	33.20
	6:00 AM	-2.67	0	0.25
	12:00 PM	-2.13	15.59	0.56
	6:00 PM	-5.17	0	0.37
0.2 mM	12:00 AM	-3.05	0.11	0.15
	6:00 AM	-12.42	0.32	0
	12:00 PM	-3.29	0.32	0.00
	6:00 PM	-7.99	0.03	0

As CYA are active during the day, oxygen production rates should be highest during the 12 PM and 6 PM time points, and in fact are for the 80 mM treatment (Table 6.4). Unexpectedly, rates indicate net consumption for all of the other profiles, suggesting that it is consumed in excess by aerobes and CSB, as well as during abiotic sulfide oxidation. In the absence of oxygen, sulfide is oxidized exclusively by PSB provided that light is available (Visscher et al., 1992). Net rates of sulfide production should therefore be

highest for the 12 AM and 6 AM profiles because PSB are not active during that time period to reoxidize sulfide produced in the lower mat layers. Indeed, with the exception of the 6 PM profile of the 80 mM treatment, sulfide production rates were the highest in the 12 AM profiles compared to other times in the diel cycle for each treatment. The anomaly occurred near dusk and could have been due to light conditions that inhibited PSB earlier than expected in the evening. Thiosulfate was produced in excess in the low sulfate treatment, was barely produced in the 1 mM treatment, and mostly consumed in the high sulfate treatment (Table 6.4). This behavior was unexpected as more thiosulfate should be produced when the activity of SRB produce sulfide in excess (i.e. at high sulfate concentrations) if thiosulfate production is a by-product of sulfate reduction. These findings suggest that thiosulfate was likely produced during reoxidation of sulfide.

Colorless sulfur bacteria (e.g. *Thiobacillus thioparus)* utilize oxygen to oxidize sulfide and other reduced sulfur compounds without the need of light as a source of energy (Pierson et al., 1987). In fact, rates of sulfate reduction during daylight hours are frequently underestimated due to rapid reoxidation of sulfide to sulfate by *Thiobacillus* if oxygen is not limiting (Visscher et al., 1991). Purple sulfur bacteria also oxidize sulfide (Table 6.1); however, unlike CSB they require light as a metabolic energy source. Therefore these bacteria provide an additional mechanism that enhances the rates of sulfide oxidation during the day only. The most common PSB and anoxygenic phototroph found in microbial mats is *Thiocapsa roseopersicina* (Stal et al., 1985; Pierson et al., 1987). Like the cyanobacteria, the PSB tend to be motile to attain optimal light conditions for photosynthesis. Certain strains of *Thiocapsa* are non-motile (Van Gemerden et al., 1989) and are able to grow chemolithotrophically in the presence of

oxygen but at significantly lower yields compared to phototrophs (de Wit and Van Gemerden, 1987). In the presence of dissolved oxygen, CSB have a much higher affinity for sulfide and may potentially out compete PSB (Visscher et al., 1992). The switch from high net thiosulfate consumption rates during the day to high net production rates at night in the 80 mM treatment suggests that CSB are stimulated during the day by the production of dissolved oxygen by CYA or that PSB are the main thiosulfate-consuming organisms in these mats. In turn, the increase in net thiosulfate production rates in the low treatments regardless of the time of the day suggests that sulfide-oxidizing bacteria are active when sulfate reduction is intense (i.e. at high sulfate concentrations).

The laboratory experiments were specifically designed to isolate the impact of PSB activity on sulfide oxidation in these mats. When the filter that removed the UV portion of the spectrum was used, virtually no sulfide was detected except at extreme depth in any of the three treatments (i.e. 8 mm in the 80 mM SO_4^{-2}, 10 mm in the 1 mM SO_4^{-2}, and never detected in the 0.2 mM SO_4^{-2} treatment) compared to the greenhouse mats where sulfide was detected around 3 mm depth. In contrast, sulfide concentrations at depth increased substantially in the laboratory experiments that removed the IR light (Figure 6.7). Thiosulfate concentrations however, were not affected significantly in any of the treatments. This suggests that while the activity of PSB is responsible for the oxidation of sulfide deep in the mats, thiosulfate is not produced as a byproduct of the bacterial sulfide oxidation by PSB. This concurs with the findings that thiosulfate, tetrathionate, and other polysulfides can be released as intermediate oxidation species only in bacterial strains that have an incomplete *Sox* system (Friedrich et al., 2005). As sulfate reduction was likely not the source of thiosulfate, and as the depth of oxygen

penetration was not deeper than 3-4 mm, these findings suggest that another anaerobic process is able to produce thiosulfate.

The one-dimensional reactive transport model (Equation 2; Berg et al., 1998; Beazley et al., 2010) was also used with the profiles in Figure 6.7 to determine net reaction rates as a function of depth in the mats. Net rates were calculated in separate depth increments (Figure 6.9) and integrated as a function of depth to provide an overall net rate of production (positive rates) or consumption (negative rates) for all of the light experiment profiles (Table 6.5).

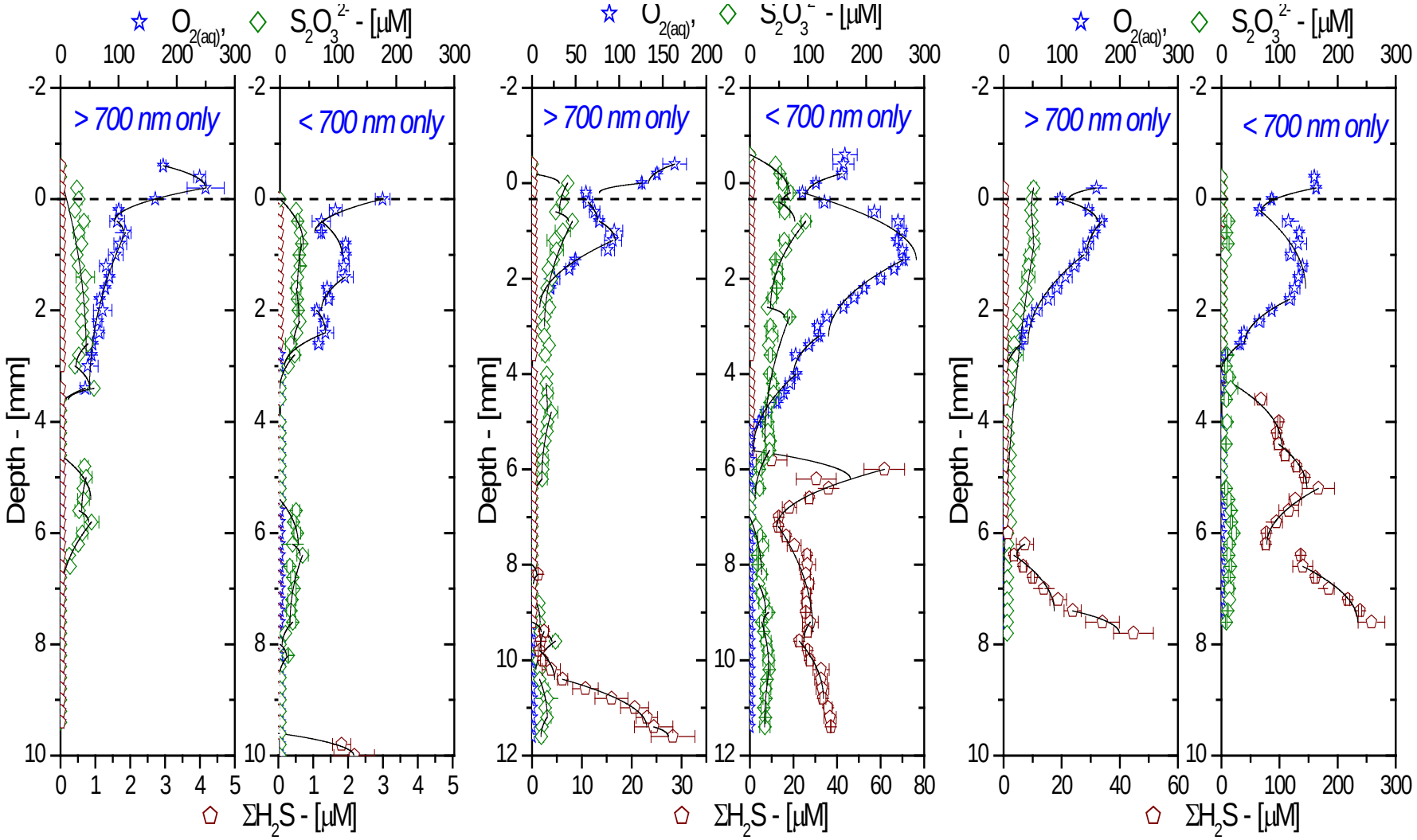

Figure 6.9: The transient one-dimensional reactive transport model (Equation 2) was applied to the profiles generated from the infrared light experiments to determine net reaction rates as a function of depth in the mats for each of the sulfate treatments 0.2 mM (left); 1 mM (middle); and 80 mM (right).

Table 6.5: A transient one-dimensional reactive transport model was used to determine net reaction rates as a function of depth for the profiles conducted during the infrared light experiments. These rates were then summed to provide an integrated net rate of production (positive sign) or consumption (negative sign) of each species.

Treatment	Light Conditions	Oxygen (mmol hr^{-1})	Thiosulfate (mmol hr^{-1})	Sulfide (mmol hr^{-1})
80 mM	> 700 nm	-10.22	-0.06	0.50
	< 700 nm	-8.33	0.64	6.43
1 mM	> 700 nm	-13.40	3.93	1.50
	< 700 nm	-4.62	2.22	1.06
0.2 mM	> 700 nm	-0.10	-4.41	0
	< 700 nm	-4.78	2.46	0.15

The high net rates of consumption of dissolved oxygen in the 1 mM and 80 mM sulfate treatments suggest that the enhanced availability of oxygen as a result of changes in the incident light spectrum may have triggered an increase in both the biological and abiotic oxidation of sulfide to thiosulfate in the first 5 mm of the mat. For all light conditions, except the infrared enhanced 0.2 mM treatment (> 700 nm), thiosulfate was produced near the top of the mat which suggests that chemical oxidation outcompeted microbial sulfide oxidation by CSB, as these organisms should not have been affected by the change in the light spectrum exposed to the mat. When the infrared wavelengths are included (> 700 nm), sulfide consumption should be enhanced compared to the treatments without the infrared portion of the spectrum as PSB are not able to oxidize sulfide without light. Indeed, net rates calculated for the 80 mM and 0.2 mM treatments and the shape of the profile in Figure 6.9 for the 1 mM mat all indicate that sulfide consumption was lestened when the IR portion of the spectrum was removed. In the deep mat (> 5 mm), however, chemical oxidation by dissolved oxygen cannot explain the formation of thiosulfate, as the oxygen penetration depth does probably not exceed a few

millimeters. Unless sulfate reducing bacteria are responsible for the production of thiosulfate, these data suggest that another source of thiosulfate has to be accounted for in the deep mats. Many SOB have the unique ability to excrete internal or external elemental sulfur in globules for future use as an energy reserve (Wirsen et al., 2002). If sulfite were produced as an intermediate in either sulfide oxidation or sulfate reduction, it could react with the elemental sulfur globules and abiotically produce thiosulfate under aerobic or anaerobic conditions. Following these experiments the mats were going to be sectioned and isotopic analysis performed on the pore waters to evaluate the sulfur isotopic content. This analysis may aid in elucidating the source of the thiosulfate measured at depth in these experiments.

Conclusion

The purpose of this study was to utilize Hg/Au microelectrodes to examine the regions of overlap between oxygen, thiosulfate, and sulfide in hypersaline microbial mats over a diel cycle. In addition, the role of PSB in the oxidation of sulfide was examined by removing the UV and IR portions of the incident light. The new single electrode system reproduced the oxygen peak shifts caused by the migration of CYA that were previously measured with the Clark type microelectrodes. Additionally, the sulfide profiles generated with the new voltammetric electrodes mimicked the profiles previously generated using an ion selective electrode. More importantly, Hg/Au microelectrodes revealed for the first time the production of thiosulfate in these microbial mats. Overall, the results of this study demonstrate that thiosulfate is mainly produced by the abiotic

oxidation of sulfide or potentially elemental sulfur near the oxic-anoxic transition in direct competition with the activity of CSB. In addition, depth profiles obtained during a diel cycle in mats exposed to different concentrations of sulfate reveal that biogenic sulfide oxidation is stimulated by the activity of SRB. Experiments that altered the incident light spectrum that the mats were exposed to indicated that PSB oxidize sulfides in the deep mats. In turn, thiosulfate production was not affected during these experiments, and the source of thiosulfate in the deep mats is hypothesized to result from the abiotic reaction of sulfite, produced as an intermediate in sulfate reduction or sulfide oxidation, and elemental sulfur, stored by SOB for use as source of energy. .

CONCLUSIONS

A number of conclusions can be drawn as a result of the research contained within this dissertation. A new autonomous lander was developed that is equipped with a potentiostat and a benthic chamber to voltammetrically monitor the flux of oxygen and other redox species across the SWI and a micromanipulator to obtain concurrent depth profiles of the main redox species in sediment pore waters. The use of benthic landers to examine sediment fluxes is not a novel concept, however, the benthic lander developed for this research is the first to combine autonomous measurement capabilities with voltammetric analyses. Furthermore, the benthic chamber was equipped with a tracer injection system to parameterize the advective transport and non-local exchange processes impingent upon these sediments. When advective transport is accounted for, in situ profiles can be used to more accurately determine carbon remineralization rates in riverine sediments such as the Satilla River (GA). Furthermore, the accumulation of reduced species evident from the in situ profiles, indicates that dissolved oxygen does not function as the ultimate oxidant in these systems. Overall, the results of this study illustrate that carbon remineralization rates are underestimated if advective transport is not considered or if oxygen is assumed to function as the ultimate oxidant.

A seasonsal study of biogeochemical processes conducted for three years in the Satilla River with this benthic lander demonstrated that the lack of rainfall, which lead to a severe drought in the southeastern United States during 2006 and 2007, substantially decreased river discharge and drastically impacted the sediment biogeochemistry of the Satilla River. The decreased river discharge steepened and relocated the salinity gradient, probably altered the delivery of mineral constituents used for microbial respiration to the

sediment, and allowed iron reduction to outcompete sulfate reduction as the dominant respiratory process active in these sediments even when the salinity of the overlying waters approached 30. Dissolved inorganic carbon and diffusive oxygen uptake fluxes measured from pore water profiles reveal that the total carbon flux from the Satilla River to the continental shelf is about 10 times larger than previously measured in other estuaries, when normalized to their discharge, and translates into 0.01% of the worldwide riverine carbon flux to the surface ocean. Simultaneously, flux calculations demonstrate that oxygen alone does not provide an adequate proxy for carbon remineralization in riverine sediments, as about 20% of carbon remineralization is not accounted for by oxygen consumption. Finally, these findings imply that an increase in the frequency of drought conditions as a result of global climate change in northern temperate regions may enhance the resilience of iron-reducing bacteria in river-fed estuarine sediments for extended periods of time.

The work performed in the Satilla River reinforces the need for long term data monitoring to adequately assess ecosystem functioning. The in situ electrochemical analyzer deployed at the Saltmarsh Ecosystem Research Facility on Skidaway Island (GA) was designed to provide scientists with a method for generating high temporal resolution data sets at off-site locals. The system requires physical improvements, but the method proved robust enough to acquire long term data sets, which adds a new tool to examine the dynamics of biogeochemical processes. The preliminary data garnered from this instrumentation illustrates the complex webs of interactions taking place in these environments. Based on the combination of water level data and in situ voltammetric pore water measurements, it can be concluded that the physical forcings, including

hydrodynamic pressure gradients and tidal fluctuations, predominantly control the biogeochemistry of salt marsh sediments. Chemical reactions, including burial and dissolution, and biological influences, including bioturbation, irrigation, and microbial respiration, also impact carbon cycling but these data indicate that hydrological processes should be considered even in fine grained sediments. The data from this study and the new method developed herein may be utilized in future research studies in other locations to improve current mathematical models, and work towards quantifying total carbon cycling for estuaries and salt marshes for incorporation into the global carbon budget.

Finally, a collaboration with scientists at the NASA Ames Research Facility was initiated to study the interplay between the chemical and biological sulfide oxidation in microbial mats from the Guerrero Negro Basin in Baja California (Mexico). This study utilized newly developed Hg/Au microelectrodes to examine the regions of overlap between oxygen, thiosulfate, sulfide in hypersaline microbial mats over a diel cycle and when the wavelengths of the incident light were altered. These measurements revealed for the first time the production of thiosulfate in these microbial mats and demonstrated that thiosulfate is mainly produced by the abiotic oxidation of sulfides near the oxic-anoxic transition, in direct competition with the activity of colorless sulfur bacteria. In addition, these measurements revealed that colorless sulfur bacteria in the oxic-anoxic transition or purple sulfur bacteria in the deep mats are stimulated by the activity of SRB. It was hypothesized that the source of thiosulfate in the deep mats was due to the chemical reaction of sulfite, produced as an intermediate in sulfate reduction or sulfide oxidation, and elemental sulfur, stored by SOB for use as a source of energy.

APPENDIX

Reactive Transport Model for Iodide Calculations

The Matlab™ code for the one dimensional reactive transport model used to model the removal of the conservative iodide tracer from the benthic chamber in Chapter 3. The main routine is Iflux_alphavD.m and Traceroptim_alphavD.m is the subroutine.

```
% This program uses iodide as tracer to calculate the advection, diffusion, and non-local
% exchange across the sediment-water interface using a central finite difference in space
% and different schemes in time (explicit if e=0, implicit id e=1 and Crank-Nicholson if
% e=0.5). The governing equation is that of Rao and Jahnke (2004), except it contains
% advection, diffusion, and non-local irrigation:
%   fi dC/dt = D d/dx(fi/et^2 dC/dx) - v d(fi C)/dx+ a (C0- fi C) where et^2 = fi^(1-m)
 % and m = 3 in fine grain sediments
%   fi dC/dt = D d/dx(fi^3 dC/dx) + a fi (C0-C)
% It assumes a exponential decrease of porosity with depth as in Boudreau (1998):
%   fi(x) = fiinf + (fi0 - fiinf) exp(-gamma x) where gamma is a coefficient
clear
global x dx t dt e i fi dfi CIexp CI0 bd
tic
%
% define the different parameters
%
P = 2;  % Peclet Number (Peclet should be < 2 for Crank-Nicholson to avoid instabilities)
C = 1.0;          % Courant Number
L=20;             % length of the domain - [cm]
fi0 = 0.88;       % Porosity at the surface
fiinf = 0.7;      % Porosity at the bottom of the domain
gamma = 0.1;  % Porosity decay constant
v = 1e-2;         % Advection - [cm/s]
D = 3e-4;         % Diffusion coefficient - [cm^2/s]
alpha=0.001;   % Irrigation constant - [1/s]
bd = 5;           % Depth of maximum biorrigation - [cm]
e=0.5;            % timde discretisation scheme (0:explicit,1:implicit, 0.5:Crank-Nicolson)
V = 18;           % Volume of the Chamber for Iodide injection - [liter]
SA = 15^2*pi; % Surface area of the benthic chamber - [cm^2]
%
% Load the data
%
load SAT3_IMay07.txt -ascii
texp = SAT3_IMay07(4:length(SAT3_IMay07),1)-SAT3_IMay07(4,1);
```

```
                % Correct time to t0 as 0 hours
tmax=texp(length(texp));              % simulation time - [hours]
Cexp = SAT3_IMay07(4:length(SAT3_IMay07),2)*1e-6;
% Calculated Parameters
if v==0
   dx = L/100;
   dt = (tmax*3600)/100;
else
   dx=abs(P*D/v);        % spatial node - [cm]
   dt=abs(C*dx/v);       % time space - [s]
end
x=(0:dx:L)';             % length of the domain - [cm]
i=length(x);             % size of the matrix
fi = fiinf + (fi0-fiinf)*exp(-gamma*x);
                % Porosity change with depth according to Boundreau (1998) p. 223
dfi = -gamma*(fi0-fiinf)*exp(-gamma*x);
                % First derivative of porosity m=D/(dx^2);
%
% Determine the parameters and write them (diagonal terms) into the matrices M at time
% n+1 (Mn) and time n (Mo) => case for dissolved oxygen
%
t = [0:dt:tmax*3600]';      % Time vector - [sec]
disp('Length of distance and time vectors are')
disp([i length(t)])
%
% Experimental concentration is extrapolated to time vector and corrected for
% concentration at steady-state. If C @ S-S = 0, use short version of CIexp. If C @ S-S
% > 0, use long version.
%
CIexp = interp1(texp*3600,Cexp-mean(Cexp(length(Cexp)-8:length(Cexp))),t);
                % Concentration calculated from the original injection
                %CIexp = interp1(texp*3600,Cexp,t);
                % Concentration calculated from the original injection
                % Standard deviation of CIexp is calculated
sdCIexp = interp1(texp*3600,SAT3_IMay07(4:length(SAT3_IMay07),3)*1e-6,t);
                % knowning the volume of the chamber and the first data point
CI0 = [CIexp(1);zeros(i-1,1)];     % Initial profile of iodide at time zero
%
% Optimize the diffusion coefficient, the alpha coefficient, and the advection to match
% the iodide data using a least square non linear method to match the experimental data
%
                % LB = [0 0]; UB = [1e-3 0.001];
                % X0 = [v alpha];
                % Estimate of the maximum volume of benthic chamber
LB = [-0.01 0 0]; UB = [0.01 0.001 1e-3];
X0 = [v alpha D];   % Estimate of the maximum volume of benthic chamber
```

```
                %LB=0; UB=0.001;
                %X0=alpha;
                %X = lsqnonlin('traceroptim_alphavD',X0)
                % Optimized chamber volume - [L]
                %options = optimset('Largescale','off');
[X,RESNORM,RESIDUAL,EXITFLAG,OUTPUT,LAMBDA] =
lsqnonlin('traceroptim_alphavD',X0,LB,UB)
                % Optimized chamber volume - [L]
                % X= [1.0000000e-002;
                %   4.2907896e-003;
                %   3.0000000e-004];
v = X(1);
alpha = X(2);
D = X(3);
%
% Calculation of Peclet and Courant Numbers
%
P = v*dx/D      % Peclet Number
C = v*dt/dx     % Courant Number
%
% Determine the parameters and write them (diagonal terms) into the matrices M at time
% n+1 (Mn) and time n (Mo) => case for iodide, the chemical tracer
%
A=e*(m*fi.^2+3*D*fi.*dfi/(2*dx)-v/(2*dx));
B=-1/dt-e*(2*m*fi.^2+alpha+(v./fi).*dfi);
E=e*(m*fi.^2-3*D*fi.*dfi/(2*dx)+v/(2*dx));

F=(e-1)*(m*fi.^2+3*D*fi.*dfi/(2*dx)-v/(2*dx));
G=-1/dt+(1-e)*(2*m*fi.^2+alpha+(v./fi).*dfi);
H=(e-1)*(m*fi.^2-3*D*fi.*dfi/(2*dx)+v/(2*dx));

d1n=ones(i-1,1).*A(2:i);
d2n=ones(i,1).*B;
d3n=ones(i-1,1).*E(1:i-1);

Mn=diag(d2n,0)+diag(d1n,-1)+diag(d3n,+1);   % Building the matrix M at time n+1
Mn(1,:)=[1 zeros(1,i-1)];
Mn(i,:)=[zeros(1,i-2) -1 1];

d1o=ones(i-1,1).*F(2:i);
d2o=ones(i,1).*G;
d3o=ones(i-1,1).*H(1:i-1);

Mo=diag(d2o,0)+diag(d1o,-1)+diag(d3o,+1);   % Building the matrix M a time n
Mo(1,:)=[1 zeros(1,i-1)];
Mo(i,:)=[zeros(1,i-2) -1 1];
```

```
%
% implement scheme for time and space and plot real time evolution of the chemical
% reactant and the chemical tracer
%
CI=CI0;
for q=1:length(t)
   Irr = [alpha*CI(1)*ones(round(bd/dx)+1,1);zeros(i-round(bd/dx)-1,1)]./fi;       %
Irrigation coefficient from surface to bioturbation depth (bd)
   Cn = inv(Mn)*(Mo*CI-Irr);              % concentration of iodide as a function of depth
   Cn1(:,q) = Cn;
   CI = Cn;

   figure(1)      % This figure plots the concentration of I as a function of
                  %    plot(x,CI/1e-3,x(1:2),CI(1:2)/1e-3,'ro')
                  % depth at each time step in the model
   plot(x,CI/1e-3)                % depth at each time step in the model
                                  %    axis([0 L 0 CI0(1)/1e-3])
   xlabel('Depth - [cm]')
   ylabel('[I^-] - [mM]')
   title('Crank-Nicholson scheme for the transport of a tracer in the sediment')
                                  %    set(gca,'xtick',[0:1:max(x)])
                                  %    pause(0.1)
end
%
% Check Mass balance at each time step by calculating the total mass transformation as a
% function of time in the system between 0 and L. No reaction are involved (chemical
% tracer), and diffusive flux and non-local exchange at x=L are negligible.
%
for q = 1:length(t)
   sink(1,q) = sum([alpha*ones(round(bd/dx+1),1);zeros(round(i-bd/dx-
1),1)].*(Cn1(1,q)-fi.*Cn1(:,q))*1e-3*dx); % mole sec-1 cm-2
end
MBt = v*(fi(1)*Cn1(1,:)-fi(i)*Cn1(i,:))*1e-3 - D*fi(1)^3*(Cn1(1,:)-Cn1(2,:))*1e-3/dx -
sink; % mole sec-1 cm-2
MBdevt = MBt*1000/L;       % Deviation from mass balance (zero) at each time step
disp('Deviation of Mass Balance does not exceed')
MBdev = max(abs(MBdevt));
disp(MBdev)
disp('Molar/sec')
%
% Plot the tracer and reactant at the sediment surface as a function of time
%
figure(2)
plot(t/3600,(Cn1(1,:)+mean(Cexp(length(Cexp)-
8:length(Cexp))))*1000,texp,Cexp*1000,'ob')
%
```

```
% plot(t/3600,(Cn1(1,:))*1000,texp,Cexp*1000,'ob') % To use only with non-corrected
% values of CIexp at steady-state
%
ylabel('[I^-] - [mM]')
xlabel('time - [hr]')
set(gca,'xtick',[0:1:max(t)])
title('Benthic Chamber Evolution of Iodide as a Function of Time')
hold on
outputSWI = [t/3600 Cn1(1,:)'*1000 CIexp*1000 Cn1(1,:)'/1e-6];
output = [x Cn1];
parameters = [X MBdev]';
save OverWaterConc.txt -ascii outputSWI;
save SedConc.txt -ascii output;
save parameters.txt -ascii parameters;
toc
```

```
% Subroutine to calculate iodide concentration decay at the sediment-water interface and
% optimize the advection, the diffusion coefficient, and the irrigation coefficient (alpha)
% needed to mimimize the theoretical and experimental data
%
function FF = traceroptim_alphavD(X)
global x dx t dt e i fi dfi CIexp CI0 bd
%
% Numerical solution for iodide
%
v = X(1);        % advection
alpha = X(2);    % Irrigation coefficient
D = X(3);        % Diffusion coefficient
                 %alpha = X;
m=D/(dx^2);

A=e*(m*fi.^2+3*D*fi.*dfi/(2*dx)-v/(2*dx));
B=-1/dt-e*(2*m*fi.^2+alpha+(v./fi).*dfi);
E=e*(m*fi.^2-3*D*fi.*dfi/(2*dx)+v/(2*dx));

F=(e-1)*(m*fi.^2+3*D*fi.*dfi/(2*dx)-v/(2*dx));
G=-1/dt+(1-e)*(2*m*fi.^2+alpha+(v./fi).*dfi);
H=(e-1)*(m*fi.^2-3*D*fi.*dfi/(2*dx)+v/(2*dx));

d1n=ones(i-1,1).*A(2:i);
d2n=ones(i,1).*B;
d3n=ones(i-1,1).*E(1:i-1);

Mn=diag(d2n,0)+diag(d1n,-1)+diag(d3n,+1);   % Building the matrix M at time n+1
Mn(1,:)=[1 zeros(1,i-1)];
```

```
Mn(i,:)=[zeros(1,i-2) -1 1];

d1o=ones(i-1,1).*F(2:i);
d2o=ones(i,1).*G;
d3o=ones(i-1,1).*H(1:i-1);

Mo=diag(d2o,0)+diag(d1o,-1)+diag(d3o,+1);   % Building the matrix M a time n
Mo(1,:)=[1 zeros(1,i-1)];
Mo(i,:)=[zeros(1,i-2) -1 1];
CI = CI0;
for q=1:length(t)
   Irr = [alpha*CI(1)*ones(round(bd/dx)+1,1);zeros(i-round(bd/dx)-1,1)]./fi;       %
Irrigation coefficient from surface to bioturbation depth (bd)
   Cn = inv(Mn)*(Mo*CI-Irr);      % concentration of iodide as a function of depth
   Cn1(:,q) = Cn;
   CI = Cn;
end
FF = norm(Cn1(1,:)'-CIexp)*1000
```

Fourier Transform Analysis

The Matlab™ code for the Fourier transform analysis used to determine the periodicity of the voltammetric porewater and level logger time series data in Chapter 5.

The main routine is LLfourier, and eqfiltfilt.m and cut.m are subroutines.

```
% This programs loads Level Loggers data and run Fourier transform to extracts the
% different frequency domains%
clear
%
% Open and read each well data individually
%
a=input('What well do you want to analyze?','s');
b=[a,'.txt'];

fid = fopen(b,'r');
Ztime=[];
Zdata=[];
line = fgetl(fid);
ti = findstr(':',line);      % Finds the index (left to right) where the 'colon' is.
%
% Read time and data from each line and stores time, water level, and temperature in two
```

```
% vectors (Ztime for time and Zdata for water level and temperature)
%
while isempty(ti) == 0
   for i = 1:length(ti)
      tim(:,i) = str2num(line((ti(i)-2):(ti(i)-1)));  % Read the first two times (hours and
minutes)
   end
   tim = [tim str2num(line((ti(i)+1:ti(i)+2)))];       % Read the last time (seconds)
   data = str2num(line((ti(i)+3):length(line)));
                  % Read the chemical data (3 = # of characters after ':' sign to find data
   if length(data)>2
                  % This is the case where the data are not chemical but from level loggers
      data = str2num(line((ti(i)+5):length(line)));
                  % Read the data (height and temperature)
end
   if length(ti) ==2
      ti = tim(1)+tim(2)/60+tim(3)/3600;     % Reformat time in hour units
   else
      ti = tim(1)+tim(2)/60;                 % Reformat time in hour units
   end
   Ztime = [Ztime; ti];                      % Time in hours
   Zdata = [Zdata; data];
   line = fgetl(fid);
   ti = findstr(':',line);                % Finds the index (left to right) where the 'colon' is.
end
fclose(fid);
%
% Transform time vector from 24 hour periods into hours from initial time (zero)
%
x = find(diff(Ztime)<0);
         % Find the position in Ztime vector when time switches from 23 hour to 0 hour
Ztimen=Ztime;
for i = 2:length(x) % Add 24 hour to each period to transform time into monotonic vector
   Ztimen(x(i-1)+1:x(i)+1) = Ztime(x(i-1)+1:x(i)+1)+24*(i-1);
end
Ztimen(x(i)+1:length(Ztimen)) = Ztime(x(i)+1:length(Ztimen))+24*i;
Ztime = (Ztimen-Ztimen(1))*3600;                  % Time adjusted to 0 at t0 - [sec]
%
% Plot the data and ask whether the data set should be cut
%
figure(1)
plot(Ztime,Zdata)
title('Data to be analyzed by FFT')
xlabel('Time - [hours]')
ylabel('Amplitude')
c=input('Initial time of consideration (0 == all data set will be considered)','s');
```

```
d=input('Final time of consideration (0 == all data set will be considered)','s');
% Cuts the data outside time domain defined by values (reads Ztime)
if c|d == 0
else
   [Ztime Zdata]=cut(Ztime, Zdata, c, d);
   if length(Zdata(1,:))>1
      Zdata=Zdata';
   end
end
%
% Remove mean height from the water levels to provide enough zeros such that FFTs is
% easy to calculate
%
meanheight = sum(Zdata)/length(Zdata);
data = Zdata-meanheight(1);
%
% Performs Discrete Fourier transform on water levels (built-in Matlab func), NOT ON
% TEMPERATURE
%
Fs = (max(Ztime)-Ztime(1))/length(Ztime);   % Define the sampling frequency - [sec]
NFFT = 2^nextpow2(length(Ztime));            % Next power of two from length of Ztime
data_fft=fft(data(:,1),NFFT);                % Take fft of data, padding with zeros such
that the length of data_fft = NFFT
NumUniquePts = ceil((NFFT+1)/2);             % Calculate the number of unique points
amp_fft=(abs(data_fft(1:NFFT/2+1))/length(Ztime)).^2;       % Define the amplitude
if rem(NFFT, 2)                              % Odd NFFT excludes Nyquist point
        amp_fft(2:end) = amp_fft(2:end)*2;
else
        amp_fft(2:end -1) = amp_fft(2:end -1)*2;
end
pha_fft=angle(data_fft);                     % Define the phase
freq = ((0:NumUniquePts-1)/Fs/NFFT)';        % Defines the frequency range
%
% Performs inverse discrete Fourier transform and compares to initial data to make sure
% calculation is accurate
%
data_bak=ifft(data_fft,NFFT);                % Performs inverse discrete Fourier transform
Ztime_bak = Ztime(1) + [0:NFFT-1].*Fs;
%
% Calculate back time vector this time of length(NFFT)
% Plots advancements through the steps from raw data, to frequency domain, to inverse
% discrete Fourier transform to ensure calculation is accurate
%
figure(2)
subplot(2,1,1),plot(Ztime_bak,data_bak,'b',Ztime,data(:,1),'r'),
title('Raw data Compared to Inverse Discrete Fourier Transform')
```

```
legend('Inverse FFT','Original data')
xlabel('Time (s)'), ylabel('Amplitude')

subplot(2,1,2), loglog(freq,amp_fft)
title('Amplitude data'),xlabel('Frequency in Hz'),ylabel('Amplitude')

filtdata = eqfiltfilt(data_fft, 1e-4, 3e-4,Fs,1);
filtdata_time = ifft(filtdata);
%
% Plots the original data (after run through FFT and then back through IFFT) against the
%  inverted filtered data (low-pass and band-pass)
%
figure(3)
plot(Ztime_bak,filtdata_time,'k',Ztime,data(:,1),'r')
title('Invert FFT after low pass 30s filter')
xlabel('Time (s)'), ylabel('Amplitude')
ylabel('Amplitude')
%
% Save frequency domain
%
output = [freq amp_fft];
filename = [a '_freqdomain.txt'];
eval(['save ' filename ' output -ascii']);
```

```
function filtdata = eqfiltfilt(data,ch1,ch2,dt,ih)
% filtdata = eqfiltfilt(data,ch1,ch2,dt,ih)
%       Function to perform butterworth       filter on "data"
%       vector, and return filtered data vector "filtdata"
%
%       filter corners (above "ch1" and         below "ch2" can         pass, in Hz)
%         if ch1 < 0,        % LOW-PASS FILTER  (-inf,ch2)
%         elseif ch2 < 0,   % HIGH-PASS      FILTER (ch1,inf)
%         elseif ch1 > ch2, % BAND-STOP    FILTER (-inf,ch2) & (ch1,inf)
%         else                % BAND-PASS     FILTER (ch1,ch2)
%       sampling rate (dt, in sec/sample)
%       butterworth filter order (ih, default = 4)


if nargin <= 4, ih=4; end
if nargin <= 3, dt=1; end
if nargin <= 2,
        error(['Not enough input argument, (at least 3,data ch1, and ch2)']);
end
samp = 1/dt;              % sampling frequency
ch1n = ch1*2/samp;
```

```
ch2n = ch2*2/samp;

if ch1 < 0,                     % LOW-PASS FILTER
  [b,a]   = butter(ih,ch2n);
elseif ch2 < 0,                 % HIGH-PASS FILTER
  [b,a]   = butter(ih,ch1n,'high');
elseif ch1 > ch2,               % BAND-STOP FILTER
  [b,a]   = butter(ih,[ch2n ch1n],'stop');
else                            % BAND-PASS FILTER
  [b,a]   = butter(ih,[ch1n ch2n]);
end

filtdata = filtfilt(b,a,data); % zero phase filter the data
```

```
%cuts data set to custom length
%input initial time (time0) and data (data0) of equal length in forms of (X,1) arrays
%reads time0 and cuts from value 'cuts' until 'cute'
%RETURNS 'time' and 'data' arrays after cutting time outside of domain

function [time data]=cut(time0, data0, cuts, cute);

[tx ty]=size(time0);
mark1=0;
mark2=0;

for i=1:1:tx-1
   if time0(i)<cuts && time0(i+1)>=cuts
      mark1=i+1;
   elseif time0(i)<=cute && time0(i+1)>cute
      mark2=i;
   end
end
if mark1==0;
   disp('Start cut time not in domain')
end
if mark2==0
   mark2=tx;
   disp('End cut time not in domain')
end


time=time0(mark1:mark2);
data=data0(mark1:mark2);
```

Reactive Transport Model for Net Reaction Rates

The Matlab™ code for the one dimensional reactive transport model used to model the oxygen, thiosulfate, and sulfide profiles in Chapter 6 to determine the net rates of production or consumption. The main routine is MatNetrates.m and Optim_netrate.m is the subroutine that optimizes the data.

```
% This program uses calculates the rate of reaction of each species measured
% voltammetrically by fitting the data with the transient advection-dispersion in one
% dimension using a central finite difference in space and different schemes in time
% (explicit if e=0, implicit id e=1 and Crank-Nicholson if e=0.5).
%
% The governing equation is the standard transient advection/dispersion equation that
% includes change in porosity as a function of depth and non-local exchange
%
%   fi dC/dt = D d/dx(fi dC/dx) + v d(fi C)/dx + alpha fi (C0 - C) + fi R
%
% It assumes a exponential decrease of porosity with depth as in Boudreau (1998):
%  fi(x) = fiinf + (fi0 - fiinf) exp(-gamma x) where gamma is a coefficient
% The physical parameters D, v, and alpha were optimized using the iodide tracer in the
% benthic chamber. The zone of irrigation is defined by the depth db (simple step
% function).
%
% The program allows the user to define zones of reaction that are used to calculate
% reaction rates in each zone. These rates should be integrated over total depth to
% calculate overall rate of consumption or production.
%
clear
global m v D fi dfi dt alpha e dx i Irr l df C0 t x Cexp
global backcolor;
tic
%
% define the different constant parameters
%
fi0 = 0.95;          % Porosity at the surface
fiinf = 0.9;         % Porosity at the bottom of the domain
gamma = 0.1;     % Porosity decay constant
v = 0;               % Advection (going down) - [cm/s]
alpha=0;             % Irrigation constant - [1/s]
bd = 0;              % Depth of maximum biorrigation - [cm]
e=0.5;           % timde discretisation scheme (0:explicit,1:implicit,0.5:Crank-Nicolson)
C = 1.0;         % Courant Number
tmax = 40;  % Maximum time for calculation, assuming steady-state is reached then - [hr]
T = 18;      % Temperature - [C]
P = 1;       % Pressure - [bar]
```

```
S = 90;        % Salinity
%
% Load the data
%
% Ask what species should be used to calculate their net rates of consumption or
% production and provide limits of rates as well as initial guess for optimization
% procedure
%
r = input('Which Sulfate Concentration?: 1: 0.2 mM; 2: 1 mM; 3: 80 mM');
%q = input('Which data file?: 1:12 AM; 2: 6 AM; 3: 12PM; 4: 6PM');
q = input('Which light treatment?: 1:FL; 2: IR');
p = input('Species you want to calculate net rates: 1: O2(aq);2: H2S; 3: S2O3','s');
p = str2num(p);
dr = input('Is the rate consumption (-1) or production (1)?');
%
% Ask for the type of boundary conditions use in the zones
%
l = input('What is the boundary condition at the top of the zone (0: Dirichlet; 1:
Neumann');
%
% Define the depth vector for the dataset and assign data concentrations to different
% variables Cp where p corresponds to: 1: O2; 2: H2S; 3: S2O3
%
if r==1                    % Sulfate treatment 0.2 mM
   if q == 1
      filename = ['AllFLdata02mM'];
      elseif q == 2
      filename = ['AllIRdata02mM'];
      else
      disp('This file name does not exist')
      break
   end
   elseif r== 2            % Sulfate treatment 1 mM
      if q == 1
         filename = ['AllFLdata1mM'];
         elseif q == 2
         filename = ['AllIRdata1mM'];
         else
         disp('This file name does not exist')
         break
      end
   elseif r== 3            % Sulfate treatment 80 mM
      if q == 1
         filename = ['AllFLdata80mM'];
         elseif q == 2
         filename = ['AllIRdata80mM'];
```

```
        else
        disp('This file name does not exist')
        break
      end
   else
   disp('This file name does not exist')
   break
end
eval(['depth = ' filename '(:,1);']);                          % Depth  - [mm]
eval(['C' num2str(q) '=' filename '(:,' num2str(2*p) ')*1e-6;']);   % Concentration - [M]
p=num2str(p);
%
% Plot the general figure style
%
axcolor = [ 0.698 0.671 0.608 ];
backcolor = [ 0.722 0.733 0.671 ];
textcolor = [.2 .3 .5];
noisecolor = [.5 .5 .5];

fig1 = figure(1);
theplot = axes;
set(theplot,'Position',[0.103 0.085 0.799 0.800],'Color',axcolor);
set(fig1,'MenuBar','none','NumberTitle','off','Color',backcolor);       % 'Position',[230 230
700 480],
informtext = uicontrol(gcf,'Style','text','Units','normalized','Position',[0.089 .905 0.536
0.06],'FontSize',10,'Visible','off','String','','BackGroundColor',backcolor,'ForegroundColo
r',textcolor,'Tag','informtext');
informbox1 = uicontrol(gcf,'Style','checkbox','Units','normalized','Position',[0.636 .951
0.088 0.024],'Visible','off','String','','BackGroundColor',backcolor,'Tag','informbox1');
informbox2 =
uicontrol(gcf,'Style','checkbox','Visible','off','Units','normalized','Position',[0.636 .912
0.088 0.024],'String','','BackGroundColor',backcolor,'Tag','informbox2');
%
% Plot the raw data
%
eval(['plot1 = plot(depth,C' num2str(q) ');'])
set(plot1,'Color',noisecolor);
hold on
set(theplot,'Color',axcolor)
xlabel('Depth - [cm]');
ylabel('Concentration - [uM]');
%
% Ask to delimit the different zones of integration in the profile for one of the chemical
% species involved.
%
sevzones=1;
```

```
zones = [];
dfs = [];
while sevzones~= 0
   quest = 0; % Are you satisfied with the zone of integration?
   while quest ~= 1
      tellthem('Select integration zone by clicking for endpoints',1);
      set(plot1,'ButtonDownFcn','getclicks');    % getclicks listens to user clicks on the line
      x = 1;
      uiwait(figure(1));
      tbrk = huh(1,1);
      while tbrk< min(depth)|tbrk>max(depth)
        clear huh;
        uiwait(figure(1));
        tbrk = huh(1,1);
      end
      a = huh(1,[1:2]);
      i = depth(:) - a(1,1);
      s1 = find(abs(i) == min(abs(i)));
      deptha = depth(s1);
      eval(['conca= C' num2str(q) '(s1);'])
      clear huh;

      set(eval('findobj("Tag","informtext")'),'Visible','on','String','Create baseline by
clicking for endpoints.');
      x = 2;
      uiwait
      b = huh(1,1:2);
      i = depth(:) - b(1,1);
      s3 = find(abs(i) == min(abs(i)));
   % deptha and depthb are the closest points in the line data to match those picked by the
user
      if s3 > s1,
         if dbg,disp('CLICKING FROM SWI TO DEEP');end
         depthb = depth(s3);
         eval(['concb = C' num2str(q) '(s3);'])
      else
         if dbg, disp('CLICKING DEEP TO SWI');end
         depthb = deptha;
         concb = conca;
         deptha = depth(s3);
         eval(['conca =  C' num2str(q) '(s1);'])
      end
      clear huh;
%
% Find the zone of integration and plot it using delimiters defined by para and parb
%
```

```
      figure(1);
      eval(['para = abs(conca-max(C' num2str(q) '));'])
      eval(['parb = abs(concb-max(C' num2str(q) '));'])
      extplot3 = plot([deptha;deptha],[conca;para],'r',[depthb;depthb],[concb;parb],'r');
      delete(coordplot(:));
      xlabel('Time - [min]');
      ylabel('Conductivity - [uS/cm]');
      tellthem('Are you satisfied with the limits of the zone?',0,1);
      uiwait
      quest = get(eval('findobj("Tag","informbox1")'),'Value');
      if quest == 0,
         if dbg,disp('NOT OKAY');end
         tellthem('',1);
         set(extplot3,'Visible','off')
      end
   end                        %quest = input('is the zone of integration okay? (yes=1/no=0)');
   if s3 > s1
      zone = [s1 s3 deptha depthb conca concb]; % Regroups limits of integration zone
   else
      zone = [s3 s1 deptha depthb conca concb]; % Regroups limits of integration zone
   end
   zones = [zones;zone];              % Compile all the zones of integration
   df = input('Is the flux zero (0) or non-zero (1)?');
   dfs = [dfs;df];
   clear df;
   tellthem('Is there another zone to integrate?',0,1);
   uiwait
   sevzones = get(eval('findobj("Tag","informbox1")'),'Value');
   if sevzones == 1,
      set(plot1,'Visible','on');
      delete(extplot3);
   else
      set(gca,'NextPlot','replace');%issues cla and reset
      tellthem('',1,0);
   end
end
figure(1)
close
%
% Now that the different zones have been defined for the profile of one species, the
% program calculates the rate of reaction for that particular species in each zone
%
% Molecular diffusion coefficient of each species is calculated according to Boudreau
% (1997). Diffusion coefficient for FeS(aq) and org-Fe(III) are presently unknown. A
% value of 2e-5 cm^2/s is used for them.
%
```

```
visc = 0.01*(1.791-6.144e-2*T+1.451e-3*T^2-1.6826e-5*T^3-1.529e-4*P...
   +8.3885e-8*P^2+2.4727e-3*S+T*(6.0574e-6*P-2.676e-9*P^2)...
   +S*(4.8429e-5*T-4.7172e-6*T^2+7.5986e-8*T^3));  % Dynamic viscosity of water -
[g/cm/s]
if str2num(p) == 1
   Vb = 27.9;                          % Molar volume of O2 - [cm^3/mol]
   D = 4.79e-9*(T+273.15)/(visc*Vb^0.6);       % Diffusion coefficient for O2 - [cm^2/s]
   elseif str2num(p) == 2
      m0 = 10.4; m1 = 0.273;                % Infinite dilution coefficients
      D = (m0 + m1*T)*1e-6;                  % Diffusion coefficient for HS-
   elseif str2num(p) == 3
      m0 = 4.82; m1 = 0.266;                % Infinite dilution coefficients
      D = (m0 + m1*T)*1e-6;                  % Diffusion coefficient for Fe(II)
   else
      D = 2e-5;                          % Diffusion coeffcient for FeS(aq) and org-Fe(III)
end
v=v*3600; D = D*3600;                        % advection and diffusion in [cm/h] and
[cm^2/h]
alpha = alpha*3600;                        % Biorrigation is in [1/hr]
%
% Find the Concentration of species in the overlying water (C0) to account for non-local
% exchange due to irrigation and defines the porosity profile in the sediment
%
dol = find(depth < 0);            % Find all the depths above the SWI (should be negative #)
if isempty(dol)|length(dol) == 1              % If no measurements in the overlying water
   eval(['C0 = C' num2str(q) '(1);']);          % C0 is the first concentration of the profile
   fi = fiinf+(fi0-fiinf)*exp(-gamma*depth);
         % Porosity change with depth according to Boundreau (1998) p. 223.
when the profile starts in the sediment
   dfi = -gamma*(fi0-fiinf)*exp(-gamma*depth);            % First derivative of porosity
else                                        % Otherwise,
   eval(['C0 = C' num2str(q) '(floor(length(dol)/2));']);
                     % C0 is the concentration in the middle of the overlying water depths
   dbswi = depth(max(dol)+1:length(depth))/10;
                     % Depth below the sediment-water interface - [cm]
   fi = [ones(max(dol),1);fiinf+(fi0-fiinf)*exp(-gamma*dbswi)];
                     % Porosity change with depth (in sediment only)
                     % Above SWI, however,porosity and derivative are zero
   dfi = [zeros(max(dol),1);-gamma*(fi0-fiinf)*exp(-gamma*dbswi)]; % First derivative
of porosity
end
dirr = find(depth/10 > bd);       % Find all the depths below the irrigation maximum (bd)
Irr = [alpha*ones(dirr(1)-1,1);zeros(length(dirr),1)];    % Irrigation as a function of depth
%
% Net rate is optimized to fit the data in each zone (j) defined by the user
%
```

```
dzones = []; Czones = []; Cnzones = []; xzones = [];
for j = 1:length(zones(:,1))
%
% Calculated the Depth Parameters
%
   L = abs(zones(j,3)-zones(j,4))/10;      % Length of the domain of integration - [cm]
   if v==0
      dx = L/500;                    % spatial node - [cm]
      dt = (tmax)/100;                % time step - [hr]
   else
      dx = L/500;
      dt=abs(C*dx/v);                 % time space - [hr]
   end
   x=(0:dx:L)';                      % depth - [cm]
   t = (0:dt:tmax)';                  % Time vector - [hour]
   i=length(x);                      % size of the matrix
   df = dfs(j);                      % Define the type of flux at the boundary condition (0 for
no flux, 1 for flux)
   disp('length of x is:');disp(i)
   disp('length of time vector is:');disp(tmax/dt)
   P = dx*v/D;
   disp('Peclet # is:'); disp(P)
   m=D/(dx^2);                        % Characteristic time of diffusion
%
% Correct the depth profiles so that model integrates from x = 0 to L, determine the
% experimental concentration, the porosity, and the biorrigation in that depth range and
% interpolate them
%
   dshift = depth(zones(j,1));                          % This is the shift in depth - [mm]
   eval(['Cexp = C' num2str(q) '(zones(j,1):zones(j,2));'])
         % Experimental concentrations in the zone of integration - [M]
   Cexp = interp1(abs(depth(zones(j,1):zones(j,2))-dshift)/10,Cexp,x);
   Irr = interp1(abs(depth(zones(j,1):zones(j,2))-dshift)/10,Irr(zones(j,1):zones(j,2)),x);
   fi = interp1(abs(depth(zones(j,1):zones(j,2))-dshift)/10,fi(zones(j,1):zones(j,2)),x);
   dfi = interp1(abs(depth(zones(j,1):zones(j,2))-dshift)/10,dfi(zones(j,1):zones(j,2)),x);
   % Determine the initial condition for each species at time zero
   if l == 0                      % If l = 0, BC is Dirichlet at the top, Neumann at the bottom
         C0 = Cexp(1)*ones(i,1);         % The entire sediment is oxygenated initially
   else
      C0 = [zeros(i-1,1);Cexp(i);];       % If l = 1, Dirichlet condition is a the bottom
   end
%
% Optimize the net rate of reaction to match the profile data using a least square non
% linear method to match the experimental data
%
   if dr>0
```

```
    LB = 0; UB = 1000;       % Lower and upper bounds of net production rates - [M/hr]
  else
    LB = -1000; UB = 0;   % Lower and upper bounds of net consumption rates - [M/hr]
  end
  X0 =  dr*5e-5;  % Estimate of the rate of net reaction (dr represents the sign: - for
consumption, + for production)
  [X,RESNORM,RESIDUAL,EXITFLAG,OUTPUT,LAMBDA] =
lsqnonlin('optim_netrate',X0,LB,UB)       % Optimization of the net rate of reaction
  R = X;                              % Net reaction rate calculated - [M/hr]
%
% Determine the parameters and write them (diagonal terms) into the matrices M at
% time n+1 (Mn) and time n (Mo)
%
  A=e*(m+(D./fi.*dfi-v)/(2*dx));
  B=-1/dt-e*(2*m+alpha+(v./fi).*dfi);
  E=e*(m-(D./fi.*dfi-v)/(2*dx));

  F=(e-1)*(m+(D./fi.*dfi-v)/(2*dx));
  G=-1/dt+(1-e)*(2*m+alpha+(v./fi).*dfi);
  H=(e-1)*(m-(D./fi.*dfi-v)/(2*dx));

  d1n=ones(i-1,1).*A(2:i);
  d2n=ones(i,1).*B;
  d3n=ones(i-1,1).*E(1:i-1);

  Mn=diag(d2n,0)+diag(d1n,-1)+diag(d3n,+1);   % Building the matrix M at time n+1

  d1o=ones(i-1,1).*F(2:i);
  d2o=ones(i,1).*G;
  d3o=ones(i-1,1).*H(1:i-1);

  Mo=diag(d2o,0)+diag(d1o,-1)+diag(d3o,+1);   % Building the matrix M a time n
%
% Boundary conditions are added to the matrix at time n. RHS represents balance
% between irrigation from
%
% surface to bioturbation depth (bd) and net rate of reaction including a zero flux
% where appropriate. It iszero at the top (l = 1) or bottom (l = 0) if the flux is zero.
% Otherwise it takes the value of the RHS equation (Irr).
%
  RHS = Irr./fi+R;                        % RHS of Matrices
  if l == 0                       % If l = 0, BC is Dirichlet at the top, Neumann at the bottom
    Mo(1,:)=[1 zeros(1,i-1)];             % for M at time o
    Mo(i,:)=[zeros(1,i-2) -1 1];
    Mn(1,:)=[1 zeros(1,i-1)];             % for M at time n
    Mn(i,:)=[zeros(1,i-2) -1 1];
```

```
      if df == 0                    % When the flux at the bottom boundary is zero
         RHS(1)=0;RHS(i) = 0;          % RHS at the top and bottom are zero
      end
   else                          % If l = 1, BC is Neumann at the top, Dirichlet at the bottom
      Mo(1,:)=[-1 1 zeros(1,i-2)];     % for M at time o
      Mo(i,:)=[zeros(1,i-1) 1];
      Mn(1,:)=[-1 1 zeros(1,i-2)];     % for M at time n
      Mn(i,:)=[zeros(1,i-1) 1];
      if df == 0                    % When the flux at the boundary is zero
         RHS(1) = 0;RHS(i) = 0;        % RHS at the top is equal to zero
      end
   end
%
% implement scheme for time and space and plot real time evolution of the chemical
% reactant and the chemical tracer
%
   CI=C0;
   for n=1:length(t)
      Cn = inv(Mn)*(Mo*CI-RHS);     % concentration of iodide as a function of depth
      Cn1(:,n) = Cn;
%
% Test whether the steady-state was reached for that reaction
%
      if n == length(t)
         if norm(CI-Cn) > 5e-5
            disp('WARNING: The profile has not reached steady-state. You should
increase tmax')
         end
      end
      CI = Cn;

      figure(1)                     % This figure plots the concentration of these species as
      plot(x,CI/1e-6)                  % function of depth at each time step in the model
      xlabel('Depth - [cm]')
      ylabel('Concentration - [uM]')
      title('Crank-Nicholson scheme for the transport of a tracer in the sediment')
      pause(0.1)
   end
%
% Piece up the depth profile calculated at steady-state (last time step) and measured in
% the different zones for plotting in Figure 3
%
   dzones = [dzones;(depth(zones(j,1):zones(j,2)))/10];     % Experimental depth - [cm]
   eval(['Conc = C' num2str(q) ' (zones(j,1):zones(j,2))/1e-6;'])
        % Experimental data in each zone
   Czones = [Czones;Conc];              % Experimental data from all the zones
```

```
   Cnzones = [Cnzones;CI/1e-6];              % Modeled concentration
      xzones = [xzones;(x+dshift/10)];       % Modeled depth - [cm]
      output = [x+dshift/10 CI/1e-6];        % Modeled depth [cm] and concentration [uM]
% In order in the vector: [minimum and maximum depths of the zones, diffusion
% coefficient (cm^2/s), advection (cm/s),
% Net reaction rate (M/h), Norm of the residuals and residual betweeen data and model]
%
parameters = [zones(j,3) zones(j,4) D/3600 v/3600 alpha/3600 R RESNORM
RESIDUAL]';
  eval(['save SedConcz_' filename num2str(j) '.txt -ascii output;'])
  eval(['save paramz_' filename num2str(j) '.txt -ascii parameters;'])
end

figure(2)
plot(xzones,Cnzones,dzones,Czones,'ob')
ylabel('Concentration - [uM]')
xlabel('Depth - [cm]')
%set(gca,'xtick',[0:1:max(dzones)])
title('Depth profile')
toc
```

```
%
% Subroutine to calculate depth concentration of the species as a function of time and
% optimize the net rate of reaction needed to mimimize the theoretical and experimental
% data at steady-state (defined by tmax). If steady-state is not reached, a warning
% message is provided. In this case, tmax must be increased.
%
function FF = optim_netrate(X)
global m v D fi dfi dt alpha e dx i Irr l df C0 t x Cexp
%
% Numerical solution for any chemical species that reacts
% Determine the parameters and write them (diagonal terms) into the matrices M at time
%
n+1 (Mn) and time n (Mo)
A=e*(m+(D./fi.*dfi-v)/(2*dx));
B=-1/dt-e*(2*m+alpha+(v./fi).*dfi);
E=e*(m-(D./fi.*dfi-v)/(2*dx));

F=(e-1)*(m+(D./fi.*dfi-v)/(2*dx));
G=-1/dt+(1-e)*(2*m+alpha+(v./fi).*dfi);
H=(e-1)*(m-(D./fi.*dfi-v)/(2*dx));

d1n=ones(i-1,1).*A(2:i);
d2n=ones(i,1).*B;
d3n=ones(i-1,1).*E(1:i-1);
```

```
Mn=diag(d2n,0)+diag(d1n,-1)+diag(d3n,+1);   % Building the matrix M at time n+1

d1o=ones(i-1,1).*F(2:i);
d2o=ones(i,1).*G;
d3o=ones(i-1,1).*H(1:i-1);

Mo=diag(d2o,0)+diag(d1o,-1)+diag(d3o,+1);   % Building the matrix M a time n
%
% Boundary conditions are added to the matrix at time n. RHS represents balance
% between irrigation from surface to bioturbation depth (bd) and net rate of reaction
% including a zero flux where appropriate. It is zero at the top (l = 1) or bottom (l = 0) if
% the flux is zero. Otherwise it takes the value of the RHS equation (Irr).
%
RHS = Irr./fi+X;                    % RHS of Matrices X = Net reaction rate optimized
if l == 0                           % If l = 0, BC is Dirichlet at the top, Neumann at the bottom
   Mo(1,:)=[1 zeros(1,i-1)];        % for M at time o
   Mo(i,:)=[zeros(1,i-2) -1 1];
   Mn(1,:)=[1 zeros(1,i-1)];        % for M at time n
   Mn(i,:)=[zeros(1,i-2) -1 1];
   if df == 0                       % When the flux at the bottom boundary is zero
      RHS(1)=0;RHS(i) = 0;          % RHS at the top and bottom are zero
   end
else                                % If l = 1, BC is Neumann at the top, Dirichlet at the bottom
   Mo(1,:)=[-1 1 zeros(1,i-2)];     % for M at time o
   Mo(i,:)=[zeros(1,i-1) 1];
   Mn(1,:)=[-1 1 zeros(1,i-2)];     % for M at time n
   Mn(i,:)=[zeros(1,i-1) 1];
   if df == 0                       % When the flux at the boundary is zero
      RHS(1) = 0;RHS(i) = 0;        % RHS at the top is equal to zero
   end
end
%
% implement scheme for time and space and plot real time evolution of the chemical
% reactant and the chemical tracer
%
CI=C0;
for n=1:length(t)
   Cn = inv(Mn)*(Mo*CI-RHS);        % concentration of iodide as a function of depth
   Cn1(:,n) = Cn;
   CI = Cn;
end
%
% Compare calculated solution as a function of depth to experimental data
%
FF= norm((CI-Cexp))*1e6;
```

REFERENCES

Afonso, M. D., and W. Stumm. 1992. Reductive dissolution of Iron(III) (hydr)oxides by hydrogen sulfide. Langmuir **8:** 1671-1675.

Alber, M., C. R. Alexander, J. Blanton, A. Chalmers, and K. Gates. 2003. The satilla river estuary system: The current state of knowledge. Report for The Georgia Sea Grant College Program and The South Carolina Sea Grant Consortium.

Aller, R. C., N. E. Blair, Q. Xia, and P. D. Rude. 1996. Remineralization rates, recycling, and storage of carbon in Amazon shelf sediments. Cont. Shelf Res. **16:** 753-786.

Aller, R. C., A. Hannides, C. Heilbrun, and C. Panzeca. 2004a. Coupling of early diagenetic processes and sedimentary dynamics in tropical shelf environments: the Gulf of Papua deltaic complex. Cont. Shelf Res. **24:** 2455-2486.

Aller, R. C., C. Heilbrun, C. Panzeca, Z. B. Zhu, and F. Baltzer. 2004b. Coupling between sedimentary dynamics, early diagenetic processes, and biogeochemical cycling in the Amazon-Guianas mobile mud belt: coastal French Guiana. Mar. Geol. **208:** 331-360.

Aller, R. C., J. E. Mackin, and R. T. Cox. 1986. Diagenesis of Fe and S in Amazon inner shelf muds - Apparent dominance of Fe reduction and implications for the genesis of ironstones. Cont. Shelf Res. **6:** 263-289.

Alongi, D. M. 1998. Coastal Ecosystem Processes, 1st ed. CRC Press.

Anderson, L. A. 1995. On the hydrogen and oxygen-content of marine-phytoplankton. Deep-Sea Res. Part I-Oceanogr. Res. Pap. **42:** 1675-1680.

Archer, D., and A. Devol. 1992. Benthic oxygen fluxes on the Washington shelf and slope - A comparison of in situ microelectrode and chamber flux measurements. Limnol. Oceanogr. **37:** 614-629.

Bard, A. J., and L. R. Faulkner. 2000. Electrochemical Methods: Fundamentals and Applications, 2nd ed. Wiley.

Bardischewsky, F., and C. G. Friedrich. 2001. The shxVW locus is essential for oxidation of inorganic sulfur and molecular hydrogen by Paracoccus pantotrophus GB17: a novel function for lithotrophy. FEMS Microbiol. Lett. **202:** 215-220.

Berelson, W. and others 2003. A time series of benthic flux measurements from Monterey Bay, CA. Cont. Shelf Res. **23:** 457-481.

Berelson, W. M., and D. E. Hammond. 1986. The calibration of a new free-vehicle benthic flux chamber for use in the deep-sea. Deep-Sea Research Part a-Oceanographic Research Papers **33:** 1439-1454.

Berelson, W. M. and others 1987. In situ benthic flux measurement devices - Bottom lander technology. Mar. Technol. Soc. J. **21:** 26-32.

Berg, P., and M. Huettel. 2008. Monitoring the Seafloor Using the Noninvasive Eddy Correlation Technique: Integrated Benthic Exchange Dynamics. Oceanography **21:** 164-167.

Berg, P., N. Risgaard-Petersen, and S. Rysgaard. 1998. Interpretation of measured concentration profiles in sediment pore water. Limnol. Oceanogr. **43:** 1500-1510.

Berg, P. and others 2003. Oxygen uptake by aquatic sediments measured with a novel non-invasive eddy-correlation technique. Mar. Ecol.-Prog. Ser. **261:** 75-83.

Berg, P., H. Roy, and P. L. Wiberg. 2007. Eddy correlation flux measurements: The sediment surface area that contributes to the flux. Limnol. Oceanogr. **52:** 1672-1684.

Berner, E. K., and R. A. Berner. 1996. Global Environment: Water, Air, and Geochemical Cycles. Prentice Hall, Inc.

Berner, R. A., and A. C. Lasaga. 1989. Modeling teh geochemical carbon cycle. Scientific American **260:** 74-81.

Bianchi, T. S. 2007. Biogeochemistry of Estuaries, 1st ed. Oxford University Press.

Black, K. S., G. R. Fones, O. C. Peppe, H. A. Kennedy, and I. Bentaleb. 2001. An autonomous benthic lander: preliminary observations from the UK BENBO thematic programme. Cont. Shelf Res. **21:** 859-877.

Blake, A. C., G. C. Kineke, T. G. Milligan, and C. R. Alexander. 2001. Sediment trapping and transport in the ACE basin, South Carolina. Estuaries **24:** 721-733.

Blanton, J. O., H. Seim, C. Alexander, J. Amft, and G. Kineke. 2003. Transport of salt and suspended sediments in a curving channel of a coastal plain estuary: Satilla River, GA. Estuar. Coast. Shelf Sci. **57:** 993-1006.

Boudreau, B. P. 1997. Diagenetic Models and Their Implementation: Modelling Transport and Reactions in Aquatic Systems. Springer.

Brendel, P. J., and G. W. Luther. 1995. Development of a gold amalgam voltammetric microelectrode for the determination of dissolved Fe, Mn, O_2 and S(-II) in porewaters of marine and freshwater sediments Environ. Sci. Technol. **29:** 751-761.

Bristow, G., and M. Taillefert. 2008. VOLTINT: A Matlabg (R)-based program for semi-automated processing of geochemical data acquired by voltammetry. Comput. Geosci. **34:** 153-162.

Browne, W. W. 1922. Halophilic bacteria. Proc. Exper. Biol. Med. **19:** 321-322.

Bull, D. C., and M. Taillefert. 2001. Seasonal and topographic variations in porewaters of a southeastern USA salt marsh as revealed by voltammetric profiling. Geochem. Trans. **13:** 1-8.

Burdick, D. M., and I. A. Mendelssohn. 1990. Relationship between anatomical and metabolic responses to soil waterlogging in the coastal grass *Spartina patens*. Journal of Experimental Botany **41:** 223-228.

Burdige, D. J. 2006. Geochemistry of Marine Sediments. Princeton University Press.

Burdige, D. J., and S. L. Zheng. 1998. The biogeochemical cycling of dissolved organic nitrogen in estuarine sediments. Limnol. Oceanogr. **43:** 1796-1813.

Caffrey, J. M. 2004. Factors controlling net ecosystem metabolism in US estuaries. Estuaries **27:** 90-101.

Cai, W. J., M. H. Dai, and Y. C. Wang. 2006. Air-sea exchange of carbon dioxide in ocean margins: A province-based synthesis. Geophys. Res. Lett. **33:** 4.

Cai, W. J., L. R. Pomeroy, M. A. Moran, and Y. C. Wang. 1999. Oxygen and carbon dioxide mass balance for the estuarine-intertidal marsh complex of five rivers in the southeastern US. Limnol. Oceanogr. **44:** 639-649.

Cai, W. J., and Y. Wang. 1998. The chemistry, fluxes, and sources of carbon dioxide in the estuarine waters of the Satilla and Altamaha Rivers, Georgia. Limnol. Oceanogr. **43:** 657-668.

Cai, W. J., W. J. Wiebe, Y. C. Wang, and J. E. Sheldon. 2000. Intertidal marsh as a source of dissolved inorganic carbon and a sink of nitrate in the Satilla River-estuarine complex in the southeastern US. Limnol. Oceanogr. **45:** 1743-1752.

Canfield, D. E. 1997. The geochemistry of river particulates from the continental USA: Major elements. Geochim. Cosmochim. Acta **61:** 3349-3365.

---. 2001. Isotope fractionation by natural populations of sulfate-reducing bacteria. Geochim. Cosmochim. Acta **65:** 1117-1124.

---. 2005. The early history of atmospheric oxygen: Homage to Robert A. Garrels. Annu. Rev. Earth Planet. Sci. **33:** 1-36.

Canfield, D. E., and D. J. Desmarais. 1994. Biogeochemical cycles of carbon, sulfur, and free oxygen in a microbial mat Geochim. Cosmochim. Acta **58:** 1044-1044.

Canfield, D. E., K. S. Habicht, and B. Thamdrup. 2000. The Archean sulfur cycle and the early history of atmospheric oxygen. Science **288:** 658-661.

Canfield, D. E. and others 1993a. Pathways of organic carbon oxidation in 3 continental margin sediments. Mar. Geol. **113:** 27-40.

Canfield, D. E., R. Raiswell, and S. Bottrell. 1992. The reactivity of sedimentary iron minerals toward sulfide Am. J. Sci. **292:** 659-683.

Canfield, D. E., B. Thamdrup, and J. W. Hansen. 1993b. The anaerobic degradation of organic matter in Danish coastal sediments - Iron reduction, manganese reduction, and sulfate reduction. Geochim. Cosmochim. Acta **57:** 3867-3883.

Carey, E., and M. Taillefert. 2005. The role of soluble Fe(III) in the cycling of iron and sulfur in coastal marine sediments. Limnol. Oceanogr. **50:** 1129-1141.

Carter, V., M. S. Bedinger, R. P. Novitzki, and W. O. Wilen. 1979. Water resources and wetlands, p. 344-376. *In* P. E. Greeson, J. R. Clark and J. E. Clark [eds.], Wetland Functions and Values: The State of Our Understanding. American Water Resources Association.

Cavicchioli, R. 2002. Extremophiles and the search for extraterrestrial life. Astrobiology **2:** 281-292.

Chanton, J., and F. G. Lewis. 2002. Examination of coupling between primary and secondary production in a river-dominated estuary: Apalachicola Bay, Florida, USA. Limnol. Oceanogr. **47:** 683-697.

Chapelle, F. H., P. M. Bradley, M. A. Thomas, and P. B. Mcmahon. 2009. Distinguishing Iron-Reducing from Sulfate-Reducing Conditions. Ground Water **47:** 300-305.

Chen, C. T. A., and A. V. Borges. 2009. Reconciling opposing views on carbon cycling in the coastal ocean: Continental shelves as sinks and near-shore ecosystems as sources of atmospheric CO2. Deep-Sea Res. Part II-Top. Stud. Oceanogr. **56:** 578-590.

Chen, K. Y., and J. C. Morris. 1971. Oxidation of aqueous sulfide by O2: General characteristics and catalytic influences. Advances in Water Pollution Research **2:** 1 - 17

---. 1972. Kinetics of oxidation of aqueous sulfide by O2. Environ. Sci. Technol. **6:** 529-&.

Christiansen, T., P. L. Wiberg, and T. G. Milligan. 2000. Flow and sediment transport on a tidal salt marsh surface. Estuar. Coast. Shelf Sci. **50:** 315-331.

Clayton, W., and W. E. Gibbs. 1927. Examination for halophilic micro-organisms. Analyst **52:** 395-397.

Clement, B. G., G. W. Luther, and B. M. Tebo. 2009. Rapid, oxygen-dependent microbial Mn(II) oxidation kinetics at sub-micromolar oxygen concentrations in the Black Sea suboxic zone. Geochim. Cosmochim. Acta **73:** 1878-1889.

Cook, P. L. M., F. Wenzhofer, R. N. Glud, F. Janssen, and M. Huettel. 2007. Benthic solute exchange and carbon mineralization in two shallow subtidal sandy sediments: Effect of advective pore-water exchange. Limnol. Oceanogr. **52:** 1943-1963.

Cowie, G. L., and J. I. Hedges. 1992. Sources of reactivities of amino-acids in a coastal marine environment Limnol. Oceanogr. **37:** 703-724.

Cypionka, H. 1994. Novel metabolic capacities of sulfate-reducing bacteria, and their activities in microbial mats, p. 367-376. *In* L. J. Stal and P. Caumette [eds.], Microbial Mats. Springer-Verlag.

Dai, J. H., and M. Y. Sun. 2007. Organic matter sources and their use by bacteria in the sediments of the Altamaha estuary during high and low discharge periods. Org. Geochem. **38:** 1-15.

Dannenberg, S., M. Kroder, W. Dilling, and H. Cypionka. 1992. Oxidation of H2, organic-compounds and inorganic sulfur-compounds coupled to reduction of O2 or nitrate by sulfate-reducing bacteria Arch. Microbiol. **158:** 93-99.

Davison, W., J. Buffle, and R. Devitre. 1988. Interpretation of speciation measurements - A case study - Direct polarographic determination of O2, Fe(II), Mn(II), S(-II), and related species in anoxic waters. Pure Appl. Chem. **60:** 1535-1548.

Davison, W., and G. Seed. 1983. The kinetics of the oxidation of ferrous iron in synthetic and natural waters. Geochim. Cosmochim. Acta **47:** 67-79.

Decker, K. L. M. and others 2005. Mathematical simulation of the diel O, S, and C biogeochemistry of a hypersaline microbial mat. FEMS Microbiol. Ecol. **52:** 377-395.

Dell'anno, A., A. Pusceddu, L. Langone, and R. Danovaro. 2008. Biochemical composition and early diagenesis of organic matter in coastal sediments of the NW Adriatic Sea influenced by riverine inputs. Chem. Ecol. **24:** 75-85.

Des Marais, D. J. 2003. Biogeochemistry of hypersaline microbial mats illustrates the dynamics of modern microbial ecosystems and the early evolution of the biosphere. Biol. Bull. **204:** 160-167.

Desmarais, D. J. 1995. The biogeochemistry of hypersaline microbial mats, p. 251-274. Advances in Microbial Ecology, Vol 14. Advances in Microbial Ecology. Plenum Press Div Plenum Publishing Corp.

Dewit, R., and H. Vangemerden. 1987. Chemolithotrophic growth of the phototrophic sulfur bacterium *Thiocapsa roseopersicina* FEMS Microbiol. Ecol. **45:** 117-126.

Di Giulio, M. 2000. The universal ancestor lived in a thermophilic or hyperthermophilic environment. J. Theor. Biol. **203:** 203-213.

Dollar, S. J., S. V. Smith, S. M. Vink, S. Obrebski, and J. T. Hollibaugh. 1991. Annual cycle of benthic nutrient fluxes in Tomales Bay, California, and contribution of the benthos to total ecosystem metabolism. Mar. Ecol.-Prog. Ser. **79:** 115-125.

Donkor, V., and D. P. Hader. 1991. Effects of solar and ultraviolet-radiation on motility, photomovement and pigmentation in filamentous, gliding cyanobacteria. FEMS Microbiol. Ecol. **86:** 159-168.

Drews, G. 1996. Forty-five years of developmental biology of photosynthetic bacteria. Photosynth. Res. **48:** 327-352.

Druschel, G. K., D. Emerson, R. Sutka, P. Suchecki, and G. W. Luther. 2008. Low-oxygen and chemical kinetic constraints on the geochemical niche of neutrophilic iron(II) oxidizing microorganisms. Geochim. Cosmochim. Acta **72:** 3358-3370.

Druschel, G. K., R. J. Hamers, and J. F. Banfield. 2003. Kinetics and mechanism of polythionate oxidation to sulfate at low pH by O-2 and Fe3+. Geochim. Cosmochim. Acta **67:** 4457-4469.

Dundas, I. 1998. Was the environment for primordial life hypersaline? Extremophiles **2:** 375-377.

Eisma, D. 1986. Flocculation and de-flocculation of suspended matter in estuaries. Neth. J. Sea Res. **20:** 183-199.

Ellwood, B. B., T. H. Chrzanowski, F. Hrouda, G. J. Long, and M. L. Buhl. 1988. Siderite formation in anoxic deep sediments - A synergetic bacterially controlled process with important implications in paleomagnetism Geology **16:** 980-982.

Fennessey, C. M., M. E. Jones, M. Taillefert, and T. J. Dichristina. 2010. Siderophores Are Not Involved in Fe(III) Solubilization during Anaerobic Fe(III) Respiration by Shewanella oneidensis MR-1. Appl. Environ. Microbiol. **76:** 2425-2432.

Fike, D. A., N. Finke, J. Zha, G. Blake, T. M. Hoehler, and V. J. Orphan. 2009. The effect of sulfate concentration on (sub)millimeter-scale sulfide delta S-34 in hypersaline cyanobacterial mats over the diurnal cycle. Geochim. Cosmochim. Acta **73:** 6187-6204.

Forster, S., M. Huettel, and W. Ziebis. 1996. Impact of boundary layer flow velocity on oxygen utilisation in coastal sediments. Mar. Ecol.-Prog. Ser. **143:** 173-185.

Franke, U., L. Polerecky, E. Precht, and M. Huettel. 2006. Wave tank study of particulate organic matter degradation in permeable sediments. Limnol. Oceanogr. **51:** 1084-1096.

Friedrich, C. G., F. Bardischewsky, D. Rother, A. Quentmeier, and J. Fischer. 2005. Prokaryotic sulfur oxidation. Curr. Opin. Microbiol. **8:** 253-259.

Friedrichs, C. T., and D. G. Aubrey. 1994. Tidal propagation in strongly convergent channels J. Geophys. Res.-Oceans **99:** 3321-3336.

Frigaard, N., and C. Dahl. 2009. Sulfur metabolism in phototropic bacteria. Advances in Microbial Physiology. Elsevier.

Froelich, P. N. and others 1979. Early oxidation of organic matter in pelagic sediments of the eastern equatorial Atlantic - Suboxic diagenesis. Geochim. Cosmochim. Acta **43:** 1075-1090.

Furukawa, Y., S. J. Bentley, and D. L. Lavoie. 2001. Bioirrigation modeling in experimental benthic mesocosms. J. Mar. Res. **59:** 417-452.

Giblin, A. E., C. S. Hopkinson, and J. Tucker. 1997. Benthic metabolism and nutrient cycling in Boston Harbor, Massachusetts. Estuaries **20:** 346-364.

Glud, R., and J. Gundersen. 2002. Exchange and microdistribution of solutes at the benthic interface: An in situ study in Aarhus Bight, Denmark, p. 144-161. *In* M. Taillefert and T. F. Rozan [eds.], Environmental Electrochemistry: Analyses of Trace Element Biogeochemistry. ACS Symposium Series. American Chemical Society.

Glud, R. N., F. Wenzhofer, A. Tengberg, M. Middelboe, K. Oguri, and H. Kitazato. 2005. Distribution of oxygen in surface sediments from central Sagami Bay, Japan: In situ measurements by microelectrodes and planar optodes. Deep-Sea Res. Part I-Oceanogr. Res. Pap. **52:** 1974-1987.

Green, M. A., J. D. Gulnick, N. Dowse, and P. Chapman. 2004. Spatiotemporal patterns of carbon remineralization and bio-irrigation in sediments of Casco Bay Estuary, Gulf of Maine. Limnol. Oceanogr. **49:** 396-407.

Green, S. J., C. Blackford, P. Bucki, L. L. Jahnke, and L. Prufert-Bebout. 2008. A salinity and sulfate manipulation of hypersaline microbial mats reveals stasis in the cyanobacterial community structure. Isme J. **2:** 457-470.

Guo, X. H., M. H. Dai, W. D. Zhai, W. J. Cai, and B. S. Chen. 2009. CO2 flux and seasonal variability in a large subtropical estuarine system, the Pearl River Estuary, China. J. Geophys. Res.-Biogeosci. **114:** 14.

Hagy, J. D., W. R. Boynton, C. W. Keefe, and K. V. Wood. 2004. Hypoxia in Chesapeake Bay, 1950-2001: Long-term change in relation to nutrient loading and river flow. Estuaries **27:** 634-658.

Hakanson, L. 2006. The relationship between salinity, suspended particulate matter and water clarity in aquatic systems. Ecol. Res. **21:** 75-90.

Hall, P. O., and R. C. Aller. 1992. Rapid, small-volume, flow injection analysis for Sigma-CO2 and NH4+ in marine and fresh waters Limnol. Oceanogr. **37:** 1113-1119.

Hammond, D. E., K. M. Cummins, J. Mcmanus, W. M. Berelson, G. Smith, and F. Spagnoli. 2004. Methods for measuring benthic nutrient flux on the California Margin: Comparing shipboard core incubations to in situ lander results. Limnol. Oceanogr. Meth. **2:** 146-159.

Hansen, T. A. 1994. Metabolism of sulfate-reducing prokaryotes. Antonie Van Leeuwenhoek **66:** 165-185.

Hedges, J. I., J. A. Baldock, Y. Gelinas, C. Lee, M. L. Peterson, and S. G. Wakeham. 2002. The biochemical and elemental compositions of marine plankton: A NMR perspective. Mar. Chem. **78:** 47-63.

Hedges, J. I., R. G. Keil, and R. Benner. 1997. What happens to terrestrial organic matter in the ocean? Org. Geochem. **27:** 195-212.

Herdan, J. and others 1998. Field evaluation of an electrochemical probe for in situ screening of heavy metals in groundwater. Environ. Sci. Technol. **32:** 131-136.

Hines, M. E., S. L. Knollmeyer, and J. B. Tugel. 1989. Sulfate reduction and other sedimentary biogeochemistry in a northern New England salt marsh Limnol. Oceanogr. **34:** 578-590.

Hollins, S. E., S. F. Heron, and P. V. Ridd. 2009. Methods for monitoring tidal flushing in large animal burrows in tropical mangrove swamps. Estuar. Coast. Shelf Sci. **82:** 615-620.

Homoky, W. B., S. Severmann, R. A. Mills, P. J. Statham, and G. R. Fones. 2009. Pore-fluid Fe isotopes reflect the extent of benthic Fe redox recycling: Evidence from continental shelf and deep-sea sediments. Geology **37:** 751-754.

Howarth, R. W. 1984. The ecological significance of sulfur in the energy dynamics of salt marsh and coastal marine sediments. Biogeochemistry **1:** 5-27.

Howarth, R. W., and A. Giblin. 1983. Sulfate reduction in the salt marshes at Sapelo Island, Georgia Limnol. Oceanogr. **28:** 70-82.

Hu, Q. H., and M. L. Brusseau. 1994. The effect of solute size on diffusive disperisive transport in porous media. J. Hydrol. **158:** 305-317.

Huettel, M., and A. Rusch. 2000. Transport and degradation of phytoplankton in permeable sediment. Limnol. Oceanogr. **45:** 534-549.

Huettel, M., W. Ziebis, S. Forster, and G. W. Luther. 1998. Advective transport affecting metal and nutrient distributions and interfacial fluxes in permeable sediments. Geochim. Cosmochim. Acta **62:** 613-631.

Hyun, J. H., A. C. Smith, and J. E. Kostka. 2007. Relative contributions of sulfate- and iron(III) reduction to organic matter mineralization and process controls in contrasting habitats of the Georgia saltmarsh. Appl. Geochem. **22:** 2637-2651.

Jahnke, R. A., C. R. Alexander, and J. E. Kostka. 2003. Advective pore water input of nutrients to the Satilla River Estuary, Georgia, USA. Estuar. Coast. Shelf Sci. **56:** 641-653.

Jahnke, R. A., and M. B. Christiansen. 1989. A free-vehicle benthic chamber instrument for sea floor studies Deep-Sea Research Part a-Oceanographic Research Papers **36:** 625-637.

Jahnke, R. A., D. B. Craven, D. C. Mccorkle, and C. E. Reimers. 1997. CaCO3 dissolution in California continental margin sediments: The influence of organic matter remineralization. Geochim. Cosmochim. Acta **61:** 3587-3604.

Javor, B. 1989. Hypersaline Environments: Microbiology and Biogeochemistry. Springer-Verlag.

Jones, M. E., C. M. Fennessey, T. J. Dichristina, and M. Taillefert. 2010. Shewanella oneidensis MR-1 mutants selected for their inability to produce soluble organic-Fe(III) complexes are unable to respire Fe(III) as anaerobic electron acceptor. Environ. Microbiol. **12:** 938-950.

Jorgensen, B. B. 1982. Mineralization of organic matter in the sea bed - The role of sulfate reduction Nature **296:** 643-645.

Kelly, D. P., and A. P. Wood. 2000. Reclassification of some species of Thiobacillus to the newly designated genera Acidithiobacillus gen. nov., Halothiobacillus gen. nov and Thermithiobacillus gen. nov. Int. J. Syst. Evol. Microbiol. **50:** 511-516.

King, D. W., H. A. Lounsbury, and F. J. Millero. 1995. Rates and mechanism of Fe(II) oxidation at nanomolar total iron concentrations Environ. Sci. Technol. **29:** 818-824.

Kobayashi, K., Y. Seki, and M. Ishimoto. 1974. Biochemical studies on sulfate-reducing bacteria - Sulfide reductase from Desulfovibrio vulgaris - Mechanism of trithionate, thiosulfate, and sulfide formation and enzymatic properties. J. Biochem. **75:** 519-529.

Konhauser, K. 2007. Introduction to Geomicrobiology, 1st ed. Blackwell Science Ltd.

Koretsky, C. M., M. Haveman, A. Cuellar, L. Beuving, T. Shattuck, and M. Wagner. 2008. Influence of Spartina and Juncus on Saltmarsh Sediments. I. Pore Water Geochemistry. Chem. Geol. **255:** 87-99.

Koretsky, C. M., C. Meile, and P. Van Cappellen. 2002. Quantifying bioirrigation using ecological parameters: a stochastic approach. Geochem. Trans. **3:** 17-30.

Kostka, J. E., B. Gribsholt, E. Petrie, D. Dalton, H. Skelton, and E. Kristensen. 2002. The rates and pathways of carbon oxidation in bioturbated saltmarsh sediments. Limnol. Oceanogr. **47:** 230-240.

Laverman, A. M., C. Meile, P. Van Cappellen, and E. B. A. Wieringa. 2007. Vertical distribution of denitrification in an estuarine sediment: Integrating sediment flowthrough reactor experiments and microprofiling via reactive transport modeling. Appl. Environ. Microbiol. **73:** 40-47.

Lee, R. W. 2003. Physiological adaptations of the invasive cordgrass Spartina anglica to reducing sediments: rhizome metabolic gas fluxes and enhanced O-2 and H2S transport. Mar. Biol. **143:** 9-15.

Ley, R. E. and others 2006. Unexpected diversity and complexity of the Guerrero Negro hypersaline microbial mat. Appl. Environ. Microbiol. **72:** 3685-3695.

Li, H. Y., M. R. Sawaya, F. R. Tabita, and D. Eisenberg. 2005. Crystal structure of a RuBisCO-like protein from the green sulfur bacterium Chibrobium tepidum. Structure **13:** 779-789.

Litchfield, C. D., A. Irby, and R. H. Vreeland. 1999. The Microbial Ecology of Solar Salt Plants, p. 39 - 52. *In* A. Oren [ed.], Microbiology and Biogeochemistry of Hypersaline Environments. The Microbiology of Extreme and Unusual Environments. CRC Press.

Liu, K. and others 2000. Exploring Continental Margin Carbon Fluxes on a Global Scale. E.O.S. **81**.

Lowe, K. L., T. J. Dichristina, A. N. Roychoudhury, and P. Van Cappellen. 2000. Microbiological and geochemical characterization of microbial Fe(III) reduction in salt marsh sediments. Geomicrobiol. J. **17:** 163-176.

Luther, G. W. and others 2008. Use of voltammetric solid-state (micro)electrodes for studying biogeochemical processes: Laboratory measurements to real time measurements with an in situ electrochemical analyzer (ISEA). Mar. Chem. **108:** 221-235.

Luther, G. W., J. E. Kostka, T. M. Church, B. Sulzberger, and W. Stumm. 1992. Seasonal iron cycling in the salt marsh sedimentary environment - The importance of ligand complexes with Fe(II) and Fe(III) in the dissolution of Fe(III) minerals and pyrite, respectively. Mar. Chem. **40:** 81-103.

Luther, G. W., C. E. Reimers, D. B. Nuzzio, and D. Lovalvo. 1999. In situ deployment of voltammetric, potentiometric. and amperometric microelectrodes from a ROV to determine dissolved O-2, Mn, Fe, S(-2), and pH in porewaters. Environ. Sci. Technol. **33:** 4352-4356.

Mann, C. J., and R. G. Wetzel. 2000. Hydrology of an impounded lotic wetland - Wetland sediment characteristics. Wetlands **20:** 23-32.

Mantoura, R. F. C., J. M. Martin, and R. Wollast. 1991. Ocean Margin Processes in Global Change. John Wiley.

Marinelli, R. L., R. A. Jahnke, D. B. Craven, J. R. Nelson, and J. E. Eckman. 1998. Sediment nutrient dynamics on the South Atlantic Bight continental shelf. Limnol. Oceanogr. **43:** 1305-1320.

Martin, J. H., G. A. Knauer, D. M. Karl, and W. W. Broenkow. 1987. VERTEX - Carbon cycling in the Northeast Pacific. Deep-Sea Research Part a-Oceanographic Research Papers **34:** 267-285.

Martin, W. R., and F. L. Sayles. 1987. Seasonal cycles of particle and solute transport processes in nearshore sediments - Rn-222/Ra-226 and Th-234/U-238 disequilibrium at a site in Buzzards Bay, MA Geochim. Cosmochim. Acta **51:** 927-943.

Mckee, B. A., R. C. Aller, M. A. Allison, T. S. Bianchi, and G. C. Kineke. 2004. Transport and transformation of dissolved and particulate materials on continental margins influenced by major rivers: benthic boundary layer and seabed processes. Cont. Shelf Res. **24:** 899-926.

Mckenzie, C., S. Schiff, R. Aravena, C. Kelly, and V. S. Louis. 1998. Effect of temperature on production of CH4 and CO2 from peat in a natural and flooded boreal forest wetland. Clim. Change **40:** 247-266.

Mcmanus, J., W. M. Berelson, K. H. Coale, K. S. Johnson, and T. E. Kilgore. 1997. Phosphorus regeneration in continental margin sediments. Geochim. Cosmochim. Acta **61:** 2891-2907.

Mendelssohn, I. A., and M. T. Postek. 1982. Elemental analysis of deposits on the roots of *Spartina alterniflora loisel* American Journal of Botany **69:** 904-912.

Metz, B., O. R. Davidson, P. R. Bosch, R. Dave, and L. A. Meyer. 2007. Climate Change 2007: Mitigation of Climate Change. Intergovernmental Panel on Climate Change.

Middelboe, M., R. N. Glud, and K. Finster. 2003. Distribution of viruses and bacteria in relation to diagenetic activity in an estuarine sediment. Limnol. Oceanogr. **48:** 1447-1456.

Middelburg, J. J., and P. M. J. Herman. 2007. Organic matter processing in tidal estuaries. Mar. Chem. **106:** 127-147.

Miller, H. L., C. Meile, and A. B. Burd. 2007. A novel 2D model of internal O-2 dynamics and H2S intrusion in seagrasses. Ecol. Model. **205:** 365-380.

Mitsch, W. J., and J. G. Gosselink. 1993. Wetlands, 2nd ed. Van Nostrand Reinhold.

Mitsch, W. J., J. S. Yan, and J. K. Cronk. 1993. Ecological engineering - Contrasting experiences in China with the West Ecol. Eng. **2:** 177-191.

Moore, T. S., D. B. Nuzzio, D. M. Di Toro, and G. W. Luther. 2009. Oxygen dynamics in a well mixed estuary, the lower Delaware Bay, USA. Mar. Chem. **117:** 11-20.

Morgan, J. J. 2005. Kinetics of reaction between O-2 and Mn(II) species in aqueous solutions. Geochim. Cosmochim. Acta **69:** 35-48.

Morris, J. T. 2006. Competition among marsh macrophytes by means of geomorphological displacement in the intertidal zone. Estuar. Coast. Shelf Sci. **69:** 395-402.

Morris, J. T., P. V. Sundareshwar, C. T. Nietch, B. Kjerfve, and D. R. Cahoon. 2002. Responses of coastal wetlands to rising sea level. Ecology **83:** 2869-2877.

Morse, J. W., J. C. Cornwell, T. Arakaki, S. Lin, and M. Huertadiaz. 1992. Iron sulfide and carbonate mineral diagenesis in Baffin Bay, Texas. Journal of Sedimentary Petrology **62:** 671-680.

Mortazavi, B., R. L. Iverson, W. M. Landing, F. G. Lewis, and W. R. Huang. 2000. Control of phytoplankton production and biomass in a river-dominated estuary: Apalachicola Bay, Florida, USA. Mar. Ecol.-Prog. Ser. **198:** 19-31.

Muller-Karger, F. E., R. Varela, R. Thunell, R. Luerssen, C. M. Hu, and J. J. Walsh. 2005. The importance of continental margins in the global carbon cycle. Geophys. Res. Lett. **32:** 4.

Murphy, J., and J. P. Riley. 1962. A modified single solution method for determination of phosphate in natural waters. Anal. Chim. Acta **26:** 31-&.

Nealson, K. H. 1997. Sediment bacteria: Who's there, what are they doing, and what's new? Annu. Rev. Earth Planet. Sci. **25:** 403-434.

Oren, A. 2005. Microscopic examination of microbial communities along a salinity gradient in saltern evaporation ponds: a 'halophilic safari'. *In* N. Gunde-Cimerman, A. Oren and A. Plemenitas [eds.], Adaptation to Life at High Salt Concentrations in Archaea, Bacteria, and Eukarya. Springer.

Osgood, D. T. 2000. Subsurface hydrology and nutrient export from barrier island marshes at different tidal ranges. Wetlands Ecology and Management **8:** 133-146.

Otero, X. L., J. M. Sanchez, and F. Macias. 2000. Nutrient status in tall and short forms of Spartina maritima in the salt marshes of ortigueira (NW Iberian Peninsula) as related to physicochemical properties of the soils. Wetlands **20:** 461-469.

Pace, M. L., G. A. Knauer, D. M. Karl, and J. H. Martin. 1987. Primary production, new production, and vertical flux in the Eastern Pacific Ocean. Nature **325:** 803-804.

Pallud, C., C. Meile, A. M. Laverman, J. Abell, and P. Van Cappellen. 2007. The use of flow-through sediment reactors in biogeochemical kinetics: Methodology and examples of applications. Mar. Chem. **106:** 256-271.

Patritskaya, V. Y., M. Y. Grabovich, M. S. Muntyan, and G. A. Dubinina. 2001. Lithoautotrophic growth of the freshwater colorless sulfur bacterium Beggiatoa "leptomitiformis" D-402. Microbiology **70:** 145-150.

Perdue, E. M. 2009. Natural organic matter, p. 806-819. *In* G. E. Likens [ed.], Encyclopedia of Inland Waters. Elsevier.

Peterson, B. J., and R. W. Howarth. 1987. Sulfur, carbon, and nitrogen isotopes used to trace organic matter flow in the salt marsh estuaries of Sapelo Island, Georgia Limnol. Oceanogr. **32:** 1195-1213.

Pierson, B., A. Oesterle, and G. L. Murphy. 1987. Pigments, light penetration, and photosynthetic activity in the multi-layered microbial mats of Great Sippewissett salt marsh in Massachusetts. FEMS Microbiol. Ecol. **45:** 365-376.

Pilson, M. E. 1998. An Introduction to the Chemistry of the Sea, 1st ed. Prentice Hall.

Plant, J. N., K. S. Johnson, J. A. Needoba, and L. J. Coletti. 2009. NH4-Digiscan: an in situ and laboratory ammonium analyzer for estuarine, coastal, and shelf waters. Limnol. Oceanogr. Meth. **7:** 144-156.

Point, D. and others 2007. Biological control of trace metal and organometal benthic fluxes in a eutrophic lagoon (Thau Lagoon, Mediterranean Sea, France). Estuar. Coast. Shelf Sci. **72:** 457-471.

Pomeroy, L. R., J. E. Sheldon, W. M. Sheldon, J. O. Blanton, J. Amft, and F. Peters. 2000. Seasonal changes in microbial processes in estuarine and continental shelf waters of the south-eastern USA. Estuar. Coast. Shelf Sci. **51:** 415-428.

Pomeroy, L. R., and R. G. Wiegert. 1981. The Ecology of a Salt Marsh, 1 ed. Springer-Verlag.

Postma, D. 1982. Pyrite and siderite formation in brackish and fresh water swamp sediments. Am. J. Sci. **282:** 1151-1183.

Pratihary, A. K. and others 2009. Benthic fluxes in a tropical Estuary and their role in the ecosystem. Estuar. Coast. Shelf Sci. **85:** 387-398.

Rabouille, C., and J. F. Gaillard. 1990. The validity of steady-state flux calculation in early diagenesis - A computer-simulation of deep-sea silica diagenesis Deep-Sea Research Part a-Oceanographic Research Papers **37:** 625-646.

Ram, A. S. P., S. Nair, and D. Chandramohan. 2003. Seasonal shift in net ecosystem production in a tropical estuary. Limnol. Oceanogr. **48:** 1601-1607.

Rao, A. M. F., and R. A. Jahnke. 2004. Quantifying porewater exchange across the sediment-water interface in the deep sea with in situ tracer studies. Limnol. Oceanogr. Meth. **2:** 75-90.

Rao, A. M. F., M. J. Mccarthy, W. S. Gardner, and R. A. Jahnke. 2008. Respiration and denitrification in permeable continental shelf deposits on the South Atlantic Bight: N-2 : Ar and isotope pairing measurements in sediment column experiments. Cont. Shelf Res. **28:** 602-613.

Reimers, C. E. and others 2004. In situ measurements of advective solute transport in permeable shelf sands. Cont. Shelf Res. **24:** 183-201.

Rickard, D., and J. W. Morse. 2005. Acid volatile sulfide (AVS). Mar. Chem. **97:** 141-197.

Roychoudhury, A. N. 2001. Dispersion in unconsolidated aquatic sediments. Estuar. Coast. Shelf Sci. **53:** 745-757.

Rozan, T. F. and others 2002. Iron-sulfur-phosphorus cycling in the sediments of a shallow coastal bay: Implications for sediment nutrient release and benthic macroalgal blooms. Limnol. Oceanogr. **47:** 1346-1354.

Sarmiento, J. L., and N. Gruber. 2002. Sinks for anthropogenic carbon. Phys. Today **55:** 30-36.

Schilling, E. B., and B. G. Lockaby. 2006. Relationships between productivity and nutrient circulation within two contrasting southeastern US floodplain forests. Wetlands **26:** 181-192.

Seim, H. E., J. O. Blanton, and S. A. Elston. 2009. The effect of secondary circulation on the salt distribution in a sinuous coastal plain estuary: Satilla River, GA, USA. Cont. Shelf Res. **29:** 15-28.

Shen, Y. A., R. Buick, and D. E. Canfield. 2001. Isotopic evidence for microbial sulphate reduction in the early Archaean era. Nature **410:** 77-81.

Sholkovitz, E. R. 1976. Flocculation of dissolved organic and inorganic matter during mixing of river water and seawater Geochim. Cosmochim. Acta **40:** 831-845.

Skoog, D. A., F. J. Holler, and T. A. Nieman. 1998. Principles of Instrumental Analysis. Thompson Learning Inc.

Solomon, D. and others 2007. Long-term impacts of anthropogenic perturbations on dynamics and speciation of organic carbon in tropical forest and subtropical grassland ecosystems. Glob. Change Biol. **13:** 511-530.

Sottile, W. S. 1973. Studies of microbial production and utilization of dissolved organic carbon in a Georgia salt marsh-estuarine ecosystem. Ph.D. University of Georgia.

Spear, J. R., R. E. Ley, A. B. Berger, and N. R. Pace. 2003. Complexity in natural microbial ecosystems: The Guerrero Negro experience. Biol. Bull. **204:** 168-173.

Stal, L. J. 1991. The metabolic versatility of the mat-building cyanobacteria *Microcoleus chthonoplastes* and *Oscillatoria limosa* and its ecological significance Arch. Hydrobiol.**:** 453-467.

---. 1995. Physiological ecology of cyanobacteria in microbial mats and other communities. New Phytol. **131:** 1-32.

Stal, L. J., H. Vangemerden, and W. E. Krumbein. 1985. Structure and development of a benthic marine microbial mat FEMS Microbiol. Ecol. **31:** 111-125.

Steuber, J., H. Cypionka, and P. M. H. Kroneck. 1994. Mechanism of dissimilatory sulfite reduction by Desulfovibrio desulfuricans - Purification of a membrane-bound sulifite reductase and coupling with cytochrome C(3) and hydrogenase Arch. Microbiol. **162:** 255-260.

Stookey, L. L. 1970. Ferrozine - A new spectrophotometric reagent for iron. Anal. Chem. **42:** 779-&.

Sundby, B., C. Vale, I. Cacador, F. Catarino, M. J. Madureira, and M. Caetano. 1998. Metal-rich concretions on the roots of salt marsh plants: Mechanism and rate of formation. Limnol. Oceanogr. **43:** 245-252.

Taillefert, M., A. B. Bono, and G. W. Luther. 2000. Reactivity of freshly formed Fe(III) in synthetic solutions and (pore)waters: Voltammetric evidence of an aging process. Environ. Sci. Technol. **34:** 2169-2177.

Taillefert, M., V. C. Hover, T. F. Rozan, S. M. Theberge, and G. W. Luther. 2002a. The influence of sulfides on soluble organic-Fe(III) in anoxic sediment porewaters. Estuaries **25:** 1088-1096.

Taillefert, M., S. Neuhuber, and G. Bristow. 2007. The effect of tidal forcing on biogeochemical processes in intertidal salt marsh sediments. Geochem. Trans. **8:** 15.

Taillefert, M., T. F. Rozan, B. T. Glazer, J. Herszage, R. E. Trouwborst, and G. W. Luther. 2002b. Seasonal variations of soluble organic-Fe(III) in sediment porewaters as revealed by voltammetric microelectrodes, p. 247-264. *In* M. Taillefert and T. F. Rozan [eds.], Environmental Electrochemistry: Analyses of Trace Element Biogeochemistry. ACS Symposium Series. American Chemical Society.

Taljaard, S., L. Van Niekerk, and W. Joubert. 2009. Extension of a qualitative model on nutrient cycling and transformation to include microtidal estuaries on wave-dominated coasts: Southern hemisphere perspective. Estuar. Coast. Shelf Sci. **85:** 407-421.

Teal, J. M. 1958. Distribution of Fiddler crabs in Georgia salt marshes. Ecology **39:** 185-193.

---. 1962. Energy-flow in salt marsh ecosystems of Georgia. Ecology **43:** 614-&.

Teal, J. M., and Kanwishe.Jw. 1966. Gas transport in marsh grass *Spartina alterniflora*. Journal of Experimental Botany **17:** 355-&.

Tercier-Waeber, M. L., and M. Taillefert. 2008. Remote in situ voltammetric techniques to characterize the biogeochemical cycling of trace metals in aquatic systems. J. Environ. Monit. **10:** 30-54.

Tercier, M. L., J. Buffle, A. Zirino, and R. R. Devitre. 1990. In situ voltammetric measurement of trace-elements in lakes and oceans. Anal. Chim. Acta **237:** 429-437.

Thamdrup, B., K. Finster, J. W. Hansen, and F. Bak. 1993. Bacterial disproportionation of elemental sulfur coupled to chemical reduction of iron or manganese. Appl. Environ. Microbiol. **59:** 101-108.

Ullman, W. J., and R. C. Aller. 1982. Diffusion coefficients in nearshore marine sediments Limnol. Oceanogr. **27:** 552-556.

Van Leeuwen, S. M., H. M. Schuttelaars, and H. E. De Swart. 2000. Tidal and morphologic properties of embayments: Effect of sediment deposition processes and length variation. Phys. Chem. Earth Pt B-Hydrol. Oceans Atmos. **25:** 365-368.

Vangemerden, H. 1993. Microbial mats - A joint venture. Mar. Geol. **113:** 3-25.

Vangemerden, H., R. Dewit, C. S. Tughan, and R. A. Herbert. 1989. Development of mass blooms of *Thiocapsa roseopersicina* on sheltered beaches on the Orkney Islands. FEMS Microbiol. Ecol. **62:** 111-118.

Ver, L. M. B., F. T. Mackenzie, and A. Lerman. 1999. Carbon cycle in the coastal zone: effects of global perturbations and change in the past three centuries. Chem. Geol. **159:** 283-304.

Visscher, P. T., P. Quist, and H. Vangemerden. 1991. Methylated sulfur compounds in microbial mats - In situ concentrations and metabolism by a colorless sulfur bacterium. Appl. Environ. Microbiol. **57:** 1758-1763.

Visscher, P. T., F. P. Vandenende, B. E. M. Schaub, and H. Vangemerden. 1992. Competition between anoxygenic phototrophic bacteria and colorless sulfur bacteria in a microbial mat. FEMS Microbiol. Ecol. **101:** 51-58.

Warnken, K. W., G. A. Gill, L. L. Griffin, and P. H. Santschi. 2001. Sediment-water exchange of Mn, Fe, Ni and Zn in Galveston Bay, Texas. Mar. Chem. **73:** 215-231.

Wei, H., Y. C. He, Q. J. Li, Z. Y. Liu, and H. T. Wang. 2007. Summer hypoxia adjacent to the Changjiang Estuary. J. Mar. Syst. **67:** 292-303.

Wenzhofer, F., and R. N. Glud. 2002. Benthic carbon mineralization in the Atlantic: a synthesis based on in situ data from the last decade. Deep-Sea Res. Part I-Oceanogr. Res. Pap. **49:** 1255-1279.

---. 2004. Small-scale spatial and temporal variability in coastal benthic O-2 dynamics: Effects of fauna activity. Limnol. Oceanogr. **49:** 1471-1481.

Wenzhofer, F., O. Greeff, and W. Riess. 2002. Benthic carbon mineralization in sediments of Gotland Basin, Baltic Sea, measured in situ with benthic landers, p. 162 - 187. *In* M. Taillefert and T. F. Rozan [eds.], Environmental Electrochemistry: Analyses of Trace Element Biogeochemistry. ACS Symposium Series. American Chemical Society.

Wenzhofer, F., O. Holby, R. N. Glud, H. K. Nielsen, and J. K. Gundersen. 2000. In situ microsensor studies of a shallow water hydrothermal vent at Milos, Greece. Mar. Chem. **69:** 43-54.

Wirsen, C. O. and others 2002. Characterization of an autotrophic sulfide-oxidizing marine Arcobacter sp that produces filamentous sulfur. Appl. Environ. Microbiol. **68:** 316-325.

Wollast, R. 2003. Continental Margins: Review of Geochemical Settings. Springer.

Wollast, R., and L. Chou. 1998. Distribution and fluxes of calcium carbonate along the continental margin in the Gulf of Biscay. Aquat. Geochem. **4:** 369-393.

Zhang, J. H., L. W. Lion, Y. M. Nelson, M. L. Shuler, and W. C. Ghiorse. 2002. Kinetics of Mn(II) oxidation by Leptothrix discophora SS1. Geochim. Cosmochim. Acta **66:** 773-781.

Zhang, J. Z., and F. J. Millero. 1993. The products from the oxidation of H2S in seawater Geochim. Cosmochim. Acta **57:** 1705-1718.

Ziebis, W., M. Huettel, and S. Forster. 1996. Impact of biogenic sediment topography on oxygen fluxes in permeable seabeds. Mar. Ecol.-Prog. Ser. **140:** 227-237.